THERMOCHEMISTRY AND REACTIVITY OF GADOLINIUM CATION (Gd^+): ENERGETICS AND MECHANISTIC INSIGHTS FOR REACTIONS WITH HYDROGEN, ITS ISOTOPOLOGUES, AND VARIOUS OXIDES

by

Maria Plamenova Demireva

A dissertation submitted to the faculty of
The University of Utah
in partial fulfillment of the requirements for the degree of

Doctor of Philosophy

Department of Chemistry

The University of Utah

May 2018

The University of Utah Graduate School

STATEMENT OF DISSERTATION APPROVAL

The dissertation of **Maria Plamenova Demireva**

has been approved by the following supervisory committee members:

Peter B. Armentrout	, Chair	**12/13/2017** Date Approved
Michael D. Morse	, Member	**12/13/2017** Date Approved
Scott L. Anderson	, Member	**12/13/2017** Date Approved
Michael Grünwald	, Member	**12/13/2017** Date Approved
Michael P. Hoepfner	, Member	**12/13/2017** Date Approved

and by **Cynthia J. Burrows** , Chair/Dean of

the Department/College/School of **Chemistry**

and by David B. Kieda, Dean of The Graduate School.

ABSTRACT

The lanthanides that make up the f-block of the periodic table remain fairly unexplored experimentally such that there is a need for thermochemical information regarding these elements to better understand their reactivity and properties, including, for example, their potential usefulness as catalysts in organometallic and oxidation catalysis. In addition, these heavy elements are difficult to describe theoretically because of spin-orbit and relativistic effects and the many electronic configurations possible from the 4f electrons. Accurate thermochemistry measured from gas-phase experiments, where systems can be probed in isolation from solvent or substrate molecules, can serve as useful benchmarks for evaluating theoretical methods. The work described in this dissertation focuses on examining the gas-phase reactivity and thermochemistry of the lanthanide gadolinium cation (Gd^+). Gd^+ is found in the middle of the lanthanide series and has a $4f^7 6s^1 5d^1$ ground state valence electron configuration. This configuration (with two non-4f electrons) is unusual compared with most lanthanide cations, which typically have $4f^n 6s^1$ configurations (n corresponding to the remaining valence electrons). Guided ion beam tandem mass spectrometry (GIBMS) is used here to investigate and measure the thermochemistry of the gas-phase activation of H_2, O_2, and CO_2 by Gd^+. Potential energy surfaces for the oxidation reactions with O_2 and CO_2 are characterized in great detail from these experiments. Quantum chemical calculations are performed and provide insight into the electronic states of the species probed in the experiments and a detailed understanding

of the reaction mechanisms. Periodic trends are elucidated, where results indicate that Gd^+ generally behaves more similarly to the group 3 transition metal cations scandium (Sc^+) and yttrium (Y^+) than to most lanthanide cations, which is attributable to similarities and differences in the electronic ground states of these ions, respectively. The extensive thermochemistry determined for Gd^+ in this work can serve as valuable standards for comparing theoretical calculations against. Moreover, the mechanistic insights provided by these studies for the activation of H_2, O_2, and CO_2 by Gd^+ can potentially be useful in understanding the activation in analogous reactions with other metals, where this information can potentially lead to insight beneficial for the design of more effective catalysts.

To my family:
My best friend Philip, my parents Iana and Plamen, and my twin-brother Atanas.

“Strength and courage aren’t always measured in medals and victories. They are measured in the struggles they overcome. The strongest people aren’t always the people who win, they are the people who don’t give up when they lose.”

Ashley Hodgeson

TABLE OF CONTENTS

ACKNOWLEDGEMENTS

First and foremost, I would like to thank my Ph.D. advisor Professor Peter B. Armentrout. He has shown me what it means to have a great mentor, one who truly cares about the science, one who works with you, and one who encourages your ambitions and wants you to succeed. Not only have I learned a great deal from Peter, but I will forever be grateful for his tremendous help and support and for the opportunities he has given me.

Next, I would like to thank my committee members Professors Michael D. Morse, Scott L. Anderson, Michael Grünwald, and Michael Hoepfner for their kindness, time, enthusiasm, and support. To Michael Morse and Scott, I am also grateful for taking their classes, which I thoroughly enjoyed and the knowledge I gained has helped me in the research presented here. I also want to express my gratitude to the Armentrout group, especially to Mr. JungSoo Kim who introduced me to the instrumentation and experiments and to Dr. Christopher McNary who was always willing to help with troubleshooting.

Lastly, I am thankful to my family for their endless love, support, and encouragement. Without them, maneuvering through this part of my life would have been extremely difficult.

Thank you! Tack! Благодаря!

CHAPTER 1

INTRODUCTION

1.1 Bond Activation by Metals

Bond making and bond breaking are the essence of chemistry. A central focus of catalysis research is to understand and control bond activation, where such knowledge can greatly benefit various industrial and synthetic processes. For example, in organometallic catalysis, the controlled activation of hydrocarbons could lead to more efficient fuel sources[1,2] and the conversion of carbon dioxide into a more useful form has the promise to be utilized in chemical synthesis as a natural source of carbon.[3-6] Removing and reusing CO_2 for such purposes could also benefit the environment because of the effect of CO_2 as a greenhouse gas. In this regard, methods using green chemistry are also being explored for the controlled and selective oxidation of organic molecules, including hydrocarbons. A possible route is by forming two high-valent oxido-metal species from activation of the oxygen molecule via a dioxygenase mechanism.[7] However, the relatively strong bonds in the aforementioned molecules make them fairly inert and to induce activation requires use of catalysts, such as metals. These catalysts can be used not only to lower the barriers of activation, but from careful consideration of the properties of the catalyst, guide the process along a desired reaction pathway. Understanding the fundamental interactions involved between the metal catalyst and target molecule can provide critical insight into the

activation process and the properties of the catalyst. Probing these interactions directly, without interference from solvent and substrate molecules, can be performed using gas phase experiments.[8,9] Although the results from gas phase studies are not directly comparable to those from solution phase catalysis (which include effects of counter ions and effects of the substrate or solvent that functions as a thermal bath to dissipate excess energy), they can still provide information about the energetics, the fundamental steps, and the intermediates involved and reveal, for example, the role of the electronic structure of the metal in the activation process. Such insight can be extended to more complicated systems and aid in the design of new and more effective catalysts targeting specific reaction pathways.

1.2 Reactivities and Energetics from Gas Phase Studies

Unlike neutrals, ions can easily be manipulated with electric fields and detected in the gas phase. Thus, most gas-phase research on metals has involved studying the chemistry of metal ions. Gas phase reactions of metal cations and their complexes with neutrals at thermal energies have been studied using sector-type instruments, trapping, and flow tube techniques,[9] including ion cyclotron resonance (ICR)[10-16] and selected-ion flow tube (SIFT) mass spectrometry.[17-21] Early work investigated the unimolecular decompositions of metastable metal ion complexes using sector type instruments.[22] However, only a limited type of system could be studied with this technique.[9] In contrast, ICR mass spectrometry, where ions are trapped in a cell and neutral reactants are introduced for reaction, has been used to investigate a much wider range of systems.[10-16] In the ICR experiments, the reaction can be monitored as a function of delay time, allowing

rate coefficients to be measured. Moreover, successive additions of the same or different neutrals can be performed to investigate consecutive reactions and observe complete catalytic cycles.[12-15] Some thermochemical information can be obtained from bracketing experiments that monitor the reactivity with neutral reactants having known bond energies.[12,23] Reactivities of several metal cations with various neutrals have also been investigated using SIFT coupled with an inductively coupled plasma (ICP) source (for metal cation generation).[17-21] In the SIFT experiments, ions pass through a reaction region, in which neutral reactants are introduced. This region is maintained at a relatively high pressure using a carrier gas such that reactants equilibrate to the temperature of the gas. Rate coefficients can be measured from analysis of the reactant and product ion profiles as a function of the neutral reactant flow.[21] Because reactivities are typically examined at thermal energies with the ICR and SIFT methods, primarily exothermic processes are investigated.

Detailed kinetic and thermochemical information can be obtained from studying the energy dependence of reactions in the gas phase, which also allows for examination of endothermic processes and those exhibiting an activation barrier. This can be accomplished using ion beam methods, where guided ion beam tandem mass spectrometry (GIBMS) has become an established technique for measuring accurately the bond energies and thermochemistry of various species and reactions.[24,25] In these experiments, reactions can be examined from thermal energies up to 1000 eV (in the lab frame). Product ion cross sections are measured as a function of energy and 0 K threshold energies for the processes are obtained through careful modeling of the data by taking into account effects of the internal and kinetic energy distributions of the reactants.[24,25] Thus, energetics can be

measured directly from experiment, where this thermochemistry can be useful in providing important insight into reaction mechanisms and be extended to other and more complicated processes to help determine their feasibility.

Because of the usefulness to organometallic catalysis, numerous GIBMS studies have focused on measuring the thermochemistry and providing understanding for the activation of C-H and C-C bonds by metal cations. In this regard, the activation of H_2 can serve as a simple model for the cleavage of single covalent bonds. Reactions of various metal cations with H_2 (HD and D_2) have been investigated extensively using GIBMS and hydride BDEs have been determined for most first,[26-33] second,[32-35] and third[36-42] row transition metal cations. Analysis of isotopic effects in the branching ratios of the product ions in reactions with HD have allowed for mechanistic information to be obtained.[43] The wealth of GIBMS results for the hydride systems have provided insight into periodic trends, where differences in reactivity have been explained by invoking molecular orbital concepts and spin conservation.

Several GIBMS experiments have also examined the reactivities of various transition metal cations and their oxides with O_2,[44-62] and CO_2.[51-54,60-64] Not only can such studies provide accurate thermochemistry for the activation of these small neutrals but they can also reveal details about the reaction mechanisms. Because the energetics of the intermediates can in many cases be characterized, nearly complete potential energy surfaces can be mapped. Many studies including those by GIBMS have predominantly explored the thermochemistry and reactivity of transition metals because of their distinct properties that arise from the variety of interactions and electronic configurations possible from the occupation of the d-orbitals. In contrast, somewhat fewer studies have

investigated the thermochemistry of the lanthanide metals, which form the f-block in the periodic table. As a result of the 4f electrons, the lanthanides can have many low-energy levels and be prone to low energy fluctuations in charge and spin, where these properties can make the lanthanides and their oxides potentially useful in catalysis.[65]

1.3 Lanthanide Oxidation Thermochemistry

Compared with most metals, many of the lanthanides (Ln) are unusual because they have larger metal oxide (MO) bond dissociation energies (D_0, BDE) than MO ionization energies (IE). This is because they can essentially form a triple bond with an O atom, where this is also true for the metal oxide cations (MO^+).[66] Effective binding is achieved from two electrons in 5d orbitals on Ln or Ln^+ that interact with the four 2p valence electrons of the O atom.[66] However, because many of the lanthanides do not have a $5d^2$ ground state configuration, promotion of 4f and/or 6s valence electrons to 5d orbitals is required to achieve the reactive configuration in Ln or Ln^+ from the ground state configurations. The LnO and LnO^+ BDEs have been shown to inversely correlate with the promotion energy cost needed to attain this reactive configuration.[66] Figure 1.1 demonstrates the inverse relationship (with a slope of -0.9) in the LnO^+ BDEs with the promotion energy cost of achieving the $5d^2$ configuration in Ln^+.[66-69] The oxide BDE for the promethium (Pm^+) cation is omitted because this element has no stable isotopes. The LnO^+ bond energies are largest for the lanthanum (La^+) and cerium (Ce^+) cations because these have $5d^2$ ground state electronic configurations and thus no promotion energy cost. For most other lanthanides, both a 6s and 4f electron must be promoted to 5d orbitals. Figure 1.1 indicates that the promotion energy cost increases across the period with increased 4f orbital

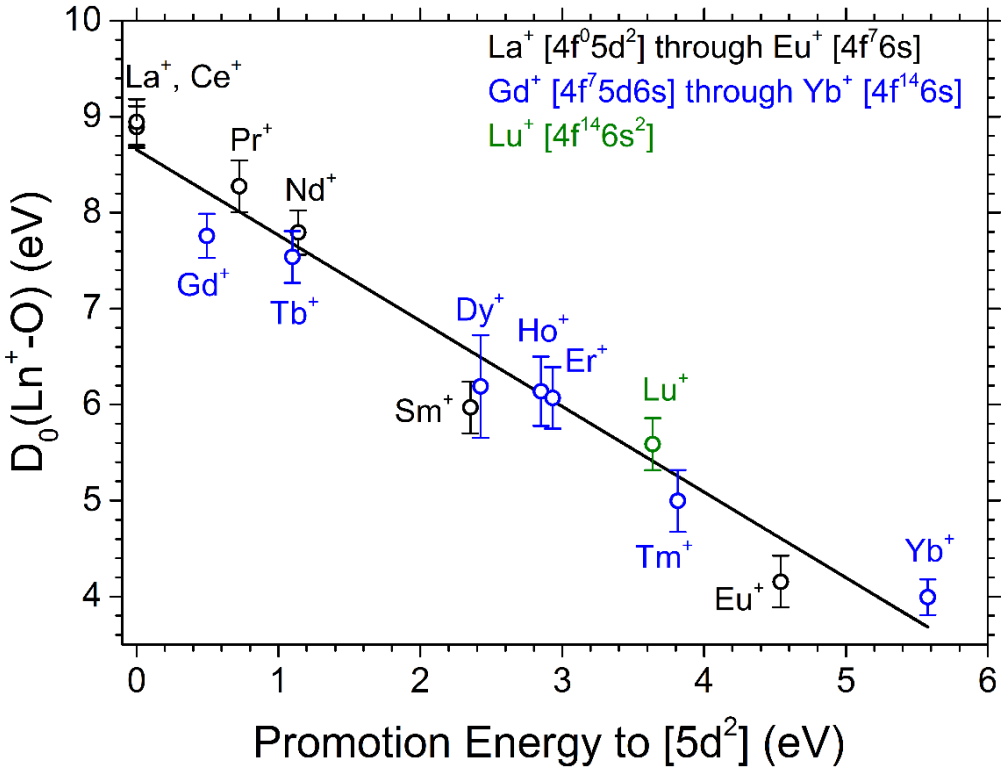

Figure 1.1. LnO^+ bond energies as a function of the promotion energy required to achieve a $5d^2$ electronic configuration in Ln^+ from the ground state electronic configuration. Bond energies are determined from references 67-69 using equation (1.2) and promotion energies are obtained from reference 66.

occupation for early (black) and late (blue) lanthanide cations. This trend can be attributed to the increasing nuclear charge along the lanthanide series that causes a larger energy separation between the 4f and 5d orbitals.

Because many lanthanides have larger metal oxide BDEs than IEs, they are expected to react exothermically via the chemi-ionization reaction (1.1), where a metal oxide cation is formed by releasing an electron from the association reaction of M and O:

$$M + O \rightarrow MO^+ + e^- \quad (1.1)$$

This reaction is anticipated to be exothermic for only a handful of other metals, besides many of the lanthanides, including some of the early transition metals.[70-72] A different

application for these unusual metal oxides has been proposed by the U. S. Air Force Research Laboratory (AFRL), where there has been a long-standing interest in creating artificial electron dense plasmas in the ionosphere (atmospheric altitudes > ~100 km) that can be used to prevent disruptions in satellite communications.[73] Because satellite communications work via radiowave transmissions, which depend on the electron density in the ionosphere,[73] naturally occurring electron density fluctuations can interrupt these communications. As one means to prevent such disruptions, AFRL researchers have proposed to generate electron enhanced plasmas in the ionosphere by releasing metals that can react exothermically with available oxygen atoms via process (1.1).[73]

The chemi-ionization reaction enthalpy, ΔH_{CI}, for (1.1) can be determined from two thermodynamic cycles using either $D_0(MO)$ and IE(MO), or $D_0(MO^+)$ and IE(M) as given in (1.2):

$$\Delta H_{CI} = IE(MO) - D_0(MO) = IE(M) - D_0(MO^+) \qquad (1.2)$$

From expression (1.2), possible candidates for the AFRL experiments that will exhibit exothermic reactions have larger $D_0(MO)$ than IE(MO) values, but can also be identified by having larger $D_0(MO^+)$ than IE(M) values. Figure 1.2 shows the IEs of the lanthanides (typically corresponding to the removal of one of the 6s electrons). These IEs generally increase along the lanthanide series because of the increasing nuclear charge resulting in more tightly bound 6s electrons. Gadolinium (Gd) and lutetium (Lu), with half- and completely filled 4f shells, respectively, deviate from the general trend where the lower IE for Lu corresponds to the energy for removal of a 5d rather than 6s electron. On the basis of the results in Figures 1.1 and 1.2, potential candidates for the atmospheric chemical release experiments, which will exhibit highly exothermic chemi-ionization reactions, are

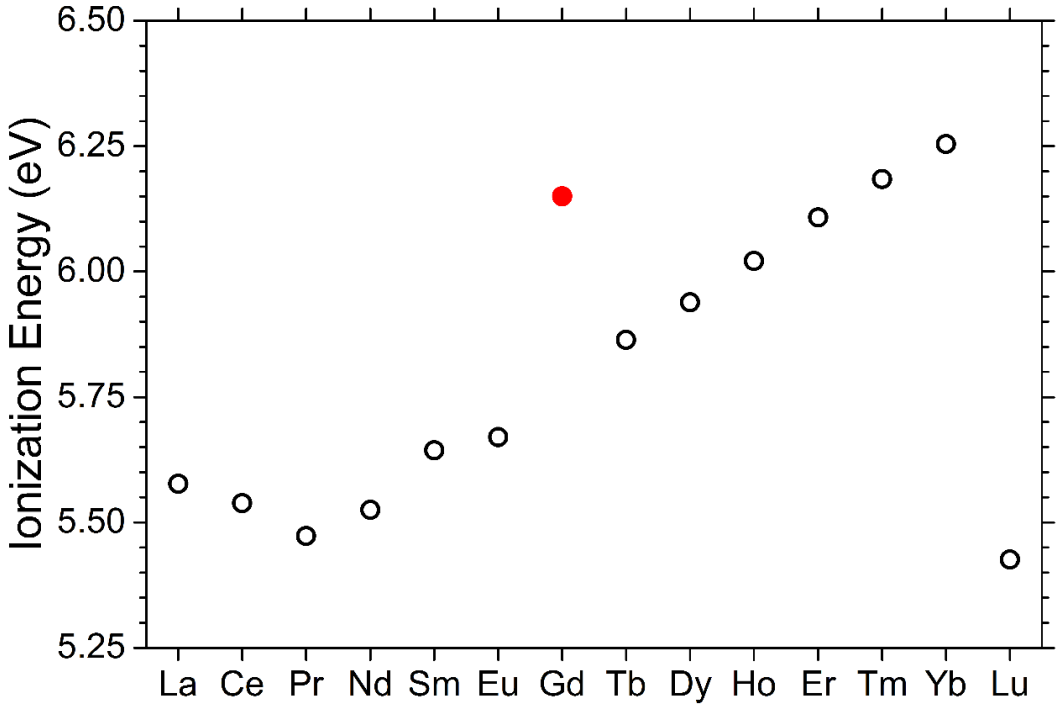

Figure 1.2. Ionization energies[67] of the lanthanide metals (excluding Pm) to form the singly charged cations.

the early lanthanides, especially La, Ce and praseodymium (Pr). However, another aspect to be considered is the relative ease with which the metals can be vaporized, i.e., their boiling points, for efficient plasma generation. A temperature of below ~3500 K is desired as this is the temperature that can be reached with a thermite reaction used for the vaporization. The boiling points[74] for the lanthanides are shown in Figure 1.3 together with their anticipated chemi-ionization reaction enthalpies deduced from the available literature thermochemistry.[70] Figure 1.3 demonstrates that although the early lanthanides indeed exhibit highly exothermic chemi-ionization reactions, these metals also have relatively high boiling temperatures and are thus not the most well-suited candidates.

Samarium (Sm) and neodymium (Nd), which have boiling temperatures below 3500 K (Figure 1.3) have been studied in early atmospheric chemical release

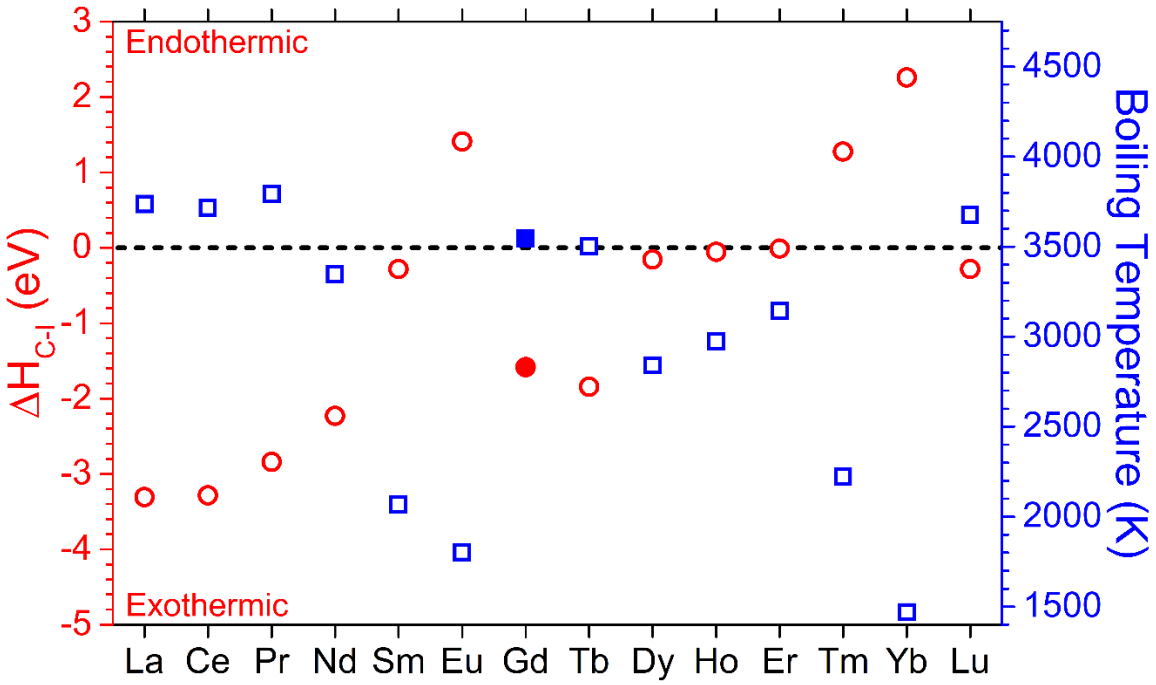

Figure 1.3. Boiling[74] temperatures of the lanthanides are indicated by the blue squares and the right y-axis. Chemi-ionization reaction enthalpies[70] for the lanthanides are indicated by the red circles and the left y-axis.

experiments.[71,73] The flows of the resulting Sm and Nd plasmas were analyzed in reference to those of known ions and neutrals, where the results suggested that Sm underwent chemi-ionization but Nd did not,[75] in contrast to expectation. Recently, the chemi-ionization rate constants for Sm and Nd have been measured using a flow tube apparatus and indicate that reaction (1.1) is at least 30 times more efficient for Nd than Sm, consistent with the chemi-ionization exothermicities for these metals.[71] Thus, the results from the early atmospheric chemical release experiments were likely misinterpreted as these were not analyzed with sophisticated methods.[71] Subsequent releases of Sm have been performed via the metal oxide space cloud (MOSC) experiment in which more advanced techniques have been used to analyze the plasmas produced.[73,76,77] Preliminary analysis of these clouds indicated that, although Sm does undergo chemi-ionization, the electron densities produced were 10 to

100 times lower than predicted from the available thermochemistry.[73] This prompted a re-evaluation of the Sm chemi-ionization exothermicity, where GIBMS was used to accurately determine the SmO^+ BDE.[78] Because the IE for Sm is well-established the chemi-ionization reaction enthalpy was determined accurately via (1.2). The revised thermochemistry for Sm indicates that its chemi-ionization exothermicity is lower by about 0.2 eV than that previously suggested by the literature.[78] The revised chem-ionization thermochemistry for Sm has been used in subsequent models to successfully reproduce the observations in the MOSC experiments.[77] As illustrated by these results for Sm, there is a need for more accurate and precise lanthanide thermochemistry that can be obtained from fundamental gas phase measurements. Not only can this information benefit the AFRL studies by avoiding the undertaking of unnecessary and expensive atmospheric chemical release experiments, but this information could more generally be useful for understanding the properties and reactivities of the lanthanides and their potential benefits in organometallic and oxidation catalysis.

1.4 Lanthanide Thermochemistry: Benchmarking Theory

Accurate lanthanide thermochemistry obtained from experiment can also be beneficial to quantum chemistry calculations because the experimental results can serve as benchmarks for evaluating and improving theoretical methods.[79,80] The lanthanides and more generally the heavy elements are challenging to describe theoretically because of spin-orbit and relativistic effects. Moreover, the multiple low energy electronic states that are possible as a result of differences in 4f orbital occupation in the lanthanides make determination of ground and excited states difficult. Relativistic effects on the core

electrons can be accounted for using specifically developed pseudopotentials such as effective core potentials (ECP)[81] that handle these effects. For all-electron basis sets, relativistic effects can be accounted for with methods like the Douglas-Kroll-Hess[82-84] Hamiltonian (DKH) and the zeroth-order regular approximation (ZORA).[85] Density functional theory (DFT) is a popular method for electronic structure calculations because it is relatively inexpensive computationally and can be applied to fairly large systems, providing in many cases reasonable results. The energy of the system is obtained by solving the electron density, where various functionals have been developed for treatment of the exchange and correlation interactions of the electrons, with the hybrid B3LYP[86,87] method being one of the most widely used. Higher levels of theory include post Hartree-Fock (HF) methods that differ from HF methods by explicit consideration of electron correlation. One such post-HF method is coupled cluster theory, where CCSD(T), which includes the full treatment of single and double excitations (with triple excitations approximated using perturbation theory), is often considered the gold standard among ab initio quantum chemistry methods. However, CCSD(T) is a single reference method, such that many of the lanthanides that have closely spaced low-energy electronic states arising from differences in 4f orbital occupation might not be adequately described. Instead these lanthanides might require multireference methods, such as multireference configuration interaction[88] and active-space coupled cluster approaches. Because these high-level calculations can become computationally costly for even small systems, there is a need for experimental thermochemistry of relatively simple lanthanide complexes. In this regard, gas phase lanthanide reactions with small neutrals for which accurate energetics can be determined from GIBMS studies can serve as useful benchmarks.

1.5 Gadolinium

Gadolinium (Gd), which is found in the middle of the lanthanide series and has a half-filled 4f shell, can serve as a simple test case for theoretical calculations because there should not be any complications in terms of low energy electronic states that could arise from differences in 4f orbital occupation. Thus, single-reference methods might in many cases be adequate in describing Gd and its cation (Gd^+), which also has a half-filled 4f shell, and is more amenable to study via gas phase reactions. Gd^+ is unusual because unlike most lanthanide cations, which have $4f^n6s^1$ configurations where n refers to the remaining valence electrons (Figure 1.4), Gd^+ with its $4f^75d^16s^1$ configuration has two non-4f valence electrons. In this regard, Gd^+ is more similar to the group 3 metal cations Sc^+ and Y^+, as well as the lanthanide cations La^+, Ce^+, and Lu^+ (Figure 1.4). Thus, Gd^+ should potentially exhibit similarities in reactivity and properties to those of the early transition metals. Additionally, because Gd has seven unpaired 4f electrons, it has a large spin quantum number (the most of any stable element), leading to interesting magnetic properties including its strong paramagnetism.[89] As a result of this, Gd makes a good contrasting

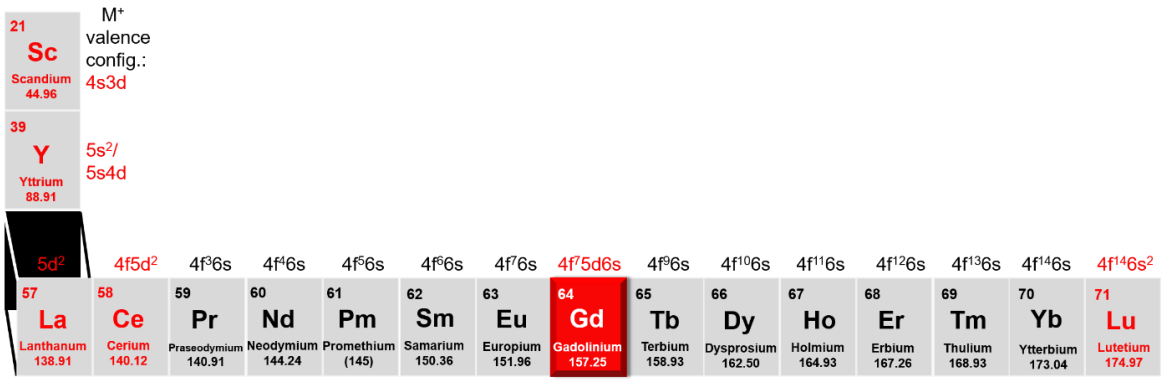

Figure 1.4. The group 3 transition metals and the lanthanide metals. Valence electron configurations for the singly charged cations are indicated, where those marked in red indicate configurations that have two non-4f valence electrons.

agent in magnetic resonance imaging (MRI),[90] because even when bound to various ligands (via interactions of the 6s and 5d orbitals), Gd retains its high spin configuration from the seven unpaired electrons. Gd, like other lanthanides, could also be a promising catalyst. For example, oxidation of small hydrocarbons at room temperature have recently been shown to occur on Gd oxide surfaces.[65] Moreover, on the basis of the oxidation chemistry discussed above, Gd is a potential candidate for the AFRL atmospheric chemical release experiments because it has a reasonably low boiling temperature (near 3500 K) and its chemi-ionization exothermicity (~1.5 eV) is predicted to be relatively high based on the available thermochemistry (Figure 1.3).

In this dissertation, the gas-phase properties and reactivity of Gd^+ in several oxidation reactions and in reactions with the hydrogen molecule and its isotopologues (HD and D_2) are investigated with GIBMS and with theoretical calculations. Extensive thermochemistry is determined for Gd^+ (including a reevaluation of the Gd chemi-ionization exothermicity), which can serve as useful benchmarks for theoretical calculations. Furthermore, the potential energy surfaces for the activation of O_2 and CO_2 by Gd^+ are mapped in great detail from experiment. Deep insight into these activation processes (and that of H_2), including the role of spin conservation, is aided by theoretical calculations. The fundamental information determined for Gd^+ here can be beneficial to understanding analogous reactions with other metals and can potentially be extended to more complicated systems, with possible implications to oxidation and organometallic catalysis and the design of more effective catalysts.

1.6 Overview and Scope

This dissertation covers studies of the energy dependent gas phase exchange reactions of Gd^+ and GdO^+ with various small neutrals and the collision induced dissociation (CID) reactions of GdO^+, GdO_2^+, and $GdCO_2^+$ using GIBMS and theoretical calculations. Because the GIBMS experiments are designed to accurately measure the thermochemistry of endothermic reactions (and those exhibiting a barrier), **Chapter 2** discusses the modeling involved (using the data analysis program CRUNCH) in fitting the energy dependent product ion cross sections and extracting the 0 K threshold energies of these reactions. Details about how the internal and kinetic energy distributions are taken into account are provided and the effects of these on the measured thresholds are addressed for the specific systems studied here. In **Chapter 3**, results for several reactions of Gd^+ (and GdO^+) are provided that allow for the first direct experimental determinations of the GdO^+, GdC^+, and $GdCO^+$ BDEs. The BDE for GdO^+ is obtained independently from five different reactions and is used to reevaluate the Gd chemi-ionization exothermicity via equation (1.2) using the well-established IE for Gd. The reevaluated exothermicity is consistent with the previous literature values and indicates that Gd indeed should have a highly exothermic chemi-ionization reaction and should thus be a promising candidate for the AFRL atmospheric chemical release experiments. For the GdC^+ and $GdCO^+$ BDEs, theory aids in identifying the interactions involved in the bonding, where the binding strengths can be rationalized on the basis of the energy cost required to promote the 6s valence electron of Gd^+ to a 5d orbital for more efficient binding with C and CO. This thermochemistry can be used to benchmark theoretical calculations, as well as be useful in determining the energetic feasibility of other reactions involving Gd^+ that are potentially

relevant for oxidation and organometallic catalysis. A detailed picture of the activation of O_2 and CO_2 by Gd^+ is provided in **Chapters 4** and **5**, respectively, which demonstrate how GIBMS can be used to map nearly complete potential energy surfaces by probing the energetics of the intermediates. Comparisons with theory provide insight into the electronic states of these intermediates and the reaction mechanisms. Interesting mechanistic differences are found between the activation of O_2 and CO_2 by Gd^+, although both reactions yield the GdO^+ product in exothermic and barrierless reactions. The differences can predominantly be attributed to the required change of spin between ground state reactants and products. As a result, the CO_2 reaction is more constrained than the O_2 reaction, requiring a surface crossing in the entrance channel to form ground state products. However, there are no barriers that exceed the reactant asymptote and thus the reaction with CO_2 can still proceed with relatively high (albeit lower than that for O_2) efficiency at thermal collision energies. Comparisons with results for the group 3 transition metal cations, Sc^+ and Y^+, indicate that Gd^+ exhibits similar reactivity with O_2 and CO_2 to these ions because of their similar ground state valence electron configurations (ignoring the 4f electrons of Gd^+), which result in similar promotion energy costs and bond strengths in the metal oxide cations. In **Chapter 6**, the activation of H_2 by Gd^+ is explored. The experimental results indicate that Gd^+ reacts with H_2 via a mixture of both direct and statistical mechanisms, consistent with theoretical calculations that indicate the availability, without exceeding the reaction endothermicity, of both types of reaction pathways. Comparisons with the metal hydride cations for Sc^+ and Y^+ indicate that different interactions are involved in forming the hydride metal cation bonds, (i.e., $Gd^+(5d_{z^2})$-H(1s) vs. Sc^+(4s)-H(1s) and Y^+(5s)-H(1s)), which explain the slight differences

in bond strengths observed for these systems. Nonetheless, Sc^+ and Y^+ cations generally exhibit similar reaction mechanisms to those of Gd^+ because of the fairly similar ground state electronic configurations leading to similar potential energy surfaces. Conclusions from the different studies on Gd^+ reactivity are presented in **Chapter 7**, where the interactions involved in O, C, and H binding with Gd^+, the influence of the electronic ground state, and the similarities and differences between activation of O_2 and CO_2 compared with H_2 are discussed. Moreover, an outlook on the broader context of these results to those of other lanthanide and metal cations and the potential applications of these results are provided.

1.7 References

(1) Labinger, J. A.; Bercaw, J. E. Understanding and Exploiting C-H Bond Activation. *Nature* **2002,** *417*, 507-514.

(2) Latimer, A. A.; Kulkarni, A. R.; Aljama, H.; Montoya, J. H.; Yoo, J. S.; Tsai, C.; Abild-Pedersen, F.; Studt, F.; Norskov, J. K. Understanding Trends in C-H Bond Activation in Heterogeneous Catalysis. *Nat. Mater.* **2017,** *16*, 225-229.

(3) Sakakura, T.; Choi, J.-C.; Yasuda, H. Transformation of Carbon Dioxide. *Chem. Rev.* **2007,** *107*, 2365-2387.

(4) Cokoja, M.; Bruckmeier, C.; Rieger, B.; Herrmann, W. A.; Kühn, F. E. Transformation of Carbon Dioxide with Homogeneous Transition-Metal Catalysts: A Molecular Solution to a Global Challenge? *Angew. Chem. Int. Ed.* **2011,** *50*, 8510-8537.

(5) Appel, A. M.; Bercaw, J. E.; Bocarsly, A. B.; Dobbek, H.; DuBois, D. L.; Dupuis, M.; Ferry, J. G.; Fujita, E.; Hille, R.; Kenis, P. J. A. et al. Frontiers, Opportunities, and Challenges in Biochemical and Chemical Catalysis of CO_2 Fixation. *Chem. Rev.* **2013,** *113*, 6621-6658.

(6) Liu, Q.; Wu, L.; Jackstell, R.; Beller, M. Using Carbon Dioxide as a Building Block in Organic Synthesis. *Nat. Commun.* **2015,** *6*, 5933(1) - (15).

(7) Shen, K.; Ben-David, H.; Laskavy, A.; Leitus, G.; Simon, L. J. W.; Neumann, R.

Electronic Control of Ru^{II} Complexes with Proximal Oxophilic Phenylselenium Tethers: Synthesis, Characterization, and Activation of Molecular Oxygen. *Eur. J. Inorg. Chem.* **2016,** *2016*, 2757-2763.

(8) Böhme, D. K.; Schwarz, H. Gas-Phase Catalysis by Atomic and Cluster Metal Ions: The Ultimate Single-Site Catalysts. *Angew. Chem. Int. Ed.* **2005,** *44*, 2336-2354.

(9) Roithová, J.; Schröder, D. Selective Activation of Alkanes by Gas-Phase Metal Ions. *Chem. Rev.* **2010,** *110*, 1170-1211.

(10) Freiser, B. S. Selected Topics in Organometallic Ion Chemistry. *Acc. Chem. Res.* **1994,** *27*, 353-360.

(11) Eller, K.; Zummack, W.; Schwarz, H. Gas-Phase Chemistry of Bare Transition-Metal Ions in Comparison. *J. Am. Chem. Soc.* **1990,** *112*, 621-627.

(12) Kappes, M. M.; Staley, R. H. Gas-Phase Oxidation Catalysis by Transition-Metal Cations. *J. Am. Chem. Soc.* **1981,** *103*, 1286-1287.

(13) Schröder, D.; Schwarz, H. Fe^+-Catalyzed Gas-Phase Oxidation of Ethane by N_2O. *Angew. Chem. Int. Ed. Engl.* **1990,** *29*, 1431-1433.

(14) Jackson, T. C.; Jacobson, D. B.; Freiser, B. S. Gas-Phase Reactions of FeO^+ with Hydrocarbons. *J. Am. Chem. Soc.* **1984,** *106*, 1252-1257.

(15) Brönstrup, M.; Schröder, D.; Kretzschmar, I.; Schwarz, H.; Harvey, J. N. PtO_2^+: Easy to Generate Experimentally but Difficult to Describe Theoretically. *J. Am. Chem. Soc.* **2001,** *123*, 142-147.

(16) Beauchamp, J. L.; Foster, M. S. Potential of Ion Cyclotron Resonance Spectroscopy for the Study of the Intrinsic Properties and Reactivity of Transition Metal Complexes in the Gas Phase. Ion-Molecule Reactions of Iron Pentacarbonyl. *J. Am. Chem. Soc.* **1971,** *93*, 4924-4926.

(17) Cheng, P.; Koyanagi, G. K.; Bohme, D. K. Gas-Phase Reactions of Atomic Lanthanide Cations with CO_2 and CS_2: Room-Temperature Kinetics and Periodicities in Reactivity. *J. Phys. Chem. A* **2006,** *110*, 12832-12838.

(18) Koyanagi, G. K.; Bohme, D. K. Oxidation Reactions of Lanthanide Cations with N_2O and O_2: Periodicities in Reactivity. *J. Phys. Chem. A* **2001,** *105*, 8964-8968.

(19) Koyanagi, G. K.; Bohme, D. K. Gas-Phase Reactions of Carbon Dioxide with Atomic Transition-Metal and Main-Group Cations: Room-Temperature Kinetics and Periodicities in Reactivity. *J. Phys. Chem. A* **2006,** *110*, 1232-1241.

(20) Koyanagi, G. K.; Caraiman, D.; Blagojevic, V.; Bohme, D. K. Gas-Phase Reactions

of Transition-Metal Ions with Molecular Oxygen: Room-Temperature Kinetics and Periodicities in Reactivity. *J. Phys. Chem. A* **2002,** *106,* 4581-4590.

(21) Böhme, D. K. Experimental Studies of Positive Ion Chemistry with Flow-Tube Mass Spectrometry: Birth, Evolution, and Achievements in the 20th Century. *Int. J. Mass Spectrom.* **2000,** *200,* 97-136.

(22) Schwarz, H. Remote Functionalization of C-H and C-C Bonds by "Naked" Transition-Metal Ions (Cosi Fan Tutte). *Acc. Chem. Res.* **1989,** *22,* 282-287.

(23) Kappes, M. M.; Staley, R. H. Oxidation of Transition-Metal Cations in the Gas Phase. Oxygen Bond Dissociation Energies and Formation of an Excited-State Product. *J. Phys. Chem.* **1981,** *85,* 942-944.

(24) Armentrout, P. B.; Beauchamp, J. L. Ion Beam Studies of Organometallic Chemistry. High Energy "Sampling" of Reaction Intermediates Involved in Carbon-Carbon Bond Cleavage by Transition Metals. *J. Am. Chem. Soc.* **1980,** *102,* 1736-1738.

(25) Armentrout, P. B.; Halle, L. F.; Beauchamp, J. L. Ion-Beam Studies of the Reactions of Atomic Cobalt Ions with Alkenes. *J. Am. Chem. Soc.* **1981,** *103,* 6624-6628.

(26) Elkind, J. L.; Armentrout, P. B. Effect of Kinetic and Electronic Energy on the Reaction of V^+ with H_2, HD, and D_2. *J. Phys. Chem.* **1985,** *89,* 5626-5636.

(27) Elkind, J. L.; Armentrout, P. B. Effect of Kinetic and Electronic Energy on the Reactions of Ti^+ with H_2, HD, and D_2. *Int. J. Mass Spectrom. Ion Processes* **1988,** *83,* 259-284.

(28) Elkind, J. L.; Armentrout, P. B. Effect of Kinetic and Electronic Energy on the Reactions of Cr^+ with H_2, HD, and D_2. *J. Chem. Phys.* **1987,** *86,* 1868-1877.

(29) Elkind, J. L.; Armentrout, P. B. Effect of Kinetic and Electronic Energy on the Reactions of Mn^+ with H_2, HD, and D_2. *J. Chem. Phys.* **1986,** *84,* 4862-4871.

(30) Elkind, J. L.; Armentrout, P. B. Effect of Kinetic and Electronic Energy on the Reactions of Fe^+ with H_2, HD, and D_2: State-Specific Cross Sections for Fe^+ (^{6}D) and Fe^+ (^{4}F). *J. Phys. Chem.* **1986,** *90,* 5736-5745.

(31) Elkind, J. L.; Armentrout, P. B. Effect of Kinetic and Electronic Energy on the Reactions of Co^+, Ni^+, and Cu^+ with H_2, HD, and D_2. *J. Phys. Chem.* **1986,** *90,* 6576-6586.

(32) Elkind, J. L.; Sunderlin, L. S.; Armentrout, P. B. Periodic Trends in Chemical Reactivity: Reactions of Sc^+, Y^+, La^+, and Lu^+ with H_2, D_2 and HD. *J. Phys. Chem.*

1989, *93*, 3151-3158.

(33) Elkind, J. L.; Armentrout, P. B. Transition-Metal Hydride Bond Energies: First and Second Row. *Inorg. Chem.* **1986,** *25*, 1078-1080.

(34) Sievers, M. R.; Chen, Y.-M.; Elkind, J. L.; Armentrout, P. B. Reactions of Y^+, Zr^+, Nb^+, and Mo^+ with H_2, HD, and D_2. *J. Phys. Chem.* **1996,** *100*, 54-62.

(35) Chen, Y.-M.; Elkind, J. L.; Armentrout, P. B. Reactions of Ru^+, Rh^+, Pd^+, and Ag^+ with H_2, HD, and D_2. *J. Phys. Chem.* **1995,** *99*, 10438-10445.

(36) Hinton, C. S.; Armentrout, P. B. Guided Ion Beam and Theoretical Study of the Reactions of Hf^+ with H_2, D_2, and HD. *J. Chem. Phys.* **2010,** *133*, 124307.

(37) Zhang, X.-G.; Rue, C.; Shin, S.-Y.; Armentrout, P. B. Reactions of Ta^+ and W^+ with H_2, D_2, and HD: Effect of Lanthanide Contraction and Spin–Orbit Interactions on Reactivity and Thermochemistry. *J. Chem. Phys.* **2002,** *116*, 5574-5583.

(38) Hinton, C. S.; Citir, M.; Armentrout, P. B. Guided Ion Beam and Theoretical Study of the Reactions of Os^+ with H_2, D_2, and HD. *J. Chem. Phys.* **2011,** *135*, 234302.

(39) Li, F.-X.; Zhang, X.-G.; Armentrout, P. B. Guided Ion Beam and Theoretical Study of the Reactions of Ir^+ with H_2, D_2, and HD. *J. Phys. Chem. B* **2005,** *109*, 8350-8357.

(40) Zhang, X.-G.; Armentrout, P. B. Reactions of Pt^+ with H_2, D_2, and HD: Effect of Lanthanide Contraction on Reactivity and Thermochemistry. *J. Chem. Phys.* **2002,** *116*, 5565-5573.

(41) Li, F.; Hinton, C. S.; Citir, M.; Liu, F.; Armentrout, P. B. Guided Ion Beam and Theoretical Study of the Reactions of Au^+ with H_2, D_2, and HD. *J. Chem. Phys.* **2011,** *134*, 024310.

(42) Armentrout, P. B.; Li, F.-X. Probes of Spin Conservation in Heavy Metal Reactions: Experimental and Theoretical Studies of the Reactions of Re^+ with H_2, D_2, and HD. *J. Chem. Phys.* **2004,** *121*, 248-256.

(43) Armentrout, P. B.; Beauchamp, J. L. The Chemistry of Atomic Transition-Metal Ions: Insight Into Fundamental Aspects of Organometallic Chemistry. *Acc. Chem. Res.* **1989,** *22*, 315-321.

(44) Aristov, N.; Armentrout, P. B. Collision-Induced Dissociation of Vanadium Monoxide Ion. *J. Phys. Chem.* **1986,** *90*, 5135-5140.

(45) Loh, S. K.; Fisher, E. R.; Lian, L.; Schultz, R. H.; Armentrout, P. B. State-Specific Reactions of Fe^+ (^6D, ^4F) with O_2 and cyclo-C_2H_4O: $D_0(Fe^+\text{-}O)$ and Effects of

Collisional Relaxation. *J. Phys. Chem.* **1989,** *93*, 3159-3167.

(46) Clemmer, D. E.; Elkind, J. L.; Aristov, N.; Armentrout, P. B. Reaction of Sc^+, Ti^+, and V^+ with CO. MC^+ and MO^+ Bond Energies. *J. Chem. Phys.* **1991,** *95*, 3387-3393.

(47) Fisher, E. R.; Elkind, J. L.; Clemmer, D. E.; Georgiadis, R.; Loh, S. K.; Aristov, N.; Sunderlin, L. S.; Armentrout, P. B. Reactions of Fourth-Period Metal Ions (Ca^+−Zn^+) with O_2: Metal-Oxide Ion Bond Energies. *J. Chem. Phys.* **1990,** *93*, 2676-2691.

(48) Clemmer, D. E.; Dalleska, N. F.; Armentrout, P. B. Gas-Phase Thermochemistry of the Group 3 Dioxides: ScO_2, YO_2 and LaO_2. *Chem. Phys. Lett.* **1992,** *190*, 259-265.

(49) Chen, Y.-M.; Armentrout, P. B. Kinetic Energy Dependence of the Reactions of Ru^+, Rh^+, Pd^+, and Ag^+ with O_2. *J. Chem. Phys.* **1995,** *103*, 618-625.

(50) Sievers, M. R.; Chen, Y.-M.; Armentrout, P. B. Metal Oxide and Carbide Thermochemistry of Y^+, Zr^+, Nb^+, and Mo^+. *J. Chem. Phys.* **1996,** *105*, 6322-6333.

(51) Sievers, M. R.; Armentrout, P. B. Gas Phase Activation of Carbon Dioxide by Niobium and Niobium Monoxide Cations. *Int. J. Mass Spectrom.* **1998,** *179–180*, 103-115.

(52) Sievers, M. R.; Armentrout, P. B. Oxidation of CO and Reduction of CO_2 by Gas Phase Zr^+, ZrO^+, and ZrO_2^+. *Int. J. Mass Spectrom.* **1999,** *185–187*, 117-129.

(53) Sievers, M. R.; Armentrout, P. B. Activation of Carbon Dioxide: Gas-Phase Reactions of Y^+, YO^+, and YO_2^+ with CO and CO_2. *Inorg. Chem.* **1999,** *38*, 397-402.

(54) Sievers, M. R.; Armentrout, P. B. Reactions of CO and CO_2 with Gas-Phase Mo^+, MoO^+, and MoO_2^+. *J. Phys. Chem. A* **1998,** *102*, 10754-10762.

(55) Hinton, C. S.; Citir, M.; Manard, M.; Armentrout, P. B. Collision-Induced Dissociation of MO^+ and MO_2^+ (M = Ta and W): Metal Oxide and Dioxide Cation Bond Energies. *Int. J. Mass Spectrom.* **2011,** *308*, 265-274.

(56) Armentrout, P. B. The Bond Energy of ReO^+: Guided Ion-Beam and Theoretical Studies of the Reaction of Re^+ (^7S) with O_2. *J. Chem. Phys.* **2013,** *139*, 084305.

(57) Hinton, C. S.; Li, F.; Armentrout, P. B. Reactions of Hf^+, Ta^+, and W^+ with O_2 and CO: Metal Carbide and Metal Oxide Cation Bond Energies. *Int. J. Mass Spectrom.* **2009,** *280*, 226-234.

(58) Hinton, C. S.; Citir, M.; Armentrout, P. B. Guided Ion-Beam and Theoretical Studies of the Reaction of Os^+ (^6D) with O_2: Adiabatic and Nonadiabatic Behavior. *Int. J. Mass Spectrom.* **2013,** *354–355*, 87-98.

(59) Zhang, X.-G.; Armentrout, P. B. Activation of O_2 and CO_2 by PtO^+: The Thermochemistry of PtO_2^+. *J. Phys. Chem. A* **2003,** *107*, 8915-8922.

(60) Rodgers, M. T.; Walker, B.; Armentrout, P. B. Reactions of Cu^+ (^1S and ^3D) with O_2, CO, CO_2, N_2, NO, N_2O, and NO_2 Studied by Guided Ion Beam Mass Spectrometry. *Int. J. Mass Spectrom.* **1999,** *182–183*, 99-120.

(61) Sievers, M. R.; Armentrout, P. B. Potential Energy Surface for Carbon-Dioxide Activation by V^+: A Guided Ion Beam Study. *J. Chem. Phys.* **1995,** *102*, 754-762.

(62) Zhang, X.-G.; Armentrout, P. B. Activation of O_2, CO, and CO_2 by Pt^+: The Thermochemistry of PtO^+. *J. Phys. Chem. A* **2003,** *107*, 8904-8914.

(63) Griffin, J. B.; Armentrout, P. B. Guided Ion-Beam Studies of the Reactions of Fe_n^+(n=1–18) with CO_2: Iron Cluster Oxide Bond Energies. *J. Chem. Phys.* **1997,** *107*, 5345-5355.

(64) Griffin, J. B.; Armentrout, P. B. Guided Ion Beam Studies of the Reactions of Cr_n^+ (n=2–18) with O_2: Chromium Cluster Oxide and Dioxide Bond Energies. *J. Chem. Phys.* **1998,** *108*, 8062-8074.

(65) Külah, E.; Marot, L.; Steiner, R.; Romanyuk, A.; Jung, T. A.; Wäckerlin, A.; Meyer, E. Surface Chemistry of Rare-Earth Oxide Surfaces at Ambient Conditions: Reactions with Water and Hydrocarbons. *Scientific Reports* **2017,** *7*, 43369.

(66) Gibson, J. K. Role of Atomic Electronics in f-Element Bond Formation: Bond Energies of Lanthanide and Actinide Oxide Molecules. *J. Phys. Chem. A* **2003,** *107*, 7891-7899.

(67) Sansonetti, J. E.; Martin, W. C. Handbook of Basic Atomic Spectroscopic Data. *J. Phys. Chem. Ref. Data* **2005,** *34*, 1559-2259.

(68) Ackermann, R. J.; Rauh, E. G.; Thorn, R. J. The Thermodynamics of Ionization of Gaseous Oxides; The First Ionization Potentials of the Lanthanide Metals and Monoxides. *J. Chem. Phys.* **1976,** *65*, 1027-1031.

(69) Pedley, J. B.; Marshall, E. M. Thermochemical Data for Gaseous Monoxides. *J. Phys. Chem. Ref. Data* **1983,** *12*, 967-1031.

(70) Schofield, K. An Overlooked Series of Gas Phase Diatomic Metal Oxide Ions that Are Long-lived. *J. Phys. Chem. A* **2006,** *110*, 6938-6947.

(71) Ard, S. G.; Shuman, N. S.; Martinez, O.; Brumbach, M. T.; Viggiano, A. A. Kinetics of Chemi-Ionization Reactions of Lanthanide Metals (Nd, Sm) from 150 to 450 K. *J. Chem. Phys.* **2015,** *143*, 204303.

(72) Konings, R. J. M.; Beneš, O.; Kovács, A.; Manara, D.; Sedmidubský, D.; Gorokhov, L.; Iorish, V. S.; Yungman, V.; Shenyavskaya, E.; Osina, E. The Thermodynamic Properties of the f-Elements and their Compounds. Part 2. The Lanthanide and Actinide Oxides. *J. Phys. Chem. Ref. Data* **2014,** *43*, 013101.

(73) Shuman, N. S.; Hunton, D. E.; Viggiano, A. A. Ambient and Modified Atmospheric Ion Chemistry: From Top to Bottom. *Chem. Rev.* **2015,** *115*, 4542-4570.

(74) Haynes, W. M. *CRC Handbook of Chemistry and Physics: A Ready-Reference Book of Chemical and Physical Data*; 96 ed.; CRC Press: Boca Raton, Florida, 2015.

(75) Larsen, M. F.; Mikkelsen, I. S.; Meriwether, J. W.; Niciejewski, R.; Vickery, K. Simultaneous Observations of Neutral Winds and Electric Fields at Spaced Locations in the Dawn Auroral Oval. *J. Geophys. Res.: Space Phys.* **1989,** *94*, 17235-17243.

(76) Caton, R. G.; Pedersen, T. R.; Groves, K. M.; Hines, J.; Cannon, P. S.; Jackson-Booth, N.; Parris, R. T.; Holmes, J. M.; Su, Y.-J.; Mishin, E. V.et al. Artificial Ionospheric Modification: The Metal Oxide Space Cloud Experiment. *Radio Sci.* **2017,** *52*, 539-558.

(77) Bernhardt, P. A.; Siefring, C. L.; Briczinski, S. J.; Viggiano, A.; Caton, R. G.; Pedersen, T. R.; Holmes, J. M.; Ard, S.; Shuman, N.; Groves, K. M. A Physics-Based Model for the Ionization of Samarium by the MOSC Chemical Releases in the Upper Atmosphere. *Radio Sci.* **2017,** *52*, 559-577.

(78) Cox, R. M.; Kim, J.; Armentrout, P. B.; Bartlett, J.; VanGundy, R. A.; Heaven, M. C.; Ard, S. G.; Melko, J. J.; Shuman, N. S.; Viggiano, A. A. Evaluation of the Exothermicity of the Chemi-Ionization Reaction Sm + O → $SmO^+ + e^-$. *J. Chem. Phys.* **2015,** *142*, 134307.

(79) Grimmel, S.; Schoendorff, G.; Wilson, A. K. Gauging the Performance of Density Functionals for Lanthanide-Containing Molecules. *J. Chem. Theory Comput.* **2016,** *12*, 1259-1266.

(80) Heiberg, H.; Gropen, O.; Laerdahl, J. K.; Swang, O.; Wahlgren, U. The Performance of Density Functional Theory for LnF (Ln=Nd, Eu, Gd, Yb) and YbH. *Theor. Chem. Acc.* **2003,** *110*, 118-125.

(81) Cao, X.; Dolg, M. Pseudopotentials and Modelpotentials. *Wiley Interdiscip. Rev. Comput. Mol. Sci.* **2011,** *1*, 200-210.

(82) Douglas, M.; Kroll, N. M. Quantum Electrodynamical Corrections to the Fine Structure of Helium. *Ann. Phys.* **1974,** *82*, 89-155.

(83) Reiher, M.; Wolf, A. Exact Decoupling of the Dirac Hamiltonian. II. The Generalized Douglas–Kroll–Hess Transformation up to Arbitrary Order. *J. Chem. Phys.* **2004,** *121*, 10945-10956.

(84) Hess, B. A. Applicability of the No-Pair Equation with Free-Particle Projection Operators to Atomic and Molecular Structure Calculations. *Phys. Rev. A* **1985,** *32*, 756-763.

(85) Lenthe, E. v.; Baerends, E. J.; Snijders, J. G. Relativistic Regular Two-Component Hamiltonians. *J. Chem. Phys.* **1993,** *99*, 4597-4610.

(86) Becke, A. D. Density-Functional Thermochemistry. III. The Role of Exact Exchange. *J. Chem. Phys.* **1993,** *98*, 5648-5652.

(87) Lee, C.; Yang, W.; Parr, R. G. Development of the Colle-Salvetti Correlation-Energy Formula into a Functional of the Electron Density. *Phys. Rev. B* **1988,** *37*, 785-789.

(88) Werner, H. J.; Knowles, P. J. An Efficient Internally Contracted Multiconfiguration-Reference Configuration Interaction Method. *J. Chem. Phys.* **1988,** *89*, 5803-5814.

(89) Coey, J. M. D.; Skumryev, V.; Gallagher, K. Is Gadolinium Really Ferromagnetic? *Nature* **1999,** *401*, 35.

(90) Lauffer, R. B. Paramagnetic Metal Complexes as Water Proton Relaxation Agents for NMR Imaging: Theory and Design. *Chem. Rev.* **1987,** *87*, 901-927.

CHAPTER 2

DATA ANALYSIS: MODELING WITH CRUNCH TO OBTAIN 0 K THRESHOLD ENERGIES (E_0)

2.1 Graphical Abstract

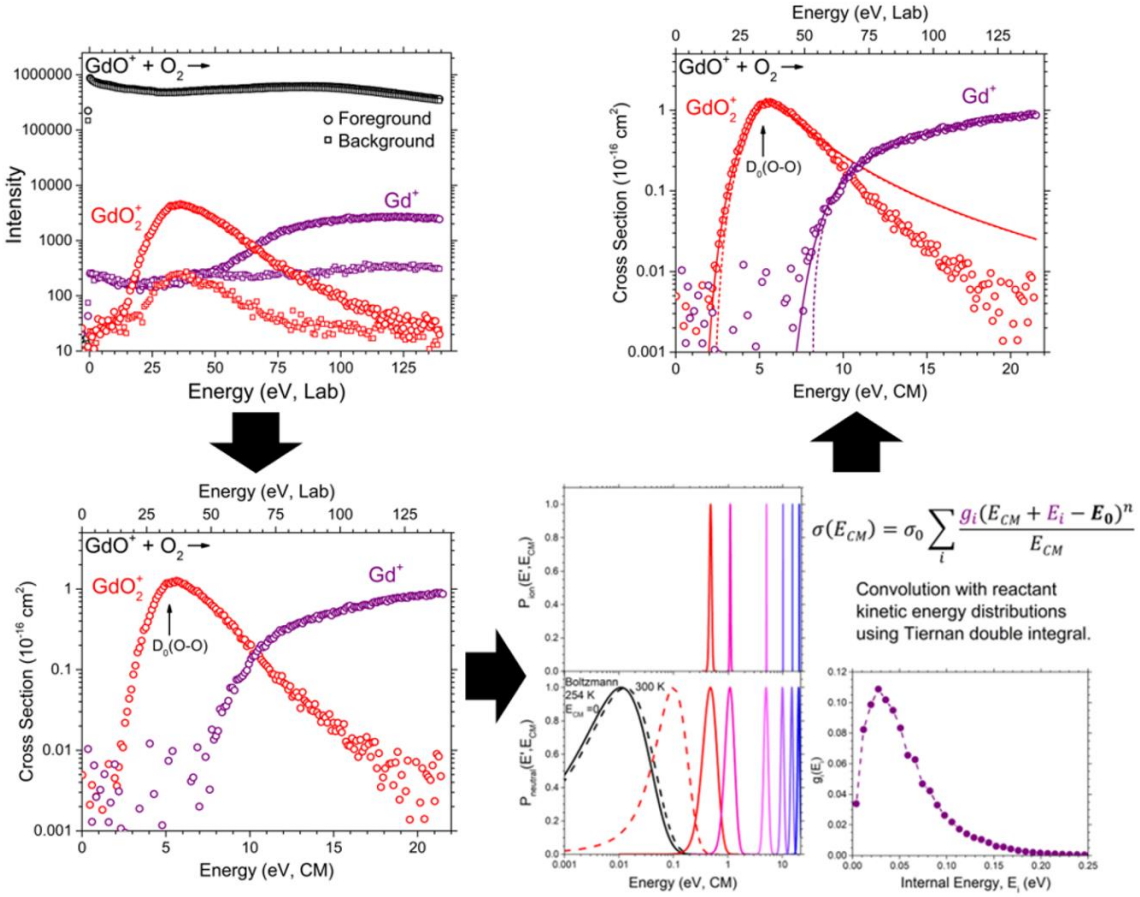

2.2 Conversion of Raw Data

Information about the experimental and theoretical procedures and the guided ion beam tandem mass spectrometer (GIBMS) used in the studies described within this dissertation are given in the separate chapters. Here, details of the equations and the modeling involved in extracting 0 K threshold energies, E_0, from the GIBMS data using the program CRUNCH are provided.[1] A brief summary of the GIBMS experiments is as follows. Gadolinium (Gd) metal ions were generated from Gd foil using a direct current discharge flow tube (DC/FT) ion source.[2] Neutral gases could be introduced into the source to form Gd^+ complexes, where, for example, GdO^+ and GdO_2^+ precursor ions were formed by introducing O_2 (Chapter 4). Mass selection of the precursor ion of interest was performed using a magnetic momentum analyzer. The precursor ions were then decelerated to a controlled and well-defined kinetic energy prior to entering an octopole ion beam guide, which was surrounded in part by a reaction cell. Neutral reactants were introduced into the cell, where pressures were kept sufficiently low to ensure that single-collision conditions dominated in the reactions with the precursor ions. Resulting precursor and product ions were mass selected and analyzed using a quadrupole mass filter, and their intensities were counted using a Daly detector.[3] Precursor and product ion intensities were measured as a function of the precursor ion kinetic energy in the lab frame. Additional measurements of the energy dependent precursor and product ion intensities were performed by directing the neutral reactant into the reaction chamber instead of the cell to correct for any background reaction not occurring in the cell. The corrected intensities were converted to a total reaction cross section (i.e., a measure of the reaction probability) using an equation analogous to the Beer-Lambert law given by (2.1) as detailed previously.[1,4]

The individual product ion cross sections were then generally determined using the background corrected intensities and equation (2.2).

$$I = I_0 e^{-\rho\sigma l} \text{ with } \sigma = -ln\left(\frac{I}{I_0}\right)/\rho l \quad (2.1)$$

$$\sigma_j = \sigma\left(\frac{I_j}{\sum_j I_j}\right) \text{ where } \sum_j I_j = I_0 - I \quad (2.2)$$

In equations (2.1) and (2.2), I_0 and I correspond to the precursor ion intensity before and after reaction, respectively, *l* (8.26 cm) is the effective reaction path length, ρ corresponds to the number density in the cell given by P/k_BT where P is the pressure, k_B is the Boltzmann constant and T is the temperature, I_j is the intensity of product j, and σ_j and σ correspond to the cross section of product j and the total reaction cross section, respectively. The energy scale was converted from the lab to the center-of-mass (CM) frame, which gives the energy available in the reaction, such that the final data were plotted in terms of cross section as a function of CM collision energy (e.g., Figure 2.1). Because of the experimental design, the neutral reactant can be assumed to be stationary relative to the ion, such that conversion from the lab to the CM frame simplifies to the equation (2.3) with M and m corresponding to the masses of the precursor ion and reactant neutral, respectively.

$$E(CM) = E(Lab)\left(\frac{m}{M+m}\right) \quad (2.3)$$

Retarding experiments were used to determine the full width at half maximum (FWHM) of the precursor ion kinetic energy distributions and to determine the zero in the energy scale as described previously.[1,4] The FWHM value is used in the modeling of the precursor ion kinetic energy distribution as discussed further below.

2.3 Exchange and Collision Induced Dissociation Reactions

The gas phase reactions that are described in this dissertation can be separated into two types: exchange and collision induced dissociation (CID) reactions. Both these processes are illustrated in Figure 2.1 in the reaction between the gadolinium oxide cation (GdO^+) and O_2 to form GdO_2^+ + O and Gd^+ + O + O_2 products. The GdO_2^+ product is formed via an exchange reaction, which involves both bond breaking and bond making. To form the GdO_2^+ + O products, the O_2 bond breaks and a new bond is formed between one of the O atoms and GdO^+. This reaction is endothermic as shown in Figure 2.1 and requires about 2 eV to yield the products from ground state reactants. The bond dissociation energy

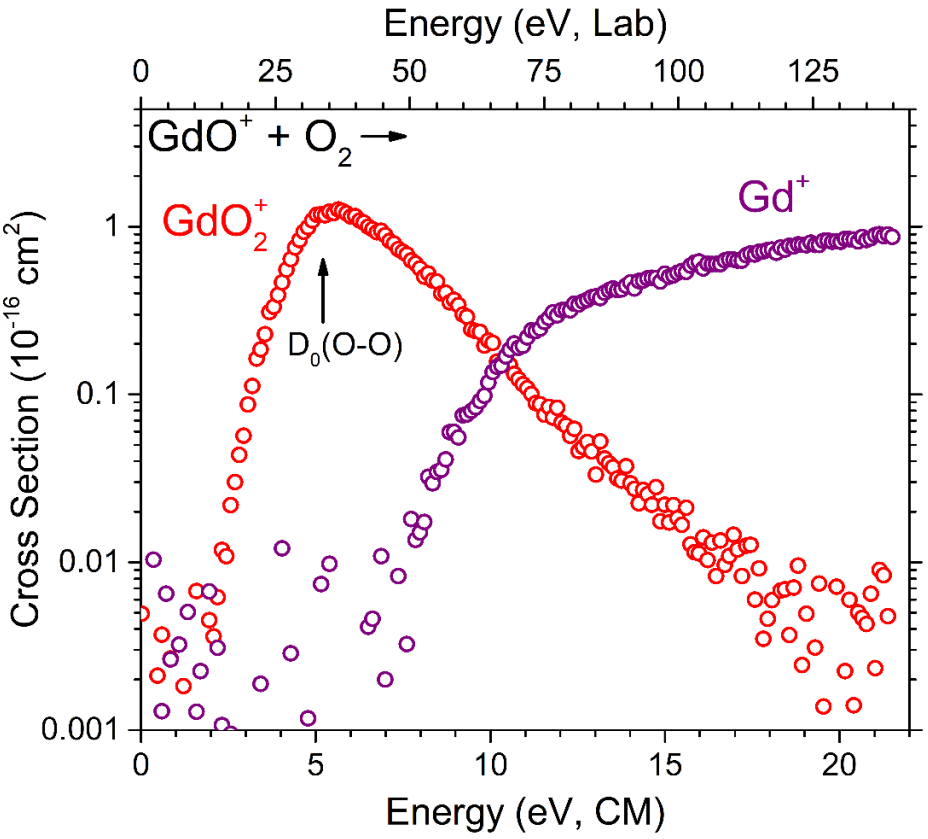

Figure 2.1. Product ion cross sections as a function of energy in the center-of-mass (CM, bottom x-axis) and lab (top x-axis) frames for the reaction between GdO^+ and O_2. The bond energy of the reactant neutral is indicated by the arrow.

(BDE) for OGd^+-O can be determined from the measured reaction endothermicity (E_0) and the BDE of the reactant neutral via $D_0(OGd^+\text{-}O) = D_0(O\text{-}O) - E_0$ where the BDEs and threshold energy, E_0, of the reaction correspond to values at 0 K. Exchange reactions can be exothermic or endothermic depending on whether the new bond formed in the product ion is stronger or weaker than the bond that breaks in the reactant neutral. In Figure 2.1, there is a decline in the GdO_2^+ product ion cross section at energies exceeding the bond energy of the reactant neutral, because at these energies, the product ion has sufficient energy to dissociate and yield $GdO^+ + O + O$ products. This decline is treated differently in the modeling and includes a dissociation probability as described elsewhere.[5] In contrast to exchange reactions, CID reactions are inherently endothermic because they involve solely the breaking of bonds. In Figure 2.1, $Gd^+ + O + O_2$ products are formed from breaking the GdO^+ bond, where O_2 serves simply as a collision gas. According to the results in Figure 2.1, this occurs around 7 eV, where the measured reaction endothermicity corresponds directly to the bond energy of GdO^+. The CID product ion cross section will level off at higher energies and requires no special treatment in the modeling.

2.4 Reactant Kinetic Energy Distributions

The generation of the precursor ions using the DC/FT source and the subsequent focusing of these ions through various stages of the instrument causes a spread in kinetic energies (typically ~0.3 – 0.5 eV in the lab frame) that is much larger than simply a thermal distribution (0.03 eV), with the specific width of the distribution characterized from retarding experiments at the entrance of the octopole ion beam guide. This distribution of precursor ion kinetic energies needs to be accounted for in the modeling, as it will affect

the threshold measured (i.e., blur and shift the threshold to lower energies) compared with the threshold of the reaction at 0 K. The precursor ion kinetic energy distribution is typically assumed to be Gaussian and centered at the nominal CM energy measured in the experiments, and is thus modeled with equation (2.4) using the FWHM (converted to the CM frame) determined from the retarding experiments.[1,4]

$$P_{ion}(E',E_{CM}) = \left(\frac{2\sqrt{2ln(2)}}{FWHM\sqrt{2\pi}}\right) e^{-0.5\left(\frac{2\sqrt{2ln(2)}\,(E'-E_{CM})}{FWHM}\right)^2} \qquad (2.4)$$

The neutral reactant introduced into the cell has a thermal kinetic energy distribution. This leads to a Doppler effect and a distribution of interaction energies between the neutrals in the reaction cell and the precursor ion directed into the cell at a given CM energy.[4] For accurate extraction of the 0 K threshold energies, this Doppler effect also needs to be accounted for and is modeled using equation (2.5), known as the Chantry distribution, where $\gamma = M/(m+M)$, and E'' is an energy index that corresponds to the relative collision energy between the reactant ion and neutral.[1,4,6,7]

$$P_{neutral}(E',E'') = \left(\frac{1}{4\pi\gamma k_B TE''}\right)^{\frac{1}{2}} \left[e^{-\left(\frac{1}{\gamma k_B T}\right)\left(E'^{1/2}-E''^{1/2}\right)^2} - e^{-\left(\frac{1}{\gamma k_B T}\right)\left(E'^{1/2}+E''^{1/2}\right)^2}\right] \qquad (2.5)$$

To consider the effect of the ion and neutral kinetic energy distributions given by (2.4) and (2.5) for typical experiments discussed in this dissertation, as an example, the GdO^+ kinetic energy distributions and the resulting Doppler distributions from the O_2 neutral (for the data in Figure 2.1) are shown in Figure 2.2 at representative CM energies (indicated by the filled circles). The GdO^+ kinetic energy distributions are given in Figure 2.2b (on a linear x-axis scale) and 2.2e (on a logarithmic x-axis scale). These have a FWHM of 0.36 eV (lab) as measured from the retarding experiments, which corresponds to 0.056 eV in the CM frame. The GdO^+ kinetic energy distributions are fairly narrow, where

Figure 2.2. The product ion cross sections resulting from the reaction between GdO^+ and O_2, and modeled kinetic energy distributions for the ion (Gaussian) and neutral (Chantry, Doppler) as a function of the center-of-mass (CM) energy are shown in (a), (b), and (c), respectively, plotted on a linear x-axis and in (d), (e), and (f) plotted on a logarithmic x-axis, respectively. The distributions are shown for selected CM energies of the experimental data indicated by the filled circles in (a) and (d).

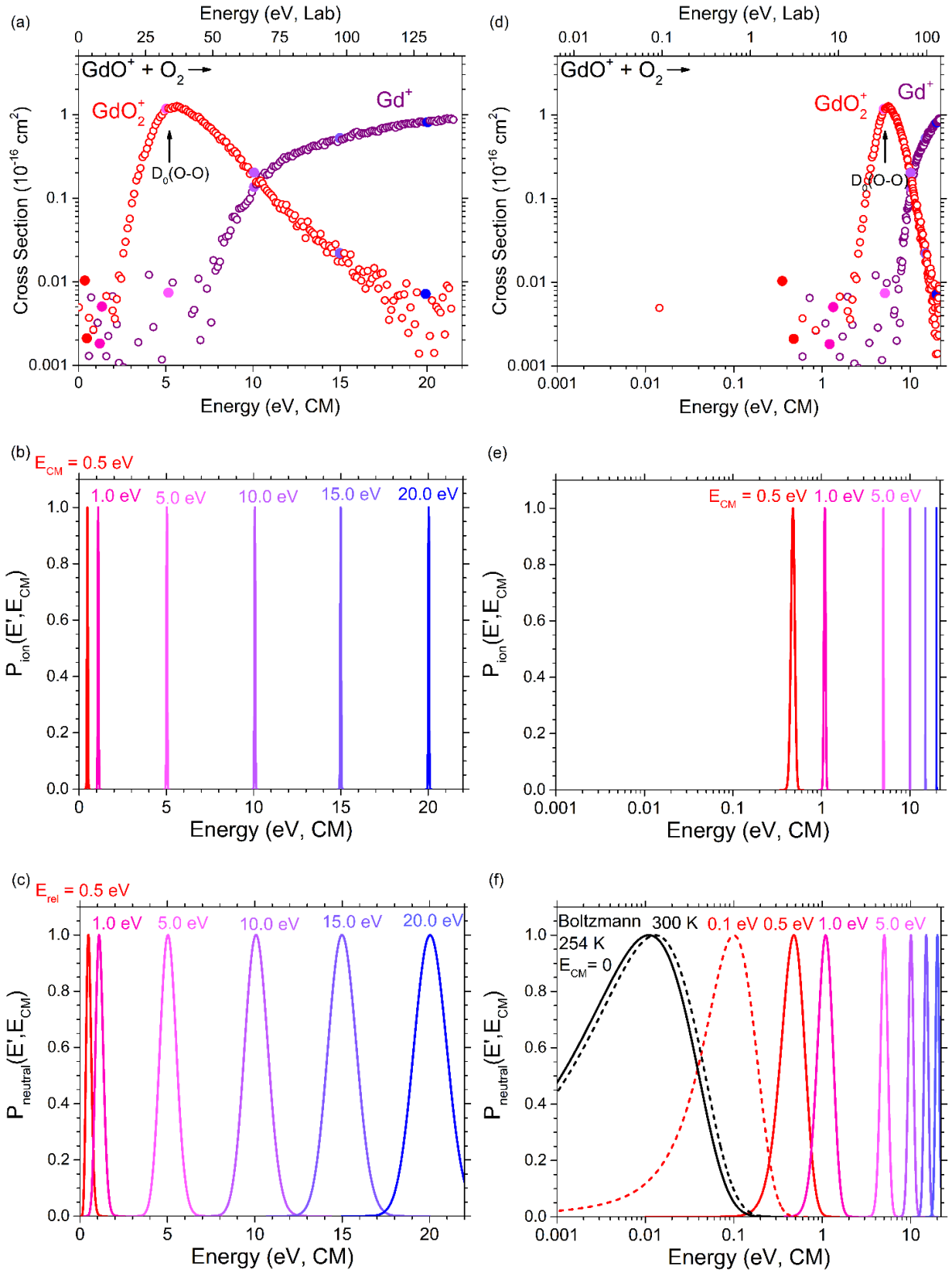
(a)
Energy (eV, Lab)
GdO+ + O2 →
GdO2+
Gd+
D0(O-O)
Cross Section (10-16 cm2)
Energy (eV, CM)
(d)
Energy (eV, Lab)
GdO+ + O2 →
GdO2+
Gd+
D0(O-O)
Cross Section (10-16 cm2)
Energy (eV, CM)
(b)
ECM = 0.5 eV
1.0 eV
5.0 eV
10.0 eV
15.0 eV
20.0 eV
Pion(E',ECM)
Energy (eV, CM)
(e)
ECM = 0.5 eV 1.0 eV 5.0 eV
Pion(E',ECM)
Energy (eV, CM)
(c)
Erel = 0.5 eV
1.0 eV
5.0 eV
10.0 eV
15.0 eV
20.0 eV
Pneutral(E',ECM)
Energy (eV, CM)
(f)
Boltzmann 300 K
254 K
ECM= 0
0.1 eV 0.5 eV 1.0 eV 5.0 eV
Pneutral(E',ECM)
Energy (eV, CM)

plotting these distributions on a logarithmic x-axis demonstrates more clearly the effect of the relative width compared with the average energy of the distribution (Figure 2.2e). The results in Figures 2.2b and 2.2e indicate that precursor ion kinetic energy distributions will generally have a greater effect in obscuring the threshold at lower CM energies, although in this case, the effect is relatively small. The narrow GdO^+ distributions in the reaction with O_2 can be attributed to the relatively large mass difference between the reactant ion (176 Da using the ^{160}Gd isotope) and the O_2 neutral (32 Da), which results in a small FWHM in the CM frame. In contrast, if the ion and neutral have similar masses, the FWHM in the CM frame will be roughly half of that in the lab frame and will thus have a larger impact on the measured threshold. For example, the GdO^+ distributions in CID experiments with Xe (131 Da) will have a FWHM in the CM frame of 0.16 eV (Chapter 3). In contrast to the relatively narrow precursor ion distributions, those resulting from the Doppler effect of the O_2 neutral for a given CM energy of the precursor ion, shown in Figures 2.2c (linear x-axis) and f (logarithmic x-axis), are significantly broader, with the absolute width increasing with increasing energy (Figure 2.2c). However, the relative width compared with the average energy of the distribution is larger at low CM energies as shown in Figure 2.2f. Thus, the effect on the measured 0 K threshold energy will again be largest at low CM energies, where this effect has been discussed in detail previously.[4] In the limit of the ion having a CM energy of zero, the Doppler distribution (equation (2.5)) reduces to a Boltzmann distribution with an effective temperature of $T' = \gamma T = 254$ K for the reaction between GdO^+ and O_2, where $\gamma = M/(m+M) = 0.846$ and $T = 300$ K.[4] Thus, at the lowest precursor ion collision energy measured in the experiments, the interaction distribution is nearly thermal.[4] The FWHM of the Doppler distribution is given approximately by FWHM

$\approx (11.1\ \gamma\ k_B\ T\ E_{CM})^{1/2}$.[4,7] Because the width depends on $\gamma = M/(m+M)$, a broader distribution results for a large precursor ion mass, M, and a small neutral mass, m, with the limit corresponding to $\gamma = 1$. This means that for the reactions examined in this dissertation, the widest Doppler distributions, at a given CM energy, will result for the reaction between Gd^+ (160 Da) and the light H_2 (2 Da) neutral (Chapter 6).

2.5 Reactant Internal Energy Distributions

The measured threshold energy in the GIBMS experiments will be lowered by the available internal energy of the reactants, and thus this effect also needs to be accounted for in the modeling of the data to extract accurate E_0 values. Because the systems described within this dissertation are at most four atoms, the internal energy will have a relatively small contribution. The internal energy of the reactants is calculated via integration over ro-vibrational density of states, where vibrational frequencies and rotational constants are obtained from the NIST WebBook[8] when available or from quantum chemical calculations. In the GdO^+ reaction with O_2, the vibrational frequencies for GdO^+ and O_2 are 898 and 1580 cm^{-1}, respectively, such that predominantly the ground vibrational states of these reactants will be populated at thermal energies (208.5 cm^{-1}). The 2D rotational constants for GdO^+ and O_2 are 0.376 and 1.438 cm^{-1}, respectively, resulting in thermal distributions of rotational energies. For these reactants, the calculated internal energy of a given state i having population g_i (with $\Sigma g_i = 1$) is shown in Figure 2.3, where this distribution results mainly from populating rotational states of the reactants. As Figure 2.3 indicates, the contribution of the internal energy is relatively small, where the average energy of the distribution is 0.054 eV, with a FWHM not much larger than the average energy. Thus, in

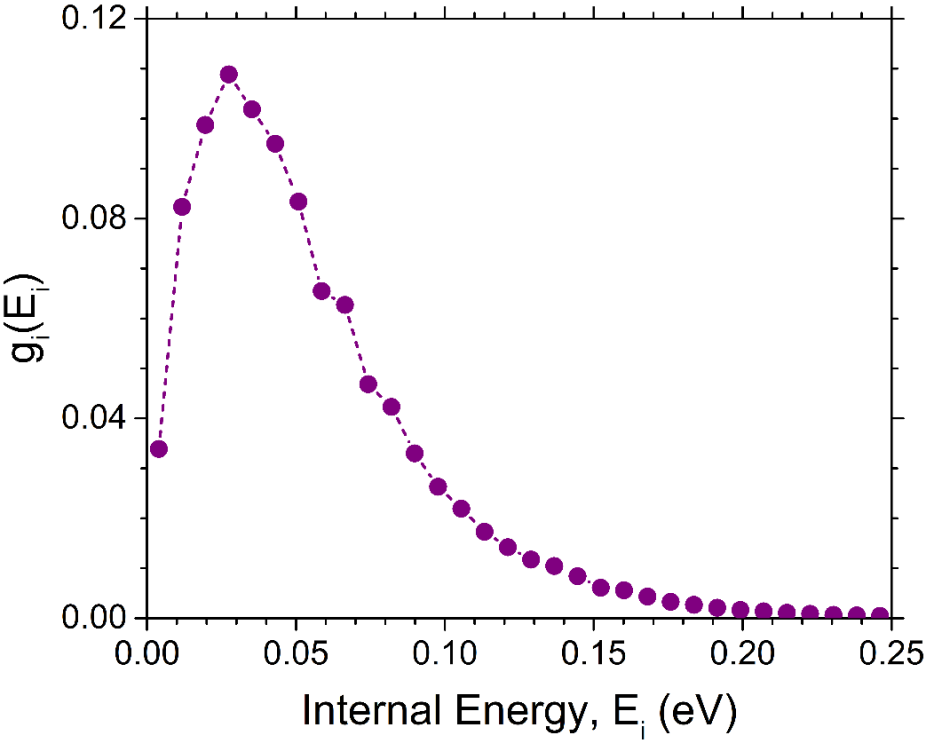

Figure 2.3. Internal energy distribution for GdO^+ and O_2 reactants determined from integration over ro-vibrational density of states.

general, for the experiments discussed here, the internal energy distribution of the reactants will not have a large effect, where predominantly population of rotational states will contribute most to the internal energy distribution of the reactants.

The contribution of the reactant electronic energy is determined and corrected for separately after modeling has been performed with CRUNCH to extract the E_0 values. In many cases, the electronic energy is zero (and no correction is needed) because the reactants are or are assumed to be in their electronic ground states (e.g., the reactant neutrals and the GdO^+, GdO_2^+, and $GdCO_2^+$ precursor ions). However, in reactions involving Gd^+, the contribution from the average electronic energy of Gd^+, as a result of predominantly populating spin-orbit (SO) levels in the ground ^{10}D state, are taken into account. Previous GIBMS experiments[9,10] indicate that metal ions generated from the DC/FT source have an

average electronic temperature of 700 ± 400 K. For Gd^+, this temperature corresponds to an average electronic energy (E_{el}) of 0.04 ± 0.03 eV, which is considered in the final E_0 reported. Table 2.1 lists the relative populations at 300, 700, and 1100 K, respectively, in the different SO levels of the ^{10}D ground state for Gd^+.

2.6 Modified Line-of-Centers Model and Convolution

Because the systems described within this dissertation are relatively small (4 atoms at most), the energy deposited is expected to go directly into the reaction coordinate, resulting in fast reactions (i.e., there should not be any kinetic shift effects to require explicit calculation of the RRKM rate constants[1,6]). Thus, the product ion cross sections from exchange reactions with a threshold and those from CID reactions studied here can be modeled with the relatively simple modified-line-of-centers equation given in (2.6) as described in detail previously.[6,11]

$$\sigma(E'') = \sigma_0 \sum_i g_i (E'' + E_i + E_{el} - E_0)^n / E'' \qquad (2.6)$$

Table 2.1. Relative populations in the different spin-orbit (SO) levels of the Gd^+ ^{10}D ground state at 300, 700, and 1100 K.

SO Level	Energy (eV)	Relative Populations (%)		
		300 K	700 K	1100 K
5/2	0.00	68.13	40.65	30.31
7/2	0.03	25.88	31.64	28.69
9/2	0.08	5.45	18.43	22.06
11/2	0.14	0.53	7.51	13.31
13/2	0.24	0.01	1.78	5.63

In equation (2.6), E″ is the same energy index as that in equation (2.5) and corresponds to the relative collision energy between the reactant ion and neutral, σ_0 is an empirical scaling factor, *n* corresponds to an empirical fitting parameter that determines the shape of the cross section, E_i as discussed above (and shown in Figure 2.3) corresponds to the vibrational and rotational energy of the reactants in state i having population g_i (where $\Sigma g_i = 1$), and E_{el} is the average electronic energy. To calculate the modeled cross sections at a given experimental CM energy, σ(E″) is obtained by convoluting with the internal energy distribution via equation (2.6) and subsequently with the reactant kinetic energy distributions given by equations (2.4) and (2.5), respectively, using the Tiernan double integral given in equation (2.7).[12]

$$\sigma(E_{CM}) = \int_0^{\infty} \int_{-\infty}^{\infty} P_{ion}(E',E_{CM})\, P_{neutral}(E',E'') \frac{\sigma(E'')E''}{E'} dE' dE'' \qquad (2.7)$$

The process and effect of convoluting the reactant ion and neutral kinetic energy distributions using the Tiernan double integral are illustrated in Figure 2.4 for the GdO^+ reaction with O_2 at an experimental CM energy of 0.5 eV. Each energy in the precursor ion kinetic energy distribution gives rise to a distribution of interaction energies with the reactant neutral. Convoluting these overlapping interaction distributions with the precursor ion kinetic energy distribution results in an overall broader distribution of kinetic energies than those of the reactant ion and neutral alone (Figure 2.4). This final distribution is subsequently convoluted with σ(E″) in equation (2.7) to give a calculated cross section, $\sigma(E_{CM})$, that includes the effects of the internal and kinetic energies of the reactants at a given CM energy measured in the experiments. The calculated cross sections are then compared with experiment and fitting parameters, including E_0, are optimized.

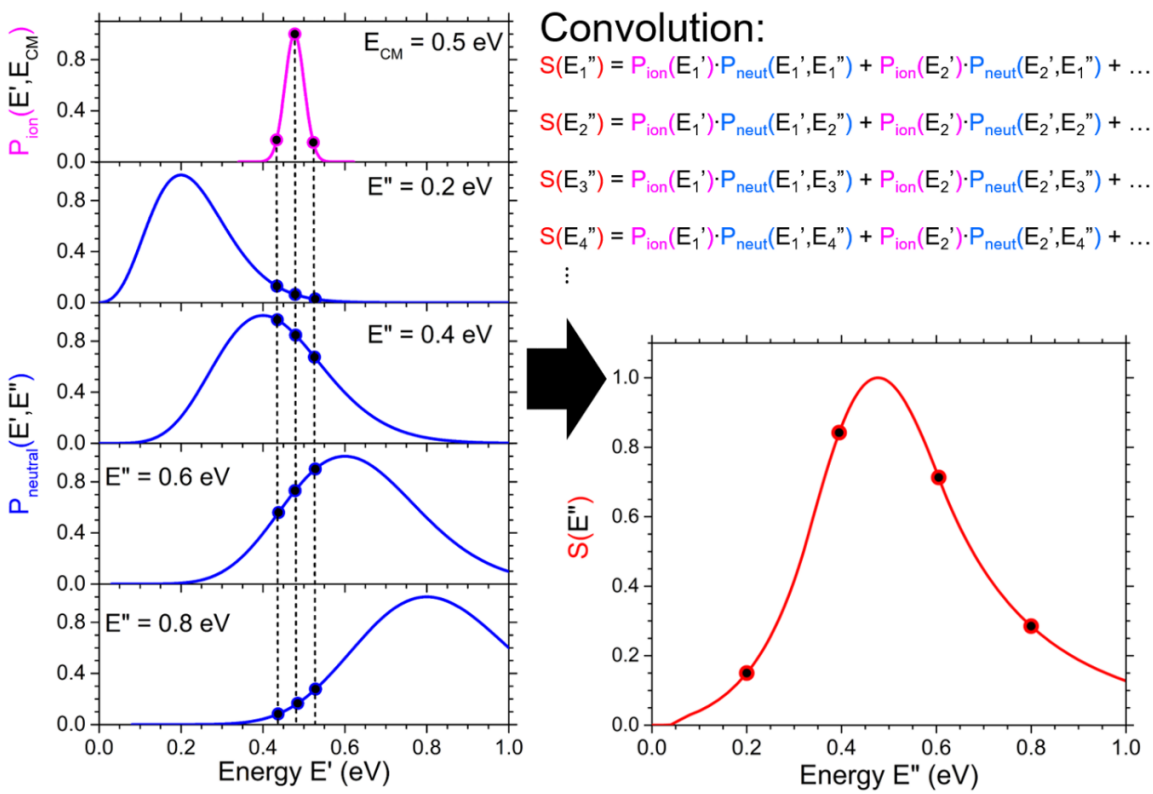

Figure 2.4. Illustration of the convolution over reactant kinetic energy distributions using the Tiernan double integral given in equation (2.7). A given precursor ion kinetic energy distribution is convoluted over several distributions of interaction energies with the neutral arising from different precursor ion kinetic energies (left). S(E″) corresponds to the resulting distribution after the convolution (right).

2.7 Modeled Parameters and Fits

The parameters that are typically varied in the modeling of the experimental cross sections are E_0, σ_0, and *n* in equation (2.6). Initial guesses for these parameters are provided prior to an optimization procedure, where an approximation for E_0 can be determined from the experimentally measured threshold, and σ_0 is simply a scaling factor that depends on the absolute magnitude of the cross section measured. The *n* parameter, which determines the shape of the cross section, can in some cases be related to the properties of the transition state to form the products.[6] For translationally driven reactions (i.e., those studied here), *n*

is suggested to range from 1 to 3.5.[6] Optimized modeled fits, using CRUNCH, are obtained using a nonlinear least-squares fitting procedure. The modeled cross sections are compared with the experimental cross sections within a specified energy range and the modeling parameters are varied in the direction that minimizes the squared-error between the calculated and experimental cross sections.[1] Figure 2.5 shows the optimized fits that are obtained from modeling the product ion cross sections in the exchange and CID processes for the GdO^+ reaction with O_2. No special high energy treatment is needed for the Gd^+ cross section resulting from the CID process, whereas the GdO_2^+ cross section resulting

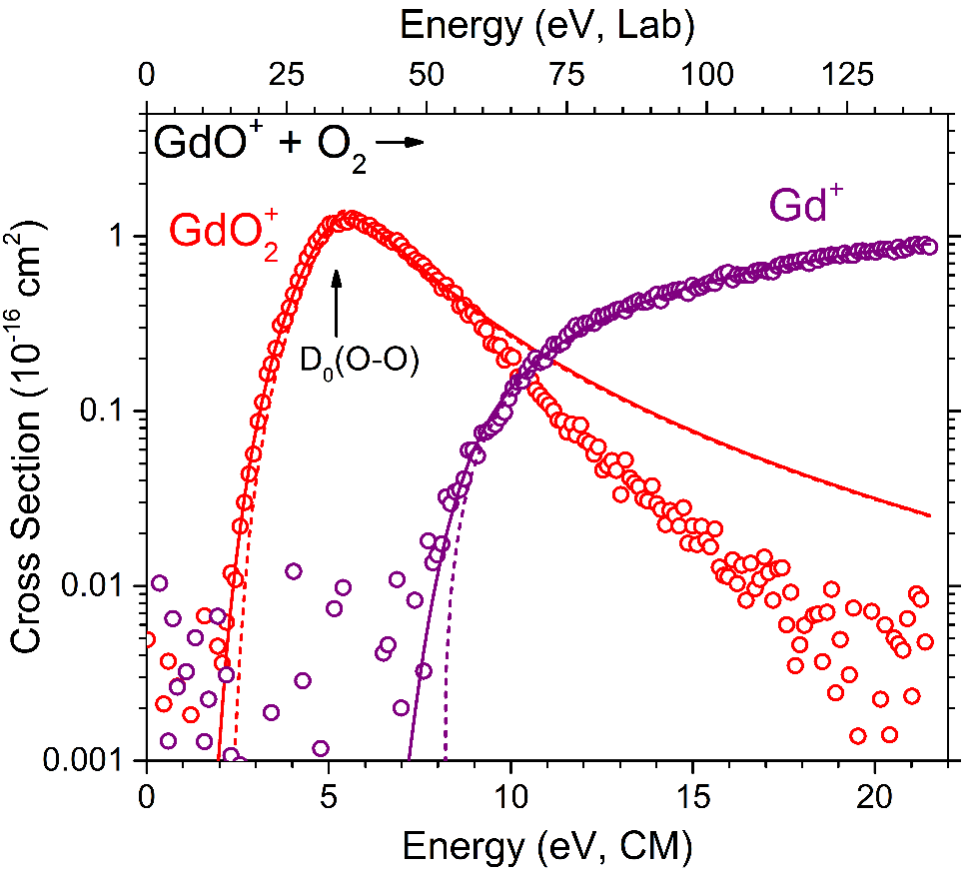

Figure 2.5. The same data as shown in Figure 2.1, but modeled to extract E_0 values. The fits indicated by the solid lines correspond to modeled cross sections using equations (2.6) and (2.7) as described in the text. The dashed lines correspond to modeled fits given by equation (2.8) that exclude convolution over the reactant internal and kinetic energy distributions.

from the exchange reaction is modeled with a modified version of equation (2.6), for energies exceeding the bond energy of the neutral, that includes a dissociation probability as described in detail elsewhere.[5] The solid lines in Figure 2.5 include the effects of the internal and kinetic energy of the reactants and correspond to the optimized fits to the experimental data. The resulting optimized parameters (E_0, σ_0, and n) from these fits are subsequently used to calculate cross sections that exclude convolution over the reactant internal and kinetic energies via equation (2.8).

$$\sigma(E_{CM}) = \frac{\sigma_0(E_{CM} - E_0)^n}{E_{CM}} \quad (2.8)$$

These modeled 0 K cross sections are given by the dashed lines and indicate the E_0 value of the reactions. Figure 2.5 illustrates the combined effect of the reactant internal and kinetic energy distributions on the measured threshold (solid) compared with E_0 (dashed line). As discussed above, the largest contribution to the deviation between the experimental threshold and E_0 for the systems studied here comes from the kinetic energy distributions of the reactant neutrals. However, the careful accounting of all these factors allows for accurate gas phase thermochemistry to be measured using GIBMS.

2.8 References

(1) Armentrout, P. B. Mass Spectrometry—Not Just a Structural Tool: The Use of Guided Ion Beam Tandem Mass Spectrometry to Determine Thermochemistry. *J. Am. Soc. Mass. Spectrom.* **2002,** *13*, 419-434.

(2) Schultz, R. H.; Armentrout, P. B. Reactions of N_4^+ with Rare Gases from Thermal to 10 eV Center-of-Mass Energy: Collision-Induced Dissociation, Charge Transfer and Ligand Exchange. *Int. J. Mass Spectrom. Ion Processes* **1991,** *107*, 29-48.

(3) Daly, N. R. Scintillation Type Mass Spectrometer Ion Detector. *Rev. Sci. Instrum.* **1960,** *31*, 264-267.

(4) Ervin, K. M.; Armentrout, P. B. Translational Energy Dependence of $Ar^+ + XY \rightarrow ArX^+ + Y$ (XY=H_2,D_2,HD) from Thermal to 30 eV C.M. *J. Chem. Phys.* **1985,** *83*, 166-189.

(5) Weber, M. E.; Elkind, J. L.; Armentrout, P. B. Kinetic Energy Dependence of $Al^+ + O_2 \rightarrow AlO^+ + O$. *J. Chem. Phys.* **1986,** *84*, 1521-1529.

(6) Armentrout, P. B. Kinetic Energy Dependence of Ion–Molecule Reactions: Guided Ion Beams and Threshold Measurements. *Int. J. Mass Spectrom.* **2000,** *200*, 219-241.

(7) Chantry, P. J. Doppler Broadening in Beam Experiments. *J. Chem. Phys.* **1971,** *55*, 2746-2759.

(8) Johnson III, R. D. NIST Computational Chemistry Comparison and Benchmark Database, NIST Standard Reference Database Number 101 Release 18, NIST, 2016, available online: http://cccbdb.nist.gov/.

(9) Kickel, B. L.; Armentrout, P. B. Guided Ion Beam Studies of the Reactions of Group 3 Metal Ions (Sc^+, Y^+, La^+, and Lu^+) with Silane. Electronic State Effects, Comparison to Reactions with Methane, and M^+-SiH_x (x = 0-3) Bond Energies. *J. Am. Chem. Soc.* **1995,** *117*, 4057-4070.

(10) Chen, Y.-M.; Elkind, J. L.; Armentrout, P. B. Reactions of Ru^+, Rh^+, Pd^+, and Ag^+ with H_2, HD, and D_2. *J. Phys. Chem.* **1995,** *99*, 10438-10445.

(11) Muntean, F.; Armentrout, P. B. Guided Ion Beam Study of Collision-Induced Dissociation Dynamics: Integral and Differential Cross Sections. *J. Chem. Phys.* **2001,** *115*, 1213-1228.

(12) Lifshitz, C.; Wu, R. L. C.; Tiernan, T. O.; Terwilliger, D. T. Negative Ion–Molecule Reactions of Ozone and Their Implications on the Thermochemistry of O_3^-. *J. Chem. Phys.* **1978,** *68*, 247-260.

CHAPTER 3

GADOLINIUM (Gd) OXIDE, CARBIDE, AND CARBONYL CATION BOND ENERGIES AND EVALUATION OF THE Gd + O → GdO^+ + e^- CHEMI-IONIZATION REACTION ENTHALPY

This chapter is reprinted with permission from Demireva, M; Kim, J.; Armentrout, P. B. Gadolinium (Gd) Oxide, Carbide, and Carbonyl Cation Bond Energies and Evaluation of the Gd + O → GdO^+ + e^- Chemi-Ionization Reaction Enthalpy. *J. Phys. Chem. A* **2016**, *120*, 8550–8563.

http://pubs.acs.org/doi/abs/10.1021/acs.jpca.6b09309

3.1 Graphical Abstract

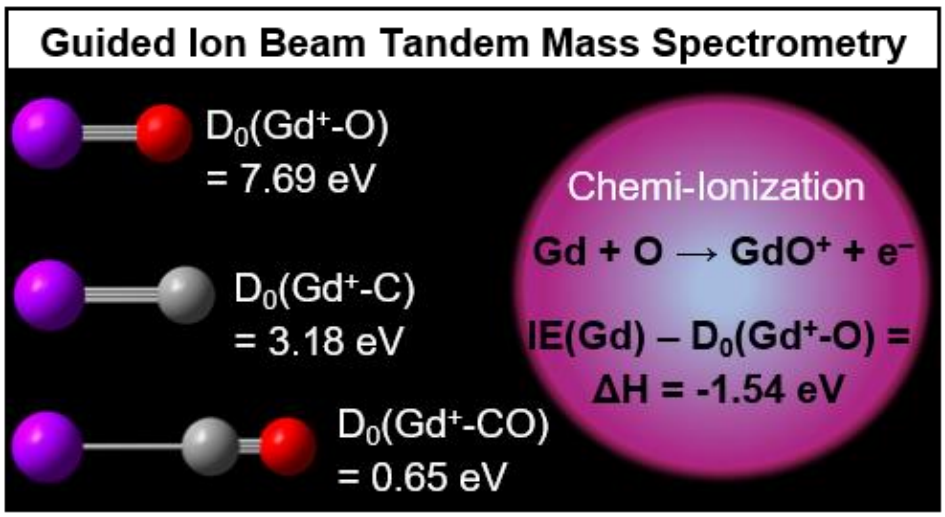

3.2 Abstract

Guided ion beam mass spectrometry (GIBMS) is used to measure the kinetic energy dependent product ion cross sections for reactions of the lanthanide metal gadolinium cation (Gd^+) with O_2, CO_2, and CO, and for reactions of GdO^+ with CO, O_2, and Xe. GdO^+ is formed through barrierless and exothermic processes in the reactions of Gd^+ with O_2 and CO_2. All other reactions observed are endothermic and analyses of their kinetic energy dependent cross sections yield 0 K bond dissociation energies (BDEs) for GdO^+, GdC^+, and $GdCO^+$. The 0 K BDE for GdO^+ is determined from five different reactions to be 7.69 ± 0.10 eV, and this value is combined with literature data to derive the ionization energy (IE) of GdO as 5.82 ± 0.16 eV. Additionally, GdC^+ and $GdCO^+$ BDEs of 3.18 ± 0.18 eV and 0.65 ± 0.06 eV are obtained from analysis of the Gd^+ reactions with CO and CO_2, respectively. Theoretical GdO^+, GdC^+, and $GdCO^+$ BDEs are calculated for comparison with experiment using various Gd basis sets with an effective core potential and several levels of theory. For calculations that correctly predict a ^{10}D ground state for Gd^+, good agreement between theoretical and measured GdC^+ and $GdCO^+$ BDEs is obtained, whereas the GdO^+ BDE is underestimated in these calculations by about 0.8 eV. Additional BDEs for GdO^+ and GdC^+ are calculated using triple and quadruple-ζ correlation consistent all-electron basis sets for Gd. Calculations with these basis sets provide better agreement with experiment for GdO^+ but not for GdC^+. The measured Gd^+ oxide, carbide, and carbonyl BDEs are similar to those for the group 3 metal ions, Sc^+ and Y^+. This is attributed to similarities in the ground state electronic configurations of these metal ions leading to similar interaction strengths. The experimental GdO^+ BDE measured here combined with the known IE of Gd is used to determine an exothermicity of 1.54 ± 0.10 eV for the Gd

chemi-ionization reaction with atomic oxygen. This value is consistent with but more precise than previous literature values.

3.3 Introduction

3.3.1 Overview. Radio wave transmission used in satellite communications depends on the electron density in the ionosphere (atmospheric altitudes > ~100 km). Disruptions in these communications can occur from natural electron density fluctuations.[1] The Air Force Research Laboratory (AFRL) is interested in creating localized electron enhanced plasmas in the ionosphere to mitigate these naturally occurring scintillation effects. One means to create such plasmas is by releasing metal atoms that can readily react with abundant free oxygen atoms in the ionosphere through the chemi-ionization reaction (3.1):[1]

$$M + O \rightarrow MO^+ + e^- \qquad (3.1)$$

Previous compilations[2-4] of thermochemical data suggest that reaction (3.1) is exothermic for many of the lanthanide metals and for a few transition and actinide metals. Atmospheric chemical release experiments have been performed using the lanthanides samarium (Sm) and neodymium (Nd).[1,3] Differences in the flows of the Nd and Sm plasmas referenced to those of known ions and neutrals were used to infer that Sm underwent chemi-ionization while Nd did not.[5] This inference, however, is inconsistent with the known chemi-ionization exothermicities for these metals where reaction (3.1) is significantly more exothermic for Nd than Sm.[2-4] Recently, the chemi-ionization reaction rate coefficients for Sm and Nd have been measured using a flow tube apparatus and indicate that reaction (3.1) is at least 30 times more efficient for Nd than Sm in good agreement with the corresponding

chemi-ionization exothermicities.[3] Ard et al. suggested that the results from the atmospheric chemical release experiments were likely misinterpreted because these relied only on the observation of a visual greenish cloud resulting from light emitted by excited neutral Nd and NdO, whereas excited NdO^+ formed in reaction (3.1) might not emit in the visible spectrum range.[3]

Subsequent Sm atmospheric release experiments have been performed in which more sophisticated instruments were used to analyze the plasmas produced.[1] Analysis of these clouds indicated that, although Sm undergoes chemi-ionization, the electron densities produced were 10 to 100 times lower than predicted on the basis of the available thermochemistry.[1] This led to a recent re-evaluation of the Sm chemi-ionization exothermicity.[6] In this study, the exothermicity of the Sm chemi-ionization reaction was determined indirectly through two thermodynamic cycles shown in Scheme 3.1 using either 1) the ionization energy (IE) of the metal and the bond dissociation energy (BDE) of the metal oxide cation or 2) the IE and BDE of the metal oxide.[6]

The SmO^+ BDE was measured using guided ion beam tandem mass spectrometry (GIBMS) and combined with the well-established IE of Sm through thermodynamic cycle 1) giving an exothermicity of 0.08 ± 0.07 eV. Independently, the SmO IE was measured using resonantly enhanced two-photon ionization and pulsed-field ionization zero kinetic energy photoelectron spectroscopy and combined with the literature BDE for SmO through thermodynamic cycle 2) yielding an exothermicity of 0.14 ± 0.17 eV.[6] These measurements are self-consistent and ~0.2 eV lower than the previous literature value and indicate that the Sm chemi-ionization reaction is barely exothermic.[1,6] This lower exothermicity potentially explains the lower than expected electron densities observed in the atmospheric

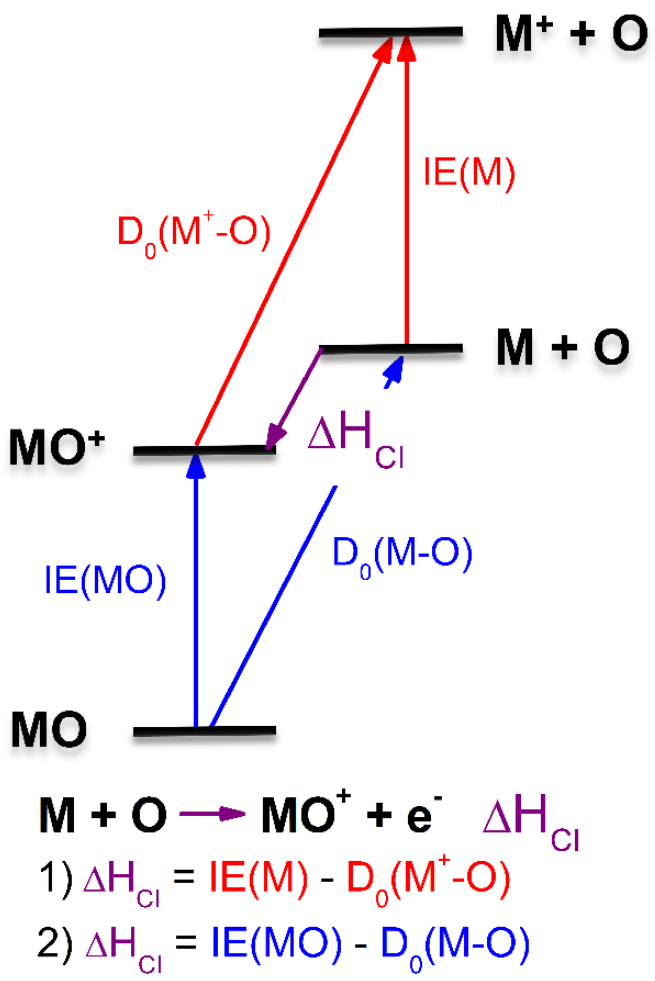

Scheme 3.1. Diagram of thermodynamic cycles that can be used to determine the exothermicity of the chemi-ionization reaction (ΔH_{CI}) via 1) the ionization energy of the metal (M) and bond energy of the metal oxide cation and 2) the ionization and bond energy of the metal oxide.

chemical release experiments and the inefficiency of the chemi-ionization process relative to Nd.[1,6,7]

Sm was chosen for the atmospheric chemical release experiments because of the relatively low boiling temperature needed to vaporize the metal. Other lanthanides could alternatively be used for these experiments including gadolinium (Gd), which has a comparable boiling temperature (3546 K) to Nd (3347 K).[8] The literature also suggests that

the Gd chemi-ionization reaction (3.1) is significantly more exothermic than that of Sm (see discussion below). Furthermore, crossed beam experiments measuring the associative ionization cross section for the Gd chemi-ionization reaction indicate that this process is exothermic and proceeds efficiently.[9]

The Sm experiments highlight the importance of accurate and precise thermochemistry measurements before undertaking expensive atmospheric chemical release experiments. Because the IE of Gd (6.14980 eV[10,11]) is well-established, the Gd chemi-ionization exothermicity could be determined accurately and precisely from thermodynamic cycle 1) in Scheme 3.1 if an accurate and precise value for the GdO^+ BDE can be measured. GIBMS has proved to be a reliable technique[12,13] for measuring thermochemical information and has been used to measure the metal oxide cation BDEs for main group metals,[14,15] for first,[16-20] second,[21,22] and third[23-27] row transition metals, Sm,[6] and Th.[28]

Here, GIBMS is used to measure the 0 K GdO^+ BDE from several different reactions. This BDE is combined with the well-established IE of Gd to determine the exothermicity of the Gd chemi-ionization reaction. BDEs for GdC^+ and $GdCO^+$ at 0 K are also obtained from these experiments. The oxide, carbide, and carbonyl bond energies for Gd^+ are compared with theoretical calculations and with experimental values for the isoelectronic (excluding the 4f electrons of Gd^+ and Lu^+) group 3 metal cations Sc^+, Y^+, La^+, and Lu^+.

3.3.2 Review of the literature thermochemistry. The chemi-ionization exothermicity for Gd can be determined indirectly from the literature IE and BDE values for GdO using thermodynamic cycle 2) in Scheme 3.1. A value of 5.75 ± 0.1 eV for the IE

of GdO has been obtained from the linear extrapolation method of ionization efficiency curves in electron ionization measurements.[29] Unfortunately, values from this work have proven to be unreliable in some cases, differing from more recent measurements by up to ~0.8 eV.[6,23,26,30] Two additional studies have reported electron ionization energies (IEs) for GdO^+ of 6.5 ± 0.8 eV[31] and 6.7 ± 0.5 eV,[32] while obtaining IEs for Gd^+ of 6.3 ± 0.6 eV and 6.1 ± 0.1 eV, respectively, consistent with the well-established IE for Gd of 6.14980 eV.[10,11] These IE measurements are designed primarily to verify that GdO^+ is not formed by fragmentation of larger molecules, and hence are generally imprecise and often inaccurate, explaining why they are clearly too high, exceeding significantly the IE of Gd. Even so, Cockett et al.[33] recommended an IE for GdO of 6.5 ± 1.0 eV, adopted from the IE measurements by Murad and Hildenbrand,[32] even though Murad and Hildenbrand utilized the 5.75 eV value in their calculations of the GdO^+ BDE (see below).

In contrast to the few IE measurements for GdO, there are several experimental measurements for the BDE of GdO, as determined from vaporization of Gd_2O_3[34,35] and equilibrium exchange reactions.[32,34,36] In an early review[37] of BDEs for gaseous monoxides, a BDE of 6.98 ± 0.26 eV was calculated on the basis of the vaporization measurements (the only values available at that time).[34,35] Unfortunately, these calculations must utilize extrapolated values of heat contents from high temperatures, which limits their accuracy. A similar BDE (but with reduced uncertainty) of 6.98 ± 0.10 eV was adopted in another report.[38] Subsequently, exchange experiments by Drowart et al. (using Y and P)[36] and later by Murad and Hildenbrand (using Ti and Y)[32] obtained GdO BDEs in good agreement with the value obtained from the exchange experiment of Ames et al. (using Tb).[34] These measurements suggested that the BDE of GdO was larger, 7.35 ± 0.13 eV. In

a compilation[39] of diatomic constants by Huber and Herzberg, a BDE of 7.37 ± 0.10 eV is provided on the basis of the exchange reactions available at that time (from Drowart et al.[36] and Ames et al.[34]). The review of Pedley and Marshall[40] on thermochemical data for gaseous metal oxides also includes the exchange measurements of Murad and Hildenbrand that had become available. This review[40] evaluates all D_0(Gd-O) measurements (notably, there have been no subsequent experimental measurements since) and recommends a BDE of 7.36 ± 0.13 eV, obtained by giving more weight to the exchange reaction results. A subsequent review by Chandrasekharaiah and Gingerich[41] gives a GdO BDE of 7.37 ± 0.13 eV, derived from the same set of thermochemical data. Likewise, Cockett et al.[33] recommended a GdO BDE of 7.3 ± 0.2 eV from Murad and Hildenbrand. Most recently, a GdO BDE of 7.36 ± 0.08 eV was adopted by Konings et al.,[4] a value determined only from the exchange reactions of Murad and Hildenbrand[32] and the vaporization study of Ames et al. (even though the latter study also includes an exchange reaction result),[34] with more weight placed on the results from the exchange reactions. These authors do not explain the reasons for excluding the other GdO BDE measurements in their GdO BDE determination. Our assessment of this literature concludes that the review of Pedley and Marshall, which considers all data available, provides the most comprehensive evaluation, leading us to recommend a GdO BDE of 7.36 ± 0.13 eV (710 ± 13 kJ/mol).

Combining the literature values discussed for the BDE (6.98 ± 0.26 and 7.36 ± 0.13 eV) and the IE (5.75 ± 0.1 and 6.5 ± 1.0 eV) for GdO through thermodynamic cycle 2) in Scheme 3.1 gives possible exothermicities for the Gd chemi-ionization reaction of 1.61 ± 0.16, 1.23 ± 0.28, 0.9 ± 1.0, and 0.5 ± 1.0 eV. The former value is consistent with chemi-electron spectroscopy experiments that measure the maximum kinetic energy of the

electrons produced in the Gd chemi-ionization reaction and yield an exothermicity of 1.50 ± 0.27 eV.[33] This value might only represent a lower limit to the true exothermicity if the maximum electron kinetic energy band is not measured. This value could also be affected by Gd excited states because the sample was vaporized at 900 K.

The BDE and IE of GdO can also be combined with the IE of Gd to determine the BDE of GdO^+. Three values can be found in the literature that utilize the IE(GdO) value of 5.75 ± 0.1 eV from Ackermann et al.[29] These authors report a value of $D_0(GdO^+)$ = 7.47 ± 0.10 eV, which is derived from their measured IE(Gd) value of 6.24 eV (instead of 6.14980 eV) along with the $D_0(GdO)$ value of 6.98 ± 0.10 eV taken from Brewer and Rosenblatt[37] (with a reduced uncertainty). Murad and Hildenbrand[32] report a GdO^+ BDE of 7.81 ± 0.13 eV, which is deduced using $D_0(GdO)$ = 7.35 ± 0.13 eV and an IE for Gd of 6.15 eV. This value has been adopted by Bohme and coworkers.[42] The third literature BDE for GdO^+ is 7.59 ± 0.16 eV as reported by Chandrasekharaiah and Gingerich[38] and adopted by Gibson.[43] The origins of this value are not explained, but it appears to correspond to the average of the two reported GdO^+ BDEs from Ackermann et al.[29] and Murad and Hildenbrand.[32] As such, it is inconsistent with their chosen values for $D_0(GdO)$ = 7.36 eV and IE(GdO) = 5.75 eV. A fourth literature value for $D_0(GdO^+)$ was reported by Schwarz and coworkers,[44] 7.0 ± 1.2 eV, determined using the BDE and IE for GdO (7.3 ± 0.2 and 6.5 ± 1.0 eV, respectively) recommended by Cockett et al.[33] This GdO^+ BDE value is questionable because of the IE(GdO) value used in this determination. Given the information reviewed above, the best value for $D_0(GdO^+)$ available in the literature is 7.76 ± 0.16 eV, as calculated using $D_0(GdO)$ = 7.36 ± 0.13 eV,[40] IE(GdO) = 5.75 ± 0.1 eV,[29] and IE(Gd) = 6.14980 eV.[10,11]

3.4 Experimental and Theoretical Methods

3.4.1 GIBMS. Experimental procedures and the guided ion beam tandem mass spectrometer used for the threshold energy measurements here have been described in detail previously.[12,13,45] Briefly, a direct current discharge flow tube (DC/FT) ion source[46] is used to generate singly charged Gd ions. A DC voltage of -1000 to -1400 V is applied to a cathode consisting of the Gd foil (Sigma-Aldrich, St. Louis, MO) attached to a Ta holder. A gas mixture of approximately 10% Ar and 90% He is continuously introduced into the source at a pressure of 0.3 to 0.4 Torr. Ar ions produced through a discharge are accelerated into the Gd foil and sputter singly charged Gd ions. The Gd ions are swept into a 1 m long flow tube where they undergo ~10^5 thermalizing collisions with the He/Ar carrier gas mixture. Previous studies indicate that the atomic metal ions generated from this DC/FT ion source form a distribution of electronic states that can be characterized by average electronic temperatures of about 700 ± 400 K[47,48] and 300 ± 100 K[49] depending on the metal ion. At 300 K, 68% of Gd ions are in their ground $^{10}D_{5/2}$ electronic spin-orbit level (and 100% in the ^{10}D ground state), whereas about 30% will be in this level at 1100 K (and 97% in the ^{10}D ground state). The average electronic energy (E_{el}) for Gd^+ at a temperature of 700 ± 400 K is 0.04 ± 0.03 eV and is accounted for in the modeling described below. GdO^+ precursor ions are generated by introducing O_2 gas into the flow tube about 15 cm downstream from the cathode where Gd^+ is produced. GdO^+ precursor ions formed in the reaction between Gd^+ and O_2 are assumed to be thermalized to the temperature of the flow tube (~300 K) and thus have an average electronic energy of zero, and a Maxwellian distribution of rovibrational states.

Precursor ions are skimmed from the flow tube, focused, and passed through a

magnetic momentum analyzer where they are mass-selected. The heaviest ^{160}Gd isotope (21% natural abundance, at least 2 Da heavier than other Gd isotopes) is selected to ensure sufficient mass separation. The precursor ions are decelerated to a desired kinetic energy and focused into a radiofrequency octopole ion beam guide.[50,51] Within the octopole, the ions pass through a static gas cell, in which neutral reactant gases (O_2, CO_2, CO, or Xe) are introduced at pressures of ~0.1 to 0.4 mTorr. This pressure range is sufficiently low to ensure that single collisions predominantly occur between the precursor ions and reactant gas. This is confirmed by performing measurements at different reactant gas pressures. In the results discussed below, products that exhibit any pressure dependence are explicitly mentioned. Precursor and product ions drift to the end of the octopole, where they are extracted and mass selected using a quadrupole mass filter. Their intensities are measured with a Daly detector[52] as a function of precursor ion kinetic energy. Product ion intensities are corrected for any background reactions that occur outside the cell and are converted to absolute product ion cross sections as a function of kinetic energy in the center-of-mass (CM) frame as detailed previously.[51] The uncertainty in the absolute cross sections is estimated as ± 20%. Retarding measurements are used to obtain the kinetic energy distribution as having a full width at half maximum of ~0.5 eV (lab), and the zero of the absolute energy scale with an uncertainty of ± 0.1 eV (lab).

3.4.2 Data analysis. Threshold energies, E_0, for product formation at 0 K are obtained by modeling the kinetic energy dependent cross sections (using the data analysis program CRUNCH) as explained elsewhere.[13,53] Briefly, a modified line-of-centers model[13] shown in equation (3.2) is used to fit the cross sections resulting from endothermic reactions to obtain E_0:

$$\sigma(E) = \sigma_0 \sum_i g_i (E + E_i + E_{el} - E_0)^n / E \qquad (3.2)$$

where E is the CM kinetic energy, σ_0 and *n* are empirical fitting parameters, E_i is the rotational and vibrational energy of reactant(s) for state i, and g_i is the fractional population of that state ($\Sigma g_i = 1$). Vibrational frequencies and rotational constants needed for calculating E_i are obtained from the NIST WebBook[54] for O_2, CO, and CO_2, and from theoretical calculations for GdO^+ (*vide infra*). Equation (3.2) is convoluted with the reactant kinetic energy distributions prior to comparison with the experimental data.[12,13,51,55] A nonlinear least-squares approach is used to find optimal fits to the experimental cross sections by varying *n*, σ_0, and E_0. Uncertainties in the E_0 values are obtained from optimized fits to several independent data sets for a range of *n* values and include the uncertainties in the electronic energy of Gd^+ and the absolute energy scale. At higher energies, there is sufficient energy to dissociate the product ion and declines in the product cross sections are observed in exchange reactions. These high energy data are modeled using a modified form of equation (3.2) as described previously,[56] which includes a statistical probability for dissociation.

In the absence of barriers in excess of the reaction endothermicity, E_0 values obtained in collision-induced dissociation (CID) experiments correspond directly to the desired BDE. For exchange reactions, $Gd^+ + AB \rightarrow GdA^+ + B$, BDEs are obtained from expression (3.3).

$$D_0\left(Gd^+\text{-}A\right) = D_0(A\text{-}B) - E_0 \qquad (3.3)$$

3.4.3 Quantum chemical calculations. Theoretical calculations are performed using the Gaussian 09 suite of programs.[57] Ground and low-energy states and bond energies

for GdO^+, GdC^+, and $GdCO^+$ are calculated using density functional and coupled cluster methods at the B3LYP,[58,59] PBE0,[60,61] and CCSD(T,full)[62-65] levels of theory. For $GdCO^+$, CCSD(T,full) single point energies are calculated using optimized B3LYP and PBE0 structures. Extensive calculations were performed using the 6-311+G(3df) Pople basis set for O and C and three different basis sets for Gd, which all use the Stuttgart Dresden relativistic effective small core (28 electron) potential.[66] The basis sets for Gd were taken from the EMSL basis set exchange[67,68] and include the Stuttgart Dresden (SDD) (12s11p9d8f)/[5s5p4d3f], atomic natural orbital[69] (ANO) (14s13p10d8f6g)/[6s6p5d4f3g], and segmented[70] Stuttgart Dresden (Seg. SDD) (14s13p10d8f6g)/[10s8p5d4f3g] basis sets. Additional BDEs for GdO^+ and GdC^+ were calculated using the 3rd-order Douglas-Kroll-Hess Hamiltonian (DKH3)[71,72] with the all-electron cc-pVXZ-DK3[73] basis sets for Gd (obtained from Prof. Kirk A. Peterson) and the aug-cc-pVXZ-DK basis sets for O and C with X = T, Q (obtained from the EMSL basis set exchange). Analytic geometry optimization and frequency calculations using the all-electron basis sets at the CCSD(T,full) level of theory were tedious and did not yield converged structures. Instead, to determine the structures, energies, and vibrational frequencies at this level of theory, the potential energy curves were mapped by performing seven single point energy calculations for each diatomic around the equilibrium bond length determined from B3LYP calculations. The equilibrium bond lengths and minimum of the potential energy curves were subsequently deduced from fifth-order polynomial fits with the vibrational frequency extracted using the analysis of Dunham.[74] For all calculations, energies for ion complexes are zero point energy corrected using computed frequencies scaled by 0.989.[75] The rotational constant (0.376 cm^{-1}) and vibrational frequency (888 cm^{-1}) for GdO^+ used in

modeling of the experimental cross sections were obtained from quantum chemical calculations at the CCSD(T,full) level of theory using the Seg. SDD basis set for Gd.

3.5 Experimental Results

3.5.1 Gd^+ reaction with O_2 and CO_2. Product ion cross sections for the Gd^+ exchange reactions with O_2 and CO_2 as a function of CM energy in the range ~0.01 to 30 eV are shown in Figure 3.1. The GdO^+ product ion is formed in these reactions according to processes (3.4) and (3.5), respectively.

$$Gd^+ + O_2 \rightarrow GdO^+ + O \quad (3.4)$$

$$Gd^+ + CO_2 \rightarrow GdO^+ + CO \quad (3.5)$$

In both reactions, GdO^+ is formed with a significant cross section (> 100 $Å^2$) at the lowest collision energy and its cross section decreases with increasing collision energy. This indicates that GdO^+ is formed exothermically through barrierless reactions in both cases. The black lines in Figure 3.1 correspond to the theoretical collision limits expected from the Langevin-Gioumousis-Stevenson (LGS)[76] model that assumes an ion-induced dipole interaction potential for these reactions.

At low collision energies (< ~1.5 eV), the experimental GdO^+ cross section in the O_2 reaction matches the LGS cross section (Figure 3.1a), whereas that in the CO_2 reaction is lower than the LGS cross section by an average fraction of ~0.4. These cross sections can be converted to rate coefficients (k) as described previously.[51] The average experimental k for reaction (3.4) obtained for collision energies below 1.0 eV is 5.7 ± 1.1 × 10^{-10} cm^3/s, which matches k_{LGS} = 5.7 × 10^{-10} cm^3/s and corresponds to a reaction efficiency (i.e., k/k_{LGS}) of 100 ± 20 %, where the uncertainty reflects that of the measured

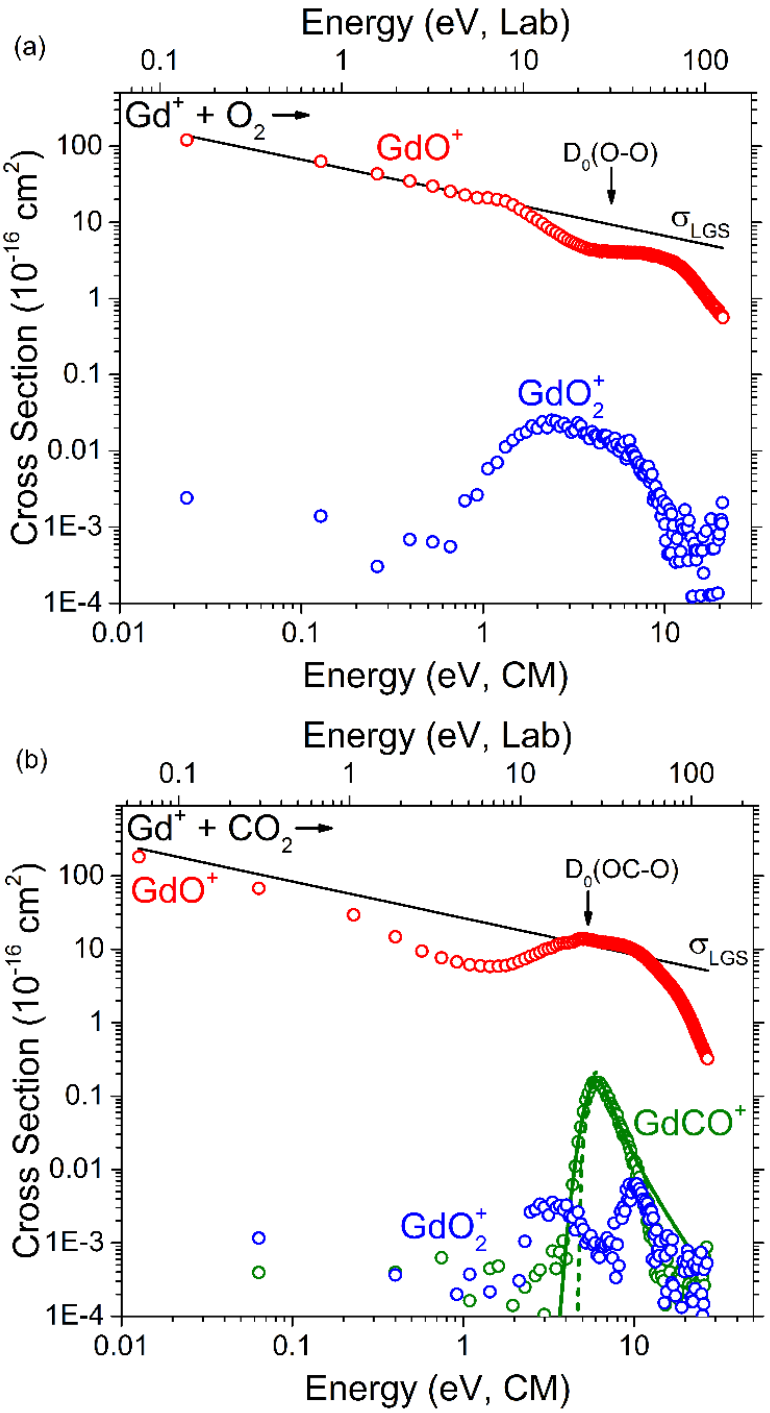

Figure 3.1. Product ion cross sections as a function of center-of-mass (bottom *x*-axis) and laboratory (top *x*-axis) frame kinetic energy for the Gd^+ reaction with (a) O_2 (0.29 mTorr) and (b) CO_2 (0.31 mTorr). The arrows indicate the O_2 and OC-O bond energies at 5.12 and 5.45 eV, respectively. The lines correspond to the Langevin-Gioumousis-Stevenson collision cross sections for these reactions. An optimized fit for the $GdCO^+$ cross section in (b) is indicated by the green solid line obtained by convoluting equation (3.2) with the Gd^+ and CO_2 kinetic energy distributions. The dashed line corresponds to the modeled 0 K cross section (i.e., no convolution over reactant internal and kinetic energy distributions).

absolute cross section. These results are consistent with the rate coefficient of 4.9 ± 1.5 × 10^{-10} cm^3/s and corresponding efficiency of 86 ± 26 % measured for the Gd^+ reaction with O_2 at thermal (~295 K) kinetic energies in inductively coupled plasma/selected-ion flow tube (ICP/SIFT) experiments.[42]

In the CO_2 reaction, the energy dependence of the GdO^+ cross section at low energies (<0.2 eV) deviates from the LGS prediction of $E^{-1/2}$, declining as $E^{-0.6\pm0.1}$. Thus, rate coefficients obtained from the corresponding GdO^+ cross sections at CM energies of 0.01 ± 0.02 eV and 0.06 ± 0.02 eV (equivalent to average translational temperatures of 100 ± 150 K and 500 ± 150 K) are 4.9 ± 1.0 × 10^{-10} and 4.0 ± 0.8 × 10^{-10} cm^3/s, respectively. Using k_{LGS} = 6.3 × 10^{-10} cm^3/s, efficiencies of 77 ± 15 % and 64 ± 13 %, respectively, are obtained at these energies measured. These values are slightly higher but comparable to the rate coefficient of 3.4 ± 1.0 × 10^{-10} cm^3/s and corresponding efficiency of 50 ± 15 % observed at thermal (295 K) kinetic energies in ICP/SIFT experiments.[77]

In the Gd^+ reactions with O_2 and CO_2 (Figure 3.1), GdO_2^+ is also formed but with relatively small cross sections. GdO_2^+ is likely formed through a sequential reaction of the abundant GdO^+ product ion with a second neutral reactant. This is consistent with the GdO_2^+ cross section exhibiting only one broad feature in the O_2 reaction but having two features in the CO_2 reaction, where these features can be explained by the observed energy dependence in the respective GdO^+ cross sections. Additionally, the GdO_2^+ product ion cross section clearly depends on the O_2 pressure, confirming that this product is formed sequentially, whereas the pressure dependence in the CO_2 reaction is more difficult to discern because of the significantly smaller GdO_2^+ cross section. A detailed analysis and

discussion of these reaction cross sections, the reaction mechanisms, and complete potential energy surfaces mapped from experiment for the exothermic reactions of Gd^+ with O_2 and CO_2 to form GdO^+ will be presented elsewhere.

In the reaction between Gd^+ and CO_2, the $GdCO^+$ product ion is additionally observed and formed according to reaction (3.6):

$$Gd^+ + CO_2 \rightarrow GdCO^+ + O \quad (3.6)$$

The data in Figure 3.1b indicate that reaction (3.6) is endothermic, with an apparent onset energy near 4 eV. The $GdCO^+$ cross section peaks around ~5.5 eV and decreases sharply as expected at CM energies exceeding D_0(OC-O) = 5.45 eV[78] because this product ion has sufficient energy to dissociate into Gd^+ and CO.

3.5.2 Gd^+ reaction with CO. Gd^+ reacts with CO to form GdO^+ and GdC^+ according to reactions (3.7) and (3.8), respectively.

$$Gd^+ + CO \rightarrow GdO^+ + C \quad (3.7)$$

$$\rightarrow GdC^+ + O \quad (3.8)$$

Product ion cross sections as a function of kinetic energy in the CM frame from ~0.01 to 20 eV are shown in Figure 3.2. The GdO^+ cross section shown in Figure 3.2 has been corrected for an exothermic tail resulting from a small O_2 impurity (~0.04 %) and the GdC^+ cross section has been corrected for overlap in intensity from the GdO^+ product ion, as described in more detail in the Supporting Information (Section 3.9). The data in Figure 3.2 indicate that reactions (3.7) and (3.8) are endothermic with apparent threshold energies of ~3 and 7 eV, respectively. Both cross sections increase with collision energy, peak near D_0(C-O) = 11.11 eV,[78] and show a decline as expected at higher energies.

3.5.3 CID of GdO^+ with Xe. The BDE for GdO^+ can potentially be measured

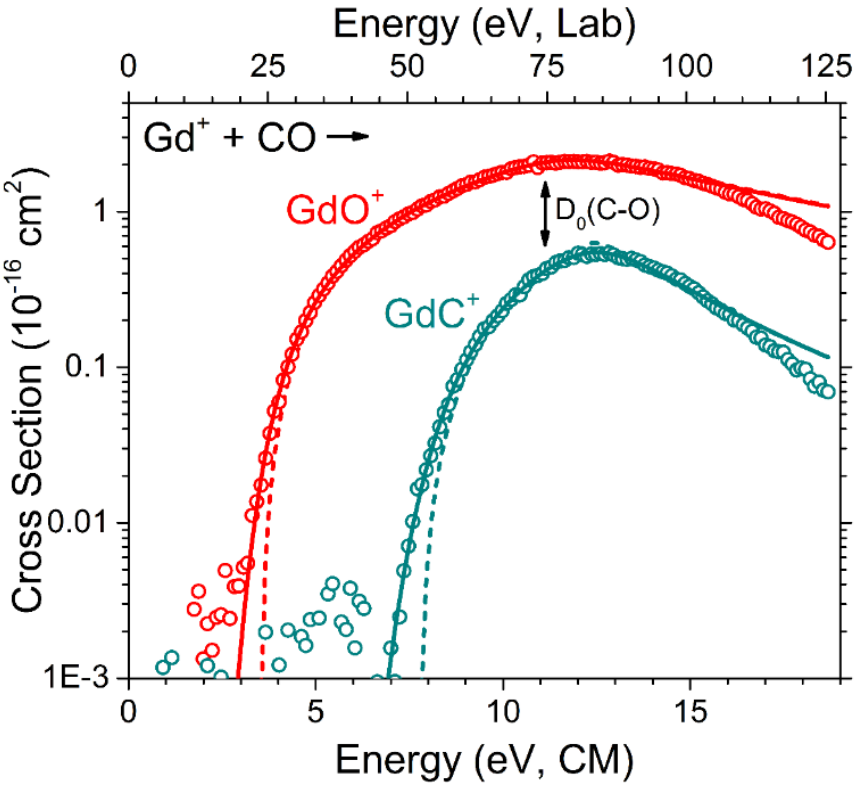

Figure 3.2. Product ion cross sections as a function of center-of-mass (bottom *x*-axis) and laboratory (top *x*-axis) frame kinetic energy for the Gd^+ reaction with CO (at a CO pressure of 0.28 mTorr). The arrow indicates the C-O bond energy of 11.11 eV. Optimized fits for the experimental GdO^+ and GdC^+ cross sections are indicated by solid lines obtained by convoluting equation (3.2) with the Gd^+ and CO kinetic energy distributions. Dashed lines correspond to the modeled 0 K cross sections (i.e., no convolution over reactant internal and kinetic energy distributions).

directly from CID of GdO^+. Previous studies have indicated that more accurate BDEs are measured from CID experiments that use Xe as the collision gas than other rare gases.[16] Thus, CID of GdO^+ was performed with Xe (results shown in Figure 3.3). This yields Gd^+ as the only product ion, reaction (3.9).

$$GdO^+ + Xe \rightarrow Gd^+ + O + Xe \qquad (3.9)$$

The energy dependent cross section shown in Figure 3.3 exhibits dissociation beginning around 8 eV.

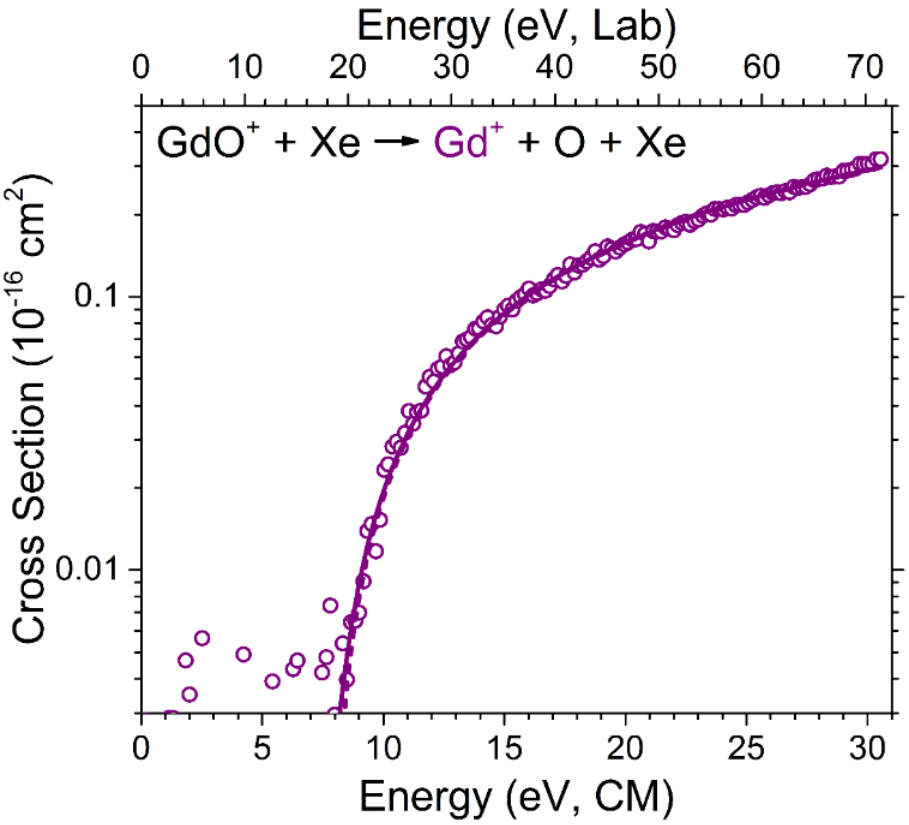

Figure 3.3. Product ion cross sections as a function of center-of-mass (bottom *x*-axis) and laboratory (top *x*-axis) frame kinetic energy resulting from CID of GdO^+ with Xe (at a Xe pressure of 0.30 mTorr). An optimized fit for the Gd^+ cross section is indicated by the solid line obtained by convoluting equation (3.2) with the GdO^+ and Xe kinetic energy distributions. The dashed line corresponds to the modeled 0 K Gd^+ cross section (i.e., no convolution over reactant internal and kinetic energy distributions).

3.5.4 GdO^+ reaction with CO. The reverse of reaction (3.5) was studied to obtain additional thermochemical information for GdO^+. Because reaction (3.5) is clearly exothermic, the reverse reaction (3.10) must be endothermic and a BDE value for GdO^+ can be obtained from modeling the reverse endothermic reaction with equation (3.2).

$$GdO^+ + CO \rightarrow Gd^+ + CO_2 \qquad (3.10)$$

Two product ions, Gd^+ and GdO_2^+, are observed in the reaction between GdO^+ and CO and the kinetic energy dependent cross sections for these product ions are shown in Figure 3.4.

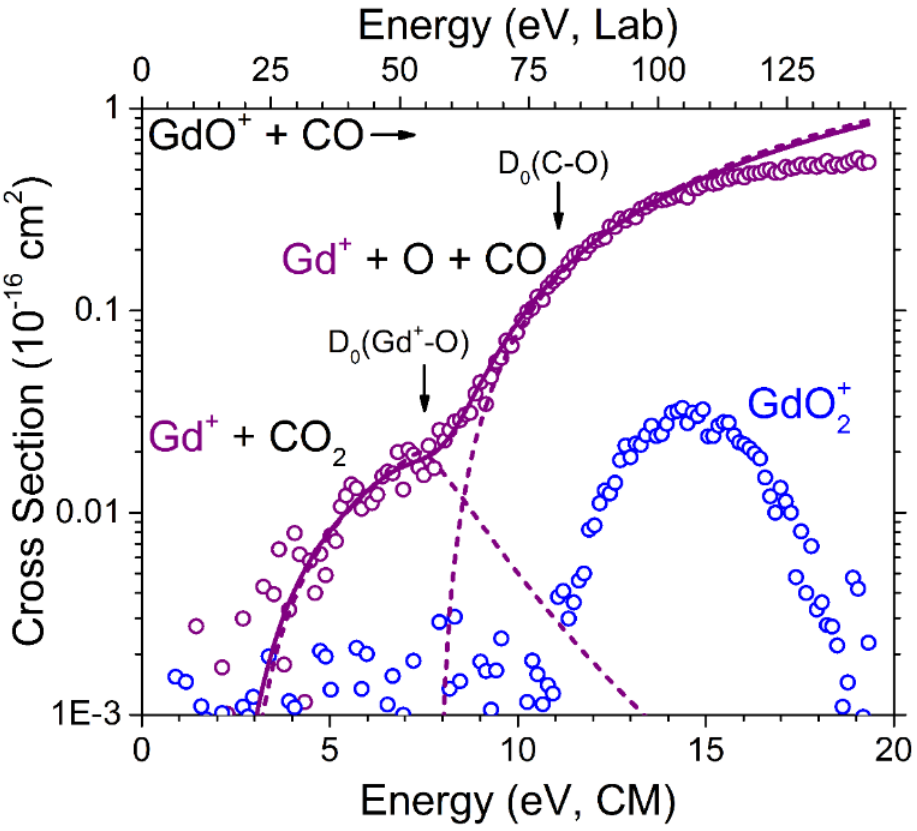

Figure 3.4. Product ion cross sections as a function of center-of-mass (bottom *x*-axis) and laboratory (top *x*-axis) frame kinetic energy for the GdO^+ reaction with CO. The arrows indicate the C-O and Gd^+-O bond energies of 11.11 and 7.69 eV, respectively. The solid line indicates a combined optimized fit for the low and high energy features of the Gd^+ cross section resulting from reactions (3.10) and (3.11) obtained by convoluting equation (3.2) for both processes with the GdO^+ and CO kinetic energy distributions. Dashed lines correspond to the modeled 0 K Gd^+ cross resulting from reactions (3.10) and (3.11) determined as described in the text.

Two features are observed in the Gd^+ cross section that have apparent threshold energies of ~3 and ~8 eV. The low energy feature can be attributed to Gd^+ being formed through exchange reaction (3.10). The high energy feature corresponds to Gd^+ being formed through CID of GdO^+ via process (3.11) and should have an onset near $D_0(Gd^+\text{-}O)$.

$$GdO^+ + CO \rightarrow Gd^+ + O + CO \qquad (3.11)$$

This is supported by the apparent onset around 8 eV, similar to the CID results for GdO^+

using Xe as the collision gas, Figure 3.3.

GdO_2^+ is formed at an apparent threshold energy of 10 – 11 eV, and its cross section increases until it peaks around 14 eV. This product ion can be formed via the exchange reaction 3.12; however, the energy at which this cross section peaks is significantly higher than the expected energy of D_0(C-O) = 11.11 eV.

$$GdO^+ + CO \rightarrow GdO_2^+ + C \qquad (3.12)$$

This shift to higher energy has also been observed in the analogous reaction between YO^+ with CO. As discussed there, such a shift could be the result of strong competition with the CID channel or an indication of an impulsive reaction mechanism.[79,80] A modified version of the spectator stripping model for endothermic reactions[81] can potentially explain this behavior and can be used to predict at what energy formation and dissociation of the GdO_2^+ product ion will occur (i.e., at what energy the cross section will begin and decline). In the spectator stripping model for exothermic reactions, the ion is assumed to interact with only one of the atoms of a diatomic neutral while the other serves as a "spectator."[51] The velocity of the spectator atom remains unchanged and linear momentum conservation thus constrains the possible translational and internal energy of the products. For an endothermic reaction, the spectator stripping model is modified such that a smaller fraction of the available energy goes into translational energy as explained previously.[79] Assuming GdO^+ interacts only with the oxygen atom in CO while the carbon remains a "spectator," the model predicts that the GdO_2^+ cross section will have a threshold of 10.1 eV and will begin to decline at 13.0 eV (using a bond energy of 2.86 eV for OGd^+-O obtained from our GIBMS measurements in progress). These predictions are in qualitative agreement with both the threshold and the onset of the decline observed experimentally. Thus, the delayed

formation of GdO_2^+ in the GdO^+ reaction with CO is plausibly explained by an impulsive reaction mechanism.

3.5.5 GdO^+ reaction with O_2. Two product ions, GdO_2^+ and Gd^+, are formed in the reaction between GdO^+ and O_2. Their energy dependent cross sections are shown in Figure 3.5. GdO_2^+ is formed with an apparent threshold energy of ~2 eV through the exchange reaction (3.13).

$$GdO^+ + O_2 \rightarrow GdO_2^+ + O \quad (3.13)$$

$$\rightarrow Gd^+ + O + O_2 \quad (3.14)$$

The GdO_2^+ cross section increases and peaks near 5 eV, which agrees well with D_0(O-O) = 5.12 eV.[78] The BDE for GdO_2^+ can be obtained from modeling this cross section using equation (3.2). A detailed analysis of these data and the corresponding BDE for GdO_2^+, believed here to be the dioxide, will be presented elsewhere. Gd^+ is likely formed through the CID reaction (3.14) rather than by an exchange reaction that would produce O_3. This assignment is supported by the apparent threshold energy for Gd^+ near ~8 eV, which is similar to that observed in the CID of GdO^+ using Xe and CO as collision gases, Figures 3.3 and 3.4. A comparison of the Gd^+ product ion cross sections that result from CID using Xe, CO, and O_2 as collision gases is shown in Figure 3.6. There is a more gradual increase in the Gd^+ cross section as a function of collision energy for Xe than for both O_2 and CO, which exhibit very similar energy dependences. For example, at a CM collision energy of ~10 eV, the measured Gd^+ cross sections are ~0.02, ~0.08, and ~0.09 × 10^{-16} cm^2 for Xe, CO, and O_2, respectively. This effect can be attributed to Xe having a significantly larger mass than O_2 and CO resulting in a different collision velocity for a given CM energy. As discussed previously, this can be related to the efficiency of translational to vibrational

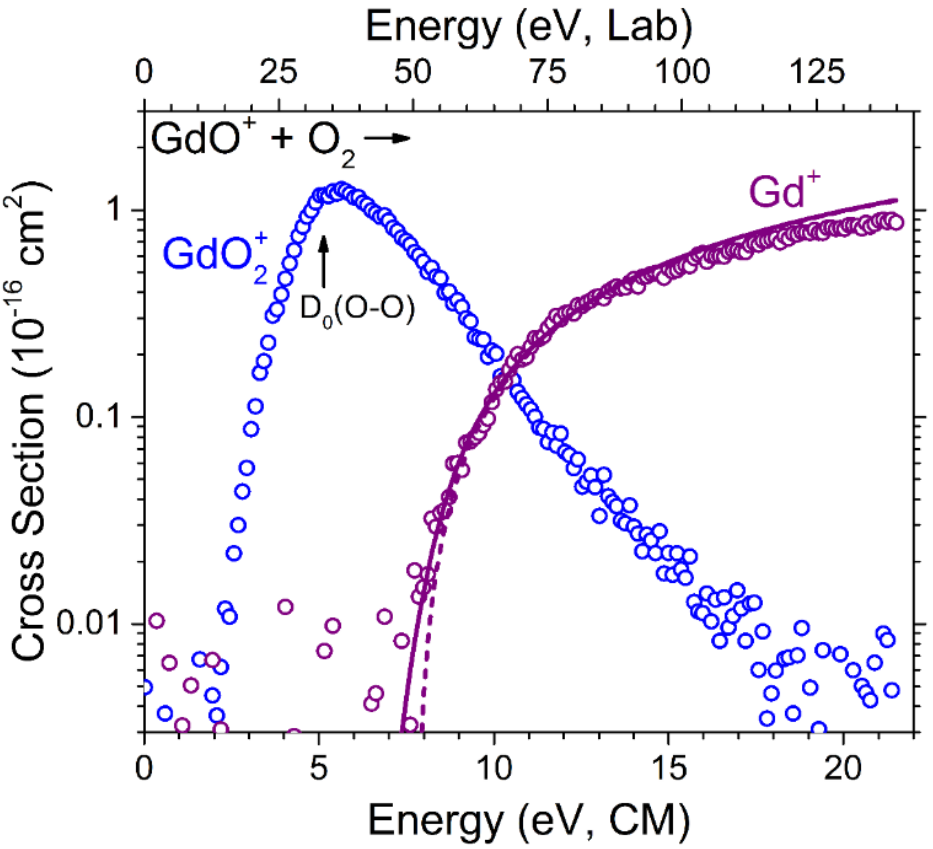

Figure 3.5. Product ion cross sections as a function of center-of-mass (bottom *x*-axis) and laboratory (top *x*-axis) frame kinetic energy for the GdO^+ reaction with O_2. The arrow indicates the O_2 bond energy at 5.12 eV. An optimized fit for the Gd^+ cross section is indicated by the solid line obtained by convoluting with equation (3.2) the GdO^+ and O_2 kinetic energy distributions. The dashed line corresponds to the modeled 0 K Gd^+ cross section (i.e., no convolution over reactant internal and kinetic energy distributions).

energy transfer, which depends on the collision time, which is inversely proportional to velocity.[16] Thus, the results for Xe give a slower rise in the Gd^+ cross section because of the smaller change in the relative velocity with increasing collision energy using this heavier collision gas. However, the strength of the interaction potential also plays a role and can explain why Xe (having a relatively large polarizability) can lead to more efficient energy transfer in the threshold region than other rare gases and typically yields more accurate threshold CID measurements.[16]

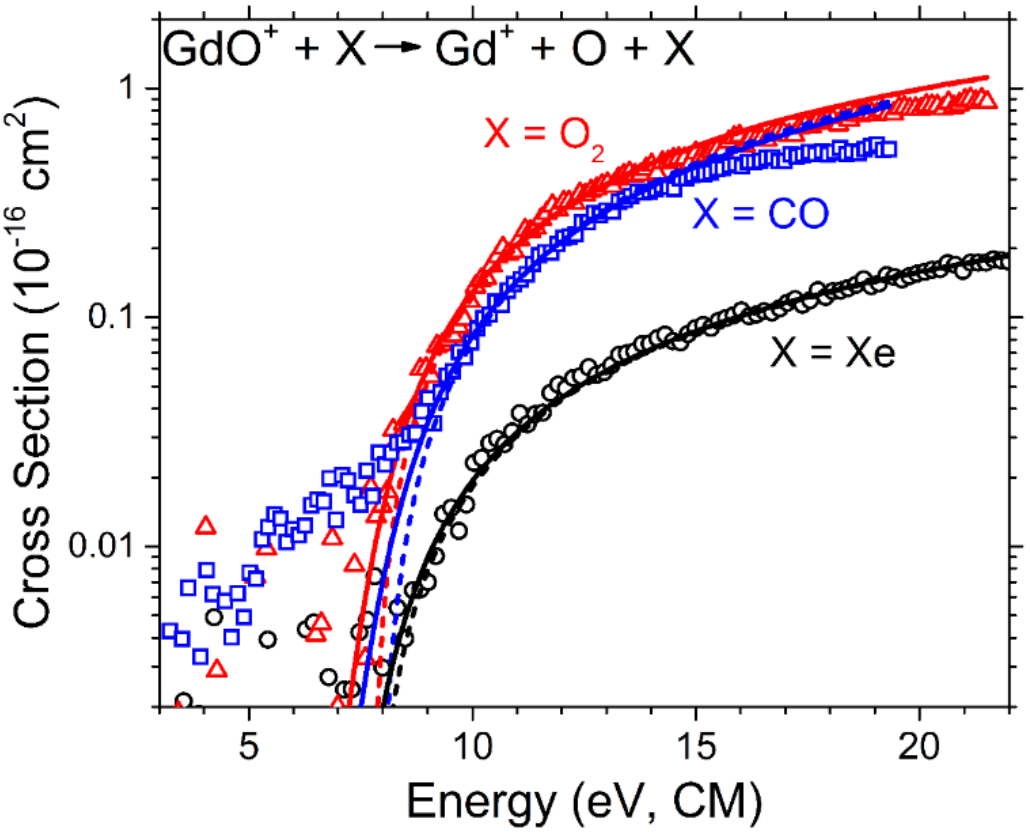

Figure 3.6. Comparison of the energy dependent Gd^+ product ion cross sections from CID of GdO^+ with Xe (black circles), O_2 (red triangles), and CO (blue squares). The optimized fits for the Gd^+ cross sections are indicated by the solid lines obtained by convoluting equation (3.2) with the reactant kinetic energy distributions. The dashed lines correspond to the modeled 0 K Gd^+ cross sections (i.e., no convolution over reactant internal and kinetic energy distributions).

3.6 Thermochemical and Theroretical Results

3.6.1 BDEs from exchange reactions. The Gd^+ exchange reactions with O_2 and CO_2 to form GdO^+ are both exothermic and barrierless (*vide supra*). Thus, $D_0(Gd^+\text{-}O)$ must exceed $D_0(O_2)$ = 5.115 eV and $D_0(OC\text{-}O)$ = 5.45 eV.[78] In contrast, GdO^+ is formed endothermically in the reaction with CO where the CO bond energy is significantly stronger at 11.11 eV. These observations bracket the GdO^+ BDE as 5.45 eV < $D_0(Gd^+\text{-}O)$ < 11.11 eV. The GdO^+ cross section resulting from the endothermic reaction between Gd^+ and CO can be modeled with equation (3.2), as shown in Figure 3.2. This yields an E_0 value

of 3.65 ± 0.26 eV (dashed red curve in Figure 3.2). Combining the E_0 value with D_0(C-O) via equation (3.3) for this exchange reaction gives a 0 K bond energy for GdO^+ of 7.46 ± 0.26 eV. Optimized fitting parameters for these data and for all other endothermic reactions modeled here are summarized in Table 3.1.

The Gd^+ reaction with CO_2 to form GdO^+ is exothermic, but the reverse reaction between GdO^+ and CO to form Gd^+ and CO_2 is endothermic. Modeling the low energy feature of the Gd^+ cross section in Figure 3.4 yields a 0 K threshold energy of 2.16 ± 0.27 eV (Table 3.1). The BDE for GdO^+ is obtained by adding D_0(OC-O) to the measured E_0 value giving $D_0(Gd^+\text{-O})$ = 7.61 ± 0.27 eV, slightly greater but consistent within experimental uncertainty with $D_0(Gd^+\text{-O})$ measured from the Gd^+ and CO reaction.

In the exchange reaction between Gd^+ and CO, GdC^+ is additionally formed endothermically. Modeling of these data (Figure 3.2) results in an E_0 value of 7.93 ± 0.18 eV, which corresponds to a 0 K bond energy for GdC^+ of 3.18 ± 0.18 eV. Similarly, $GdCO^+$ is formed endothermically in the reaction between Gd^+ and CO_2. Modeling this product ion cross section (Figure 3.1b) yields an E_0 value of 4.80 ± 0.06 eV, which combined with D_0(OC-O) gives $D_0(Gd^+\text{-CO})$ = 0.65 ± 0.06 eV.

3.6.2 BDEs from CID. Three additional values for $D_0(Gd^+\text{-O})$ are obtained from modeling the Gd^+ cross section data in the CID experiments of GdO^+ with Xe, CO, and O_2 (Figure 3.6). In these experiments, GdO^+ dissociates when its internal energy exceeds its BDE. Thus, the E_0 values determined from modeling these Gd^+ cross sections correspond directly to the 0 K BDE for GdO^+. The CID experiments using Xe and O_2 as collision gases yield $D_0(Gd^+\text{-O})$ values of 7.57 ± 0.34 and 7.83 ± 0.19 eV, respectively. An accurate threshold energy in the CID experiment of GdO^+ and CO is more difficult to obtain because

Table 3.1. Summary of optimized modeling parameters in equation (3.2) for the indicated product ion cross sections.[a]

Reaction	σ_0	n	E_0 (eV)	D_0 (eV)
$Gd^+ + CO_2 \rightarrow GdCO^+ + O$	0.8 ± 0.2	2.0 ± 0.2	4.80 ± 0.06	0.65 ± 0.06
$Gd^+ + CO \rightarrow GdO^+ + C$	0.7 ± 0.3	1.8 ± 0.2	3.65 ± 0.26	7.46 ± 0.26
$\rightarrow GdC^+ + O$	0.9 ± 0.3	1.5 ± 0.2	7.93 ± 0.18	3.18 ± 0.18
$GdO^+ + CO \rightarrow Gd^+ + CO_2$	0.003 ± 0.002	2.4 ± 0.2	2.16 ± 0.27	7.61 ± 0.27
$\rightarrow Gd^+ + O + CO$	0.17 ± 0.04	1.8 ± 0.1	7.75 ± 0.17	7.75 ± 0.17
$\rightarrow Gd^+ + O + CO$[b]	0.43 ± 0.2	1.4 ± 0.2	9.20 ± 0.25	9.20 ± 0.25
$GdO^+ + O_2 \rightarrow Gd^+ + O + O_2$	0.3 ± 0.1	1.8 ± 0.1	7.83 ± 0.19	7.83 ± 0.19
$GdO^+ + Xe \rightarrow Gd^+ + O + Xe$	0.03 ± 0.01	1.9 ± 0.1	7.57 ± 0.34	7.57 ± 0.34

[a] Uncertainties are one standard deviation.
[b] Modeled after subtracting the $Gd^+ + CO_2$ cross section.

of interference from the low energy feature that results from reaction (3.10). Correcting for this low energy feature by extrapolating the model for the threshold region to higher energies and subtracting this modeled cross section from the overall Gd^+ cross section yields a cross section with a threshold of 9.20 ± 0.25 eV for process (3.11) (fit not shown). This value is ~1.5 eV larger than that obtained from the other two CID measurements, presumably because the extrapolation of the low-energy model for reaction (3.10) to higher energies is inaccurate. If the high energy feature is modeled directly, without correcting for the low energy feature, a threshold of 7.75 ± 0.17 eV is obtained, in good agreement with the Xe and O_2 CID values. This suggests that the Gd^+ cross section resulting from reaction (3.10) exhibits a sharp decline (dashed purple line in Figure 3.4) that starts at the energy onset for the CID process (3.11), which then completely dominates at the high energies.

The three BDEs obtained from the CID experiments are all consistent, within experimental uncertainty, with each other and with the values obtained in the exchange reactions, Table 3.1. The slightly larger E_0 values obtained from the CID experiments with O_2 and CO could possibly be explained by less efficient collision energy transfer, because these neutrals can carry away vibrational energy. Furthermore, this could be an effect of the interaction strength between GdO^+ and the neutrals where Xe has a polarizability of 3.99 $Å^3$,[8] a factor of about two larger than that for O_2 (1.562 $Å^3$)[54] and CO (1.953 $Å^3$),[54] leading to more efficient collision energy transfer in the threshold region for the CID experiments with Xe. For some strongly bound species with few internal degrees-of-freedom, CID experiments have been shown to yield only upper limits to the true BDEs because of inefficiencies in collision energy transfer.[22,82] However, this does not seem to be the case here because the BDEs obtained from the CID experiments are consistent with

those measured from the two exchange reactions. Combining all five independent measurements of $D_0(Gd^+\text{-}O)$ through a weighted average gives a value of 7.69 ± 0.10 eV for the 0 K bond energy of GdO^+, where the uncertainty is one standard deviation of the mean.

3.6.3 Theoretical calculations for Gd^+. To test how well different Gd basis sets and levels of theory perform in predicting the electronic properties of Gd^+, energies of the ground and low-lying excited states for Gd^+ are calculated using the SDD, ANO, and Seg. SDD basis sets at the B3LYP, PBE0, and CCSD(T,full) levels of theory. The relative energies for each state obtained from these calculations are compared with the corresponding experimental energies[11] (which are taken as the average of the spin-orbit energy levels weighted by the 2J+1 degeneracy for each level such that the $^{10}D_{5/2}$ ground level lies 0.123 eV below the average energy of the ^{10}D ground state) and are shown in Figure 3.7 and summarized in the Supporting Information (Section 3.9). The experimental ground state for Gd^+ (^{10}D, $4f^7\ 5d^1\ 6s^1$) is accurately predicted in the calculations that use the ANO basis set at all three levels of theory. Additionally, the correct ground state is predicted using the Seg. SDD basis set at the PBE0 and CCSD(T,full) levels of theory. Poor agreement with the experimental Gd^+ energy levels is seen for the SDD basis set at all three levels of theory and for the Seg. SDD basis set using density functional theory (DFT). The ANO basis set performs reasonably well in reproducing qualitatively the Gd^+ energy levels at the B3LYP and PBE0 levels of theory. In many of the calculations, the excitation energy from the ^{10}D ground state to the ^{10}F state ($4f^75d^2$) is significantly overestimated. This value exceeds 2.5 eV for the SDD basis set at all three levels of theory and for the Seg. SDD basis set at the B3LYP and PBE0 levels of theory as shown in the

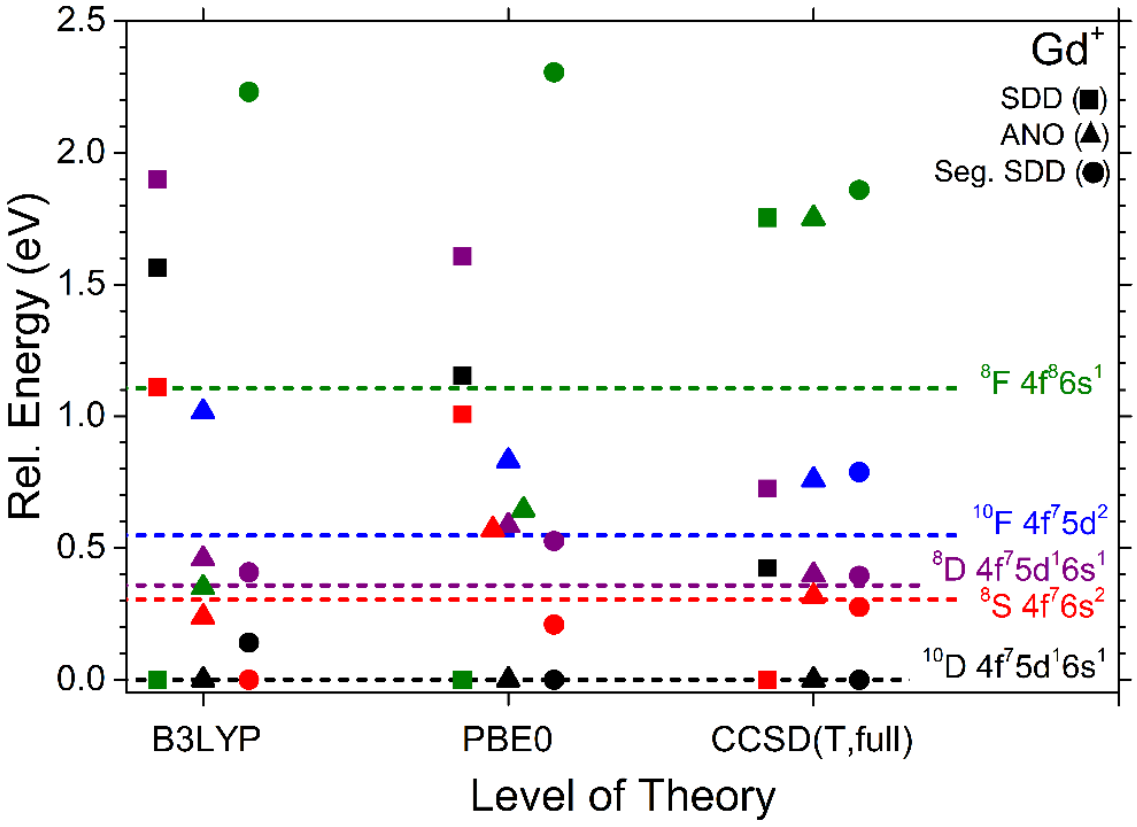

Figure 3.7. Comparison between experimental (dashed lines) and calculated (symbols) relative energies for the ground state and several excited states of Gd^+ at the B3LYP, PBE0, and CCSD(T,full) levels of theory. The basis sets used for Gd are indicated by squares for SDD, triangles for ANO, and circles for Seg. SDD. The experimental ground state for Gd^+ is indicated by the black dashed line, and the various experimental excited state energies (obtained from an average over the SO levels weighted by 2J+1) are shown by the red, purple, blue, and green dashed lines with the corresponding electronic configurations indicated in the figure.

Supporting Infromation, Section 3.9. The ANO and Seg. SDD basis sets at the CCSD(T,full) level of theory achieve good quantitative agreement with all experimental Gd^+ energy levels. Thus, these calculations will potentially provide the most reliable bond energies for GdO^+, GdC^+, and $GdCO^+$ for comparison with the measured experimental values. Because the smallest basis set for Gd (SDD basis set) performs poorly at all three levels of theory, results for this basis set are not included in the discussion that follows. For a more complete discussion of all theoretical calculations, including those for the SDD

basis set, the reader is referred to the Supporting Information (Section 3.9).

3.6.4 Ground states for GdO^+, GdC^+, and $GdCO^+$ from theory. Calculations were performed to determine the ground states for GdO^+, GdC^+, and $GdCO^+$ using the SDD, ANO, and Seg. SDD basis sets for Gd and the 6-311+G(3df) basis set for O and C at the B3LYP, PBE0, and CCSD(T,full) levels of theory. The results from these calculations are summarized and discussed in detail in the Supporting Information (Section 3.9). Calculations using the ANO and Seg. SDD basis sets for Gd predict ground states for GdO^+ and $GdCO^+$ of $^8\Sigma^-$ ($[1\phi^2 1\delta^2 1\pi^2 1\sigma^1]$ $2\pi^4$ $2\sigma^2$) and $^{10}\Pi$ ($[1\varphi^2 1\delta^2 1\pi^2 1\sigma^1]$ $2\pi^4 2\sigma^2 3\pi^1$ $3\sigma^1$), respectively, with the valence electron configurations indicated in parenthesis and 4f electrons in square brackets (mostly nonbonding). The valence electrons include the 4f, 6s, and 5d electrons of Gd^+ (^{10}D, $4f^7 5d6s$), the four 2p electrons of O (^{3}P, $2p^4$), and/or the two 2p electrons of C (^{3}P, $2p^2$). For GdC^+, most calculations predict a $^{10}\Pi$ ($[1\phi^2 1\delta^2 1\pi^2 1\sigma^1]$ $2\sigma^1 2\pi^3$) ground state. Exceptions are B3LYP and PBE0/Seg. SDD calculations, for which a $^{12}\Sigma^+$ state ($[1\phi^2 1\delta^2 1\pi^2 1\sigma^1]$ $2\sigma^1 2\pi^2 3\sigma^1$) is found to be lowest in energy, with the $^{10}\Pi$ state about 1 eV higher in energy. As discussed in detail in the Supporting Information (Section 3.9), B3LYP and PBE0/Seg. SDD results tend to favor electronic states in which the exchange energy is maximized and appears to be overestimated.

The molecular orbitals (mos) for the ground states of GdO^+ ($^8\Sigma^-$), GdC^+ ($^{10}\Pi$), and $GdCO^+$ ($^{10}\Pi$) calculated using CCSD(T,full)/Seg. SDD are shown in Figure 3.8a. The mos for $GdCO^+$ are obtained from a single point energy calculation at the CCSD(T,full)/Seg. SDD//B3LYP/Seg. SDD level. For an internuclear axis along the z direction, the 2π mos for GdO^+ and GdC^+ are bonding and arise from Gd($5d_{xz}$) and Gd($5d_{yz}$) orbitals interacting with the $2p_x$ and $2p_y$ orbitals on O or C. The $2p_z$ orbital on O or C forms the 2σ bond with

Figure 3.8. (a) Molecular orbitals (mos) for the ground state configurations of GdO^+, GdC^+, and $GdCO^+$ determined at the CCSD(T,full) level of theory using the Seg. SDD basis set for Gd. The mos for $GdCO^+$ are obtained from a single point energy calculation using the B3LYP geometry. (b) Comparison between experimental (solid lines) with associated uncertainties (dashed lines) and theoretical GdO^+, GdC^+, and $GdCO^+$ bond energies at the B3LYP, PBE0, and CCSD(T,full) levels of theory using the ANO (filled triangles) and Seg. SDD (filled circles) basis sets for Gd. The $GdCO^+$ bond energies at the CCSD(T,full) level are obtained from single point energies for $GdCO^+$ using the B3LYP geometry. BDEs for GdO^+ and GdC^+ calculated using the all-electron cc-pVXZ-DK3 basis sets for Gd^+ are given by open triangles and circles for X = T and Q, respectively. Theoretical bond energies are SO corrected as explained in detail in the Supporting Information (Section 3.9). All BDEs are referenced to the calculated energy of the Gd^+ (^{10}D) state, the experimentally determined ground state.

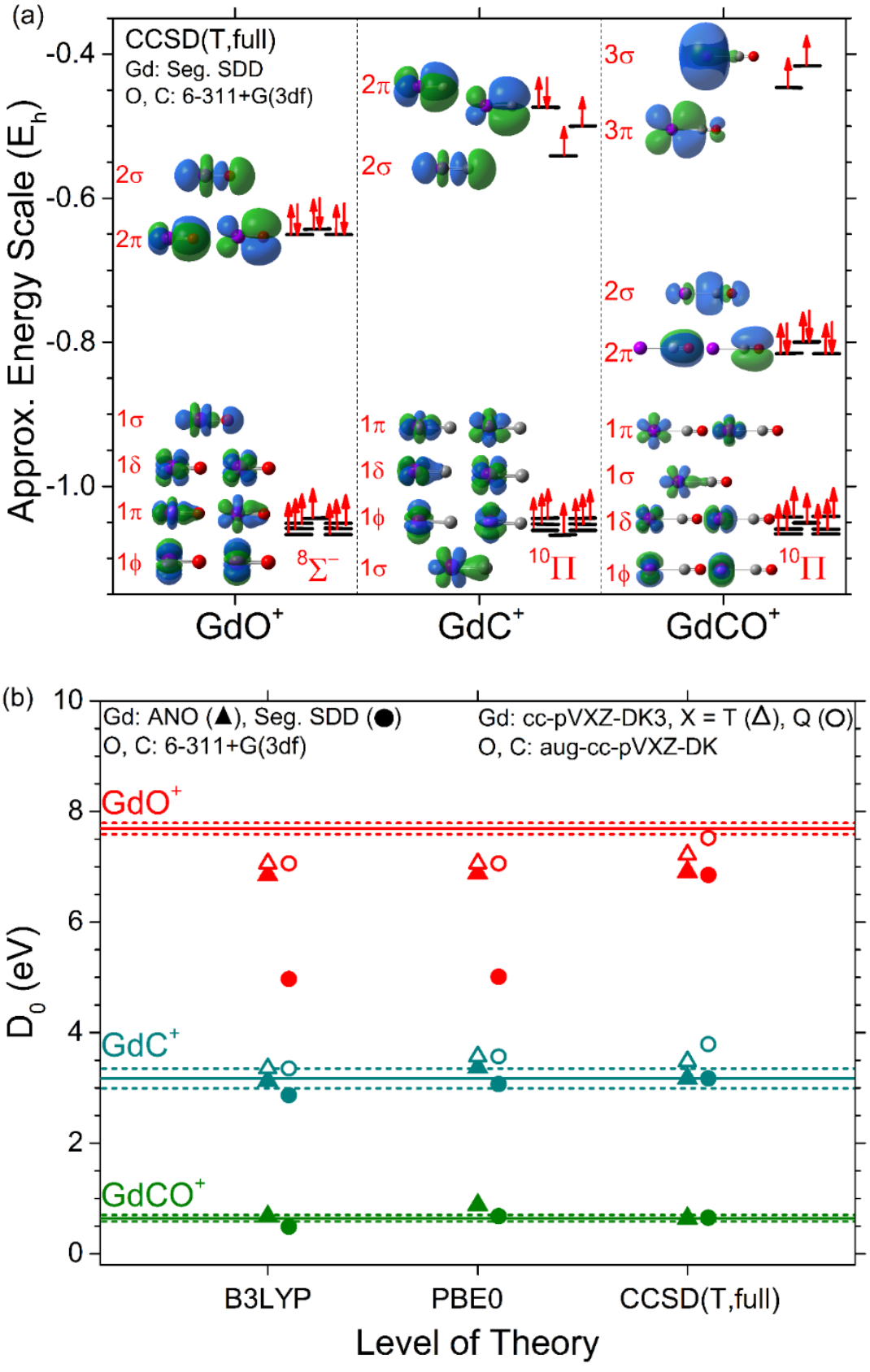
(a)
CCSD(T,full)
Gd: Seg. SDD
O, C: 6-311+G(3df)
Approx. Energy Scale (E_h)
-0.4
-0.6
-0.8
-1.0
2σ
2π
1σ
1δ
1π
1φ
8Σ−
2π
2σ
1π
1δ
1φ
1σ
10Π
3σ
3π
2σ
2π
1π
1σ
1δ
1φ
10Π
GdO+
GdC+
GdCO+
(b)
Gd: ANO (▲), Seg. SDD (●)
O, C: 6-311+G(3df)
Gd: cc-pVXZ-DK3, X = T (Δ), Q (O)
O, C: aug-cc-pVXZ-DK
D0 (eV)
10
8
6
4
2
0
GdO+
GdC+
GdCO+
B3LYP
PBE0
CCSD(T,full)
Level of Theory

the Gd($5d_z^2$) orbital. For $GdCO^+$, the valence electrons of C and O form similar mos ($2\pi^4 2\sigma^2$) to those for carbon monoxide. However, here the pair of electrons in the 2σ orbital of CO donates into the empty $5d_z^2$ orbital of Gd^+ to form a slightly bonding interaction. Additionally, a 3π bonding orbital arises from back-bonding of a $5d_\pi$ electron on Gd^+ interacting with the corresponding $2p_\pi$ orbital of C. Both these interactions in $GdCO^+$ lead to slightly elongated C-O bond lengths of 1.13 – 1.17 Å (Supporting Information, Section 3.9) compared to free CO, which has an experimental (calculated) bond length of 1.128 Å (1.124 and 1.131 Å at B3LYP and CCSD(T,full) levels of theory.[54] The 3σ mo in $GdCO^+$ corresponds largely to a nonbonding Gd^+ 6s atomic orbital with some $5d_z^2$ character.

3.6.5 BDEs from theory. Theoretical BDEs for GdO^+, GdC^+, and $GdCO^+$ are calculated from the energy difference between the ground states of GdX^+ and those of $Gd^+ + X$ with X = O, C, or CO. For calculations where the correct ground state for Gd^+ was not predicted (B3LYP/Seg. SDD), theoretical BDEs are still referenced to the energy calculated for the experimental Gd^+ (^{10}D) ground state. If the calculated ground state were used instead, worse agreement between theory and experiment would be obtained. The energies from theory for a given state correspond to an average energy over all spin-orbit (SO) levels for that state. Because the experimental values measure the difference between the ground SO level of reactants and products, a more accurate comparison between the calculated and experimental BDEs requires making an empirical SO energy correction, as described in detail in the Supporting Information (Section 3.9). The first-order SO energy correction to the calculated GdO^+ BDE is easily obtained because the ground state for GdO^+ is $^8\Sigma^-$ and thus the calculated BDE needs to be corrected only for the SO averaged energy of Gd^+ (0.12 eV) and O (0.01 eV). For GdC^+ and $GdCO^+$, the predicted ground state

is Π for most calculations. The BDEs calculated for a Π ground state include an additional SO energy correction of 0.06 eV as described in the Supporting Information (Section 3.9). This empirical SO correction utilizes the $\zeta_{5d}(Gd^+)$ SO constant, which is calculated by Professor Michael D. Morse using a modified version of a Hartree-Fock program developed by Fischer,[83,84] see Supporting Information (Section 3.9). A comparison between theoretical SO corrected and experimental BDEs for GdO^+, GdC^+, and $GdCO^+$ is shown in Figure 3.8b and listed in Table 3.2. BDEs for $GdCO^+$ at the CCSD(T,full) level in Figure 3.8b and Table 3.2 are calculated from single point energies of the B3LYP geometry optimized structures for $GdCO^+$. BDEs for $GdCO^+$ determined from single point energies using the PBE0 optimized $GdCO^+$ geometries are listed in the Supporting Information (Section 3.9) and do not differ significantly from those shown in Figure 3.8b and listed in Table 3.2.

The results in Figure 3.8b and Table 3.2 indicate that the GdO^+ BDEs are underestimated by almost 3 eV from the experimental values at the B3LYP/Seg. SDD and PBE0/Seg. SDD levels, whereas these calculations yield good agreement for the GdC^+ and $GdCO^+$ BDEs. Both GdC^+ and $GdCO^+$ are predicted in these calculations to have ground state electronic configurations that maximize the exchange energy in contrast with the $^8\Sigma^-$ ground state for GdO^+. As mentioned above and discussed further in the Supporting Information (Section 3.9), B3LYP/Seg. SDD and PBE0/Seg. SDD approaches appear to favor configurations that maximize the exchange energy, such that these calculations perform poorly in estimating the energy for the GdO^+ $^8\Sigma^-$ ground state. The ANO basis set is able to reproduce the experimental GdC^+ and $GdCO^+$ BDEs well at all levels of theory and similar BDEs are obtained using the Seg. SDD basis set at the CCSD(T, full) level of

Table 3.2 Summary of experimental and calculated BDEs (in eV) for GdO^+, GdC^+, and $GdCO^+$.[a]

Level	Basis set	GdO^+	GdC^+	$GdCO^+$
Exp.		7.69 ± 0.10	3.18 ± 0.18	0.65 ± 0.06
B3LYP	ANO	6.85	3.14	0.68
	Seg. SDD	4.97	2.87	0.50
	cc-pVTZ-DK3	7.06	3.36	
	cc-pVQZ-DK3	7.06	3.36	
PBE0	ANO	6.88	3.38	0.89
	Seg. SDD	5.01	3.07	0.69
	cc-pVTZ-DK3	7.06	3.58	
	cc-pVQZ-DK3	7.06	3.58	
CCSD(T)	ANO	6.91	3.18	0.65
	Seg. SDD	6.85	3.18	0.66
	cc-pVTZ-DK3	7.22	3.49	
	cc-pVQZ-DK3	7.52	3.80	

[a] Calculated BDEs are spin-orbit and zero point energy corrected. BDEs for $GdCO^+$ at the CCSD(T,full) level are calculated from single point energies of the B3LYP geometry optimized structures for $GdCO^+$.

theory. These results are consistent with those found for the calculated excited state energies of Gd^+ (Figure 3.7). However, the GdO^+ BDEs from these calculations are consistently lower by ~0.8 eV from the experimental value (Figure 3.8b and Table 3.2). This deviation could be a result of repulsive interactions between the 4f and bonding mos as a result of insufficient polarization on the 4f orbitals of Gd because the ANO and Seg. SDD basis sets include only up to g functions. Additional GdO^+ and GdC^+ BDE

calculations were performed using the all-electron cc-pVXZ-DKH3 basis sets[73] for Gd, which include up to h and i functions for X = T and Q, respectively. The results of these calculations are also summarized in Table 3.2 and shown in Figure 3.8b. Generally, there is better agreement with experiment for GdO^+, especially at the CCSD(T,full) level of theory, yielding BDEs of 7.22 and 7.52 eV for X = T and Q, respectively (Table 3.2). However, these calculations also yield larger values for GdC^+ and thus overestimate its BDE by up to 0.6 eV for the quadruple-ζ all-electron basis set at the CCSD(T,full) level of theory.

3.7 Discussion

3.7.1 GdO^+, GdC^+, and $GdCO^+$ bond energies. The measured BDEs for GdO^+, GdC^+, and $GdCO^+$ are 7.69 ± 0.10 eV, 3.18 ± 0.18 eV, and 0.65 ± 0.06 eV, respectively. The large BDE measured for GdO^+ is consistent with this ion having effectively a triple bond, as shown in Figure 3.8a. The strength of lanthanide oxide cation bonds has been shown by Gibson to inversely correlate with the promotion energy needed to achieve a $5d^2$ electronic configuration in the lanthanide cation that can then effectively interact with the four 2p electrons of O.[43] This promotion costs approximately 0.55 eV in energy, estimated from the experimentally measured excitation energy (weighted average over all SO levels) to the Gd^+ (^{10}F, $4f^75d^2$) state.[11]

The BDE measured for GdC^+ is somewhat less than half of that for GdO^+ suggesting that the bond order for GdC^+ is about 1.5 and the bonding interaction is thus weaker than a double bond. Because C has two fewer electrons than O, GdC^+ can at most have a double bond, as suggested by the $^{10}\Pi$ ground state found for GdC^+ from theory

(Figure 3.8a). The weaker interaction in GdC^+ can be attributed to the lower electronegativity of C compared with O resulting in bonding mos that are higher in energy than those for GdO^+ (Figure 3.8a).

In the $GdCO^+$ complex, CO binds weakly as an adduct to Gd^+ consistent with the low bond energy of 0.65 ± 0.06 eV. The predicted ground state of $GdCO^+$ is $^{10}\Pi$, where the interaction between Gd^+ and CO arises from one 5d valence electron of Gd^+ involved in π back-bonding with a C(2p) orbital coupled with a small amount of σ donation between CO(2σ) and Gd($5d_z^2$) (Figure 3.8a). In this configuration, the 6s electron on Gd^+ (^{10}D) remains in this atomic orbital, such that the metal ion essentially maintains its $5d^16s^1$ ground state electronic configuration. Although this 6s electron forms a largely nonbonding mo, it must have some repulsive interaction with the 2σ mo of CO (the sp hybrid localized on C), weakening the bonding. The measured BDE of 0.65 ± 0.06 eV for $GdCO^+$ is about 20% that for GdC^+ (3.18 ± 0.18 eV). Assuming that the bond order for GdC^+ is 2, this gives a bond order of at most 0.5 for $GdCO^+$ consistent with the calculations for the $^{10}\Pi$ state. In the $^{10}\Sigma^+$ state of $GdCO^+$ (see Supporting Information, Section 3.9), the 6s electron is promoted to a 5d Gd^+ orbital, such that two 5d Gd^+ electrons can be involved in π back-bonding with the C(2p) orbitals and there is no repulsion between the 6s and CO valence electrons. This state is at most ~0.2 eV higher in energy than the $^{10}\Pi$ state (disregarding B3LYP and PBE0/Seg. SDD calculations), and relative to the ^{10}F state of Gd^+ is bound by ~1.4 eV, a bond order of ~0.9. These results suggest that the promotion energy needed to achieve a $5d^2$ configuration in Gd^+ is similar to the energy gained from the interaction between an additional 5d Gd^+ electron and the 2p orbital of C in the CO adduct. The promotion energy to the $5d^2$ Gd^+ state of 0.55 eV is indeed comparable to the measured

BDE for $GdCO^+$ of 0.65 ± 0.06 eV.

3.7.2 Thermochemistry compared to the literature. The BDE reported here for GdO^+ is the first direct experimental measurement. BDEs for GdO^+ have previously been determined indirectly through Scheme 3.1 as detailed above with values of 7.47 ± 0.10 eV,[29] 7.81 ± 0.13 eV,[32] 7.59 ± 0.16 eV,[41,43] and 7.0 ± 1.2 eV[44] being reported and 7.76 ± 0.16 eV suggested here. These derived values are in relatively good agreement (within the combined uncertainties) with our measured GdO^+ BDE of 7.69 ± 0.10 eV, with the latter value agreeing the best. The GdO^+ BDE reported by Ackermann et al.[29] of 7.47 ± 0.10 eV is likely too low because it was determined using a GdO BDE of 6.98 eV, although the slightly higher IE for Gd of 6.24 eV (instead of 6.14980 eV) also used compensated somewhat. Because the Ackermann et al. value was included in the average reported by Chandrasekharaiah and Gingerich,[41] 7.59 ± 0.16 eV, this value is too low as well. The GdO^+ BDE of 7.81 ± 0.13 eV reported by Murad and Hildenbrand is in good agreement with the GdO^+ BDE measured here, whereas the GdO^+ BDE of 7.0 ± 1.2 eV[44] is significantly lower than our measured value because it was determined using a much too high value of IE(GdO).

The GdO^+ BDE measured here can be combined through Scheme 3.1 with the well-known IE of Gd and the GdO BDE of 7.36 ± 0.13 eV[40] to evaluate the IE of GdO, which is not well-established. This gives an IE for GdO of 5.82 ± 0.16 eV, consistent with 5.75 ± 0.1 eV obtained from the electron ionization measurements.[29] This comparison also verifies that the rough ionization energy values of 6.5 ± 0.8[31] and 6.7 ± 0.5 eV[32] are much too high.

3.7.3 Periodic trends. Gd^+ with its $4f^7 5d^1 6s^1$ ground state valence electron configuration, like La^+ ($5d^2$) and Lu^+ ($4f^{14} 6s^2$), is unusual compared with most other

lanthanide cations, which have $4f^n6s^1$ configurations (where n corresponds to the number of remaining valence electrons). Instead, Gd^+ (excluding the half-filled 4f shell) is more similar to the isovalent group 3 metal cations Sc^+ ($3d^14s^1$) and Y^+ ($5s^2$, with the $4d^15s^1$ excited state only 0.15 eV higher in energy), which have similar valence electron configurations. A comparison between the oxide, carbide, and carbonyl BDEs for Gd^+ with those previously measured[18,22,80] for Sc^+ and Y^+ is shown in Figure 3.9. Figure 3.9 also

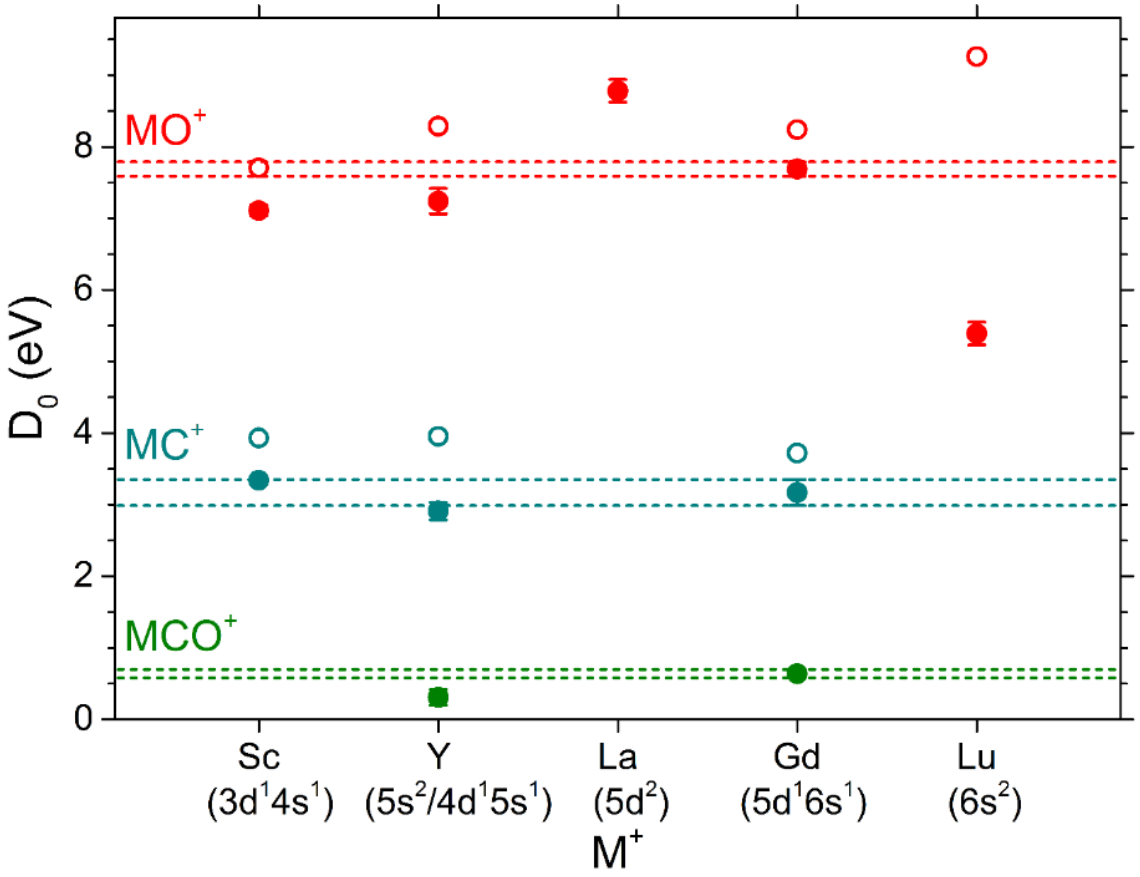

Figure 3.9. Comparison of the Gd^+ oxide, carbide, and carbonyl bond energies measured here with those previously measured for the group 3 metal ions Sc^+ and Y^+.[18,22,80] Also included are oxide BDEs for La^+ and Lu^+ obtained from the literature.[41,43] Dashed lines correspond to Gd^+ BDEs including the uncertainty and are used as guides for the eye to facilitate comparison. Open symbols indicate the intrinsic BDE for the oxides and carbides determined by adding the promotion energy needed to achieve a d^2 electronic configuration from the ground state in the metal cation, see text.

includes the BDEs obtained from the literature[41,43] for LaO^+ and LuO^+ (carbide and carbonyl values have not been determined). The results in Figure 3.9 indicate that the oxide, carbide, and carbonyl BDEs measured for Gd^+ here are similar to those for Sc^+ and Y^+. In contrast, the corresponding oxide BDEs for La^+ and Lu^+ are greater and smaller, respectively, than the GdO^+ BDE. The similarities and differences in these BDEs can be rationalized on the basis of the ground state valence electron configurations of the metal cations, invoking a promotion energy concept to achieve a reactive d^2 configuration in the metal cation as was done by Gibson for the lanthanide series.[43] Because of their similar configurations, Sc^+, Y^+, and Gd^+ react and bind similarly in these complexes, where a single s electron needs to be promoted to a d orbital for effective binding (from the low-lying excited state for Y^+). The relatively stronger oxide bond of LaO^+ compared with that of GdO^+ can be attributed to La^+ already having the favorable $5d^2$ electronic configuration needed to bind effectively with the oxygen atom, such that there is no promotion energy cost.[43] Likewise, the significantly smaller LuO^+ bond energy can be explained by the Lu^+ ground state valence electron configuration. Here both 6s electrons need to be promoted to 5d orbitals for efficient binding with an oxygen atom,[43] with the promotion energy being appreciable at 3.87 eV.[11] The differences in the ground state electronic configurations between La^+, Gd^+, and Lu^+ result from the different number of electrons occupying the 4f shell (empty, half, and completely-filled 4f shell, respectively) such that the 6s orbital becomes favored over a 5d orbital with increasing number of 4f electrons.

Because the results indicate that effective binding for the oxides and carbides occurs by achieving a d^2 electronic configuration in the metal cation, an "intrinsic" oxide and carbide BDE for these metal cations can be determined by adding the promotion energy

to the measured BDEs,[43] open circles in Figure 3.9. The oxide values show significant variability suggesting that there are other effects besides the promotion energy that affect the oxide BDE strength (e.g., orbital overlap). Here, the average intrinsic oxide BDE for the group 3 metal cations and La^+, Gd^+, and Lu^+ is 8.45 ± 0.59 eV. This intrinsic oxide BDE is comparable to the literature BDE for LaO^+ (8.78 eV), which should be a good estimate because the promotion energy cost for La^+ is zero, as previously suggested by Gibson.[43] In contrast to the oxides, the intrinsic carbide BDEs are relatively constant with an average value of 3.87 ± 0.13 eV for the group 3 metal cations and Gd^+. As stated above, the LaC^+ and LuC^+ BDEs have not been determined but can be estimated invoking a promotion energy argument. Thus, the LaC^+ BDE should be in the vicinity of the intrinsic BDE of 3.87 eV determined here, whereas the LuC^+ BDE should be very weak because the d^2 promotion energy cost for Lu^+ is comparable to this intrinsic carbide BDE. On the basis of similar arguments, the carbonyl BDEs for La^+ and Lu^+ are expected to show similar trends and be larger and smaller, respectively, relative to the $GdCO^+$ BDE. Indeed, on this basis, any interaction between Lu^+ and CO has to be electrostatic in nature because the promotion energy to 5d orbitals is far too costly.

3.7.4 Gd chemi-ionization reaction. The GdO^+ BDE (7.69 ± 0.10 eV) can be combined with the well-established IE for Gd of 6.14980 eV[10,11] to determine the exothermicity of the Gd chemi-ionization reaction through thermodynamic cycle 1) in Scheme 3.1. This gives an exothermicity of 1.54 ± 0.10 eV. The exothermicity determined here is more precise but consistent (within experimental uncertainty) with the values of 1.61 ± 0.16, 1.23 ± 0.28, 0.9 ± 1.0, and 0.5 ± 1.0 eV eV[29,37,40] and 1.50 ± 0.27 eV[33] that can be determined from the literature. The results here confirm that the Gd chemi-ionization

reaction is significantly exothermic and should be efficient. Thus, Gd could potentially be a good candidate for producing localized electron dense plasmas in the ionosphere via reaction (3.1).

3.8 Conclusions

The BDEs for GdO^+, GdC^+, and $GdCO^+$ are measured from GIBMS experiments to be 7.69 ± 0.10 eV, 3.18 ± 0.18 eV, and 0.65 ± 0.06 eV, respectively. These bond strengths indicate bond orders of about 3, 1.5 to 2, and 0.5 for GdO^+, GdC^+, and $GdCO^+$, respectively, consistent with the theoretical ground state electronic configurations for these complexes. Good agreement between theoretical and measured BDEs for GdC^+ and $GdCO^+$ is obtained using DFT and coupled cluster theory with the quadruple-ζ quality ANO or Seg. SDD basis set for Gd and the 6-311+G(3df) basis set for O and C. In contrast, the GdO^+ BDEs are underestimated significantly in these calculations. Good agreement with the measured BDE for GdO^+ is obtained using correlation consistent all-electron basis sets for Gd and coupled-cluster theory; however, these same calculations overestimate the GdC^+ BDE. The well-established experimental method used here combined with the small number of atoms in the Gd^+ complexes investigated make the measured BDEs for these complexes a useful benchmark for theoretical calculations.

Measured BDEs for the Gd^+ complexes are found to be comparable to those for the group 3 metals Sc^+ and Y^+. This is attributed to their similar electronic configurations (d^1s^1, ignoring the half-filled 4f shell of Gd^+), which lead to similar reactivity and binding in the corresponding complexes. Additionally, the GdO^+ bond energy is found to be smaller and larger than literature values for La^+ ($4f^0$) and Lu^+ ($4f^{14}$), respectively. These differences

arise from the systematic change in the ground state electronic configuration for La^+ ($5d^2$), Gd^+ ($5d^16s^1$), and Lu^+ ($6s^2$) with increasing number of 4f electrons. The oxide BDEs correlate with the energy needed to achieve a $5d^2$ configuration in the metal for effective binding with the oxygen atom. This cost is zero for La^+ resulting in the strongest oxide bond, and increases systematically for Gd^+ (0.55 eV) and Lu^+ (3.87 eV) leading to weaker oxide bonds. On the basis of these results, the carbide and carbonyl BDEs for La^+ and Lu^+ (which have not been determined) are expected to be larger and smaller, respectively, than those for the corresponding Gd^+ complexes.

The GdO^+ BDE measured here combined with the well-established ionization energy for Gd is used to evaluate the exothermicity of the Gd chemi-ionization reaction. From these results, an exothermicity of 1.54 ± 0.10 eV is obtained that is consistent with, but more precise than, previous values. The results here confirm that the Gd chemi-ionization reaction is significantly exothermic and should be efficient. Gd is also a fairly abundant rare earth metal and should thus be relatively inexpensive. This makes Gd a potential candidate to be used in atmospheric chemical release experiments for creating localized electron enhanced plasmas.

3.9 Supporting Information

3.9.1 Gd^+ reaction with CO. Uncorrected data for the product ion cross sections resulting from the Gd^+ and CO reaction are shown in Figure 3.10. There is a minor exothermic feature in the GdO^+ cross section that is attributed to an O_2 impurity as it exhibits similar kinetic energy dependence as the GdO^+ cross section in the Gd^+ reaction with O_2 (Figure 3.1a). The exothermic feature can be reproduced by properly scaling the

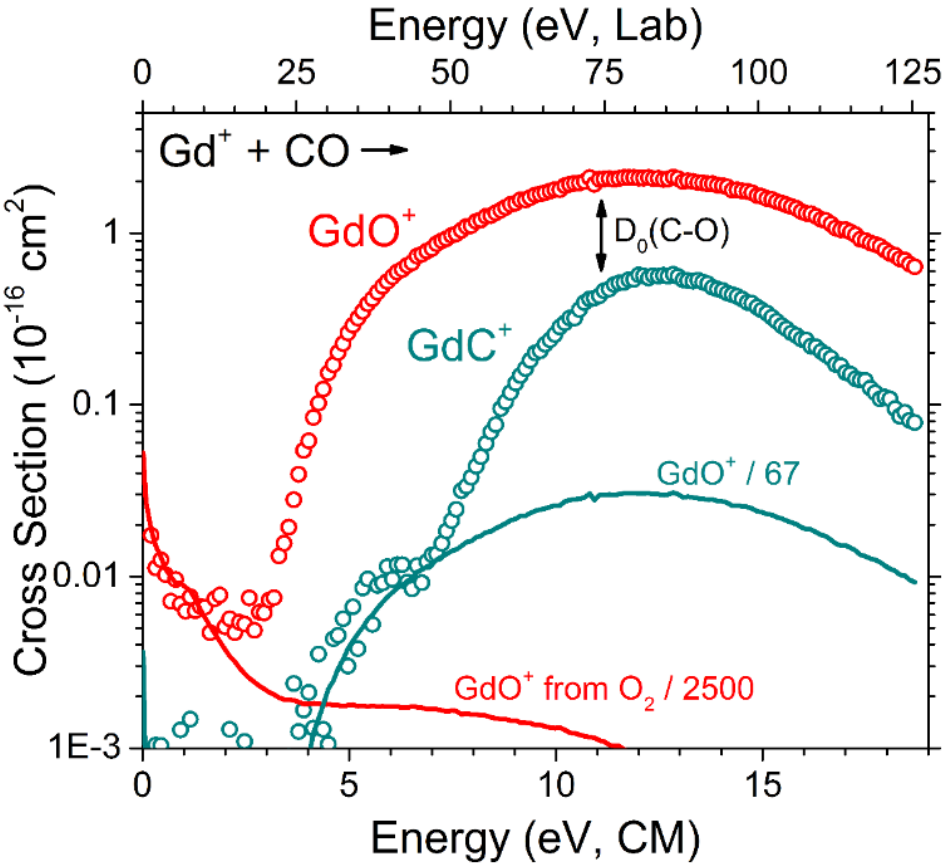

Figure 3.10. Product ion cross sections as a function of center-of-mass (bottom *x*-axis) and laboratory (top *x*-axis) frame kinetic energy for the Gd^+ reaction with CO at a pressure of 0.28 mTorr. The arrow indicates the C-O bond energy (11.11 eV). The exothermic tail in the GdO^+ cross section is caused by a small amount (0.04%) of O_2 impurity. The low energy feature in the GdC^+ cross section results from overlap in intensity from the abundant GdO^+ product ion and is corrected for by appropriately scaling the GdO^+ cross section (dark cyan line) to fit the low energy feature prior to obtaining E_0. Corrected GdO^+ and GdC^+ cross sections are shown in Figure 3.3.

GdO^+ cross section down by a factor of 2500 from Figure 3.1a (solid red line in Figure 3.10). Accurate threshold energies can be obtained from these data by subtracting out this scaled GdO^+ cross section. The corrected GdO^+ cross section that results solely from the Gd^+ + CO reaction is shown in Figure 3.3 above. The amount of O_2 impurity could be reduced significantly, but could not entirely be eliminated and is estimated to be ~0.04% in the data shown here from the scaling factor.

There is a low energy endothermic feature in the GdC^+ cross section shown in Figure 3.10, which has an apparent threshold energy of ~4 eV and does not exceed a cross section of ~1.5×10^{-18} cm^2. This feature is an artifact caused by overlapping intensity from the abundant GdO^+ product ion. For accurate threshold energies to be measured with guided ion beam mass spectrometry, ion transmission and sensitivity need to be high and therefore resolution is kept relatively low.[12] To obtain an accurate threshold energy for forming GdC^+ from these data, the energy dependent GdO^+ cross section is scaled down by a factor of 67 and subtracted from the GdC^+ cross section (dark cyan line), effectively removing this artificial low energy feature, as shown in Figure 3.3.

3.9.2 Theoretical calculations. Calculations are performed to evaluate how well different basis sets and levels of theory predict the Gd^+ ground state and excited state energies in order to deduce how reliable these calculations are in determining ground states for GdO^+, GdC^+, and $GdCO^+$. The SDD, ANO, and Seg. SDD basis sets for Gd and the 6-311+G(3df) basis set for O and C are used with calculations performed at the B3LYP, PBE0, and CCSD(T,full) levels of theory. Excited state energies for Gd^+ from these calculations are summarized in Table 3.3 and compared with the corresponding experimental values in Figure 3.7 and discussed in detail above. Computed energies, vibrational frequencies, and bond lengths for several different electronic states of GdO^+, GdC^+, and $GdCO^+$ are listed in Tables 3.4 through 3.6, respectively.

For all three levels of theory and basis sets for Gd, calculations predict that the ground state for GdO^+ is $^8\Sigma^-$ with a valence electron configuration of $[1\phi^2 1\delta^2 1\pi^2 1\sigma^1]$ $2\pi^4$ $2\sigma^2$ (Table 3.4). The valence electrons are the seven 4f electrons (in square brackets) and the 5d and 5s electrons of Gd^+ (^{10}D, $4f^7 5d6s$) and the four 2p electrons of O (^3P, $2p^4$). For

Table 3.3. Relative energies for various excited states of Gd^+ calculated at different levels of theory and basis sets, and ground state electronic energies for O, C, and CO calculated using the 6-311+G(3df) basis set.

Species	State	Configuration	Level	Gd^+ basis set	s(s+1)[a]	E (E_h)	E_{rel} (eV)	E_{rel} (eV)[b]
Gd^+	^{10}D	$4f^7\ 5d^1\ 5s^1$	B3LYP	SDD	24.75	-765.218083	1.564	0.000
				ANO	24.75	-765.364990	**0.000**	
				Seg. SDD	24.77	-765.594933	0.141	
			PBE0	SDD	24.75	-765.108599	1.152	
				ANO	24.75	-765.242091	**0.000**	
				Seg. SDD	24.77	-765.417193	**0.000**	
			CCSD(T,full)	SDD	24.76	-763.858935	0.424	
				ANO	24.76	-764.755135	**0.000**	
				Seg. SDD	24.76	-764.617082	**0.000**	
	^{8}D	$4f^7\ 5d^1\ 5s^1$	B3LYP	SDD	16.76*	-765.205817	1.899	0.358
				ANO	16.76*	-765.348173	0.458	
				Seg. SDD	16.78*	-765.585110	0.408	
			PBE0	SDD	16.76*	-765.091962	1.605	

Table 3.3 continued

Species	State	Configuration	Level	Gd^+ basis set	$s(s+1)^a$	E (E_h)	E_{rel} (eV)	E_{rel} (eV)^b
				ANO	16.76*	-765.220607	0.585	
				Seg. SDD	16.78*	-765.397853	0.526	
			CCSD(T,full)	SDD	16.76*	-763.847915	0.724	
				ANO	16.76*	-764.740555	0.397	
				Seg. SDD	16.76*	-764.602598	0.394	
	^8S	$4f^7\ 6s^2$	B3LYP	SDD	15.76	-765.234779	1.110	0.304
				ANO	15.76	-765.356246	0.238	
				Seg. SDD	16.06*	-765.600106	**0.000**	
			PBE0	SDD	15.76	-765.113918	1.007	
				ANO	15.76	-765.221186	0.569	
				Seg. SDD	16.05*	-765.409517	0.209	
			CCSD(T,full)	SDD	15.76	-763.874514	**0.000**	
				ANO	15.76	-764.743529	0.316	

Table 3.3 continued

Species	State	Configuration	Level	Gd^+ basis set	$s(s+1)^a$	E (E_h)	E_{rel} (eV)	E_{rel} (eV)^b
				Seg. SDD	15.76	-764.606938	0.276	
	^{10}F	$4f^7\ 5d^2$	B3LYP	SDD	24.76	-765.127030	4.042	0.547
				ANO	24.75	-765.327602	1.017	
				Seg. SDD	24.82	-765.379452	6.004	
			PBE0	SDD	24.75	-765.026922	3.375	
				ANO	24.75	-765.211542	0.831	
				Seg. SDD	24.78	-765.234958	4.959	
			CCSD(T,full)	SDD	24.76	-763.773791	2.741	
				ANO	24.76	-764.727265	0.758	
				Seg. SDD	24.76	-764.588137	0.788	
	^8F	$4f^8\ 6s^1$	B3LYP	SDD	15.76	-765.275588	**0.000**	1.107
				ANO	15.76	-765.352178	0.349	
				Seg. SDD	15.77	-765.518127	2.231	

Table 3.3 continued

Species	State	Configuration	Level	Gd^+ basis set	s(s+1)[a]	E (E_h)	E_{rel} (eV)	E_{rel} (eV)[b]
			PBE0	SDD	15.76	-765.150941	**0.000**	
				ANO	15.76	-765.218439	0.644	
				Seg. SDD	15.77	-765.332497	2.305	
			CCSD(T,full)	SDD	15.76	-763.810100	1.753	
				ANO	15.76	-764.690740	1.752	
				Seg. SDD	15.76	-764.548786	1.858	
O	^3P	$2s^2\,2p^4$	B3LYP	6-311+G(3df)	2.00	-75.090915		0.0097
			PBE0	6-311+G(3df)	2.00	-75.012915		
			CCSD(T,full)	6-311+G(3df)	2.01	-74.994166		
C	^3P	$2s^2\,2p^2$	B3LYP	6-311+G(3df)	2.00	-37.857471		0.0037
			PBE0	6-311+G(3df)	2.00	-37.803210		
			CCSD(T,full)	6-311+G(3df)	2.01	-37.799083		
CO	$^1\Sigma$	$1\sigma^2\,2\sigma^2\,1\pi^4\,3\sigma^2$	B3LYP	6-311+G(3df)	0.00	-113.356793		0.004995[c]

Table 3.3 continued

Species	State	Configuration	Level	Gd^+ basis set	$s(s+1)^a$	E (E_h)	E_{rel} (eV)	E_{rel} (eV)[b]
			PBE0	6-311+G(3df)	0.00	-113.224997		0.005054[c]
			CCSD(T,full)	6-311+G(3df)	0.00	-113.201731		0.004894[c]

[a]* = spin-contaminated state.
[b]E_{rel} = average experimental energy of a given state relative to the average energy of the ^{10}D ground state.
[c]Zero point energy.

Table 3.4. Summary of GdO^+ bond lengths (Å), energies, and vibrational frequencies (cm^{-1}, scaled by 0.989) calculated at various levels of theory and basis sets for Gd. Orbitals in brackets are those from the 4f electrons of Gd^+.

State	Configuration	Level	Gd^+ basis set	s(s+1)[a]	E (E_h)	Bond length	Vibrational Frequency	D_0 / E_{rel} (eV) wo SO	w SO[b]
$^8\Sigma^-$	$[1\varphi^2 1\delta^2 1\pi^2 1\sigma^1]\ 2\sigma^2 2\pi^4$	B3LYP	SDD	15.77	-840.620351	1.742	943	**8.41**[c]	**8.28**
			ANO	15.77	-840.714362	1.752	900	**6.98**	**6.85**
			Seg. SDD	16.14*	-840.875138	1.812	756	**5.10**[d]	**4.97**
		PBE0	SDD	15.77	-840.431277	1.728	968	**8.37**[c]	**8.24**
			ANO	15.77	-840.514921	1.737	929	**7.01**	**6.88**
			Seg. SDD	15.98*	-840.620688	1.757	797	**5.14**	**5.01**
		CCSD(T,full)	SDD	15.79	-839.155779	1.742	933	**8.18**[d]	**8.05**
			ANO	15.81	-840.010139	1.755	893	**7.04**	**6.91**
			Seg. SDD	15.81	-839.869889	1.757	888	**6.98**	**6.85**
$^{10}\Pi$	$[1\varphi^2 1\delta^2 1\pi^2 1\sigma^1]\ 2\sigma^2 2\pi^3\ 3\sigma^1$	B3LYP	SDD	24.76	-840.504907	2.000	661	*3.12*	*3.06*
			ANO	24.76	-840.610406	2.011	634	*2.81*	*2.75*
			Seg. SDD	24.78	-840.838661	2.038	599	*0.98*	*0.92*
		PBE0	SDD	24.76	-840.310387	1.982	677	*3.27*	*3.21*

Table 3.4 continued

State	Configuration	Level	Gd^+ basis set	s(s+1)[a]	E (E_h)	Bond length	Vibrational Frequency	D_0 / E_{rel} (eV) wo SO	D_0 / E_{rel} (eV) w SO[b]
			ANO	24.76	-840.404947	1.997	648	*2.98*	*2.92*
			Seg. SDD	24.78	-840.578172	2.017	619	*1.15*	*1.09*
		CCSD(T,full)	SDD	24.76	-839.033525	1.995	658	*3.31*	*3.25*
			ANO	24.76	-839.891779	2.008	656	*3.21*	*3.15*
			Seg. SDD	24.76	-839.753457	2.009	655	*3.15*	*3.09*
$^8\Pi$	$[1\varphi^2 1\delta^2 1\pi^2 1\sigma^1]\ 2\sigma^2 2\pi^3\ 3\sigma^1$	B3LYP	SDD	16.34*	-840.503709	2.028	601	*3.15*	*3.09*
			ANO	16.68*	-840.598358	2.010	629	*3.14*	*3.08*
			Seg. SDD	16.78*	-840.834598	2.036	601	*1.09*	*1.03*
		PBE0	SDD	16.44*	-840.302580	2.005	620	*3.48*	*1.42*
			ANO	16.75*	-840.390128	1.993	655	*3.38*	*3.32*
			Seg. SDD	16.78*	-840.568293	2.017	620	*1.41*	*1.35*
		CCSD(T,full)	SDD	16.77*	-839.022362	1.995	662	*3.61*	*3.55*
			ANO	16.77*	-839.878764	2.009	639	*3.56*	*3.50*

Table 3.4 continued

State	Configuration	Level	Gd^+ basis set	s(s+1)[a]	E (E_h)	Bond length	Vibrational Frequency	D_0 / E_{rel} (eV) wo SO	D_0 / E_{rel} (eV) w SO[b]
			Seg. SDD	16.77*	-839.740430	2.011	636	*3.51*	*3.45*
$^{10}\Sigma^-$	$[1\varphi^2 1\delta^2 1\pi^2 1\sigma^1]\ 2\sigma^1 2\pi^4\ 3\sigma^1$	B3LYP	SDD	24.76	-840.499437	1.899	721	*3.28*	*3.28*
			ANO	24.76	-840.604381	1.909	696	*2.98*	*2.98*
			Seg. SDD	24.77	-840.835210	1.928	663	*1.08*	*1.08*
		PBE0	SDD	24.76	-840.305565	1.883	732	*3.41*	*3.41*
			ANO	24.76	-840.399253	1.892	708	*3.13*	*3.13*
			Seg. SDD	24.77	-840.575579	1.905	680	*1.22*	*1.22*
		CCSD(T,full)	SDD	24.76	-839.032355	1.899	723	*3.35*	*3.35*
			ANO	24.76	-839.889089	1.883	696	*3.28*	*3.28*
			Seg. SDD	24.76	-839.750836	1.883	694	*3.23*	*3.23*
$^{6}\Sigma^-$	$[1\varphi^2 1\delta^2 1\pi^2 1\sigma^1]\ 2\sigma^1 2\pi^4\ 3\sigma^1$	B3LYP	SDD			Collapses to $^6\Delta$			
			ANO	10.54*	-840.593190	1.894	657	*3.28*	*3.28*
			Seg. SDD	10.70*	-840.831752	1.902	621	*1.17*	*1.17*

Table 3.4 continued

State	Configuration	Level	Gd^+ basis set	$s(s+1)$[a]	E (E_h)	Bond length	Vibrational Frequency	D_0 / E_{rel} (eV) wo SO	D_0 / E_{rel} (eV) w SO[b]
		PBE0	SDD			Collapses to $^6\Delta$			
			ANO	10.69*	-840.384702	1.894	689	*3.53*	*3.53*
			Seg. SDD	10.77*	-840.570306	2.007	606	*1.36*	*1.36*
		CCSD(T,full)	SDD	10.77*	-839.019964	1.878	703	*3.68*	*3.68*
			ANO	10.77*	-839.874941	1.892	679	*3.67*	*3.67*
			Seg. SDD	10.77*	-839.736612	1.893	675	*3.61*	*3.61*
$^6\Delta$	$[1\varphi^2 1\delta^3 1\pi^2]\ 2\sigma^2 2\pi^4$	B3LYP	SDD	9.51*	-840.498253	1.879	484	*3.29*	*3.08*
			ANO	9.24*	-840.577103	1.806	519	*3.71*	*3.50*
			Seg. SDD	9.12*	-840.716353	1.775	621	*4.31*	*4.10*
		PBE0	SDD	9.57*	-840.296227	1.879	473	*3.64*	*3.43*
			ANO	9.27*	-840.365030	1.790	464	*4.05*	*3.84*
			Seg. SDD	9.24*	-840.447536	1.792	619	*4.70*	*4.49*
		CCSD(T,full)	SDD	8.78	-838.957282	1.725	904	*5.40*	*5.19*

Table 3.4 continued

State	Configuration	Level	Gd^+ basis set	s(s+1)[a]	E (E_h)	Bond length	Vibrational Frequency	**D_0** / E_{rel} (eV) wo SO	w SO[b]
			ANO	8.78	-839.821040	1.734	859	*5.14*	*4.93*
			Seg. SDD	8.78	-839.679730	1.763	851	*5.17*	*4.96*

[a]* = spin-contaminated state.
[b]SO corrected BDE or relative energy to the calculated ground state.
[c]Value relative to Gd^+ ^{10}D ($4f^75d^16s^1$) state although ^8F state ($4f^86s^1$) calculated as lowest in energy.
[d]Value relative to Gd^+ ^{10}D ($4f^75d^16s^1$) state although ^8S state ($4f^76s^2$) calculated as lowest in energy.

Table 3.5. Summary of GdC^+ bond lengths (Å), energies, and vibrational frequencies (cm^{-1}, scaled by 0.989) calculated at various levels of theory and basis sets for Gd. Orbitals in brackets are those from the 4f electrons of Gd^+. Ground state values in bold.

State	Configuration	Level	Gd^+ basis set	s(s+1)[a]	E (E_h)	Bond length	Vibrational Frequency	D_0 / E_{rel} (eV) wo SO	D_0 / E_{rel} (eV) w SO[b]
$^{10}\Pi$	$[1\varphi^2 1\delta^2 1\pi^2 1\sigma^1]\ 2\sigma^1 2\pi^3$	B3LYP	SDD	24.76	-803.244764	1.957	748	**4.56**[c]	**4.50**
			ANO	24.77	-803.341563	1.983	721	**3.20**	**3.14**
			Seg. SDD	24.80	-803.524487	2.030	646	*1.08*	*1.02*
		PBE0	SDD	24.76	-803.087066	1.935	806	**4.72**[c]	**4.66**
			ANO	24.77	-803.173518	1.964	747	**3.44**	**3.38**
			Seg. SDD	24.81	-803.298493	1.995	681	*1.12*	*1.06*
		CCSD(T,full)	SDD	24.82	-801.818956	1.930	825	**4.33**[d]	**4.27**
			ANO	24.95*	-802.675015	1.970	757	**3.24**	**3.18**
			Seg. SDD	24.95*	-802.537082	1.972	755	**3.24**	**3.18**
$^{12}\Sigma^+$	$[1\varphi^2 1\delta^2 1\pi^2 1\sigma^1]\ 2\sigma^1 2\pi^2\ 3\sigma^1$	B3LYP	SDD	35.76	-803.228836	2.168	606	*0.42*	*0.48*
			ANO	35.76	-803.335817	2.195	577	*0.15*	*0.21*
			Seg. SDD	35.77	-803.563937	2.218	551	**3.00**[d]	**2.87**
		PBE0	SDD	35.75	-803.071415	2.151	626	*0.41*	*0.47*

Table 3.5 continued

State	Configuration	Level	Gd^+ basis set	s(s+1)[a]	E (E_h)	Bond length	Vibrational Frequency	D_0 / E_{rel} (eV) wo SO	D_0 / E_{rel} (eV) w SO[b]
			ANO	35.76	-803.166330	2.176	596	*0.19*	*0.25*
			Seg. SDD	35.77	-803.339339	2.192	571	**3.20**	**3.07**
		CCSD(T,full)	SDD	35.76	-801.807884	2.143	632	*0.29*	*0.35*
			ANO	35.76	-802.665800	2.175	611	*0.24*	*0.30*
			Seg. SDD	35.76	-802.528995	2.175	613	*0.21*	*0.26*
$^{10}\Sigma^+$	$[1\varphi^2 1\delta^2 1\pi^2 1\sigma^1]\ 2\sigma^2 2\pi^2$	B3LYP	SDD	24.80	-803.230519	2.049	617	*0.38*	*0.44*
			ANO	24.76	-803.323243	2.093	521	*0.49*	*0.55*
			Seg. SDD	Collapses to $^{10}\Sigma^+ [1\varphi^2 1\delta^2 1\pi^2 1\sigma^1]\ 2\sigma^1 2\pi^2\ 3\sigma^1$					
		PBE0	SDD	24.77	-803.067621	2.015	690	*0.52*	*0.58*
			ANO	24.77	-803.151535	2.059	603	*0.59*	*0.64*
			Seg. SDD	Collapses to $^{10}\Sigma^+ [1\varphi^2 1\delta^2 1\pi^2 1\sigma^1]\ 2\sigma^1 2\pi^2\ 3\sigma^1$					
		CCSD(T,full)	SDD	24.86	-801.795186	2.007	717	*0.64*	*0.70*
			ANO	24.88	-802.651068	2.064	526	*0.64*	*0.70*

Table 3.5 continued

State	Configuration	Level	Gd^+ basis set	s(s+1)[a]	E (E_h)	Bond length	Vibrational Frequency	**D_0** / E_{rel} (eV) wo SO	w SO[b]
			Seg. SDD		Collapses to $^{10}\Sigma^+$ $[1\varphi^2 1\delta^2 1\pi^2 1\sigma^1]$ $2\sigma^1 2\pi^2$ $3\sigma^1$				
$^{10}\Sigma^+$	$[1\varphi^2 1\delta^2 1\pi^2 1\sigma^1]$ $2\sigma^1 2\pi^2$ $3\sigma^1$	B3LYP	SDD		Collapses to $^{10}\Sigma^+$ $[1\varphi^2 1\delta^2 1\pi^2 1\sigma^1]$ $2\sigma^2 2\pi^2$				
			ANO	25.66*	-803.320239	2.201	470	*0.56*	*0.62*
			Seg. SDD	25.67*	-803.561420	2.238	525	*0.07*	*0.07*
		PBE0	SDD		Collapses to $^{10}\Sigma^+$ $[1\varphi^2 1\delta^2 1\pi^2 1\sigma^1]$ $2\sigma^2 2\pi^2$				
			ANO	25.73*	-803.146011	2.171	492	*0.73*	*0.79*
			Seg. SDD	25.70*	-803.327396	2.223	558	*0.32*	*0.32*
		CCSD(T,full)	SDD	25.75*	-801.792286	1.940	1215	*0.75*	*0.81*
			ANO	25.75*	-802.643446	1.962	893	*0.87*	*0.93*
			Seg. SDD	25.73*	-802.515067	2.086	930	*0.61*	*0.67*
$^{6}\Pi$	$[1\varphi^2 1\delta^2 1\pi^2 1\sigma^1]$ $2\sigma^1 2\pi^3$	B3LYP	SDD	10.65*	-803.238431	1.931	757	*0.17*	*0.17*
			ANO	10.73*	-803.334671	1.974	674	*0.18*	*0.18*
			Seg. SDD	10.80*	-803.524109	2.024	629	*1.09*	*1.03*

Table 3.5 continued

State	Configuration	Level	Gd^+ basis set	s(s+1)[a]	E (E_h)	Bond length	Vibrational Frequency	**D_0** / E_{rel} (eV) wo SO	w SO[b]
		PBE0	SDD	10.69*	-803.079698	1.922	779	*0.20*	*0.20*
			ANO	10.76*	-803.165572	1.963	687	*0.21*	*0.21*
			Seg. SDD	10.82*	-803.293560	1.992	661	*1.25*	*1.19*
		CCSD(T,full)	SDD	11.13*	-801.805440	1.932	766	*0.36*	*0.36*
			ANO	11.28*	-802.663274	1.986	675	*0.31*	*0.31*
			Seg. SDD	11.28*	-802.525368	1.988	671	*0.31*	*0.31*
$^8\Pi$	$[1\varphi^2 1\delta^2 1\pi^2 1\sigma^1]\ 2\sigma^1 2\pi^3$	B3LYP	SDD	16.69*	-803.233092	1.937	772	*0.32*	*0.32*
			ANO	16.73*	-803.329109	1.968	708	*0.34*	*0.34*
			Seg. SDD	16.80*	-803.518779	2.027	644	*1.23*	*1.17*
		PBE0	SDD	16.72*	-803.074290	1.920	807	*0.35*	*0.35*
			ANO	16.75*	-803.159793	1.950	734	*0.37*	*0.37*
			Seg. SDD	16.81*	-803.287515	1.996	639	*1.41*	*1.35*
		CCSD(T,full)	SDD	16.96*	-801.802218	1.921	803	*0.45*	*0.45*

Table 3.5 continued

State	Configuration	Level	Gd^+ basis set	s(s+1)[a]	E (E_h)	Bond length	Vibrational Frequency	D_0 / E_{rel} (eV) wo SO	D_0 / E_{rel} (eV) w SO[b]
			ANO	17.15*	-802.658179	1.968	717	*0.46*	*0.46*
			Seg. SDD	17.15*	-802.520107	1.969	714	*0.46*	*0.46*
$^8\Sigma^-$	$[1\varphi^2 1\delta^2 1\pi^2 1\sigma^1]\ 2\pi^4$	B3LYP	SDD	15.78	-803.221452	1.829	849	*0.64*	*0.70*
			ANO	15.80	-803.315995	1.853	802	*0.70*	*0.76*
			Seg. SDD	15.91*	-803.446786	2.027	816	*3.20*	*3.20*
		PBE0	SDD	15.79	-803.060620	1.813	870	*0.72*	*0.78*
			ANO	15.81	-803.144667	1.836	823	*0.79*	*0.85*
			Seg. SDD	15.93*	-803.226585	1.824	835	*3.08*	*3.08*
		CCSD(T,full)	SDD	16.07*	-801.799840	1.820	865	*0.52*	*0.58*
			ANO	16.23*	-802.653777	1.859	798	*0.58*	*0.64*
			Seg. SDD	16.23*	-802.515621	1.860	795	*0.59*	*0.65*

[a]* = spin-contaminated state.
[b]SO corrected BDE or relative energy to the calculated ground state.
[c]Value relative to Gd^+ ^{10}D ($4f^7 5d^1 6s^1$) state although ^8F state ($4f^8 6s^1$) calculated as lowest in energy.
[d]Value relative to Gd^+ ^{10}D ($4f^7 5d^1 6s^1$) state although ^8S state ($4f^7 6s^2$) calculated as lowest in energy.

Table 3.6. Summary of $GdCO^+$ bond lengths and energies calculated at various levels of theory and basis sets for Gd. Only single point energies are calculated at the CCSD(T,full) level using optimized B3LYP and PBE0 structures. Zero point energy corrections use the scaled B3LYP and PBE0 frequencies. Electrons from the 2s orbitals of O and C are omitted in the valence configurations. The 4f electrons of Gd^+ form $1\varphi^2 1\delta^2 1\pi^2 1\sigma^1$ orbitals, omitted in the configuration designation. Ground state values in bold.

State	Configuration	Level	Gd^+ basis set	s(s+1)[a]	r(CO) (Å)	r(MC) (Å)	E (E_h)	**D_0** / E_{rel} (eV) wo SO	w SO[b]
$^{10}\Pi$	$2\pi^4 2\sigma^2 3\pi^1 3\sigma^1$	B3LYP	SDD	24.76	1.135	2.298	**-878.643250**	**1.68**[c]	**1.62**
			ANO	24.76	1.128	2.395	**-878.755425**	**0.74**	**0.68**
			Seg. SDD	24.77	1.131	2.474	**-878.978626**	**0.56**[d]	**0.50**
		PBE0	SDD	24.76	1.132	2.282	-878.403750	*0.02*[c]	**1.78**
			ANO	24.76	1.126	2.371	-878.503724	*0.04*	**0.89**
			Seg. SDD	24.77	1.128	2.438	**-878.671000**	**0.75**	**0.69**
		CCSD(T,full)	SDD	24.78	1.135	2.298	-877.105882	*0.19*	*0.13*
		//B3LYP	ANO	24.76	1.128	2.395	**-877.984415**	**0.71**	**0.65**
			Seg. SDD	24.76	1.131	2.474	**-877.846737**	**0.72**	**0.66**
		CCSD(T,full)	SDD	24.77	1.132	2.282	**-877.118486**	**1.52**[d]	**1.46**
		//PBE0	ANO	24.76	1.126	2.371	**-877.984154**	**0.69**	**0.63**
			Seg. SDD	24.76	1.128	2.438	**-877.846865**	**0.72**	**0.66**

Table 3.6 continued

State	Configuration	Level	Gd^+ basis set	s(s+1)[a]	r(CO) (Å)	r(MC) (Å)	E (E_h)	**D_0** / E_{rel} (eV) wo SO	w SO[b]
$^{10}\Sigma^+$	$2\pi^4 2\sigma^2 3\pi^2$	B3LYP	SDD	24.76	1.155	2.140	-878.636033	*0.20*	*0.26*
			ANO	24.76	1.144	2.240	-878.747988	*0.21*	*0.27*
			Seg. SDD	25.03*	1.165	2.134	-878.884836	*2.56*	*2.62*
		PBE0	SDD	24.76	1.152	2.127	**-878.404473**	**1.86**[c]	*0.04*
			ANO	24.76	1.142	2.217	**-878.503977**	**0.99**	*0.02*
			Seg. SDD	24.76	1.145	2.185	-878.531377	*3.81*	*3.87*
		CCSD(T,full)	SDD	24.80	1.155	2.140	**-877.112984**	**1.37**[d]	**1.25**
		//B3LYP	ANO	24.79	1.144	2.240	-877.982835	*0.05*	*0.11*
			Seg. SDD	24.80	1.165	2.134	-877.841041	*0.16*	*0.22*
		CCSD(T,full)	SDD	24.80	1.152	2.127	-877.112953	*0.15*	*0.21*
		//PBE0	ANO	24.79	1.142	2.217	-877.982613	*0.04*	*0.10*
			Seg. SDD	24.79	1.145	2.185	-877.843395	*0.11*	*0.17*
$^8\Pi$	$2\pi^4 2\sigma^2 3\pi^1 3\sigma^1$	B3LYP	SDD	16.42*	1.139	2.306	-878.635782	*0.20*	*0.20*

Table 3.6 continued

State	Configuration	Level	Gd^+ basis set	$s(s+1)^a$	r(CO) (Å)	r(MC) (Å)	E (E_h)	D_0 / E_{rel} (eV) wo SO	w SO[b]
			ANO	16.73*	1.128	2.392	-878.740409	*0.41*	*0.41*
			Seg. SDD	16.78*	1.132	2.456	-878.972094	*0.18*	*0.18*
		PBE0	SDD	16.57*	1.135	2.283	-878.388452	*0.43*	*0.37*
			ANO	16.75*	1.126	2.369	-878.485076	*0.51*	*0.45*
			Seg. SDD	16.76*	1.140	2.334	-878.649441	*0.59*	*0.59*
		CCSD(T,full)	SDD	16.76*	1.139	2.306	-877.096531	*0.44*	*0.38*
		//B3LYP	ANO	16.77*	1.128	2.392	-877.969074	*0.42*	*0.42*
			Seg. SDD	16.77*	1.132	2.456	-877.831890	*0.40*	*0.40*
		CCSD(T,full)	SDD	16.76*	1.135	2.283	-877.096905	*0.58*	*0.58*
		//PBE0	ANO	16.77*	1.126	2.369	-877.968719	*0.39*	*0.39*
			Seg. SDD	16.77*	1.140	2.334	-877.830292	*0.45*	*0.45*
$^8\Sigma^+$	$2\pi^4 2\sigma^2 3\pi^2$	B3LYP	SDD	16.11*	1.155	2.222	-878.627258	*0.42*	*0.48*
			ANO	16.63*	1.151	2.205	-878.726859	*0.78*	*0.84*

Table 3.6 continued

State	Configuration	Level	Gd^+ basis set	s(s+1)[a]	r(CO) (Å)	r(MC) (Å)	E (E_h)	**D_0** / E_{rel} (eV) wo SO	w SO[b]
			Seg. SDD	16.69*	1.156	2.160	-878.773053	*5.61*	*5.67*
		PBE0	SDD	16.49*	1.157	2.123	-878.385292	*0.52*	*0.52*
			ANO	16.70*	1.150	2.178	-878.478703	*0.72*	*0.72*
			Seg. SDD	16.71*	1.152	2.150	-878.506840	*4.48*	*4.54*
		CCSD(T,full)	SDD	16.37*	1.155	2.222	-877.067700	*1.22*	*1.22*
		//B3LYP	ANO	16.28*	1.151	2.205	-877.939896	*1.22*	*1.28*
			Seg. SDD	16.26*	1.156	2.160	-877.801032	*1.26*	*1.32*
		CCSD(T,full)	SDD	16.29*	1.157	2.123	-877.070677	*1.30*	*1.36*
		//PBE0	ANO	16.26*	1.150	2.178	-877.939581	*1.21*	*1.27*
			Seg. SDD	16.25*	1.152	2.150	-877.800688	*1.27*	*1.33*

[a]* = spin-contaminated state.
[b]SO corrected BDE or relative energy to the calculated ground state.
[c]Value relative to Gd^+ ^{10}D ($4f^7 5d^1 6s^1$) state although ^8F state ($4f^8 6s^1$) calculated as lowest in energy.
[d]Value relative to Gd^+ ^{10}D ($4f^7 5d^1 6s^1$) state although ^8S state ($4f^7 6s^2$) calculated as lowest in energy.

an internuclear axis along the z direction, the 2π mos are bonding and arise from Gd($5d_{xz}$) and Gd($5d_{yz}$) orbitals interacting with O($2p_x$) and O($2p_y$) orbitals, respectively. The 2σ orbital is formed from the O($2p_z$) and Gd($5d_z^2$) orbitals. The first excited state for GdO^+ is calculated to be the $^{10}\Pi$ state ($[1\phi^2 1\delta^2 1\pi^2 1\sigma^1]$ $2\sigma^2 2\pi^3 3\sigma^1$) with relative energies ranging from 1.0 to 3.3 eV above the $^8\Sigma^-$ ground state (Table 3.4). In this configuration, the 3σ mo is largely nonbonding and comprises mainly the Gd^+ 6s atomic orbital with some $5d_z^2$ character. The smallest energy difference (~1 eV) between the ground $^8\Sigma^-$ and excited $^{10}\Pi$ states is obtained for the Seg. SDD basis set at the B3LYP and PBE0 levels of theory. This Gd basis set combined with DFT tends to prefer electronic states in which the exchange energy is maximized, as is also seen in the results for GdC^+ and $GdCO^+$. The GdO^+ $^{10}\Sigma^-$ ($[1\phi^2 1\delta^2 1\pi^2 1\sigma^1]$ $2\sigma^1 2\pi^4 3\sigma^1$) excited state where the 2π (instead of the 2σ) bonding orbital is fully occupied results in slightly higher but comparable excitation energy to that for the $^{10}\Pi$ state. Flipping the spin of the electron in the 3σ orbital in the $^{10}\Pi$ state to give the $^8\Pi$ state results in an additional increase in the excitation energy of about 0.3 eV at theCCSD(T,full) level of theory, and this is also the case for flipping the spins of the electrons in the 2σ and 3σ orbitals in the $^{10}\Sigma^-$ state to give the $^6\Sigma^-$ state. Changing the spin of one of the 4f electrons increases the excitation energy substantially, where the $^6\Delta$ $[1\phi^2 1\delta^3 1\pi^2]$ $2\sigma^2 2\pi^4$ state is predicted to be about 5 eV higher in energy than the GdO^+ $^8\Sigma^-$ ground state at the CCSD(T,full) level of theory.

The ground state for GdC^+ is more difficult to ascertain from the calculations because there are several low energy states. For the Seg. SDD basis set at the B3LYP and PBE0 levels of theory (Table 3.5), the $^{12}\Sigma^+$ state ($[1\phi^2 1\delta^2 1\pi^2 1\sigma^1]$ $2\sigma^1 2\pi^2 3\sigma^1$) is found to be lowest in energy. The character of these mos is the same as those for GdO^+. For the SDD

and ANO basis sets, the predicted ground state is $^{10}\Pi$ ($[1\phi^2 1\delta^2 1\pi^2 1\sigma^1]$ $2\sigma^1 2\pi^3$) at all levels of theory and this is also the ground state determined at the CCSD(T,full)/Seg. SDD level of theory. This $^{10}\Pi$ state is calculated to be about 1 eV higher in energy than the $^{12}\Sigma^+$ state for the Seg. SDD basis set using DFT. These results again indicate that the Seg. SDD basis set combined with DFT favors electronic states in which the exchange energy is maximized. Good quantitative agreement with the experimental Gd^+ excited state energies was obtained only for the ANO and Seg. SDD basis sets at the CCSD(T,full) level of theory. Thus, these combinations should potentially be most accurate in predicting the ground state for GdC^+, here $^{10}\Pi$. Taking into account first-order spin-orbit (SO) energy corrections described below lowers the energy for the $^{10}\Pi$ state relative to that for $^{12}\Sigma^+$ by 0.06 eV. Calculations indicate that both the $^{10}\Sigma^+$ ($[1\phi^2 1\delta^2 1\pi^2 1\sigma^1]$ $2\sigma^2 2\pi^2$) and $^{8}\Sigma^-$ ($[1\phi^2 1\delta^2 1\pi^2 1\sigma^1]$ $2\pi^4$) states for GdC^+ are higher in energy for all basis sets and levels of theory by ~0.4 to 0.7 and ~0.6 to 3 eV, respectively. These two Σ states are higher in energy than the $^{8}\Pi$ ($^{6}\Pi$) state that results from flipping the spin of the electron(s) in the 2σ (2σ and 2π) orbital(s) in the $^{10}\Pi$ ground state.

Similar difficulties to those for GdC^+ are encountered in determining the ground state for $GdCO^+$, where CO binds as an adduct to Gd^+. Two different electronic states are predicted to be the ground state depending on the basis set and level of theory used and several states are close in energy (Table 3.6). Only single point energies are computed at the CCSD(T,full) level of theory using the geometries from the B3LYP and PBE0 calculations. Zero point energy corrections use the scaled frequencies determined for the corresponding level of theory. In all calculations, the valence electrons of C and O in $GdCO^+$ form similar mos to those for carbon monoxide with resulting bond lengths ranging

from 1.13 – 1.17 Å (summarized in Table 3.6) in good agreement with the experimental[54] (calculated) bond length(s) of 1.128 Å (1.124 and 1.131 Å at B3LYP and CCSD(T,full) levels of theory) for CO. These calculations indicate that the interaction between Gd^+ and CO arises from the 6s and 5d valence electrons of Gd^+. If both valence electrons are in 5d orbitals, they engage in π back-bonding with the C(2p) orbitals, giving a $^{10}\Sigma^+$ state that correlates with the Gd^+ (^{10}F, $4f^7 5d^2$) state. Alternatively, if one electron remains in the 6s atomic orbital to form a mainly nonbonding 3σ mo, a $^{10}\Pi$ state results. Either one of these two states is predicted to be the ground state for $GdCO^+$ depending on the basis set and level of theory used. If first-order SO energy effects are taken into account, the $^{10}\Pi$ state is lowered slightly in energy (0.06 eV) relative to the $^{10}\Sigma^+$ state making it the favored ground state for all calculations except for the SDD basis set at the CCSD(T,full) level of theory using the B3LYP geometry. The $^{10}\Sigma^+$ state is higher in energy by at most ~0.20 eV for all calculations except those that use the Seg. SDD basis set with DFT where this state is significantly higher in energy. As was observed for GdO^+ and GdC^+, the Seg. SDD basis set combined with DFT tends to favor states that maximize the exchange energy and thus these calculations predict the $GdCO^+$ $^{10}\Sigma^+$ state to be 2.56 and 3.81 eV higher in energy than the $^{10}\Pi$ state for B3LYP and PBE0, respectively.

3.9.3 Theoretical BDEs using the SDD basis set for Gd. A comparison between experimental and theoretical BDEs is shown in Figure 3.11, which unlike Figure 3.8b also includes results from calculations that use the SDD basis set for Gd. This basis set performed poorly at all three levels of theory (B3LYP, PBE0, and CCSD(T,full)) in predicting correctly the ^{10}D ground state for Gd^+ (Table 3.3). The BDEs in Figure 3.11 for this basis set are referenced to the energy of the calculated ^{10}D state even though this state

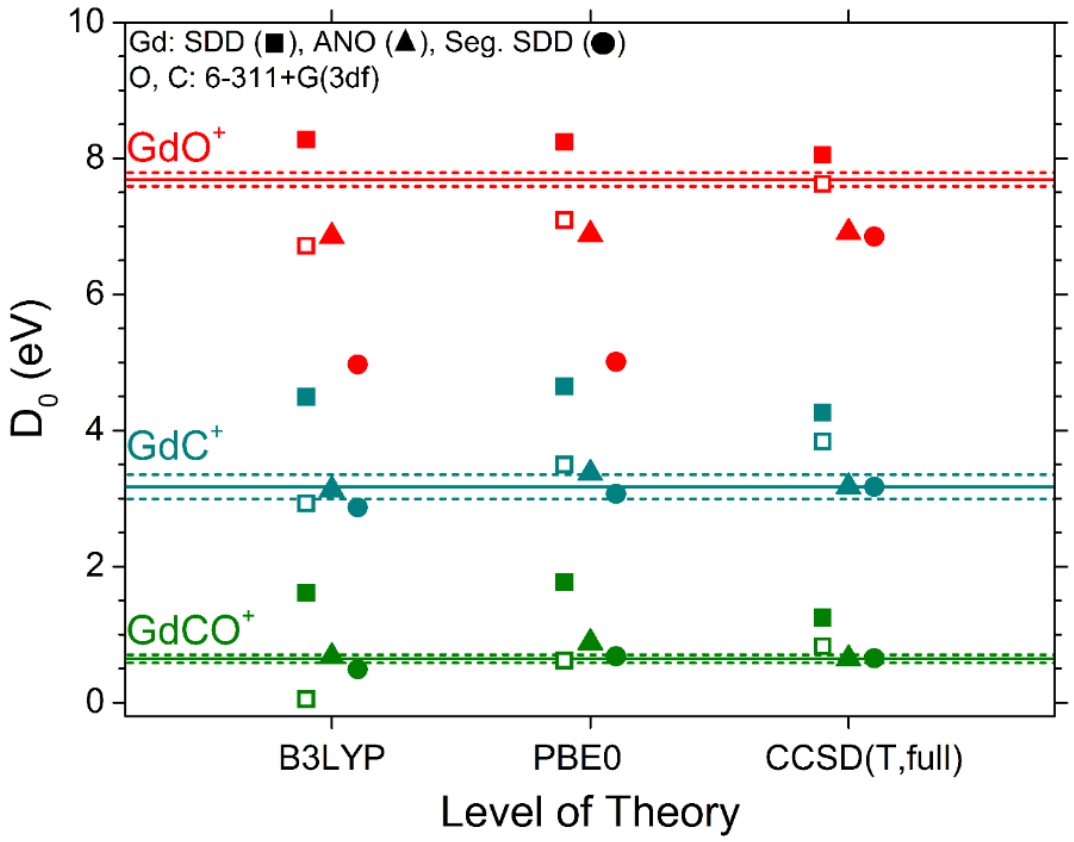

Figure 3.11. Comparison between experimental (solid lines) with associated uncertainties (dashed lines) and theoretical GdO^+, GdC^+, and $GdCO^+$ bond energies at the B3LYP, PBE0, and CCSD(T,full) levels of theory using the SDD (square), ANO (triangle), and Seg. SDD (circle) basis sets for Gd. The $GdCO^+$ bond energies at the CCSD(T, full) level are obtained from single point energies for $GdCO^+$ using the B3LYP geometry. Theoretical bond energies are SO corrected. Closed symbols correspond to calculated bond energies referenced to the calculated energy of the Gd^+ (^{10}D) state, which is the experimentally determined ground state for Gd^+. Open squares correspond to calculated bond energies referenced to the calculated Gd^+ ground states for the SDD basis set of Gd.

was not determined to be lowest in energy, and had calculated excitation energies of 1.56, 1.15, and 0.42 eV at the B3LYP, PBE0, and CCSD(T,full) levels of theory, respectively (Table 3.3). The results in Figure 3.11 indicate that the SDD basis set at all levels of theory overestimates the BDEs for GdO^+, GdC^+, and $GdCO^+$. This can partially be attributed to the calculated ^{10}D state not being identified correctly as the ground state for Gd^+, but rather is significantly higher in energy, especially for the DFT calculations, than the lowest energy

state found (Table 3.3). If the calculated ground states were used instead, better agreement with the experimental values would generally be obtained as shown in Figure 3.11 where these BDEs are indicated by the open squares.

3.9.4. Spin-orbit (SO) energy correction. The energies obtained from the quantum chemical calculations correspond to an average over all SO levels for a given electronic configuration. In contrast, the guided ion beam experiments measure energy differences between the ground state SO levels of reactants and products. Thus, for a more accurate comparison between theoretical and experimental BDEs, an empirical SO energy correction is employed, as done previously for other heavy metals.[24,27,85] For Gd^+ and the neutral reactants, the SO energy correction to the calculated energies is determined from a weighted average of the experimental SO levels. For example, the SO energy correction for the ground states of Gd^+ (^{10}D) and O (^3P) is 0.123 eV and 0.010 eV, respectively.[11] For GdO^+, GdC^+, and $GdCO^+$, the first-order SO energy is given by $E^{SO} = A\ \Lambda\ M_S$ where A is the SO splitting constant, Λ is the orbital angular momentum quantum number, and M_S is the spin quantum number for a specific SO level $\Omega = \Lambda + M_S$. For Σ ($\Lambda = 0$) or singlet states ($M_S = 0$), the first-order SO energy correction is zero. E^{SO} can also be calculated by summing the SO energy contributions from each electron i using $E^{SO} = \Sigma\ a_i \bullet l_i \bullet s_i$ where a_i is the splitting constant, l_i is the orbital angular momentum, and s_i is the spin of electron i, respectively. Here, a_i is approximated as $\zeta_{5d}(Gd^+)$ or $\zeta_{4f}(Gd^+)$, corresponding to either the atomic SO splitting constant for a 5d or 4f electron of Gd^+. The $\zeta_{5d}(Gd^+)$ and $\zeta_{4f}(Gd^+)$ SO constants were calculated as 956.7 and 1712.7 cm^{-1} by Professor Michael D. Morse using a modified version of a Hartree-Fock program developed by Fischer.[83,84] This value is slightly higher but comparable with the 4f spin-orbit splitting constant of 1456 cm^{-1} for

Gd.[86]

The first-order SO energy correction for GdO^+ and GdC^+ where $\Lambda \neq 0$ can be estimated using the values for $\zeta_{5d}(Gd^+)$ and $\zeta_{4f}(Gd^+)$ and $E^{SO} = A\ \Lambda\ M_S = \Sigma\ a_i \bullet l_i \bullet s_i$. For example, the SO energy correction for the $GdO^+\ ^{10}\Pi$ state ($[1\phi^2 1\delta^2 2\pi^2 2\sigma^1]1\sigma^2 1\pi^3 3\sigma^1$) is 4.5 $A(^{10}\Pi) = -0.5\ \zeta_{5d}(Gd^+) = -478.4\ cm^{-1}$. The $^{10}\Pi_{9/2}$ state is lower in energy by 478.4 cm^{-1} (0.059 eV) from the unperturbed $GdO^+\ ^{10}\Pi$ state. The SO splitting constant $A(^{10}\Pi)$ is 106.3 cm^{-1} from 478.4 cm^{-1}/4.5. For comparison, the experimentally measured energy difference between the $^9\Pi_4$ and $^9\Pi_1$ state for neutral GdO is 291 cm^{-1},[86,87] giving an SO splitting constant of $A(^9\Pi) = 291\ cm^{-1}/3 = 97\ cm^{-1}$ in good agreement with that for the $^{10}\Pi$ state of GdO^+ determined here. Tables 3.4 – 3.6 list the SO corrected bond energies and relative energies for the various electronic states of GdO^+, GdC^+, and $GdCO^+$.

3.10 Acknowledgements

This work is supported by the US Air Force Office of Scientific Research (FA9550-14-1-0357). The authors thank Professor Michael D. Morse for help with calculating $\zeta_{5d}(Gd^+)$ and $\zeta_{4f}(Gd^+)$ used in the determination of the empirical spin-orbit corrections. The authors also thank Professor Kirk A. Peterson for providing the cc-pVXZ-DK3 (with X = T, Q) basis sets for Gd and for helpful advice in performing these calculations, and the Center for High Performance Computing at the University of Utah for generous allocation of computer time.

3.11 References

(1) Shuman, N. S.; Hunton, D. E.; Viggiano, A. A. Ambient and Modified Atmospheric Ion Chemistry: From Top to Bottom. *Chem. Rev.* **2015,** *115*, 4542-4570.

(2) Schofield, K. An Overlooked Series of Gas Phase Diatomic Metal Oxide Ions that Are Long-lived. *J. Phys. Chem. A* **2006,** *110*, 6938-6947.

(3) Ard, S. G.; Shuman, N. S.; Martinez, O.; Brumbach, M. T.; Viggiano, A. A. Kinetics of Chemi-Ionization Reactions of Lanthanide Metals (Nd, Sm) from 150 to 450 K. *J. Chem. Phys.* **2015,** *143*, 204303.

(4) Konings, R. J. M.; Beneš, O.; Kovács, A.; Manara, D.; Sedmidubský, D.; Gorokhov, L.; Iorish, V. S.; Yungman, V.; Shenyavskaya, E.; Osina, E. The Thermodynamic Properties of the f-Elements and their Compounds. Part 2. The Lanthanide and Actinide Oxides. *J. Phys. Chem. Ref. Data* **2014,** *43*, 013101.

(5) Larsen, M. F.; Mikkelsen, I. S.; Meriwether, J. W.; Niciejewski, R.; Vickery, K. Simultaneous Observations of Neutral Winds and Electric Fields at Spaced Locations in the Dawn Auroral Oval. *J. Geophys. Res.: Space Phys.* **1989,** *94*, 17235-17243.

(6) Cox, R. M.; Kim, J.; Armentrout, P. B.; Bartlett, J.; VanGundy, R. A.; Heaven, M. C.; Ard, S. G.; Melko, J. J.; Shuman, N. S.; Viggiano, A. A. Evaluation of the Exothermicity of the Chemi-Ionization Reaction Sm + O → $SmO^+ + e^-$. *J. Chem. Phys.* **2015,** *142*, 134307.

(7) Ard, S. G.; Shuman, N. S.; Martinez, O.; Armentrout, P. B.; Viggiano, A. A. Chemi-Ionization Reactions of La, Pr, Tb, and Ho with Atomic O and La with N_2O from 200 to 450 K. *J. Chem. Phys.* **2016,** *145*, 084302.

(8) Haynes, W. M. *CRC Handbook of Chemistry and Physics: A Ready-Reference Book of Chemical and Physical Data*; 96 ed.; CRC Press: Boca Raton, Florida, 2015.

(9) Lo, H. H.; Fite, W. L. Associative Ionization of Ti, Zr, Gd, and Th in Collisions with O and O_2. *Chem. Phys. Lett.* **1974,** *29*, 39-41.

(10) Miyabe, M.; Oba, M.; Wakaida, I. Analysis of the Even-Parity Rydberg Series of Gd I to Determine Its Ionization Potential and Isotope Shift. *J. Phys. B: At. Mol. Opt. Phys.* **1998,** *31*, 4559.

(11) Sansonetti, J. E.; Martin, W. C. Handbook of Basic Atomic Spectroscopic Data. *J. Phys. Chem. Ref. Data* **2005,** *34*, 1559-2259.

(12) Armentrout, P. B. Mass Spectrometry—Not Just a Structural Tool: The Use of Guided Ion Beam Tandem Mass Spectrometry to Determine Thermochemistry. *J. Am. Soc. Mass. Spectrom.* **2002,** *13*, 419-434.

(13) Armentrout, P. B. Kinetic Energy Dependence of Ion–Molecule Reactions: Guided Ion Beams and Threshold Measurements. *Int. J. Mass Spectrom.* **2000,** *200*, 219-

241.

(14) Clemmer, D. E.; Weber, M. E.; Armentrout, P. B. Reactions of Al^+ (^1S) with NO_2, N_2O, and CO_2: Thermochemistry of AlO and AlO^+. *J. Phys. Chem.* **1992,** *96*, 10888-10893.

(15) Dalleska, N. F.; Armentrout, P. B. Guided Ion Beam Studies of Reactions of Alkaline Earth Ions with O_2. *Int. J. Mass Spectrom. Ion Processes* **1994,** *134*, 203-212.

(16) Aristov, N.; Armentrout, P. B. Collision-Induced Dissociation of Vanadium Monoxide Ion. *J. Phys. Chem.* **1986,** *90*, 5135-5140.

(17) Loh, S. K.; Fisher, E. R.; Lian, L.; Schultz, R. H.; Armentrout, P. B. State-Specific Reactions of Fe^+ (^6D, ^4F) with O_2 and cyclo-C_2H_4O: $D°_0(Fe^+\text{-}O)$ and Effects of Collisional Relaxation. *J. Phys. Chem.* **1989,** *93*, 3159-3167.

(18) Clemmer, D. E.; Elkind, J. L.; Aristov, N.; Armentrout, P. B. Reaction of Sc^+, Ti^+, and V^+ with CO. MC^+ and MO^+ Bond Energies. *J. Chem. Phys.* **1991,** *95*, 3387-3393.

(19) Rodgers, M. T.; Walker, B.; Armentrout, P. B. Reactions of Cu^+ (^1S and ^3D) with O_2, CO, CO_2, N_2, NO, N_2O, and NO_2 Studied by Guided Ion Beam Mass Spectrometry. *Int. J. Mass Spectrom.* **1999,** *182–183*, 99-120.

(20) Fisher, E. R.; Elkind, J. L.; Clemmer, D. E.; Georgiadis, R.; Loh, S. K.; Aristov, N.; Sunderlin, L. S.; Armentrout, P. B. Reactions of Fourth-Period Metal Ions (Ca^+–Zn^+) with O_2: Metal-Oxide Ion Bond Energies. *J. Chem. Phys.* **1990,** *93*, 2676-2691.

(21) Chen, Y.-M.; Armentrout, P. B. Kinetic Energy Dependence of the Reactions of Ru^+, Rh^+, Pd^+, and Ag^+ with O_2. *J. Chem. Phys.* **1995,** *103*, 618-625.

(22) Sievers, M. R.; Chen, Y.-M.; Armentrout, P. B. Metal Oxide and Carbide Thermochemistry of Y^+, Zr^+, Nb^+, and Mo^+. *J. Chem. Phys.* **1996,** *105*, 6322-6333.

(23) Hinton, C. S.; Citir, M.; Manard, M.; Armentrout, P. B. Collision-Induced Dissociation of MO^+ and MO_2^+ (M = Ta and W): Metal Oxide and Dioxide Cation Bond Energies. *Int. J. Mass Spectrom.* **2011,** *308*, 265-274.

(24) Armentrout, P. B. The Bond Energy of ReO^+: Guided Ion-Beam and Theoretical Studies of the Reaction of Re^+ (^7S) with O_2. *J. Chem. Phys.* **2013,** *139*, 084305.

(25) Zhang, X.-G.; Armentrout, P. B. Activation of O_2, CO, and CO_2 by Pt^+: The Thermochemistry of PtO^+. *J. Phys. Chem. A* **2003,** *107*, 8904-8914.

(26) Hinton, C. S.; Li, F.; Armentrout, P. B. Reactions of Hf^+, Ta^+, and W^+ with O_2 and CO: Metal Carbide and Metal Oxide Cation Bond Energies. *Int. J. Mass Spectrom.* **2009,** *280*, 226-234.

(27) Hinton, C. S.; Citir, M.; Armentrout, P. B. Guided Ion-Beam and Theoretical Studies of the Reaction of Os^+ (^6D) with O_2: Adiabatic and Nonadiabatic Behavior. *Int. J. Mass Spectrom.* **2013,** *354–355*, 87-98.

(28) Cox, R. M.; Citir, M.; Armentrout, P. B.; Battey, S. R.; Peterson, K. A. Bond Energies of ThO^+ and ThC^+: A Guided Ion Beam and Quantum Chemical Investigation of the Reactions of Thorium Cation with O_2 and CO. *J. Chem. Phys.* **2016,** *144*, 184309.

(29) Ackermann, R. J.; Rauh, E. G.; Thorn, R. J. The Thermodynamics of Ionization of Gaseous Oxides; The First Ionization Potentials of the Lanthanide Metals and Monoxides. *J. Chem. Phys.* **1976,** *65*, 1027-1031.

(30) Dyke, J. M.; Ellis, A. M.; Feher, M.; Morris, A.; Paul, A. J.; Stevens, J. C. H. High-Temperature Photoelectron Spectroscopy. A Study of Niobium Monoxide and Tantalum Monoxide. *J. Chem. Soc., Faraday Trans. 2: Mol. Chem. Phys.* **1987,** *83*, 1555-1565.

(31) Kordis, J.; Gingerich, K. A. Mass Spectrometric Observations of Some Polyatomic Gaseous Rare Earth Oxides and Their Atomization Energies. *J. Chem. Phys.* **1977,** *66*, 483-491.

(32) Murad, E.; Hildenbrand, D. L. Dissociation Energies of GdO, HoO, ErO, TmO, and LuO; Correlation of Results for the Lanthanide Monoxide Series. *J. Chem. Phys.* **1980,** *73*, 4005-4011.

(33) Cockett, M. C. R.; Nyulászi, L.; Veszprémi, T.; Wright, T. G.; Dyke, J. M. A Study of Some Gas-Phase Lanthanide Plus Oxidant Chemiionization Reactions with Chemielectron Spectroscopy. *J. Electron. Spectrosc. Relat. Phenom.* **1991,** *57*, 373-397.

(34) Ames, L. L.; Walsh, P. N.; White, D. Rare Earths. IV. Dissociation Energies of the Gaseous Monoxides of the Rare Earths. *J. Phys. Chem.* **1967,** *71*, 2707-2718.

(35) Messier, D. R. Vapor Pressure of Gd_2O_3 from 2350° to 2590°K. *J. Am. Ceram. Soc.* **1967,** *50*, 665-668.

(36) Drowart, J.; Myers, C. E.; Szwarc, R.; Auwera-Mahieu, A. V.; Uy, O. M. Determination by the Mass Spectrometric Knudsen Cell Method of the Atomization Energies of the Molecules PO and PO_2. *J. Chem. Soc., Faraday Trans. 2: Mol. Chem. Phys.* **1972,** *68*, 1749-1757.

(37) Brewer, L.; Rosenblatt, G. M. *Advances in High Temperature Chemistry*; Academic Press: New York, 1969.

(38) Ackermann, R. J.; Chandrasekharaiah, M. S. *Thermodynamics of Nuclear Materials*; IAEA: Vienna, 1975.

(39) Huber, K. P.; Herzberg, G. *Molecular Spectra and Molecular Structure: IV. Constants of Diatomic Molecules*; Van Nostrand Reinhold: New York, 1979.

(40) Pedley, J. B.; Marshall, E. M. Thermochemical Data for Gaseous Monoxides. *J. Phys. Chem. Ref. Data* **1983,** *12*, 967-1031.

(41) Chandrasekharaiah, M. S.; Gingerich, K. A. In *Handbook on the Physics and Chemistry of Rare Earths*; Elsevier, 1989; Vol. 12.

(42) Koyanagi, G. K.; Bohme, D. K. Oxidation Reactions of Lanthanide Cations with N_2O and O_2: Periodicities in Reactivity. *J. Phys. Chem. A* **2001,** *105*, 8964-8968.

(43) Gibson, J. K. Role of Atomic Electronics in f-Element Bond Formation: Bond Energies of Lanthanide and Actinide Oxide Molecules. *J. Phys. Chem. A* **2003,** *107*, 7891-7899.

(44) Cornehl, H. H.; Heinemann, C.; Schroeder, D.; Schwarz, H. Gas-Phase Reactivity of Lanthanide Cations with Hydrocarbons. *Organometallics* **1995,** *14*, 992-999.

(45) Loh, S. K.; Hales, D. A.; Lian, L.; Armentrout, P. B. Collision-Induced Dissociation of Fe_n^+ (n=2–10) with Xe: Ionic and Neutral Iron Binding Energies. *J. Chem. Phys.* **1989,** *90*, 5466-5485.

(46) Schultz, R. H.; Armentrout, P. B. Reactions of N_4^+ with Rare Gases from Thermal to 10eV Center-of-Mass Energy: Collision-Induced Dissociation, Charge Transfer and Ligand Exchange. *Int. J. Mass Spectrom. Ion Processes* **1991,** *107*, 29-48.

(47) Kickel, B. L.; Armentrout, P. B. Guided Ion Beam Studies of the Reactions of Group 3 Metal Ions (Sc^+, Y^+, La^+, and Lu^+) with Silane. Electronic State Effects, Comparison to Reactions with Methane, and M^+-SiH_x (x = 0-3) Bond Energies. *J. Am. Chem. Soc.* **1995,** *117*, 4057-4070.

(48) Chen, Y.-M.; Elkind, J. L.; Armentrout, P. B. Reactions of Ru^+, Rh^+, Pd^+, and Ag^+ with H_2, HD, and D_2. *J. Phys. Chem.* **1995,** *99*, 10438-10445.

(49) Sievers, M. R.; Chen, Y.-M.; Elkind, J. L.; Armentrout, P. B. Reactions of Y^+, Zr^+, Nb^+, and Mo^+ with H_2, HD, and D_2. *J. Phys. Chem.* **1996,** *100*, 54-62.

(50) Teloy, E.; Gerlich, D. Integral Cross Sections for Ion-Molecule Reactions. I. The Guided Beam Technique. *Chem. Phys.* **1974,** *4*, 417-427.

(51) Ervin, K. M.; Armentrout, P. B. Translational Energy Dependence of $Ar^+ + XY \rightarrow ArX^+ + Y$ (XY=H_2,D_2,HD) from Thermal to 30 eV C.M. *J. Chem. Phys.* **1985,** *83*, 166-189.

(52) Daly, N. R. Scintillation Type Mass Spectrometer Ion Detector. *Rev. Sci. Instrum.* **1960,** *31*, 264-267.

(53) Muntean, F.; Armentrout, P. B. Guided Ion Beam Study of Collision-Induced Dissociation Dynamics: Integral and Differential Cross Sections. *J. Chem. Phys.* **2001,** *115*, 1213-1228.

(54) Johnson III, R. D. NIST Computational Chemistry Comparison and Benchmark Database, NIST Standard Reference Database Number 101 Release 18, NIST, 2016, available online: http://cccbdb.nist.gov/.

(55) Lifshitz, C.; Wu, R. L. C.; Tiernan, T. O.; Terwilliger, D. T. Negative Ion–Molecule Reactions of Ozone and Their Implications on the Thermochemistry of O_3^-. *J. Chem. Phys.* **1978,** *68*, 247-260.

(56) Weber, M. E.; Elkind, J. L.; Armentrout, P. B. Kinetic Energy Dependence of $Al^+ + O_2 \rightarrow AlO^+ + O$. *J. Chem. Phys.* **1986,** *84*, 1521-1529.

(57) Frisch, M. J.; Trucks, G. W.; Schlegel, H. B.; Scuseria, G. E.; Robb, M. A.; Cheeseman, J. R.; Scalmani, G.; Barone, V.; Mennucci, B.; Petersson, G. A.et al.; Gaussian, Inc.: Wallingford, CT, USA, 2009.

(58) Becke, A. D. Density-Functional Thermochemistry. III. The Role of Exact Exchange. *J. Chem. Phys.* **1993,** *98*, 5648-5652.

(59) Lee, C.; Yang, W.; Parr, R. G. Development of the Colle-Salvetti Correlation-Energy Formula into a Functional of the Electron Density. *Phys. Rev. B* **1988,** *37*, 785-789.

(60) Perdew, J. P.; Ernzerhof, M.; Burke, K. Rationale for Mixing Exact Exchange with Density Functional Approximations. *J. Chem. Phys.* **1996,** *105*, 9982-9985.

(61) Adamo, C.; Barone, V. Toward Reliable Density Functional Methods without Adjustable Parameters: The PBE0 Model. *J. Chem. Phys.* **1999,** *110*, 6158-6170.

(62) Raghavachari, K.; Trucks, G. W.; Pople, J. A.; Head-Gordon, M. A Fifth-Order Perturbation Comparison of Electron Correlation Theories. *Chem. Phys. Lett.* **1989,** *157*, 479-483.

(63) Bartlett, R. J.; Watts, J. D.; Kucharski, S. A.; Noga, J. Non-Iterative Fifth-Order Triple and Quadruple Excitation Energy Corrections in Correlated Methods. *Chem. Phys. Lett.* **1990,** *165*, 513-522.

(64) Scuseria, G. E.; Lee, T. J. Comparison of Coupled-Cluster Methods which Include the Effects of Connected Triple Excitations. *J. Chem. Phys.* **1990,** *93*, 5851-5855.

(65) Crawford, T. D.; Stanton, J. F. Investigation of an Asymmetric Triple-Excitation Correction for Coupled-Cluster Energies. *Int. J. Quantum Chem.* **1998,** *70*, 601-611.

(66) Dolg, M.; Stoll, H.; Preuss, H. Energy-Adjusted Ab Initio Pseudopotentials for the Rare Earth Elements. *J. Chem. Phys.* **1989,** *90*, 1730-1734.

(67) Schuchardt, K. L.; Didier, B. T.; Elsethagen, T.; Sun, L.; Gurumoorthi, V.; Chase, J.; Li, J.; Windus, T. L. Basis Set Exchange: A Community Database for Computational Sciences. *J. Chem. Inf. Model.* **2007,** *47*, 1045-1052.

(68) Feller, D. The Role of Databases in Support of Computational Chemistry Calculations. *J. Comput. Chem.* **1996,** *17*, 1571-1586.

(69) Cao, X.; Dolg, M. Valence Basis Sets for Relativistic Energy-Consistent Small-Core Lanthanide Pseudopotentials. *J. Chem. Phys.* **2001,** *115*, 7348-7355.

(70) Cao, X.; Dolg, M. Segmented Contraction Scheme for Small-Core Lanthanide Pseudopotential Basis Sets. *J. Mol. Struct.: THEOCHEM* **2002,** *581*, 139-147.

(71) Douglas, M.; Kroll, N. M. Quantum Electrodynamical Corrections to the Fine Structure of Helium. *Ann. Phys.* **1974,** *82*, 89-155.

(72) Reiher, M.; Wolf, A. Exact Decoupling of the Dirac Hamiltonian. II. The Generalized Douglas–Kroll–Hess Transformation up to Arbitrary Order. *J. Chem. Phys.* **2004,** *121*, 10945-10956.

(73) Lu, Q.; Peterson, K. A. Correlation Consistent Basis Sets for Lanthanides: The Atoms La–Lu. *J. Chem. Phys.* **2016,** *145*, 054111.

(74) Dunham, J. L. The Energy Levels of a Rotating Vibrator. *Phys. Rev.* **1932,** *41*, 721-731.

(75) Foresman, J. B.; Frisch, A. *Exploring Chemistry with Electronic Structure Methods*; Gaussian: Pittsburgh, Pa., 1996.

(76) Gioumousis, G.; Stevenson, D. P. Reactions of Gaseous Molecule Ions with Gaseous Molecules. V. Theory. *J. Chem. Phys.* **1958,** *29*, 294-299.

(77) Cheng, P.; Koyanagi, G. K.; Bohme, D. K. Gas-Phase Reactions of Atomic Lanthanide Cations with CO_2 and CS_2: Room-Temperature Kinetics and Periodicities in Reactivity. *J. Phys. Chem. A* **2006,** *110*, 12832-12838.

(78) Darwent, B. d. *Bond Dissociation Energies in Simple Molecules*; U.S. National Bureau of Standards; for sale by the Supt. of Docs., U.S. Govt. Print. Off.: Washington, 1970.

(79) Burley, J. D.; Ervin, K. M.; Armentrout, P. B. Translational Energy Dependence of $O^+(^4S) + H_2(D_2, HD) \rightarrow OH^+(OD^+) + H(D)$ from Thermal Energies to 30 eV C.M. *Int. J. Mass Spectrom. Ion Processes* **1987,** *80*, 153-175.

(80) Sievers, M. R.; Armentrout, P. B. Activation of Carbon Dioxide: Gas-Phase Reactions of Y^+, YO^+, and YO_2^+ with CO and CO_2. *Inorg. Chem.* **1999,** *38*, 397-402.

(81) Elkind, J. L.; Armentrout, P. B. Effect of Kinetic and Electronic Energy on the Reaction of V^+ with H_2, HD, and D_2. *J. Phys. Chem.* **1985,** *89*, 5626-5636.

(82) Zhang, X.-G.; Liyanage, R.; Armentrout, P. B. Potential Energy Surface for Activation of Methane by Pt^+: A Combined Guided Ion Beam and DFT Study. *J. Am. Chem. Soc.* **2001,** *123*, 5563-5575.

(83) Fischer, C. F. General Hartree-Fock Program. *Comput. Phys. Commun.* **1987,** *43*, 355-365.

(84) Fischer, C. F. *The Hartree-Fock Method for Atoms, A Numerical Approach*; John Wiley & Sons: New York, 1977.

(85) Armentrout, P. B.; Li, F.-X. Bond Energy of IrO^+: Guided Ion-Beam and Theoretical Studies of the Reaction of Ir^+ (^5F) with O_2. *J. Phys. Chem. A* **2013,** *117*, 7754-7766.

(86) Kotzian, M.; Rösch, N.; Zerner, M. C. Intermediate Neglect of Differential Overlap Spectroscopic Studies on Lanthanide Complexes. *Theor. Chim. Acta* **1992,** *81*, 201-222.

(87) Carette, P.; Hocquet, A.; Douay, M.; Pinchemel, B. Laser-Induced Fluorescence of GdO. *J. Mol. Spectrosc.* **1987,** *124*, 243-271.

CHAPTER 4

GADOLINIUM CATION (Gd^+) REACTION WITH O_2: POTENTIAL ENERGY SURFACE MAPPED EXPERIMENTALLY AND WITH THEORY

This chapter is reprinted with permission from Demireva, M; Armentrout, P. B. Gadolinium Cation (Gd^+) Reaction with O_2: Potential Energy Surface Mapped Experimentally and with Theory. *J. Chem. Phys.* **2017**, *146*, 174302. © 2017 AIP Publishing. http://aip.scitation.org/doi/10.1063/1.4982683

4.1 Graphical Abstract

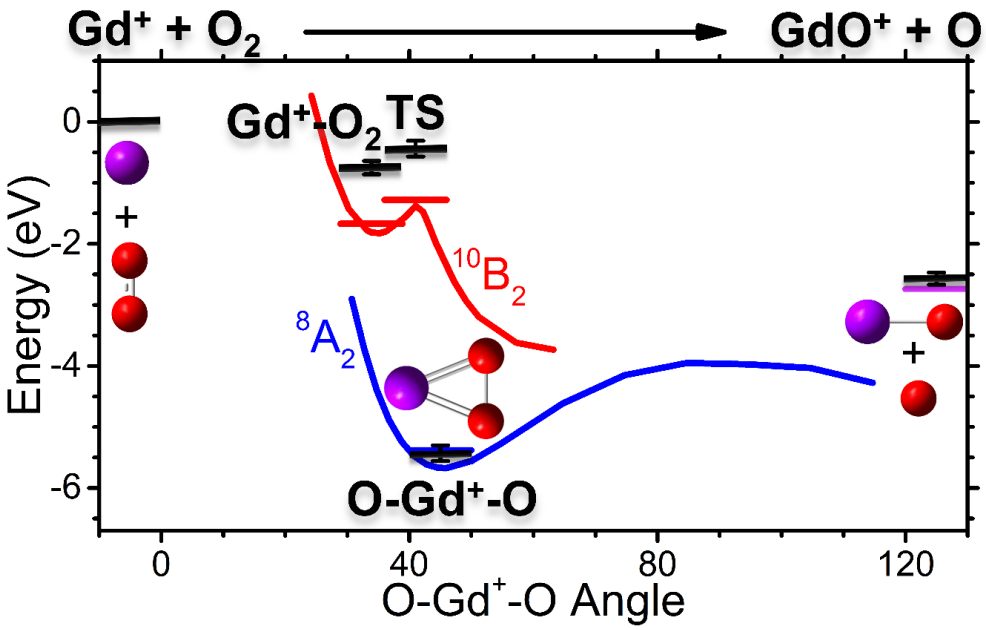

4.2 Abstract

Guided ion beam tandem mass spectrometry is used to measure the kinetic energy dependent cross sections for reactions of the lanthanide metal gadolinium cation (Gd^+) and GdO^+ with O_2 and for collision-induced dissociation (CID) of GdO_2^+ with Xe. Gd^+ reacts with O_2 in an exothermic and barrierless reaction to form GdO^+ and O. GdO_2^+ is also formed in this reaction, but this product ion is formed in a sequential reaction, as verified by pressure dependent measurements and comparison with the results for the reaction of GdO^+ with O_2. The CID experiments of GdO_2^+ indicate the presence of two GdO_2^+ precursor ion populations, assigned to a weakly bound oxygen molecule adduct (Gd^+-O_2) and an inserted cyclic Gd^+ dioxide species (O-Gd^+-O). Analysis of the resulting product ion cross sections yields bond dissociation energies (BDE, D_0) for Gd^+-O_2 and OGd^+-O, where the latter BDE is also independently measured in an exchange reaction between GdO^+ and O_2. The CID experiments also provide the energy of the barrier for the rearrangement of the Gd^+-O_2 adduct to the inserted O-Gd^+-O structure (as identified by loss of a single oxygen atom). The thermochemistry measured here yields D_0(OGd^+-O) = 2.86 ± 0.08 eV, D_0(Gd^+-O_2) = 0.75 ± 0.11 eV, and a barrier height relative to Gd^+-O_2 of 0.31 ± 0.07 eV. These data are sufficient to characterize in some detail the potential energy surface of the Gd^+ reaction with O_2 entirely from experiment. Theoretical calculations are performed for comparison with the experimental energetics and for further insight into the reaction mechanisms.

4.3 Introduction

Oxygen binding and reactivity with metals play a pivotal role in many biological and catalytic processes. Numerous experimental and theoretical studies have thus focused on investigating various metal oxide complexes formed as intermediates or products in these processes.[1] A different application of metal oxides has been explored by the Air Force Research Laboratory, where there has been a longstanding interest in creating localized electron enhanced plasmas in the atmosphere that can be used to prevent disruptions in satellite communications from natural electron density fluctuations.[2] One possibility for generating such plasmas is by releasing metals in the atmosphere that can react with available oxygen atoms via the chemi-ionization reaction (4.1).[2]

$$M + O \rightarrow MO^+ + e^- \qquad (4.1)$$

Literature thermochemistry[3-5] suggests that only a few metals, many of them lanthanides, undergo reaction (4.1) exothermically. These metals are rare because they must have a greater MO bond dissociation energy (BDE, D_0) than ionization energy (IE).[3] In recent work, we measured the thermochemistry for reaction (4.1) in the cases of Sm^+ and Gd^+ using guided ion beam tandem mass spectrometry (GIBMS).[6,7] This technique[8,9] has been shown to provide reliable thermochemical information and insights into the reaction mechanisms for many metal oxidation reactions including the reactivity of O_2 with atomic cations of several main group metals,[10,11] first,[12-18] second,[17,19-24] and third[25-30] row transition metals, lanthanides,[6,7,17] and actinides.[31]

Our recent GIBMS results for Gd indicate that reaction (4.1) is significantly exothermic for this metal and thus Gd could be a good candidate for the Air Force experiments.[7] However, in the atmospheric chemical release experiments, the metal oxide

cation can potentially react further to form the metal dioxide cation via reaction (4.2) or (4.3), which could affect the plasma and the electron density produced.

$$MO^+ + O \rightarrow MO_2^+ \quad (4.2)$$

$$MO^+ + O_2 \rightarrow MO_2^+ + O \quad (4.3)$$

Thus, determining this thermochemistry (i.e., the metal dioxide cation BDE) can provide additional insight into the usefulness of Gd for atmospheric chemical release. The BDE for GdO_2^+ has been reported as 2.60 eV in a compilation of thermochemistry by Schofield,[3] although no details are given about how this value was determined. This BDE appears to have been deduced indirectly from a thermodynamic cycle involving D_0(OGd-O), IE(GdO_2), and IE(GdO). The same report by Schofield[3] gives an IE for GdO of 5.75 eV (uncertainty of 0.1 eV), which corresponds to a value measured by Ackermann et al.,[32] and an IE for GdO_2 of 9.5 eV (uncertainty of 1.0 eV), which is in agreement with a value obtained by Kordis and Gingerich[33] and subsequently reported by Cockett et al.[34] in their compilation of lanthanide dioxide thermochemistry. Cockett et al.[34] have also reported BDEs for the neutral lanthanide dioxides based on empirical estimates from Kordis and Gingerich,[33] suggesting a BDE for OGd-O of 6.4 ± 1.1 eV. Using this BDE combined with the IEs for GdO and GdO_2 would give a BDE for GdO_2^+ of 2.60 ± 1.5 eV, in agreement with the value reported by Schofield. However, there seems to be no direct experimental measurement for the BDE of GdO_2^+. Furthermore, the IE and BDE values for GdO_2 from Kordis and Gingerich and Cockett et al. used in the derivation of the GdO_2^+ BDE may have questionable accuracy. For example, these authors predicted a BDE for LaO_2 of 7.5 ± 1.0 eV;[33,34] however, a direct measurement using GIBMS indicated a significantly lower BDE of 4.20 ± 0.33 eV.[17] Similar discrepancies have been found between the BDEs measured

for ScO_2 and YO_2 using GIBMS[17] and those predicted by Kordis and Gingerich.[33] In addition, Cockett et al.[34] estimated the IE for LaO_2 to be 9.5 ± 0.5 eV, whereas the IE for LaO_2 was found to be lower at 8.11 ± 0.33 eV from GIBMS measurements.[17] This lower value is more consistent with IE values for ScO_2 and YO_2 of 8.66 ± 0.20 eV and 8.23 ± 0.16 eV, respectively, also reported in the GIBMS study. Because Gd has a half-filled 4f shell and is isovalent (disregarding the 4f electrons) with Sc, Y, and La, it should exhibit similar reactivity and binding as these metals. Thus, a BDE of 6.4 ± 1.1 eV and an IE of 9.5 eV for GdO_2 are likely too large and are expected to be more similar to the values measured for the Sc, Y, and La dioxide molecules.[17]

Here, GIBMS is used to study reaction (4.3) directly and to measure the 0 K BDE for Gd^+-O_2 and OGd^+-O from exchange and collision-induced dissociation (CID) reactions. This thermochemistry, together with our recently measured BDE for GdO^+,[7] is used to map the potential energy surface for the Gd^+ reaction with O_2 entirely from experiment. Theoretical calculations are performed for comparison with experiment and for insight into the reaction mechanisms to characterize the Gd^+ reaction with O_2 in detail. Experimental results are compared with those for the group 3 metal cations, Sc^+ and Y^+, and the lanthanides La^+ and Lu^+ and periodic trends are discussed.

4.4 Experimental and Theoretical Methods

4.4.1 Experiments. The guided ion beam tandem mass spectrometer and experimental procedure used have been discussed in detail elsewhere.[8,9,35] Briefly, singly charged Gd precursor ions were formed from Gd foil (Sigma-Aldrich, St. Louis, MO) using a direct current flow tube (DC/FT) ion source. A DC discharge voltage ranging from -1100

to -2000 V was applied to a Ta holder containing the Gd foil. A 90:10% mixture of He:Ar gas was introduced in the source at a pressure of ~0.4 Torr. Singly charged Ar ions formed via the DC discharge were accelerated into the Gd cathode, sputtering singly charged Gd^+ ions. GdO^+ and GdO_2^+ precursor ions were produced by introducing O_2 gas in the source about 15 cm downstream from the DC discharge source. These precursor ions underwent ~10^5 collisions with the He and Ar carrier gas mixture in a meter long flow tube and are assumed to be thermalized to the temperature of the flow tube (~300 K). Ions were skimmed, focused, and subsequently mass selected using a magnet momentum analyzer where the heaviest ^{160}Gd isotope (at least 2 Da heavier than all other isotopes) was chosen to ensure adequate mass separation. Prior to entering a radio frequency octopole ion beam guide, the mass-selected precursor ions were decelerated to a desired kinetic energy. Neutral reactant gases (O_2 or Xe) were introduced into a reaction cell that surrounds the octopole ion beam guide at pressures ranging from ~0.1 to 0.4 mTorr. These pressures were sufficiently low to ensure that single collisions dominated in the reactions, a conclusion verified by measurements of the cross sections at different pressures. With one exception, explicitly mentioned and analyzed in detail below, the cross sections measured here exhibited no pressure dependence. The precursor ions entered the octopole with well-defined kinetic energies and passed through the reaction cell where they reacted with the neutrals. The precursor and resulting product ions were subsequently extracted, mass analyzed using a quadrupole mass filter, and a Daly detector[36] measured their intensities as a function of precursor ion kinetic energy in the lab frame. Product ion intensities were corrected for any background reaction not occurring in the cell and were converted to product ion cross sections as a function of energy in the center-of-mass (CM) frame as

described elsewhere.[37] The uncertainty in the absolute product ion cross sections is estimated to be ± 20%.[37] Using a retarding technique, the precursor ion kinetic energy distributions were measured to have a full width at half maximum of approximately 0.5 eV in the lab frame and an absolute zero in the energy scale calibration having an uncertainty of ± 0.1 eV in the lab frame.

4.4.2 Data analysis. As explained in detail previously,[9,38] the measured product ion cross sections resulting from endothermic processes were modeled with a modified line-of-centers equation (4.4) to determine the 0 K threshold energy, E_0, of the reaction.

$$\sigma(E) = \sigma_0 \sum_i g_i(E + E_i - E_0)^n/E \qquad (4.4)$$

Here, E corresponds to the CM kinetic energy, σ_0 is a scaling factor, *n* determines the shape of the cross section, E_i is the rotational and vibrational energy of the reactants for state i, and g_i is the population degeneracy for that state ($\Sigma g_i = 1$). Vibrational frequencies and rotational constants needed for calculating E_i are obtained from the NIST Webbook[39] (O_2) or from quantum chemical calculations (GdO^+ and GdO_2^+) as described below. Prior to comparison with the experimental cross sections, equation (4.4) was convolved with the reactant kinetic energy distributions. Optimized fits to the experimental cross sections were obtained by varying E_0, σ_0, and *n* using a nonlinear least-squares method. Uncertainties in E_0 values were determined from optimized fits to several independent data sets for a range of *n* values that can reproduce the experimental cross section and also include the ± 0.1 eV uncertainty in the lab frame energy scale. In exchange reactions (i.e., $M^+ + AB \rightarrow MA^+ + B$), the product ion cross section begins to decline at energies greater than the BDE of the AB neutral because there is sufficient energy to dissociate the product ion. This decline in the cross section was modeled using a modified form of equation (4.4) that includes the

dissociation probability, as explained elsewhere.[40]

In endothermic exchange reactions, if there are no barriers in excess of the endothermicity of the reaction, the BDE of the product ion can be determined from expression (4.5) using the measured E_0 value and the neutral BDE.

$$D_0\left(M^+\text{-}A\right) = D_0(A\text{-}B) - E_0 \qquad (4.5)$$

For collision-induced dissociation (CID) experiments, i.e., $MA^+ + Xe \rightarrow M^+ + A + Xe$, the measured E_0 corresponds directly to the BDE of the precursor ion, i.e., $D_0(M^+\text{-}A)$.

4.4.3 Theoretical calculations. Quantum chemical calculations were performed using the Gaussian09 suite of programs[41] to determine the energies for ground and low-energy states of GdO_2^+ for comparison with the experimental thermochemistry. Extensive calculations including relaxed potential energy scans for GdO_2^+ as a function of the O-Gd^+-O angle were carried out with density functional theory (DFT) at the B3LYP[42,43] level using the relativistic Stuttgart Dresden[44] (SDD) effective (28 electron) core potential (ECP) and the atomic natural orbital[45] (ANO) basis set for Gd and the Pople 6-311+G(3df) basis set for O. These basis sets and level of theory were chosen becuase the calculations are computationally inexpensive and our previous results have indicated that they provide reasonable BDEs with similar values obtained using coupled cluster theory at the CCSD(T,full)[46-49] level for the ANO or segmented[50] SDD basis sets for Gd.[7] Calculations utilizing the 2nd-order Douglas-Kroll-Hess Hamiltonian (DKH2)[51,52] and the cc-pVXZ-DK3 (with X = T and Q) all-electron basis sets[53] for Gd developed by the Peterson group with the corresponding aug-cc-pVXZ-DK basis set for O performed slightly better in reproducing the GdO^+ BDE.[7] Here, additional calculations using the ANO basis set and the SDD ECP or the cc-pVXZ-DK3 with X = T and Q all-electron basis sets for Gd at the

density functional (B3LYP, PBE0[54,55]) and coupled cluster (CCSD(T,full)) levels of theory were performed and evaluated against the experimental thermochemistry obtained for GdO_2^+. With the exception of the cc-pVXZ-DK3 basis sets for Gd, which were obtained from Professor Kirk A. Peterson, all other basis sets (and ECP) were obtained from the EMSL basis set exchange.[56,57] For all levels of theory and basis sets, zero point energies were calculated using frequencies scaled by 0.989.[58] Theoretical BDEs for Gd^+-O_2 and OGd^+-O were obtained from the energy difference between the calculated ground states of the corresponding bound and dissociated GdO_2^+ species. Rotational constants and vibrational frequencies for GdO^+, Gd^+-O_2, and OGd^+-O necessary in the modeling of the experimental cross sections were taken from B3LYP calculations that use the ANO basis set and SDD ECP for Gd.

4.5 Experimental and Theoretical Results

4.5.1 Gd^+ reaction with O_2 to form GdO^+ and O. In the reaction between Gd^+ and O_2, the GdO^+ product was formed with significant abundance. Its energy dependent cross section is shown in Figure 4.1a at two different O_2 pressures. The GdO^+ cross sections measured at the two O_2 pressures are practically identical indicating that GdO^+ is formed according to reaction (4.6) via single collisions at both pressures:

$$Gd^+ + O_2 \rightarrow GdO^+ + O \qquad (4.6)$$

The magnitude of the GdO^+ cross section exceeds 100 $Å^2$ at the lowest collision energy examined (~0.02 eV) and decreases with increasing energy. This is consistent with GdO^+ being formed via an exothermic and barrierless reaction as previously discussed.[7] At energies below ~1.5 eV, the experimental GdO^+ cross section matches the theoretical

Figure 4.1. (a) Product ion cross sections as a function of center-of-mass (bottom *x*-axis) and laboratory (top *x*-axis) frame kinetic energy for the Gd^+ reaction with O_2 at 0.29 mTorr (open circles) and 0.15 mTorr (closed squares). Arrows indicate the O-O BDE (5.12 eV) and the predicted energy (9.39 eV) for the decline in the cross section from the spectator stripping model (SSM). The black line corresponds to the Langevin-Gioumousis-Stevenson (LGS) collision cross section. (b) Experimental cross sections for the $Gd^+ + O_2$ reaction (open red cirlces) compared to calculated cross sections from phase space theory for exothermicities of 1 (dashed black line), 2.57 (solid red line), and 4 eV (blue dashed line), respectively. The dashed red line corresponds to the phase space theory cross section for returning to reactants at an exothermicity of 2.57 eV.

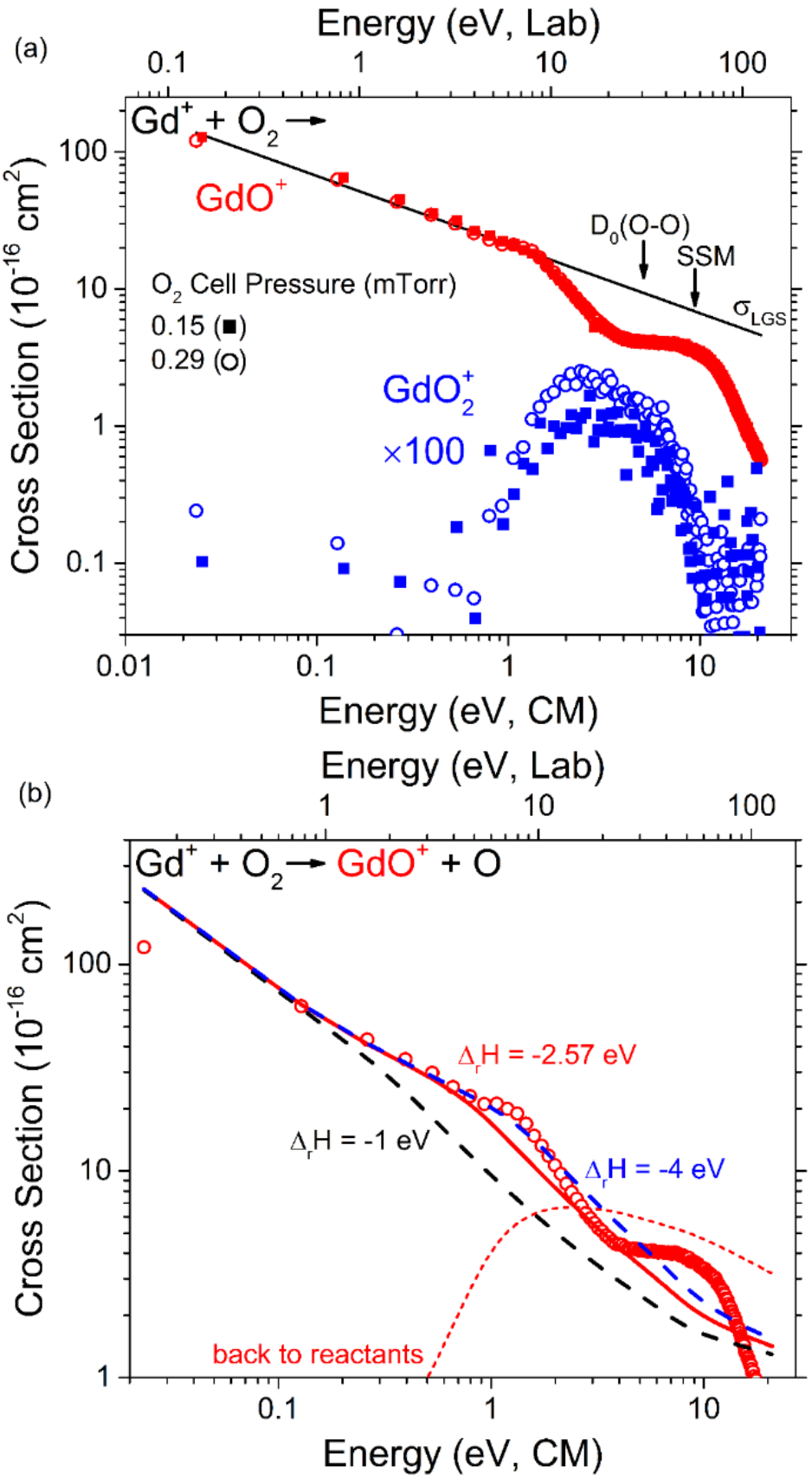
(a)
Energy (eV, Lab)
0.1
1
10
100
Gd+ + O2 →
GdO+
D0(O-O)
SSM
σLGS
O2 Cell Pressure (mTorr)
0.15 (■)
0.29 (○)
GdO2+
×100
Cross Section (10-16 cm2)
100
10
1
0.1
0.01
0.1
1
10
Energy (eV, CM)
(b)
Energy (eV, Lab)
1
10
100
Gd+ + O2 → GdO+ + O
ΔrH = -2.57 eV
ΔrH = -1 eV
ΔrH = -4 eV
back to reactants
Cross Section (10-16 cm2)
100
10
1
0.1
1
10
Energy (eV, CM)

collision limit given by the Langevin-Gioumousis-Stevenson (LGS)[59] cross section (black line in Figure 4.1a), indicating that the reaction proceeds with 100% efficiency at thermal energies. The cross sections can be converted to rate coefficients as explained elsewhere.[37] As discussed previously,[7] the average rate coefficient, k, for reaction (4.6) is 5.7 ± 1.1 × 10^{-10} cm^3/s for collision energies below 1 eV, which is consistent with k_{LGS} of 5.7 × 10^{-10} cm^3/s and that of 4.9 ± 1.5 × 10^{-10} cm^3/s measured for the same reaction at thermal (~295 K) kinetic energies from inductively coupled plasma/selected-ion flow tube experiments.[60]

For collision energies greater than ~1.5 eV, there is a steep decline in the GdO^+ cross section such that it becomes smaller than the LGS cross section. This sharp decrease in reaction efficiency is believed to be the result of angular momentum constraints, as also observed in other similar systems.[16,61] In reaction (4.6), the reduced mass of the products is smaller than that of the reactants, such that angular momentum conservation means that the centrifugal barrier in the product channel increases more rapidly with energy than that in the reactant channel. Eventually, the centrifugal barrier in the product channel can exceed that in the reactant channel, which means that the transiently formed GdO_2^+ intermediate will dissociate back to reactants, resulting in decreased reaction efficiency. As outlined previously,[61] a simple model can be used to predict at what energy this effect will cause a deviation from the LGS cross section. Using an exothermicity for reaction (4.6) of 2.57 ± 0.10 eV (determined from $D_0(Gd^+\text{-}O)$ = 7.69 ± 0.10 eV[7] and $D_0(O\text{-}O)$ = 5.12 eV[62]), the model predicts that the experimental GdO^+ cross section will begin to deviate from the theoretical limit at ~0.5 eV. This is somewhat lower than the actual deviation observed at ~1.5 eV in Figure 4.1a. Phase space theory (PST) calculations can investigate the behavior of the GdO^+ cross section in more detail and are performed using

programs modified from those developed by Chesnavich and Bowers.[25,63] PST cross sections calculated for three different exothermicities (1, 2.57, and 4 eV) are compared with the experimental GdO^+ cross section in Figure 4.1b. Using an exothermicity of 2.57 eV reproduces the GdO^+ cross section reasonably well and provides additional support for the accuracy of the GdO^+ BDE measurements.[7] In contrast, the GdO^+ cross section is clearly underestimated for the PST calculations that use an exothermicity of 1 eV, whereas an exothermicity of 4 eV overestimates the GdO^+ cross section in the ~2 to 5 eV energy range while reproducing the cross section relatively well at lower energies. The PST cross section calculated for an exothermicity of 2.57 eV is slightly smaller than the experimental cross section in the ~1 to ~2 eV energy range. This difference could be caused by formation of an electronically excited GdO^+ product, not accounted for in the model. Calculations indicate that $^{10}\Pi$ and $^{10}\Sigma^-$ excited states of GdO^+ are roughly 3 eV higher in energy than the $^{8}\Sigma^-$ ground state.[7] Assuming all of the exothermicity of the reaction is converted into internal energy, these electronically excited GdO^+ products could be formed at an energy of ~0.5 eV or higher.

Beginning at a collision energy of D_0(O-O) = 5.12 eV, the GdO^+ product should have sufficient energy to dissociate, which would result in a decline in the cross section. However, the GdO^+ cross section remains relatively constant between ~4 and ~9 eV, and begins to decline quickly at significantly higher energies than D_0(O-O). This leveling off could be the result of forming excited GdO^+ states as suggested for other metal cations exhibiting similar behavior,[16] or potentially correspond to the hard sphere collision limit although this limit is estimated to be about a factor of two larger (13 $Å^2$, using an atomic radius for Gd and O of 0.960 Å and 0.450 Å,[64] respectively, and r(O-O) of 1.208 Å[65]) than

the observed cross section. The delayed onset in the decline of the GdO^+ cross section suggests an impulsive reaction mechanism, where only a fraction of the available CM collision energy is converted into internal energy in the reaction. A simple impulsive model is the spectator stripping model (SSM),[61] in which the ion is assumed to react with only one of the atoms in the diatomic neutral while the other atom remains a "spectator" and maintains its velocity during the reaction. The kinetic energy of the products is determined from linear momentum conservation and the internal energy deposited into GdO^+ equals the BDE at a significantly larger collision energy than D_0(O-O).[61] SSM predicts that this will occur at a collision energy of 9.39 eV, in good agreement with the onset of the decline in the GdO^+ cross section, Figure 4.1.

4.5.2 Gd^+ reaction with O_2 to form GdO_2^+. In the reaction between Gd^+ and O_2, the GdO_2^+ product is also observed, although it is formed with a relatively low abundance. Its energy-dependent cross section is shown in Figure 4.1a at two different O_2 pressures. In contrast to the results for the GdO^+ cross section, the magnitude of the GdO_2^+ cross section exhibits a clear pressure dependence with a cross section larger by about a factor of two for the higher O_2 pressure. This indicates that GdO_2^+ is formed in a sequential reaction where the abundant GdO^+ product reacts with a second oxygen molecule to form GdO_2^+ via reaction (4.3). Thus, the GdO_2^+ cross section is more appropriately analyzed using the abundant GdO^+ product as the precursor ion, an approach that proved useful for the analogous reactions of Re^+ and Os^+.[26,29] Here, the CM energy scale is also reanalyzed assuming a reaction between GdO^+ and O_2. The reanalyzed GdO_2^+ cross sections at the two different O_2 pressures are shown in Figure 4.2 and exhibit no pressure dependence, which provides further evidence that GdO_2^+ is formed sequentially via reaction (4.3).

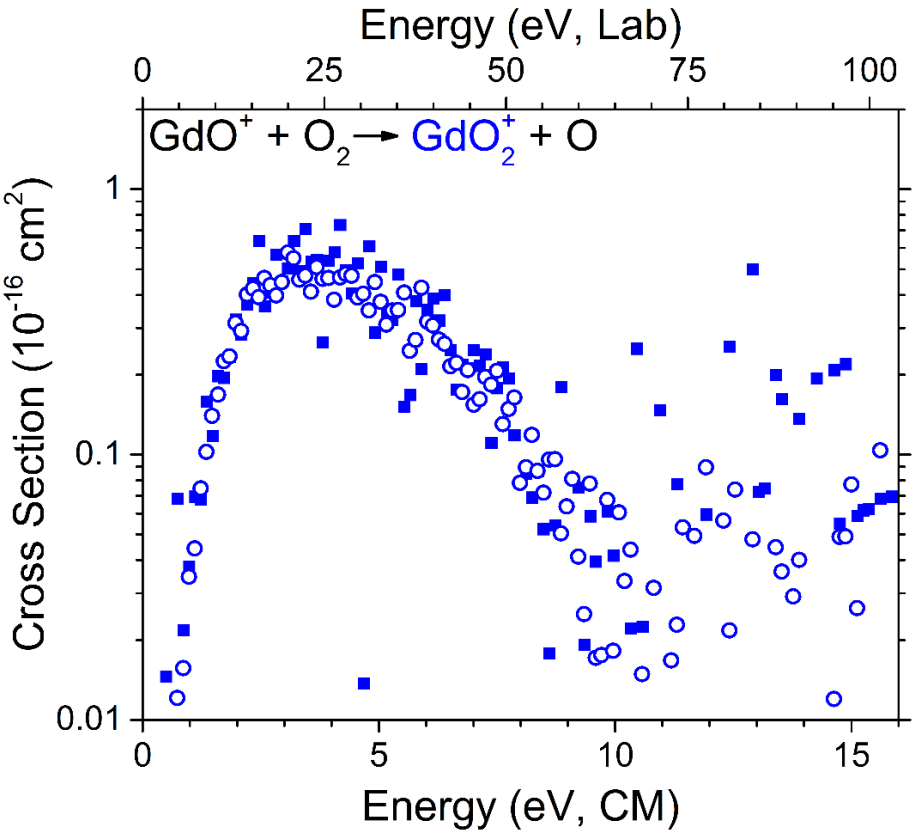

Figure 4.2. Estimated GdO_2^+ cross section from the reaction in Figure 4.1 reanalyzed using GdO^+ as the precursor ion in a sequential reaction with a second O_2 molecule as described in the text. Open circles and closed squares correspond to O_2 pressures of 0.29 and 0.15 mTorr, respectively.

4.5.3 GdO^+ exchange reaction with O_2 to form GdO_2^+ and O. The GdO^+ reaction with O_2 to form GdO_2^+ can be investigated directly by forming GdO^+ as a precursor ion in the source and reacting this ion at well-defined kinetic energies with O_2 in the reaction cell. The resulting energy dependent GdO_2^+ cross section is shown in Figure 4.3. In this reaction, the Gd^+ product is also formed via CID at higher energies (data not shown) and can be modeled to obtain a value for the GdO^+ BDE, as presented elsewhere.[7] The GdO_2^+ product has an apparent threshold of ~2 eV with its cross section peaking around 5 eV (consistent with the O_2 BDE) and declining as expected at energies exceeding D_0(O-O). The reanalyzed GdO_2^+ cross section from the sequential reaction, Figure 4.2, can

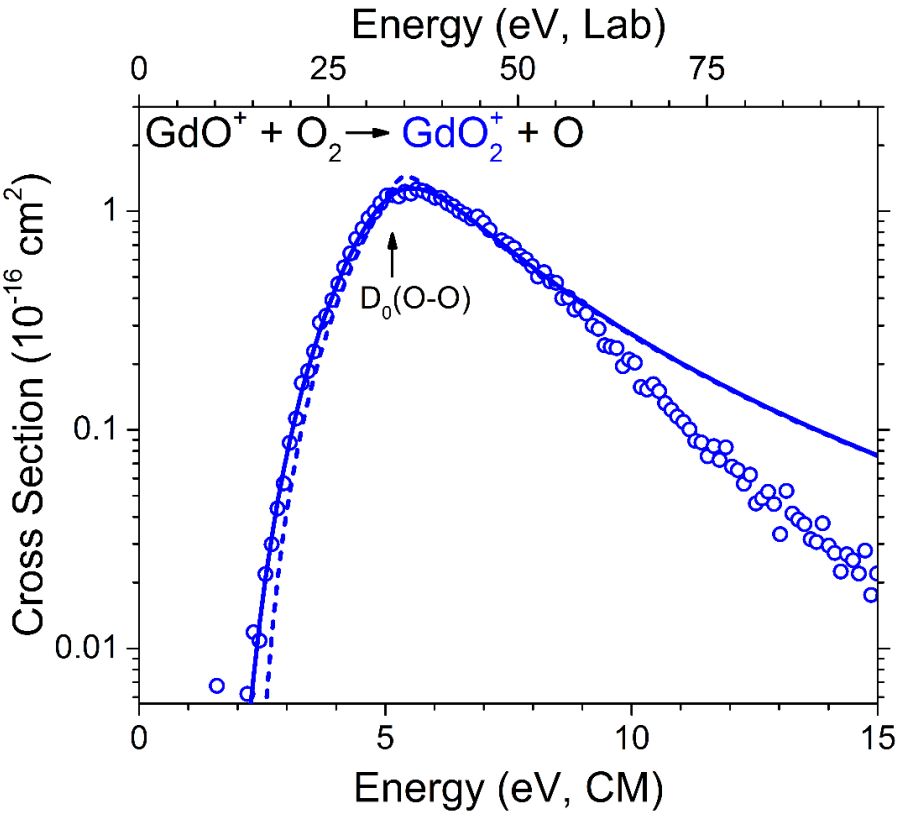

Figure 4.3 GdO_2^+ cross section as a function of center-of-mass (bottom *x*-axis) and laboratory (top *x*-axis) frame kinetic energy resulting from the direct reaction between GdO^+ and O_2 (open circles). The cross section for Gd^+ omitted here is presented and discussed elsewhere.[7] The arrow indicates the O-O BDE (5.12 eV). An optimized model for the GdO_2^+ cross section is indicated by the solid line, obtained by convolving equation (4.4) with the GdO^+ and O_2 kinetic energy distributions. The dashed line corresponds to the modeled GdO_2^+ cross section at 0 K by excluding convolution over reactant internal and kinetic energy distributions.

be compared with that measured in the direct exchange reaction, as shown in the Supporting Information, Section 4.7. There, the energy scale for the sequential reaction includes the 2.57 eV exothermicity of reaction (4.6) and the cross section has been scaled by a factor of 2.5 to match the magnitude of the GdO_2^+ cross section from the direct reaction. This scaling factor is a result of the shorter reaction path length (not accounted for in the cross section conversion) available for GdO^+ to react with a second O_2 in the sequential reaction. On average, this path length should be about a factor of two smaller,

consistent with the 2.5 scaling factor. Modeling the GdO_2^+ cross section from the direct reaction in Figure 4.3 yields a threshold energy of 2.27 ± 0.09 eV. $D_0(OGd^+\text{-}O)$ can be determined from this exchange reaction using the modeled E_0 value and expression (4.5), which gives a BDE of 2.85 ± 0.09 eV. The optimized modeling parameters for these data and for all other endothermic reactions are summarized in Table 4.1. In contrast, modeling the GdO_2^+ cross section from the sequential reaction with equation (4.4) as shown in the Supporting Information (Section 4.7) yields a threshold energy of 3.11 ± 0.13 eV (including the uncertainty from the exothermicity of reaction (4.6)), 0.84 eV larger than the threshold energy obtained for the direct reaction. This difference suggests that 0.84 eV (i.e., 33%) of the 2.57 eV exothermicity from reaction (4.6) is lost, probably as translational energy of the O atom product (which can be appreciable because of momentum conservation), and is thus not available to drive the sequential reaction of the GdO^+ product ion.

Table 4.1. Summary of optimized parameters obtained from modeling the experimental product ion cross sections with equation (4.4).[a]

Reaction	σ_0	n	E_0 (eV)
$GdO^+ + O_2 \rightarrow GdO_2^+ + O$	0.3 ± 0.1	2.9 ± 0.3	2.27 ± 0.09
$GdO^+ + O_2 \rightarrow GdO_2^+ + O$ (sequential)[b]	0.5 ± 0.1	2.6 ± 0.3	3.11 ± 0.13
$GdO_2^+ + Xe \rightarrow Gd^+ + O_2 + Xe$	0.5 ± 0.1	0.7 ± 0.2	0.75 ± 0.11
$GdO_2^+ + Xe \rightarrow GdO^+ + O + Xe$[c]	0.25 ± 0.05	0.8 ± 0.2	0.31 ± 0.07
$GdO_2^+ + Xe \rightarrow GdO^+ + O + Xe$[d]	0.6 ± 0.2	1.6 ± 0.2	2.90 ± 0.22

[a] Uncertainties correspond to one standard deviation.
[b] GdO_2^+ cross section (scaled by 2.5) from the sequential reaction.
[c] Low-energy feature.
[d] High-energy feature.

4.5.4 CID of GdO_2^+ with Xe. A BDE value for OGd^+-O can also be measured directly from CID of GdO_2^+ using Xe as collision gas. Two product ions, Gd^+ and GdO^+, are observed in these CID experiments, as shown in Figures 4.4a and 4.4b, respectively. The GdO^+ cross section exhibits two features, with apparent thresholds of ~0 and 2.5 eV, respectively, indicating the presence of two different GdO_2^+ precursor ion populations. To probe and alter the relative abundances of these GdO_2^+ precursor ion populations, the source conditions were changed by varying the DC discharge voltage used to produce Gd^+ ions. The effect of varying the DC discharge voltage on the magnitude of the Gd^+ and GdO^+ product ion cross sections from CID of GdO_2^+ is shown in Figure 4.4. Increasing the DC discharge voltage increases the Gd^+ cross section (Figure 4.4a) significantly while not changing the shape of the cross section (except above 7 eV). In contrast, the magnitude of the GdO^+ high-energy feature (Figure 4.4b) remains almost constant, whereas the GdO^+ low-energy feature exhibits a similar trend to that for the Gd^+ cross section with increasing DC discharge voltage. The results in Figure 4.4 can be explained by one precursor ion population that corresponds to Gd^+ bound to an oxygen molecule, i.e., a Gd^+-O_2 adduct, and the other to Gd^+ inserted between the two oxygen atoms, i.e., O-Gd^+-O. The Gd^+-O_2 adduct can dissociate by loss of O_2 (to form Gd^+) or by loss of O (to form GdO^+, low-energy feature), whereas O-Gd^+-O dissociates primarily by loss of O (to form GdO^+, high-energy feature). Increasing the DC discharge voltage generates more of the Gd^+-O_2 precursor ion relative to the inserted O-Gd^+-O species, which retains most of the population at all discharge voltages (otherwise the high-energy feature would decline in magnitude as the DC voltage was increased).

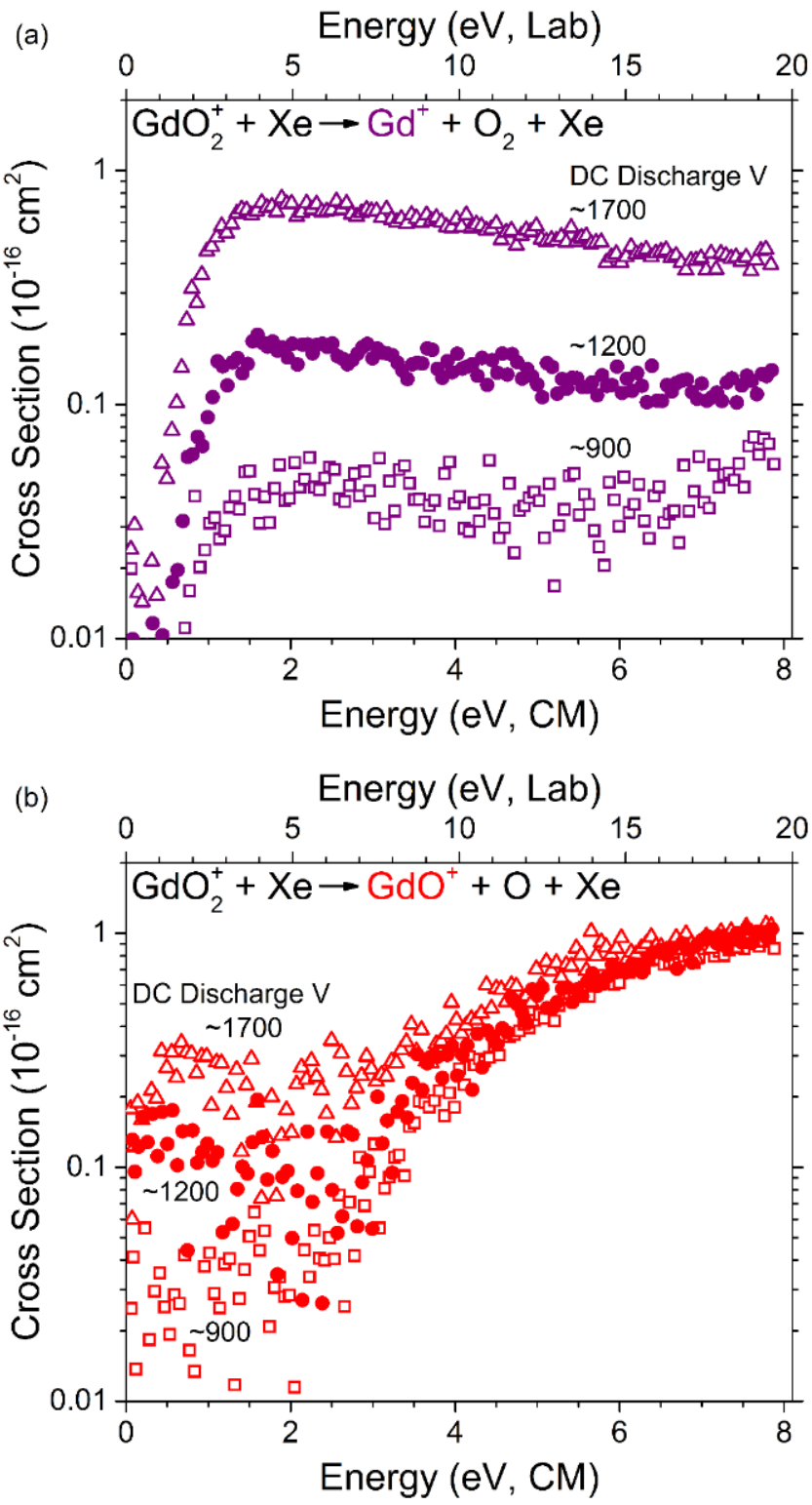

Figure 4.4. Effect of DC discharge voltage on the kinetic energy dependent product ion cross sections from CID of GdO_2^+ for (a) $Gd^+ + O_2$ and (b) $GdO^+ + O$ products. Solid symbols indicate the typical DC discharge voltage used to generate singly charged Gd^+ in the experiments.

4.5.5 Thermochemistry of O-Gd$^+$-O and Gd$^+$-O$_2$. A BDE of OGd$^+$-O can be obtained by modeling the high-energy GdO$^+$ feature using equation (4.4) as shown in Figure 4.5. This yields an E_0 and corresponding D_0 value of 2.90 ± 0.22 eV, which is consistent with that measured for OGd$^+$-O from the exchange reaction discussed above. Thus, the high-energy GdO$^+$ feature in the CID experiments arises from the dissociation of the same Gd$^+$ dioxide species that is formed in the exchange reaction (4.3). Combining these two independent BDE measurements through a weighted average gives D_0(OGd$^+$-O) = 2.86 ± 0.08 eV. This value is consistent with that of 2.60 ± 1.5 eV reported by Schofield[3]

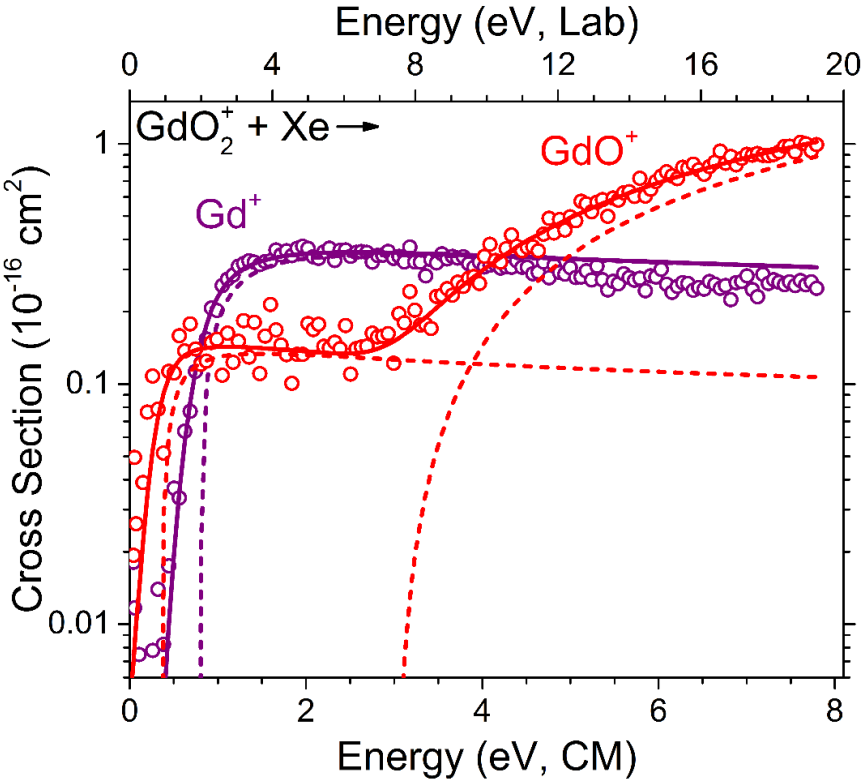

Figure 4.5. Product ion cross sections from CID of GdO$_2^+$ as a funciton of center-of-mass (bottom *x*-axis) and laboratory (top *x*-axis) frame kinetic energy obtained using a DC discharge voltage of ~1200 V. Optimized models for the GdO$^+$ and Gd$^+$ cross sections are indicated by the solid lines obained by convolving equation (4.4) with the reactant kinetic energy distributions. The dashed lines correspond to the modeled cross sections at 0 K obtained by excluding convolutions over the reactant internal and kinetic energy distributions.

as determined from a thermodynamic cycle. The BDE for Gd^+-O_2 is obtained by modeling the Gd^+ cross section (Figure 4.5), which yields $D_0(Gd^+\text{-}O_2) = 0.75 \pm 0.11$ eV.

4.5.6 Experimental potential energy surface (PES). The thermochemistry for GdO_2^+ measured here together with the GdO^+ BDE determined recently[7] can be used to construct a PES entirely from experiment for the reaction between Gd^+ and O_2 to form GdO^+ and O. This PES is shown in Figure 4.6. The energy level for the GdO^+ and O products relative to the Gd^+ and O_2 reactants is given by the reaction exothermicity, i.e., 2.57 ± 0.10 eV below reactants. The energy level for O-Gd^+-O relative to the GdO^+ + O level is determined from the BDE of the dioxide (2.86 ± 0.08 eV), and lies at 5.43 ± 0.13 eV below reactants. The energy level for Gd^+-O_2 relative to Gd^+ + O_2 equals the measured

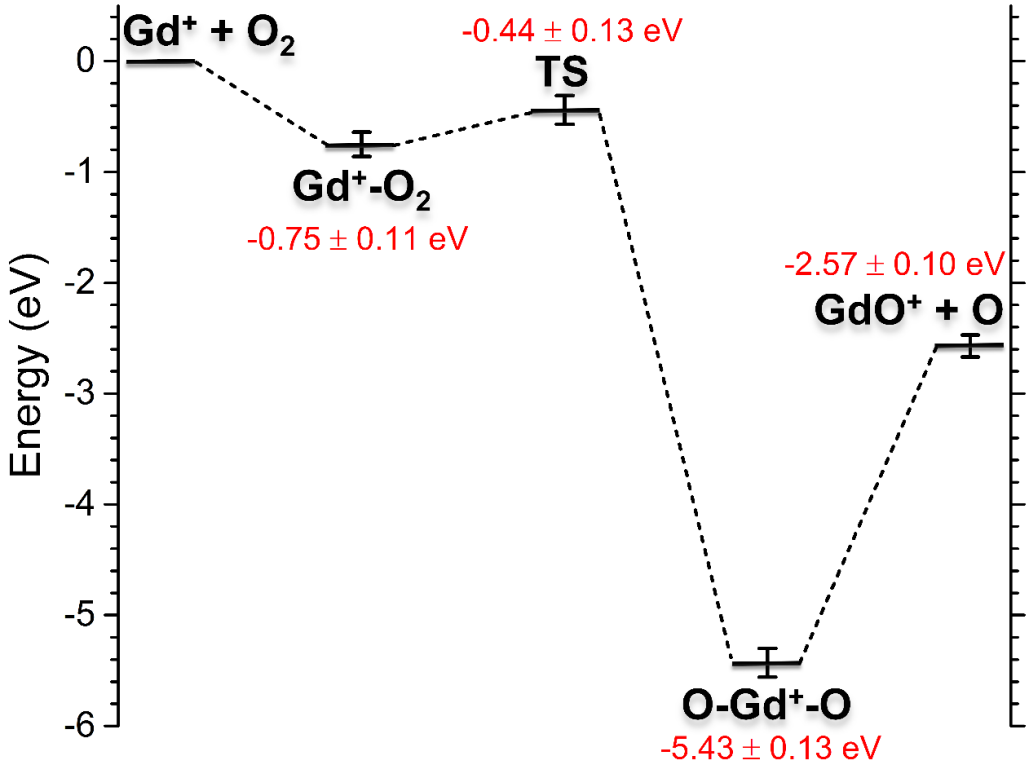

Figure 4.6. Potential energy surface for the Gd^+ reaction with O_2 determined from the GIBMS expeiments.

BDE of 0.75 ± 0.11 eV. Gd^+-O_2 can also dissociate by loss of a single oxygen atom. According to the PES in Figure 4.6, this process is exothermic; however, the low-energy GdO^+ feature in Figure 4.5 has a threshold, indicating that there must be a barrier to this process. This barrier height is determined from modeling the low-energy feature for this reaction with equation (4.4) as shown in Figure 4.5, giving a barrier height of 0.31 ± 0.07 eV (Table 4.1), such that the barrier lies 0.44 ± 0.13 eV below the $Gd^+ + O_2$ level (Figure 4.6).

4.5.7 Theoretical calculations for GdO_2^+. Theoretical calculations were performed to determine the ground and low-energy states for the Gd^+ dioxide species probed experimentally. Several different geometries and multiplicities for GdO_2^+ were explored at the B3LYP/ANO level of theory. The energies, electronic configurations, vibrational frequencies, bond lengths, and angles for stable GdO_2^+ species are summarized in the Supporting Information (Section 4.7). Figure 4.7 shows the molecular orbitals (mos) that are formed from the interactions between the valence electrons of Gd^+ (^{10}D, $4f^7 5d6s$) and O (^3P, $2p^4$) for different GdO_2^+ structures and electronic configurations. For simplicity, the seven 4f valence electrons of Gd^+ are omitted from Figure 4.7 as these form largely nonbonding mos similar to their atomic orbitals. Representative mos for the 4f electrons are shown in the Supporting Information (Section 4.7) for GdO_2^+ structures having $C_{\infty v}$, $D_{\infty h}$, and C_{2v} symmetry.

For an end-on linear Gd^+-O_2 adduct, with $C_{\infty v}$ symmetry and the z-axis defined along the internuclear axis, the $5d_z^2$ orbital of Gd^+ can interact with the $2p_z$ orbitals of the O atoms to form a 2σ bonding mo (Figure 4.7a). In- and out-of-phase combinations of the $2p_x$ and $2p_y$ orbitals on the two O atoms give rise to a 2π bonding and 3π antibonding set

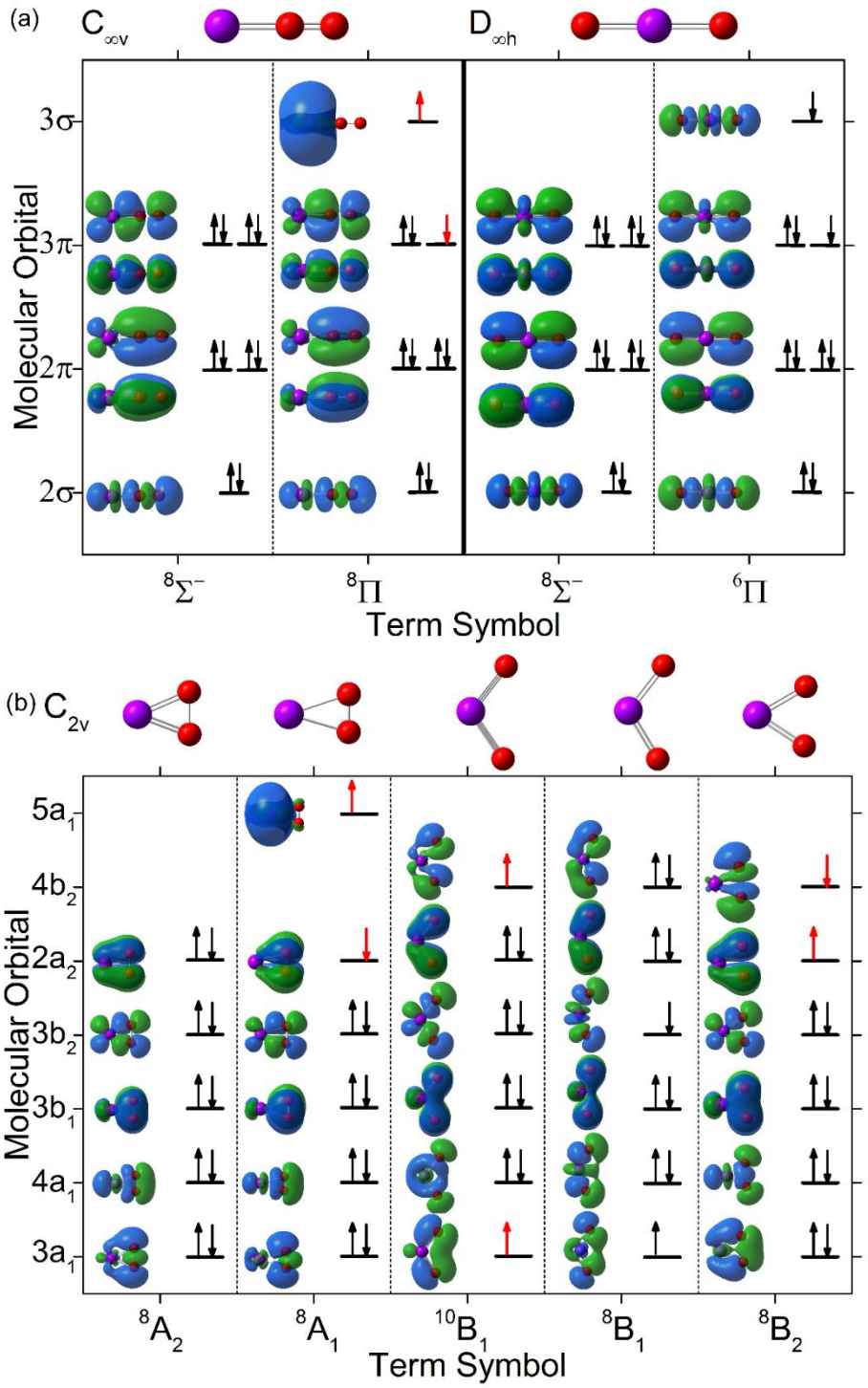

Figure 4.7. Electronic configurations and molecular orbitals resulting from the valence electrons of Gd^+ and O atoms for different GdO_2^+ species with (a) $C_{\infty v}$ and $D_{\infty h}$ symmetry and (b) C_{2v} symmetry as calculated at the B3LYP level of theory using the ANO basis set with the SDD ECP for Gd and the 6-311+G(3df) basis set for O. The nonbonding 4f electrons of Gd^+ are omitted for simplicity. The electronic configurations given are those for a multiplicity of 8 unless otherwise noted, with electrons indicated in red resulting in states with multiplicities of 10 or 6 if both these electrons are spin up or down, respectively.

of orbitals (similar to those in a free O_2 molecule), respectively, which combine in-phase with the Gd^+ $5d_{xz}$ and $5d_{yz}$ orbitals for π bonding interactions with the metal cation. The 6s valence electron of Gd^+ can also remain in this orbital resulting in a mainly nonbonding 3σ mo. The calculations indicate that the linear Gd^+-O_2 adduct has a Π ($2\sigma^2 2\pi^4 3\pi^3 3\sigma^1$) ground state with a multiplicity of 8 or 10 being practically the same energy (difference of only 0.004 eV, 1.93 eV below the Gd^+ and O_2 ground state reactants), where the unpaired 3π electron can be low or high spin coupled to the 4f electrons (Figure 4.7). These states are only 0.25 eV lower in energy than the $^8\Sigma^-$ ($2\sigma^2 2\pi^4 3\pi^4$) state (Supporting Information, Section 4.7), where the 6s electron of Gd^+ has been promoted to a 5d orbital to more effectively interact with the 2p electrons of the O atoms (Figure 4.7a). The $^6\Pi$ state (low-spin coupling of the 4f electrons with both the 3π and 3σ unpaired electrons), which differs from the $^{10}\Pi$ and $^8\Pi$ states only in electron spin, is not significantly higher in energy at 0.33 eV above these states. The interaction between Gd^+ and O_2 is relatively weak in these adducts such that the O_2 bond length (ranging from 1.29 – 1.30 Å) is not significantly perturbed from that in unbound O_2 (1.21 Å).

For an inserted O-Gd^+-O dioxide with linear $D_{\infty h}$ symmmetry, the $5d_z^2$ orbital of Gd^+ combines with the $2p_z$ orbitals on the O atoms to form a 2σ bonding mo (Figure 4.7a). A bonding set of 2π orbitals are formed from out-of-phase $2p_x$ and $2p_y$ orbitals on the two O atoms that combine in-phase with the Gd^+ $5d_{xz}$ and $5d_{yz}$ orbitals. Combining the $2p_x$ and $2p_y$ orbitals in-phase with a small amount of 4f character on Gd^+ gives largely nonbonding 3π orbitals. A 3σ bonding mo is formed from an out-of-phase combination of the $2p_z$ orbitals on the O atoms with the $4f_z^3$ orbital on Gd^+. The calculations yield only a couple of electronic states with stable inserted linear O-Gd^+-O geometries that correspond to

minima. These are the closed shell $^8\Sigma^-$ ($2\sigma^2 2\pi^4 3\pi^4$) state (where a structure with unequal bond lengths is found to be 0.13 eV lower in energy than that with equal bond lengths) and the $^6\Pi$ ($2\sigma^2 2\pi^4 3\pi^3 3\sigma^1$) state (Figure 4.7a, Supporting Information, Section 4.7), which has similar energy to the symmetric $^8\Sigma^-$ state. The corresponding $^{10}\Pi$ and $^8\Pi$ states resulted in optimizations with two imaginary bending frequencies.

Allowing the O-Gd^+-O angle to vary gives the global minimum GdO_2^+ structure having an O-Gd^+-O angle of ~45° and Gd^+-O bond lengths of 1.96 Å with an $^8A_2$ electronic state (Figure 4.7b, Supporting Information, Section 4.7). In this cyclic structure, the bond distance between the two oxygen atoms is 1.49 Å, larger than the bond length in a free oxygen molecule of 1.21 Å. Here, O-Gd^+-O is defined to lie in the yz plane with C_{2v} symmetry along the z-axis. In the $^8A_2$ ground state, the $2p_y$ orbitals of the O atoms mainly combine to form a bonding $3a_1$ mo similar to the bonding σ mo in O_2 (Figure 4.7b). Combining the $2p_z$ and $2p_x$ orbitals of the O atoms in-phase results in orbitals similar to the π bonding orbitals in free O_2. These combine with the $5d_z^2$ and $5d_{xz}$ orbitals of Gd^+, respectively, to form bonding $4a_1$ and $3b_1$ mos. Two additional bonding mos, $3b_2$ and $2a_2$, are formed by combining the $5d_{yz}$ and $5d_{xy}$ orbitals of Gd^+ with out-of-phase $2p_z$ and $2p_x$ orbitals of the O atoms, respectively. These out-of-phase combinations of the $2p_z$ and $2p_x$ orbtials result in mos between the two O atoms similar to the π antibonding orbitals in free O_2. Other low-energy O-Gd^+-O structures are found at excitation energies of about ~1.4 eV above the $^8A_2$ ground state having $^{10}A_1$, $^8A_1$, $^{10}B_1$, $^8B_1$, and $^6B_1$ electronic states (Supporting Information, Section 4.7). The GdO_2^+ structures having A_1 electronic states resemble cyclic side-on O_2 adducts with O-Gd^+-O angles of ~35° and O-O bond distances of ~1.32 Å. Here, one of the $2a_2$ electrons has moved to occupy a $5a_1$ nonbonding mo

comprising mainly the 6s atomic orbital of Gd^+, and the $2a_2$ electron can be either high or low-spin coupled with the 4f electrons. For the B_1 states, the O-Gd^+-O angles are much greater, ~110° for multiplicities of 6 and 10 and ~137° for the octet spin. This moves the oxygen atoms apart sufficiently that they no longer interact strongly. In the $^6B_1$ and $^{10}B_1$ states, an electron from the slightly bonding $3a_1$ mo has moved to occupy a $4b_2$ mo corresponding to the slightly antibonding version of the $3a_1$ mo (Figure 4.7b). For a multiplicity of 8, the $4b_2$ mo is fully occupied with only one electron occupying the $3b_2$ mo (Figure 4.7b). A B_2 electronic state is obtained by moving one of the $2a_2$ electrons to the $4b_2$ antibonding mo (Figure 4.7b). This state is about 2 eV higher in energy than the $^8A_2$ ground state for a multiplicity of 8 and has an O-Gd^+-O angle of ~65°. For multiplicities of 6 and 10, the B_2 structures have one imaginary frequency and collapse to A′ states where the two Gd^+-O bond lengths differ slightly. Additional local minima with B_2 electronic states and muliplicities of 6, 8, and 10 are found for structures that resemble Gd^+-O_2 adducts rather than inserted dioxide species. These structures have bond angles of ~34° and Gd^+-O bond lengths of ~2.25 Å, where the mos have similar character to those shown in Figure 4.7b for the $^8A_1$ state. For a multiplicity of 10, the B_2 state is 3.5 eV higher in energy than the $^8A_2$ O-Gd^+-O ground state, whereas the corresponding B_2 states with multiplicities of 6 and 8 are both approximately 2.6 eV higher in energy than the ground state (Supporting Information, Section 4.7).

4.5.8 Theoretical PESs. To gain insight into the interactions between ground state Gd^+ (^{10}D) and O_2 ($^3\Sigma_g^-$) and the role of the various GdO_2^+ intermediates that lead to formation of ground state GdO^+ ($^8\Sigma^-$) and O (^3P) products, PESs where the O-Gd^+-O angle is varied were calculated. Resulting surfaces are separated into A′ and A″ symmetry and

are shown in Figures 4.8a and b, respectively. Ground state Gd^+ (^{10}D) can react with ground state O_2 ($^3\Sigma_g^-$) in spin-allowed processes to form GdO_2^+ intermediates with multiplicities of 8, 10, and 12. For intermediates with a multiplicity of 12, no additional covalent interactions can be formed and thus these will be higher in energy. For completeness, surfaces with states having a multiplicity of 6 were also considered. The results in Figure 4.8 indicate that the reaction of Gd^+ (^{10}D) with O_2 can be initiated by forming a linear Gd^+-O_2 adduct on $^{10}A'$, $^{10}A''$, $^8A'$, and $^8A''$ surfaces that are approximately 2 eV lower in energy than the reactants. A linear intermediate can also be formed on a $^{12}A'$ surface, which is only slightly below the energy of the ground state Gd^+ and O_2 reactants (Figure 4.8a). Along most of the surfaces with multiplicities of 8 and 10, there is a barrier of 0.1–0.2 eV (more clearly shown in the Supporting Information, Section 4.7) that occurs at an O-Gd^+-O angle of ~20° as Gd^+ begins to insert between the two oxygen atoms. At O-Gd^+-O angles of ~30°, the $^{10}A'$, $^8A'$, and $^8A''$ surfaces cross with the $^{10}A_1$, $^8A_1$, and $^8A_2$ surfaces, respectively, which lead to the minima of O-Gd^+-O discussed above (Figure 4.7, Supporting Information, Section 4.7). The high energy $^{10}B_2$ Gd^+-O_2 adduct can be formed from the crossing between the $^{12}A'$ and $^{10}B_2$ surfaces. The surfaces in Figure 4.8 indicate that ground state GdO^+ ($^8\Sigma^-$) and O (^3P) products, calculated as ~1.7 eV below reactants, can be formed via several low-energy intermediates and pathways that have no barriers exceeding the reactant asymptote, where the lowest such pathway is via the $^8A_2$ GdO_2^+ intermediate at ~4.2 eV below reactants. These results are consistent with the experimental observation of an efficient, barrierless, and exothermic reaction.

4.5.9 Comparison with experiment. The quantum chemical calculations provide insight into the electronic states of the GdO_2^+ intermediates probed experimentally. The

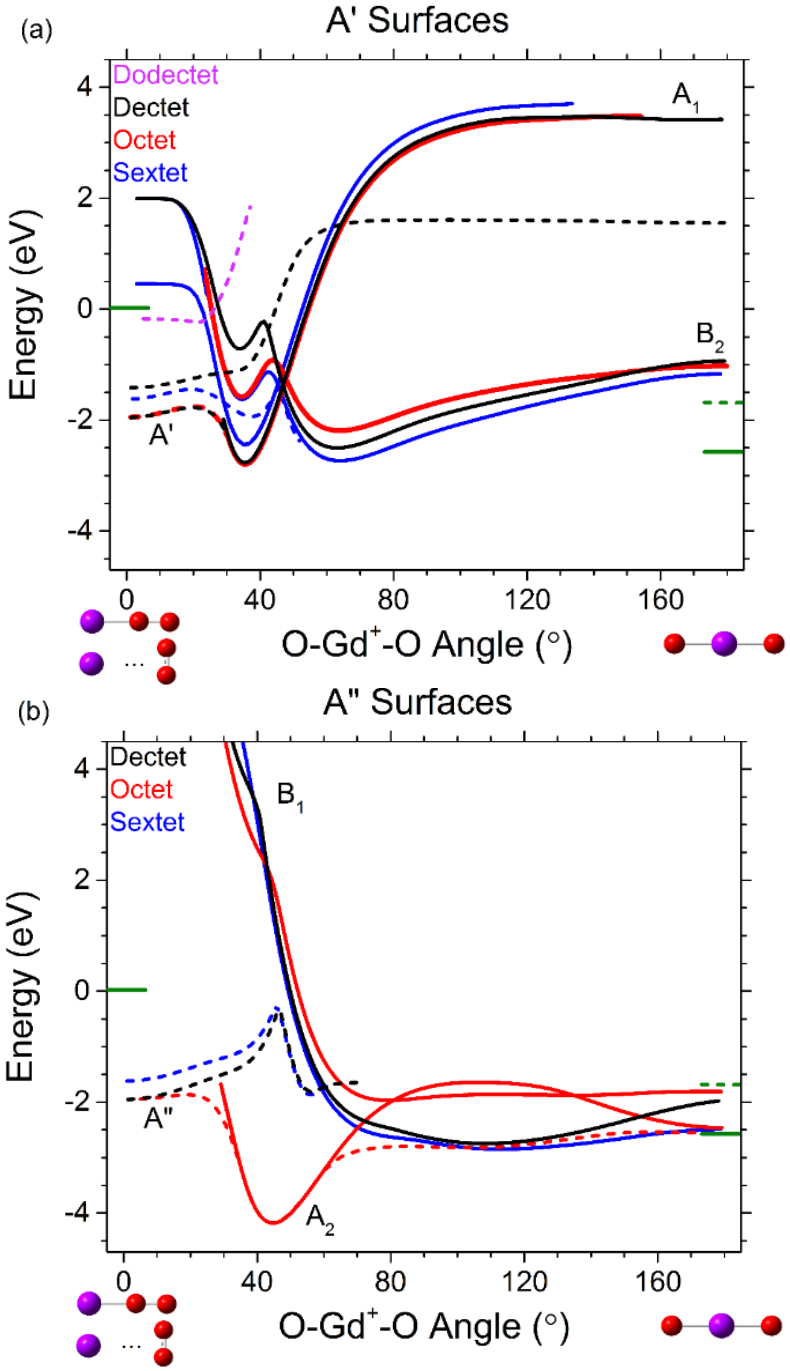

Figure 4.8. Relaxed potential energy surface scans as a function of the O-Gd^+-O angle calculated at the B3LYP level of theory using the ANO basis set with the SDD ECP for Gd and the 6-311+G(3df) basis set for O. These are separated into (a) A′ and (b) A″ surfaces. Hextet, octet, dectet, and dodectet surfaces are indicated by blue, red, black, and purple lines, respectively. Solid lines correspond to surfaces where GdO_2^+ maintains C_{2v} symmetry whereas dashed lines correspond to species with C_s symmetry. The solid and dashed green bars indicate the experimental and calculated exothermicities for reaction (4.6) at 2.57 and 1.70 eV, respecitvely.

O-Gd^+-O intermediate is easily identified from the calculations as the ground-state inserted cyclic dioxide having an $^8A_2$ electronic state. In contrast, the Gd^+-O_2 adduct is more difficult to assign. Linear or nearly linear end-on O_2 adducts having $^{10}A'$, $^{10}A''$, $^8A'$, or $^8A''$ electronic states are about 2 eV lower in energy than the reactants, thus having significantly higher Gd^+-O_2 BDEs than the measured value of 0.75 ± 0.11 eV. Furthermore, the barrier for loss of O from these adducts is at most 0.2 eV such that these adducts are likely to readily lose an O atom rather than O_2 upon activation (Supporting Information, Section 4.7). Similarly, the calculations predict that the side-on $^{10}A_1$, $^8A_1$, $^6A_1$, $^6B_2$, and $^8B_2$ O_2 adducts have much stronger Gd^+-O_2 BDEs than that measured experimentally. In contrast, the side-on adduct with a $^{10}B_2$ electronic state has a Gd^+-O_2 BDE calculated as 0.67 eV (Figure 4.8a, Table 4.2), consistent with the experimental BDE of 0.75 ± 0.11 eV. Additionally, there is a barrier along the $^{10}B_2$ surface of 0.45 eV, which is in relatively good agreement with the experimental value of 0.31 ± 0.07 eV for loss of an O atom. The CID experiments are thus likely probing this high energy $^{10}B_2$ Gd^+-O_2 adduct because this adduct will predominantly dissociate by loss of O_2, whereas other low-energy O_2 adducts will readily lose an O atom. These conclusions are supported by Rice-Ramsperger-Kassel-Marcus (RRKM) calculations (not shown), which demonstrate that the rate constant for loss of O_2 is a factor of 2 to 10 larger compared with O atom loss for the $^{10}B_2$ Gd^+-O_2 adduct, but the inverse is true for the $^8B_2$ Gd^+-O_2 adduct (as well as any lower lying state of the Gd^+-O_2 adduct).

It seems likely that several of these adduct states are formed experimentally, with increasing populations as the DC discharge voltage is increased, and might contribute to the observed dissociation behavior (Figure 4.4). This conclusion is further supported by

Table 4.2. Summary of experimental and calculated BDEs in eV for OGd^+-O and Gd^+-O_2, the transition state (TS) barrier for loss of O from Gd^+-O_2, and the exothermicity, $\Delta_rH(4.3)$, of reaction (4.3).

Level	Basis Set	OGd^+-O	Gd^+-O_2	TS	$\Delta_rH(3.3)$
Expt.		2.86 ± 0.08	0.75 ± 0.11	0.31 ± 0.07	-2.57 ± 0.10
B3LYP	ANO	2.46	0.67	0.45	-1.70
	cc-pVTZ-DK3	2.47	0.98[a]	0.42[a]	-1.95
	cc-pVQZ-DK3	2.47	1.00[a]	0.47[a]	-1.92
PBE0	ANO	2.72	0.68	0.57[b]	-1.71
	cc-pVTZ-DK3	2.48	0.96[a]	0.53[a,b]	-1.92
	cc-pVQZ-DK3	2.49	0.94[a]	0.54[a,b]	-1.89
CCSD(T,full)	ANO	2.34	0.81	0.49[c]	-2.08
	cc-pVTZ-DK3	2.59[c]	1.21[c]	0.41[c]	-2.33
	cc-pVQZ-DK3	2.73[c]	1.50[c]	0.40[c]	-2.59
	CBS[d]	2.81	1.67	0.39	-2.74

[a] Single point energy calculation using the geometry determined for the ANO basis set and the corresponding vibrational frequencies for the zero point energy correction.
[b] Zero point energy from the B3LYP calculation is used. The PBE0 calculation yields a significantly larger zero point energy as a result of a much larger frequency predicted for the TS structure (1170 vs. 4521 cm^{-1} at the B3LYP vs. PBE0 levels of theory, respectively) as summarized in the Supporting Information (Section 4.7).
[c] Single point energy calculation using the geometry at the B3LYP/ANO level and corresponding vibrational frequencies for the zero point energy correction.
[d] Complete basis set (CBS) limit.

the changes in the relative magnitudes of the cross sections for the GdO^+ low-energy feature (O atom loss) and Gd^+ product (O_2 loss) with DC discharge voltage (Figure 4.4). The Gd^+ cross section increases by a factor of ~4 when changing the DC discharge voltage from ~900 to 1200 V and 1200 to 1700 V (Figure 4.4a), whereas the low-energy GdO^+ feature only changes by a factor of ~2 for each voltage increase (Figure 4.4b). This behavior is consistent with the higher energy $^{10}B_2$ Gd^+-O_2 state becoming increasingly populated relative to lower energy O_2 adduct states as the DC discharge voltage is increased. This observation also suggests that the measured barrier to lose an O atom probably has contributions from the other Gd^+-O_2 intermediates that can be stabilized, Figure 4.7.

To investigate the possibility of other Gd^+-O_2 adducts that could explain the experimental data, additional relaxed PES scans were calculated at the B3LYP/ANO level for linear adducts where the bond distances were varied between an O_2 adduct and Gd^+ and between an O atom and GdO^+. These surfaces are shown in the Supporting Information, Section 4.7. No other intermediates were found besides the linear Gd^+-O_2 intermediates already discussed (Supporting Information, Section 4.7). Thus, the GdO_2^+ intermediates probed experimentally along the PES of the Gd^+ reaction with O_2 are assigned to a Gd^+-O_2 adduct and transition state (TS) with $^{10}B_2$ electronic states, and the inserted ground-state $^8A_2$ O-Gd^+-O complex. Mos for these intermediates as well as the GdO^+ ($^8\Sigma^-$) product are shown in Figure 4.9a. The $^{10}B_2$ TS has an imaginary frequency of 1713i cm^{-1} corresponding to an O-Gd^+-O bend that yields the inserted O-Gd^+-O intermediate by following this reaction coordinate. The B3LYP/ANO calculations perform quantitatively relatively well for the Gd^+-O_2 BDE and TS barrier, but underestimate the O-Gd^+-O BDE by ~0.4 eV and

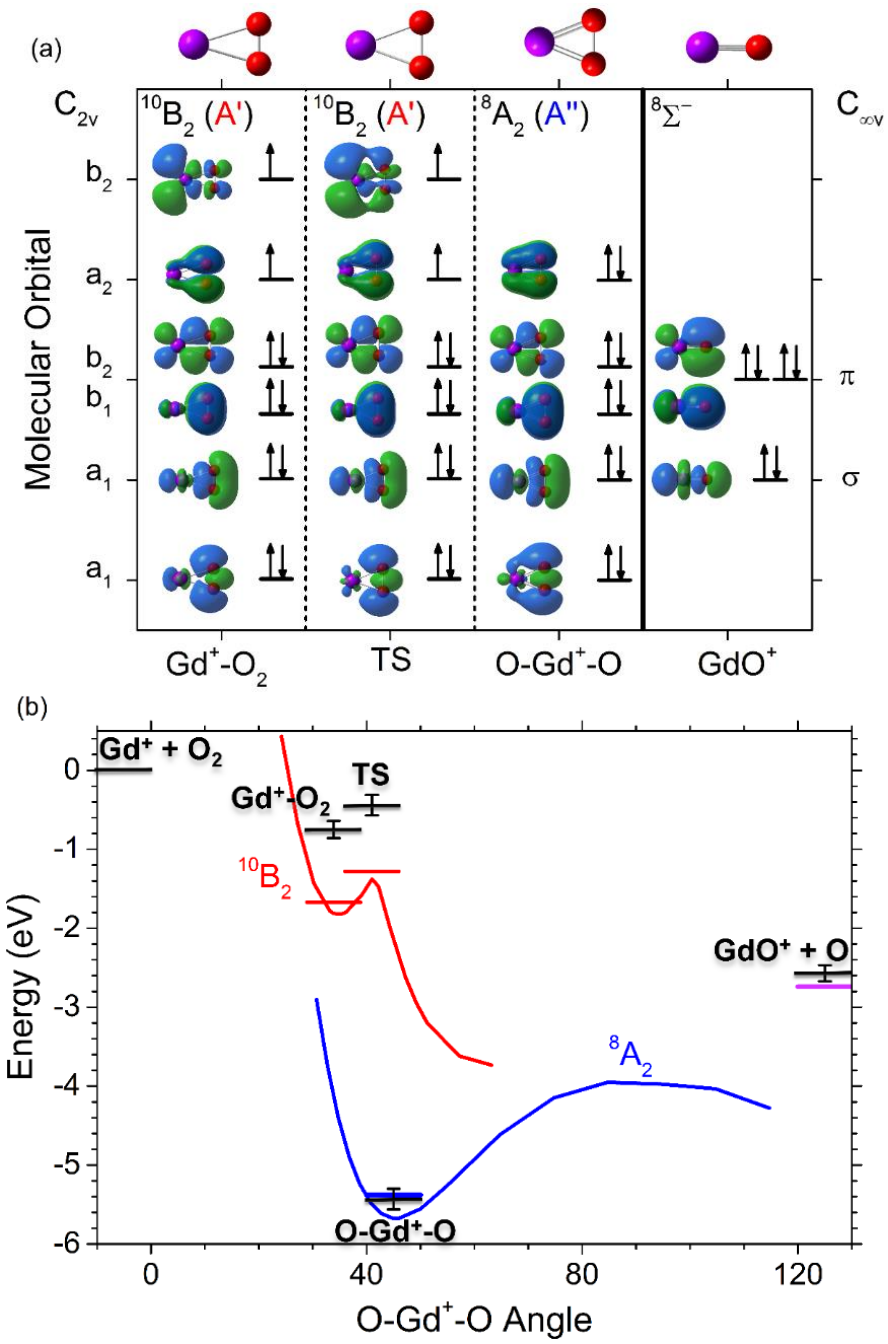

Figure 4.9. (a) Electronic states and molecular orbitals resulting from the valence electrons of Gd^+ and O atoms calculated at the B3LYP/ANO level for the GdO_2^+ intermediates probed in the experiments. (b) Complete basis set (CBS) extrapolated potential energy surfaces from single point energies at the CCSD(T)/cc-pVXZ-DK3//B3LYP/ANO level (where X = T and Q) as a function of O-Gd^+-O angle, where red and blue lines correspond to $^{10}B_2$ and $^8A_2$ surfaces, respectively. The energy levels for Gd^+-O_2 ($^{10}B_2$), the TS ($^{10}B_2$), O-Gd^+-O ($^8A_2$), and GdO^+ ($^8\Sigma^-$) and O (^3P) from the CBS extrapolation are shown by horizontal bars and include zero point energies from vibrational frequencies calculated at the B3LYP/ANO level. Experimentally determined energy levels are indicated by the black horizontal bars with associated uncertainties.

the exothermicity of the $Gd^+ + O_2$ reaction, $\Delta_rH(4.3)$, by ~0.9 eV, as summarized in Table 4.2. Additional calculations at the PBE0 and CCSD(T,full) levels of theory using the ANO basis set and the SDD ECP for Gd were performed for evaluation against the experimentally measured thermochemistry (Table 4.2). Calculations at the PBE0 level give significantly better agreement with experiment for the O-Gd^+-O BDE, but otherwise provide similar results to those at the B3LYP/ANO level for the Gd^+-O_2 adduct and $\Delta_rH(4.3)$ (Table 4.2). For the Gd^+-O_2 TS, signficiantly larger frequencies are predicted and appear to be overestimated at the PBE0 level compared with those at the B3LYP level as summarized in the Supporting Information (Section 4.7). This results in a larger zero point energy at the PBE0 level, which gives a TS barrier of 0.78 eV (Supporting Information, Section 4.7) in poor agreement with the experimental value of 0.31 ± 0.07 eV. If the frequencies from the B3LYP calculation are instead used for the zero point energy, a barrier height of 0.57 eV is obtained at the PBE0 level (Table 4.2), which agrees better with experiment. At the CCSD(T,full)/ANO level, the calculations predict a larger $\Delta_rH(4.3)$ (using our previous calculations[7] for GdO^+) in better agreement with experiment, but perform worse for the BDE of O-Gd^+-O than the calculations at the B3LYP and PBE0 levels (Table 4.2). In contrast, these calculations perform well in predicting the BDE for the Gd^+-O_2 adduct as 0.81 eV, which is consistent with experiment (0.75 ± 0.11 eV). A slightly larger value is predicted for the TS barrier at 0.49 eV compared with experiment (0.31 ± 0.07). This calculated TS barrier is obtained from a single point energy calculation using the optimized geometry and frequencies at the B3LYP level.

Previously, we found the all-electron cc-pVXZ-DK3 basis sets[53] (with X = T and Q) for Gd to provide better agreement with the measured GdO^+ BDE at the B3LYP and

PBE0 levels of theory.[7] These basis sets performed even better at the CCSD(T,full) level predicting BDEs of 7.35 and 7.65 eV (excluding an empirical spin-orbit correction, which lowers these values by 0.13 eV) for X = T and Q, respectively, compared with the experimental BDE of 7.69 ± 0.10 eV. Because the exothermicity of the Gd^+ reaction with O_2 is related to the BDE of GdO^+, these calculations also reproduce the experimental exothermicity well (Table 4.2). For the Gd^+ dioxide complexes, these calculations become exceedingly costly computationally. Converged geometries and vibrational frequencies were obtained only for the inserted O-Gd-O^+ ($^8A_2$) intermediate at the B3LYP and PBE0 levels of theory. These calculations became impractical for the Gd^+-O_2 adduct and TS, where single point energies are computed instead using the optimized geometries at the B3LYP or PBE0/ANO level of theory with zero point energy corrections determined from the corresponding frequencies of these optimized structures. The zero point energy calculations of the Gd^+-O_2 TS at the PBE0 level, utilize the frequencies of the TS determined at the B3LYP/ANO level because the frequencies at the PBE0 level appear to be overestimated. The BDEs for OGd^+-O obtained with the all-electron basis sets are similar to those determined from the more inexpensive calculations that utilize the ANO basis set and SDD ECP for Gd (Table 4.2). This is also the case for the TS barrier. In contrast, BDEs near 1 eV for the Gd^+-O_2 adduct are predicted with the all-electron basis sets compared with those using the ANO basis set at ~0.7 eV. These results indicate that, overall, the DFT calculations that utilize the all-electron Gd basis sets do not perform signficantly better than the more inexpensive calculations with the ANO basis set and SDD ECP.

At the CCSD(T,full)/cc-pVXZ-DK3 level, only single point energies are computed

for all Gd^+ dioxide complexes using the geometries at the B3LYP/ANO level. The single point energy calculations at the CCSD(T,full) level for the triple-ζ and quadruple-ζ basis sets yield OGd^+-O BDEs and exothermicites in relatively good agreement with the experimental values (Table 4.2). Extrapolating these values to the complete basis set (CBS) limit using the formula $E[CBS] = 1.577163 \cdot E[Q] - 0.577163 \cdot E[T]$[66] gives an exothermicity of 2.74 eV and an OGd^+-O BDE of 2.81 eV (Table 4.2), which compare favorably with the experimental values of 2.57 ± 0.10 eV and 2.86 ± 0.08 eV, respectively. This agreement is also demonstrated in Figure 4.9b, where $^{10}B_2$ and $^8A_2$ surfaces are constructed from CBS extrapolated single point energies and are compared with the experimental energy levels. The CCSD(T,full)/cc-pVXZ-DK3//B3LYP/ANO calculations overestimate the measured Gd^+-O_2 BDE of 0.75 ± 0.11 eV somewhat, yielding BDEs of 1.21 and 1.50 eV for X = T and Q, respectively, with a CBS extrapolated value of 1.67 eV (Table 4.2). This is also the case for the TS complex relative to the $Gd^+ + O_2$ reactant asymptote (Figure 4.9b). However, the TS barrier is reproduced well relative to the Gd^+-O_2 adduct, giving values at the CCSD(T,full)/cc-pVXZ-DK3//B3LYP/ANO level of 0.41 and 0.40 eV for X = T and Q, respectively, with a CBS extrapolated value of 0.39 eV, consistent with that from experiment of 0.31 ± 0.07 eV.

It is possible that the electronic state of the Gd^+-O_2 adduct has some multireference character (for example, this effect needs to be considered in calculations[67] for FeO_2^+ isomers). Such character is not taken into account in the present calculations and could contribute to the deviation in the theoretical BDEs compared with the experimental value. However, for the $^{10}B_2$ state of the Gd^+-O_2 adduct, the calculations here indicate that there is no significant spin-contamination (s(s+1) = 24.76, Supporting Information, Section 4.7)

at the DFT level to suggest a multiconfigurational nature. This is also consistent with the T1 diagnostics obtained for the $^{10}B_2$ state at the CCSD(T,full) level, which give values of 0.0163, 0.0130, and 0.0127 (i.e., less than 0.02) using the ANO, and cc-pVXZ-DK3 with X = T and Q basis sets for Gd, respectively.[68] The lower energy linear $^{10}\Pi$ and side-on $^{10}A_1$ Gd^+-O_2 adducts also do not show significant spin contamination at the DFT level (Supporting Information, Section 4.7), but their T1 diagnostics are slightly above 0.02 at the CCSD(T,full)/ANO level with values of 0.0241 and 0.0276, respectively. In contrast, the calculations using the all-electron Gd basis set have T1 diagnostics near or below 0.02 with vlaues for X = T (Q) of 0.0183 (0.0179) and 0.0210 (0.0190) for the $^{10}\Pi$ and $^{10}A_1$ Gd^+-O_2 adducts, respectively, consistent with the DFT spin-contamination results. The T1 evaluations, especially those for the all-electron Gd basis sets, suggest that a multi-reference treatment is not necessary and thus such calculations were not pursued.

In the quantum chemical calculations, the energy obtained for a given electronic state corresponds to an average energy over all the spin-orbit (SO) levels for that state. In contrast, the experiments here measure the energy difference between the ground state SO level of the reactants and that of the products. Thus, for a more accurate comparison with experiment, the calculated energies of the reactant and product ground states should be corrected to reflect the energies of the lowest SO levels. This can be performed by employing an empirical first-order SO energy correction as described in detail elsewhere.[7] On this basis, the calculated OGd^+-O BDEs would need to be corrected only for the SO averaged energy of O (0.01 eV for the ^3P ground state), because the ground states for OGd^+-O ($^8A_2$) and GdO^+ ($^8\Sigma^-$) have zero orbital angular momentum and thus have no first-order SO splittings. Similarly, the calculated $Gd^+ + O_2$ reaction exothermicities should be

lowered by 0.11 eV as a result of the SO averaged energies of Gd^+ (0.12 eV for the ^{10}D ground state) and O. However, including this SO correction yields worse agreement with experiment. Assuming a side-on $^{10}B_2$ Gd^+-O_2 adduct, the empirical SO correction for this state is zero. Thus, the calculated BDEs for Gd^+-O_2 need to only be corrected for the SO averaged energy of Gd^+ and should be lowered by 0.12 eV. This would provide better agreement with experiment. The TS complex has no first-order SO corrections such that the calculated TS barrier is unaffected. Overall, the SO corrections to the theoretical values discussed here are not significant and cannot alone explain any discrepancies between the calculated and experimental thermochemistry.

4.5.10 Periodic trends. Compared with most lanthanide cations, which have ground state valence electron configurations of $4f^n6s^1$ (where n corresponds to the number of remaining valence electrons), Gd^+ is unusual with its $4f^75d^16s^1$ ground state configuration. Gd^+ is in this regard more similar to the group 3 transition metals Sc^+ ($3d^14s^1$) and Y^+ ($5s^2$ ground state, with $4d^15s^1$ only 0.15 eV higher in energy) and the lanthanides La^+ ($5d^2$) and Lu^+ ($4f^{14}6s^2$) with empty and completely filled 4f shells. Effective binding in metal oxide cations can be achieved from interaction of two d electrons on the metal cation with the four 2p valence electrons of the oxygen atom to form a triple bond [σ^2 π^4]. Achieving this d^2 reactive configuration in most lanthanide cations requires promotion of 4f and 6s electrons to 5d orbitals and correspondingly it has been shown that the Ln^+-O bond strength[69] and reactivity[60] with O_2 correlates inversely with this promotion energy. In contrast, Gd^+, like Sc^+ and Y^+ ($4d^15s^1$ low-lying excited state), requires promotion of a single s electron and thus has a similar oxide BDE[7] and exhibits similar reactivity[60,70] with O_2 as these metal cations, while differing from La^+ and Lu^+, which

require promotion of zero and two 6s electrons, respectively (Figure 4.10). The ground state MO^+ electronic configurations for these metals have no unpaired valence electrons (except the 4f electrons of Gd^+).

To form the dioxide species, the additional oxygen atom that binds to MO^+ must interact through donation of its available 2p electrons into d orbitals of the metal cation. There is no promotion energy cost for forming a second oxide BDE and thus $D_0(OM^+\text{-}O)$ for these metal cations should be similar. A comparison of the experimentally determined dioxide BDEs for these metal cations is shown in Figure 4.10 and indicates that there are

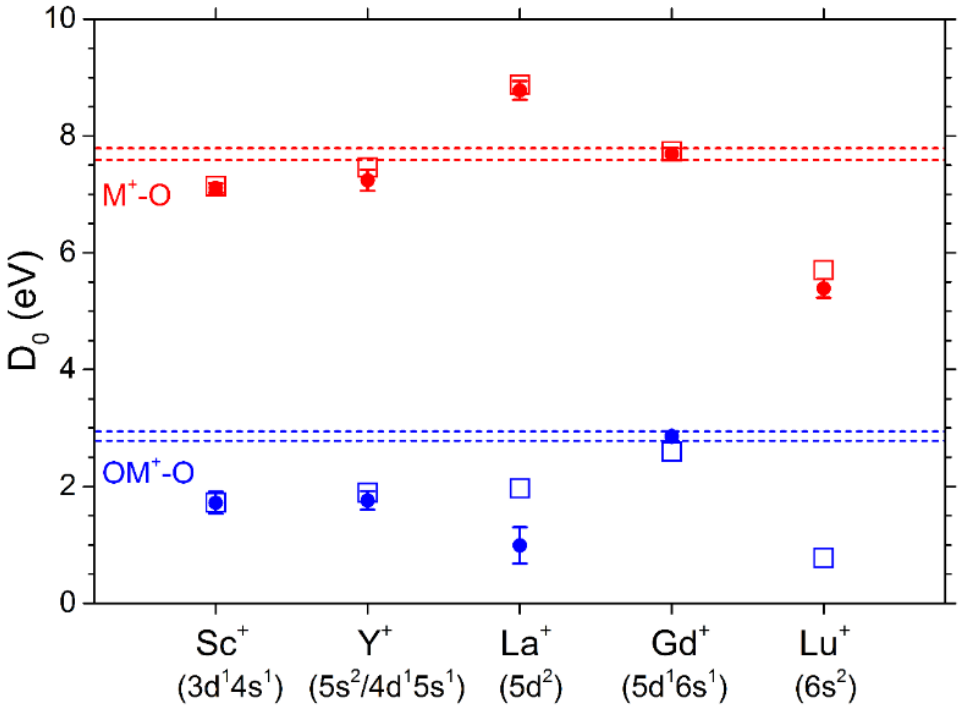

Figure 4.10. Experimental M^+-O and OM^+-O BDEs for the group 3 metal cations including the lanthanides with an empty (La^+), half (Gd^+), and completely filled (Lu^+) 4f shell. The solid circles for the OGd^+-O and Gd^+-O BDEs are from GIBMS results presented here and elsewhere,[7] respectively. Dashed lines corresponding to the uncertainty in the BDEs of the Gd^+ complexes are used as guides to the eye. The solid circles for the Sc^+-O and Y^+-O BDEs are obtained from references 14 and 20, and those for La^+-O and Lu^+-O are from reference 69. Dioxide BDEs indicated by the solid circles are obtained from reference 17. The M^+-O and OM^+-O BDEs designated by the open squares are from reference 3.

differences. Sc^+ and Y^+ have similar dioxide BDEs, which are slightly smaller than the OGd^+-O BDE measured here. The BDEs for La^+ and Lu^+ are even smaller (as indicated by the GIBMS measurement[17] for La^+). Laser ablation studies[71,72] of various metals with O_2 in argon matrices identify the ground state structures for ScO_2^+ and YO_2^+ to be the cyclic $^1A_1$ structures with O-M^+-O angles close to 45°, similar to the $^8A_2$ ground state structure found for O-Gd^+-O here. For LaO_2^+, the laser ablation experiments indicate the presence of both a cyclic and linear inserted structure with calculations predicting the cyclic $^1A_1$ structure to be more stable than the linear $^1\Sigma_g^+$ structure.[71] In contrast, recent theoretical work reports the ground state structure for LaO_2^+ to be the linear inserted species ($^1\Sigma_g^+$); although it is unclear whether a cyclic structure was considered.[73] For GdO_2^+, the corresponding linear inserted $^8\Sigma^-$ structure is calculated to be significantly higher in energy at 1.7 eV above the $^8A_2$ ground state (Supporting Information, Section 4.7). A different geometry for LaO_2^+ could explain its lower BDE relative to the values for ScO_2^+, YO_2^+, and GdO_2^+. The lower BDE for LuO_2^+ suggests that this dioxide potentially also has a different structure. Differences in geometries could arise from differences in orbital overlap and effects of filling the 4f shell in the lanthanides, where occupation of the 6s orbital becomes energetically favored over the 5d orbital with increasing number of 4f electrons.

4.6 Conclusions

The BDEs for OGd^+-O and Gd^+-O_2 have been measured using GIBMS to be 2.86 ± 0.08 eV and 0.75 ± 0.11 eV, respectively. These are the first direct experimental BDEs for these Gd^+ dioxide species. Additionally, the barrier height for rearrangement of the Gd^+-O_2 adduct to an inserted dioxide (as evidenced by loss of a single oxygen atom) is

measured to be 0.31 ± 0.07 eV. From these results, the PES for the Gd^+ reaction with O_2 is constructed entirely from experiment. Theoretical calculations indicate that O-Gd^+-O has a cyclic ground state structure with an O-Gd^+-O angle of ~45° and an $^8A_2$ electronic state. This assignment is additionally supported by single point energy calculations at the CCSD(T,full)/cc-pVQZ-DK3//B3LYP/ANO level of theory, which yield an OGd^+-O BDE in good agreement with the experimental value. In contrast, the Gd^+-O_2 adduct is more difficult to assign. The calculations indicate that there are several low-energy Gd^+-O_2 adducts that can be formed, but O atom loss is energetically favored over O_2 loss upon activation for these complexes such that they should yield the GdO^+ product ion. The CID experiments are thus likely probing a higher energy Gd^+-O_2 adduct for which O_2 loss is energetically competitive with and entropically favored over O atom loss. One such complex identified by the calculations is a side-on Gd^+-O_2 adduct with a $^{10}B_2$ electronic state. This intermediate is also located in a well with a barrier that has a height consistent with the experimental barrier observed for loss of O from the Gd^+-O_2 adduct. Furthermore, the thermochemistry measured for this intermediate is in relatively good agreement with the theoretical calculations. The extensive experimental thermochemistry obtained here for the $Gd^+ + O_2$ reaction can serve as useful benchmarks in evaluating and improving theoretical methods.

The cyclic O-Gd^+-O ground state geometry is similar to that suggested in the literature for ScO_2^+ and YO_2^+, but contrasts with a linear inserted structure predicted for LaO_2^+, and could explain the similarities and differences in the dioxide BDEs between these metal cations. The difference in geometry between the La^+ and Gd^+ dioxides is interesting and, if real, could arise from effects of filling the 4f shell, which alter the relative

energetics of the 5d and 6s orbitals. Similar to our recent findings[7] for GdO^+, GdC^+, and $GdCO^+$, these results support the conclusion that Gd^+ behaves more similarly to Sc^+ and Y^+ than most of the lanthanide cations. On the basis of these results, Sc^+ and Y^+ should thus exhibit similar PESs with O_2 to that measured here for Gd^+.

The BDE measured for OGd^+-O at 2.86 ± 0.08 eV is relatively large indicating that reaction (4.2) will be significantly exothermic and could proceed efficiently in the atmospheric chemical release experiments. This sequential reaction might thus have some implications in the atmospheric experiments and could potentially compete with reaction (4.1) for available oxygen atoms to reduce the efficiency in generating electron density. The thermochemistry of the metal dioxide could therefore be important in evaluating possible candidates for the Air Force experiments.

4.7 Supporting Information

4.7.1 Comparison of GdO_2^+ cross sections from direct and sequential reactions. In the reaction between Gd^+ and O_2, the GdO_2^+ product is observed in addition to the abundant GdO^+ product formed in an exothermic and barrierless reaction. As discussed in detail above, the GdO_2^+ product is formed in a sequential reaction where the GdO^+ product reacts with a second O_2 molecule. This cross section can be reanalyzed using the GdO^+ product as the precursor ion and by accounting for the different center-of-mass energy scale of the new reactants. The reanalysis yields a GdO_2^+ cross section that is about a factor of 2.5 smaller than the GdO_2^+ cross section measured in the direct reaction between GdO^+ and O_2 to form GdO_2^+, Figure 4.3. This is attributed to GdO^+, in the sequential reaction, having a reaction path length that is on average half that in the direct reaction (not

accounted for in the analysis), which is in fairly good agreement with the 2.5 scaling factor needed. A comparison of the GdO_2^+ cross sections from the direct and sequential reactions (where that from the sequential reaction has been scaled by 2.5) is shown in Figure 4.11. The energy scale for the sequential reaction includes the 2.57 eV exothermicity to form GdO^+ from the Gd^+ reaction with O_2. However, as described above, not all of this exothermicity goes into internal energy that is available in the sequential reaction to form

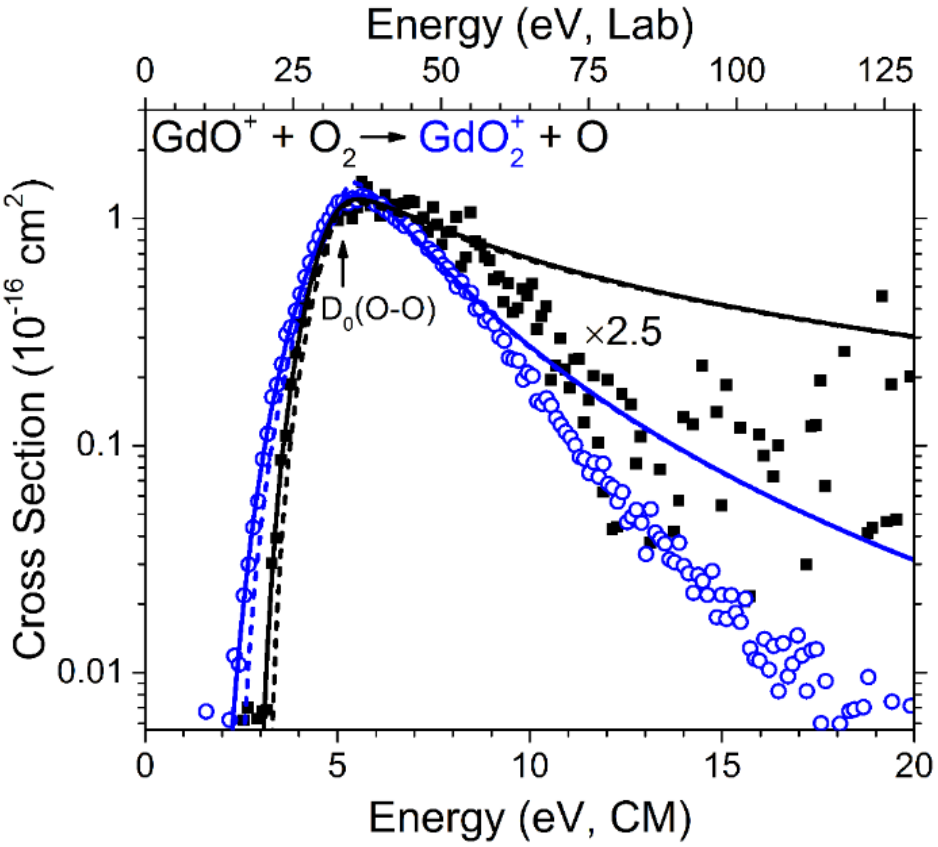

Figure 4.11. Comparison of the GdO_2^+ cross sections from the direct (open circles) and sequential reactions (filled squares) between GdO^+ and O_2 as a function of center-of-mass (bottom *x*-axis) and laboratory (top *x*-axis) frame kinetic energy. The GdO_2^+ cross section from the sequential reaction has been scaled up by 2.5 and the energy scale includes the 2.57 eV exothermicity for reaction (4.6). The arrow indicates the O-O BDE (5.12 eV). Optimized fits are indicated by the solid lines, obtained by convolving equation (4.4) with the GdO^+ and O_2 kinetic energy distributions. The dashed lines correspond to the modeled GdO_2^+ cross sections at 0 K by excluding convolution over reactant internal and kinetic energy distributions.

GdO_2^+, as evident from the different onsets in Figure 4.11. The threshold energy for GdO_2^+ from the sequential reaction is overestimated as a result of including all of the exothermicity in the energy scale. Thus, the difference between the two thresholds obtained from modeling the cross sections in Figure 4.11 should correspond to the average fraction of the exothermicity that is lost to translational energy of the O atom product and therefore not available in the sequential reaction. This energy difference is 0.84 eV, suggesting that about 33% of the 2.57 eV exothermicity remains in O translation.

4.7.2 GdO_2^+ structures and electronic states. Extensive quantum chemical calculations to determine the ground and excited states for GdO_2^+ were performed using the atomic natural orbital[45] (ANO) basis set with the relativistic Stuttgart Dresden[44] (SDD) effective (28 electron) core potential (ECP) for Gd and the Pople 6-311+G(3df) basis set for O. The bond lengths, angles, vibrational frequencies, and energies for these GdO_2^+ structures and electronic states are summarized in Table 4.3. These states and structures are discussed above with representative molecular orbitals (mos) that give rise to the bonding interactions shown in Figure 4.7. The mos for the seven 4f electrons of Gd^+ were omitted from Figure 4.7 as these form mainly nonbonding mos similar to their atomic orbitals. Representative mos for these 4f electrons are shown in Figure 4.12 for linear (Gd^+-O_2 and O-Gd^+-O) and bent (O-Gd^+-O angles of ~45° and 110°) geometries with $C_{\infty v}/D_{\infty h}$ and C_{2v} symmetry, respectively. Relaxed potential energy scans of the GdO_2^+ species separated into A′ and A″ surfaces as a function of O-Gd^+-O angle are shown in Figure 4.8 and discussed in detail above for insight into the mechanism of the exothermic reaction between Gd^+ and O_2. A graph expanded over the region near the barriers along the ^{10}A′, ^{10}A″, ^{8}A′, and ^{8}A″ surfaces for insertion of Gd^+ into the O-O bond of linear Gd^+-O_2 adducts

Table 4.3. Electronic configurations, optimized geometries, vibrational frequencies, and energies for various Gd^+ dioxide states calculated at the B3LYP level of theory using the ANO basis set and SDD ECP for Gd and the 6-311+G(3df) basis set for O.

Species	State	Configuration[a]	s(s+1)[b]	∠O-Gd^+-O (°)	r(Gd^+-O) (Å)	r(O-O) (Å)	Vibrational Frequencies (cm^{-1})[c]	E (E_h)	E_{rel} (eV)
O-Gd^+-O	$^8A_2$	$3a_1^2 3b_1^2 4a_1^2 3b_2^2 2a_2^2$	15.77	44.71	1.962	1.492	561, 592, 865	-915.898116	0.00
	$^{10}B_2$[d]	$3a_1^2 3b_1^2 4a_1^2 3b_2^2 2a_2^1 4b_2^1$	24.79	63.20	2.001	2.097	1175i, 343, 682	-915.836355	1.62
	$^8B_2$	$3a_1^2 3b_1^2 4a_1^2 3b_2^2 2a_2^1 4b_2^1$	16.76*	63.85	1.995	2.110	328, 447, 682	-915.824923	1.96
	$^6B_2$[d]	$3a_1^2 3b_1^2 4a_1^2 3b_2^2 2a_2^1 4b_2^1$	10.79*	63.99	1.994	2.113	615i, 329, 664	-915.844874	1.39
	$^{10}A'$	$3a_1^2 3b_1^2 4a_1^2 3b_2^2 2a_2^1 4b_2^1$	24.77	67.49	2.165 1.885	2.262	170, 335, 695	-915.841422	1.50
	$^6A'$	$3a_1^2 3b_1^2 4a_1^2 3b_2^2 2a_2^1 4b_2^1$	10.77*	68.48	2.128 1.896	2.272	165, 352, 678	-915.847697	1.32
	$^{10}B_1$	$3a_1^1 3b_1^2 4a_1^2 3b_2^2 2a_2^2 4b_2^1$	24.76	108.18	2.032	3.292	143, 570, 595	-915.845402	1.39
	$^8B_1$	$3a_1^1 3b_1^2 4a_1^2 3b_2^1 2a_2^2 4b_2^2$	16.65*	137.08	1.940	3.610	78, 416, 600	-915.813401	2.25
	$^6B_1$	$3a_1^1 3b_1^2 4a_1^2 3b_2^2 2a_2^2 4b_2^1$	10.75*	112.94	2.023	3.373	122, 547, 573	-915.849098	1.29
	$^8\Sigma^-$	$2\sigma^2 2\pi^4 3\pi^4$	16.25*	180.00	1.898 1.859	3.757	103, 103, 468, 666	-915.838750	1.58
	$^8\Sigma^-$	$2\sigma^2 2\pi^4 3\pi^4$	15.76	180.00	1.794	3.588	173, 173, 639, 809	-915.835043	1.71

Table 4.3 continued

Species	State	Configuration[a]	s(s+1)[b]	∠O-Gd^+-O (°)	r(Gd^+-O) (Å)	r(O-O) (Å)	Vibrational Frequencies (cm^{-1})[c]	E (E_h)	E_{rel} (eV)
	$^6\Pi$	$2\sigma^2 2\pi^4 3\pi^3 3\sigma^1$	10.52*	180.00	1.932	3.864	87, 93, 569, 1077	-915.835189	1.70
Gd^+-O_2	$^{10}A_1$	$3a_1^2 3b_1^2 4a_1^2 3b_2^2 2a_2^1 4a_1^1$	24.76	35.46	2.167	1.320	405, 459, 1186	-915.846167	1.42
	$^8A_1$	$3a_1^2 3b_1^2 4a_1^2 3b_2^2 2a_2^1 4a_1^1$	16.76*	35.51	2.166	1.321	415, 455, 1183	-915.847237	1.39
	$^6A_1$	$3a_1^2 3b_1^2 4a_1^2 3b_2^2 2a_2^1 4a_1^1$	10.65*	35.51	2.166	1.321	402, 446, 1181	-915.834360	1.74
	$^{10}B_2$	$3a_1^2 3b_1^2 4a_1^2 3b_2^2 2a_2^1 4b_2^1$	24.76	33.89	2.294	1.338	389, 901, 1151	-915.770816	3.49
	$^8B_2$	$3a_1^2 3b_1^2 4a_1^2 3b_2^2 2a_2^1 4b_2^1$	15.76	34.38	2.248	1.329	387, 413, 1175	-915.802037	2.62
	$^6B_2$	$3a_1^2 3b_1^2 4a_1^2 3b_2^2 2a_2^1 4b_2^1$	9.76*	34.54	2.240	1.330	394, 403, 1170	-915.803737	2.57
	$^{10}B_2$ TS	$3a_1^2 3b_1^2 4a_1^2 3b_2^2 2a_2^1 4b_2^1$	24.78	40.99	2.153	1.507	1713i, 570, 1170	-915.752554	3.95
	$^8B_2$ TS	$3a_1^2 3b_1^2 4a_1^2 3b_2^2 2a_2^1 4b_2^1$	16.10*	43.67	2.105	1.566	1094i, 190, 618	-915.778210	3.19
	$^6B_2$ TS	$3a_1^2 3b_1^2 4a_1^2 3b_2^2 2a_2^1 4b_2^1$	10.06*	42.40	2.113	1.528	1148i, 167, 591	-915.785254	3.00
Gd^+-O-O	$^{10}\Pi$	$2\sigma^2 2\pi^4 3\pi^3 3\sigma^1$	24.76	0.00	1.966	1.292	163, 181, 473, 1187	-915.816202	2.23
	$^8\Pi$	$2\sigma^2 2\pi^4 3\pi^3 3\sigma^1$	16.68*	0.00	1.966	1.292	108, 184, 469, 1182	-915.816113	2.23
	$^8\Pi^e$	$2\sigma^2 2\pi^4 3\pi^3 3\sigma^1$	16.68*	0.00	1.963	1.294	117i, 182, 469, 1185	-915.803668	2.56

Table 4.3 continued

Species	State	Configuration[a]	s(s+1)[b]	∠O-Gd^+-O (°)	r(Gd^+-O) (Å)	r(O-O) (Å)	Vibrational Frequencies (cm^{-1})[c]	E (E_h)	E_{rel} (eV)
	$^6\Pi$	$2\sigma^2 2\pi^4 3\pi^3 3\sigma^1$	10.68*	0.00	1.961	1.294	166, 186, 466, 1180	-915.804070	2.56
	$^8\Sigma^-$	$2\sigma^2 2\pi^4 3\pi^4$	15.92*	0.00	1.883	1.297	345, 345, 502, 1121	-915.807573	2.49
	$^8A''$ TS	$5a'^2 6a'^2 5a''^2 7a'^1 5a''^2 8a'^1$	16.56*	19.07	1.941 2.993	1.321	180i, 502, 1056	-915.813089	2.29
	$^8A'$ TS	$5a'^2 6a'^2 5a''^2 7a'^2 5a''^1 8a'^1$	16.75*	20.11	2.006 3.009	1.319	228i, 500, 1116	-915.808982	2.40
	$^{10}A'$ TS	$5a'^2 6a'^2 5a''^2 7a'^2 5a''^1 8a'^1$	24.76	19.84	2.008 3.015	1.316	219i, 503, 1120	-915.809648	2.39
	$^{10}\Pi$ TS	$2\sigma^2 2\pi^4 3\pi^3 3\sigma^1$	24.79	0.00	1.819	1.672	1522i, 114, 118, 515	-915.771779	3.36
	$^8\Pi$ TS	$2\sigma^2 2\pi^4 3\pi^3 3\sigma^1$	16.77*	0.00	1.804	1.740	1455i, 108, 111, 524	-915.758452	3.72

[a] In the C_{2v} symmetry structures, the seven 4f valence electrons of Gd^+ form nonbonding MOs given by $1a_1^1 1b_1^1 1b_2^1 2a_1^1 1a_2^1 2b_1^1 2b_2^1$ (overall $^8A_2$) (see Figure 3.11) and are omitted in the configuration designation for simplicity. These mos correspond to $1a'^1 1a''^1 2a'^1 3a'^1 2a''^1 3a''^1 4a'^1$ (overall $^8A''$) in C_s symmetry for the transition state (TS) structures. For linear structures with $C_{\infty V}$ and $D_{\infty h}$ symmetry, the 4f electrons form $1\sigma^1 1\varphi^2 1\delta^2 1\pi^2$ (overall $^8\Sigma$) non-bonding mos.

[b] * = spin-contaminated state.

[c] Calculated vibrational frequencies are scaled by 0.989. Imaginary frequencies indicated by i.

[d] Has one imaginary frequency and collapses to the A′ state.

[e] Differs from the lower energy $^8\Pi$ state in the electron spins of the 3σ and 3π orbitals. Additionally, has one imaginary frequency and collapses to the $^8\Sigma^-$ state.

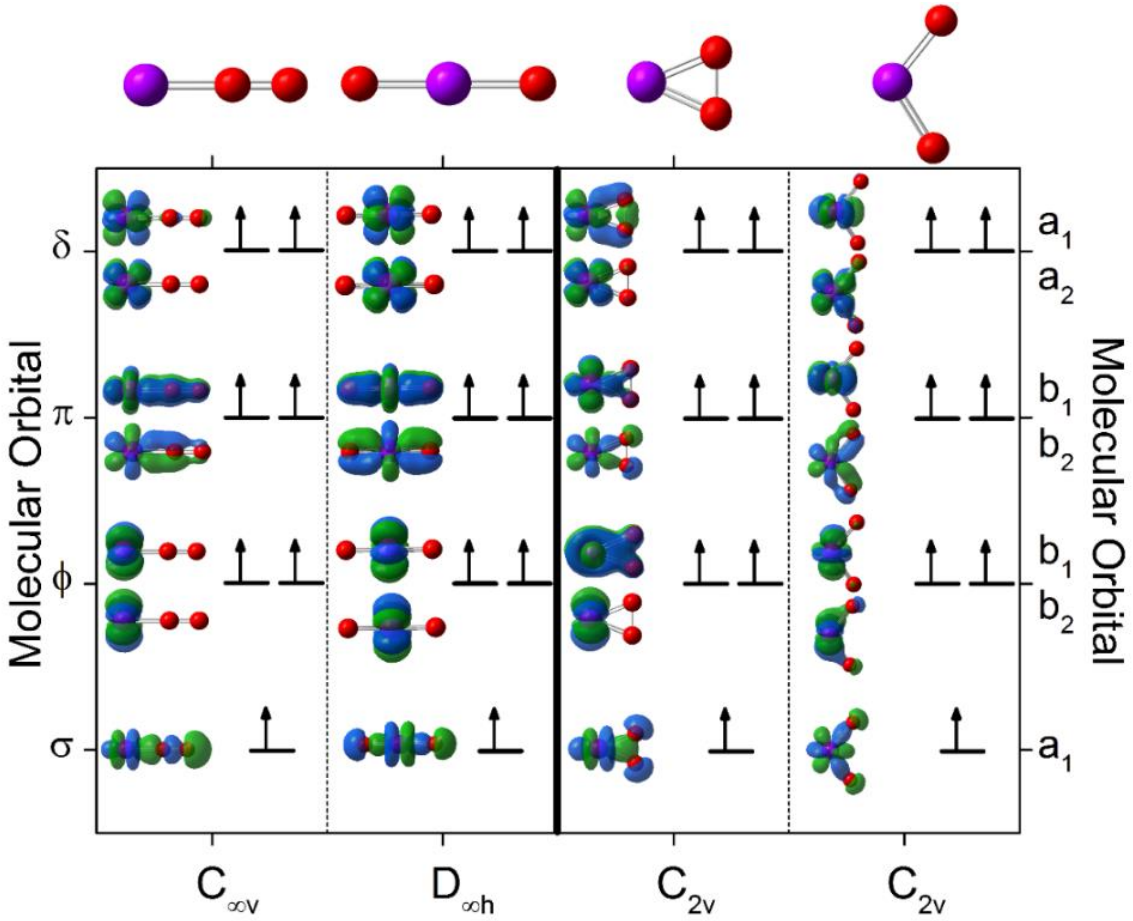

Figure 4.12. Representative molecular orbitals for the seven 4f valence electrons of Gd^+ in GdO_2^+ structures with $C_{\infty v}$, $D_{\infty h}$, and C_{2v} symmetry obtained at the B3LYP level of theory using the ANO basis set and SDD ECP for Gd and the 6-311+G(3df) basis set for O.

to form the cyclic dioxides is shown in Figure 4.13a. The linear Gd^+-O_2 adducts on these surfaces have BDEs close to 2 eV and cannot explain the adduct probed in the CID experiments with a measured BDE of 0.75 ± 0.11 eV.

Additional relaxed potential energy surface scans were calculated to explore if there are other intermediates that can explain the experimental results. Potential energy surface scans as functions of the Gd^+-O_2 and GdO^+-O distances are shown in Figures 4.13 b and c, respectively. Besides the local minima already discussed, no other minima were located on

Figure 4.13. Part a) Relaxed potential energy scans as a function of O-Gd^+-O angle from Figure 4.8 expanded in the region of the barrier for insertion of Gd^+ into the O-O bond of linear Gd^+-O_2 adducts to form inserted O-Gd^+-O dioxides. A′ (solid lines) and A″ (dashed lines) surfaces are indicated for multiplicities of 10 (black) and 8 (red). Relaxed potential energy scans for linear GdO_2^+ complexes as a function of Gd^+-O_2 (part b) and GdO^+-O (part c) distances with the various electronic states indicated in the figures.

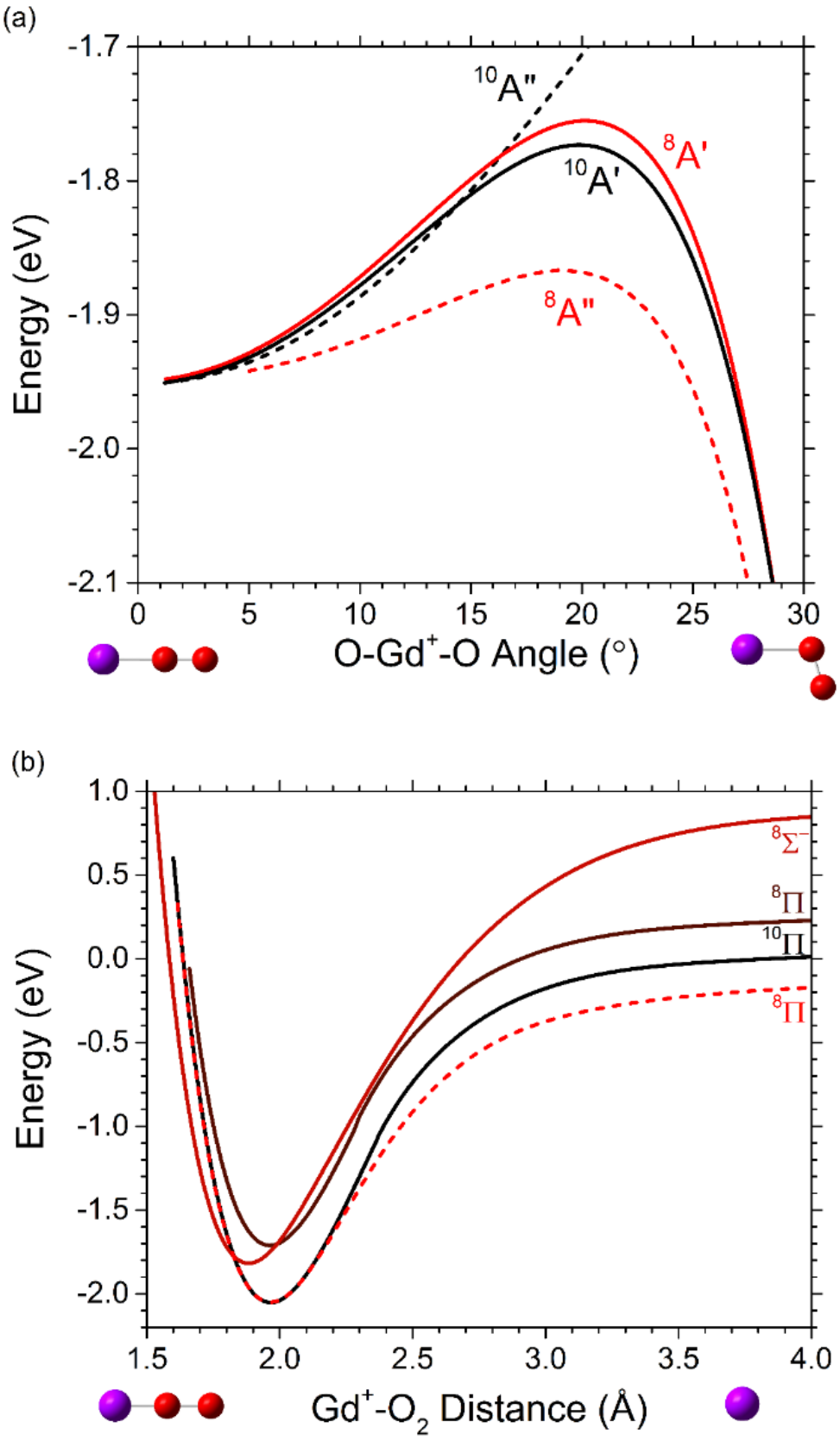
(a)
-1.7
-1.8
-1.9
-2.0
-2.1
Energy (eV)
^{10}A"
^{8}A'
^{10}A'
^{8}A"
0
5
10
15
20
25
30
O-Gd^{+}-O Angle (°)
(b)
1.0
0.5
0.0
-0.5
-1.0
-1.5
-2.0
Energy (eV)
$^{8}\Sigma^{-}$
$^{8}\Pi$
$^{10}\Pi$
$^{8}\Pi$
1.5
2.0
2.5
3.0
3.5
4.0
Gd^{+}-O$_2$ Distance (Å)

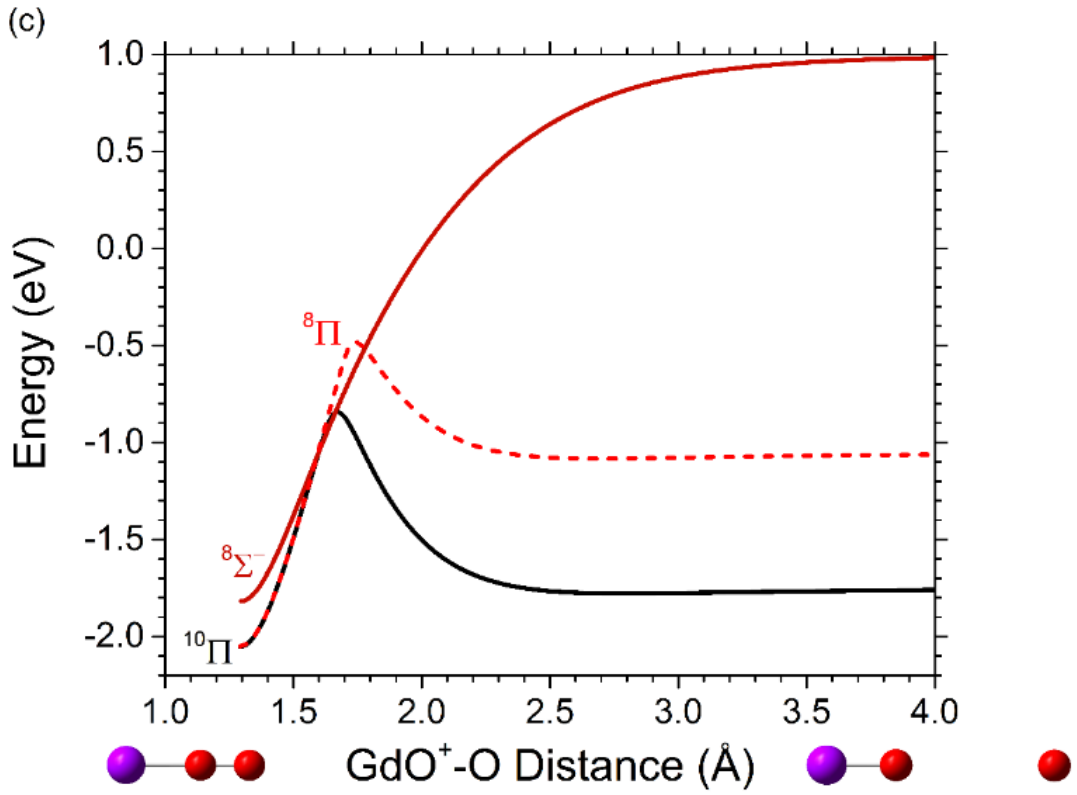

Figure 4.13 continued

these surfaces. From the present calculations, the Gd^+-O_2 adduct probed in the CID experiments is best explained by a side-on Gd^+-O_2 complex with a $^{10}B_2$ electronic state, as discussed in more detail above.

Additional calculations at the B3LYP, PBE0, and CCSD(T,full) levels of theory, also utilizing the correlation consistent all-electron cc-pVXZ-DK3 (with X = T, Q) basis sets[53] for Gd were carried out for comparison with the experimental thermochemistry. The resulting bond lengths, angles, vibrational frequencies, and energies for O-Gd^+-O ($^8A_2$) are summarized in Table 4.4, which also includes the results for GdO^+ ($^8\Sigma^-$) from our previous work.[7] For the Gd^+-O_2 ($^{10}B_2$) adduct and transition state (TS), optimized structures were obtained only for the ANO basis set and these are also listed in Table 4.4. These calculations indicate that there is not a large variability in the bond lengths and angles of the optimized structures between the various basis sets and levels of theory. The exception is the Gd^+-O_2 TS ($^{10}B_2$), which is predicted to have signficantly different frequencies at the B3LYP and PBE0 levels of theory (Table 4.4). The significantly larger frequencies at the PBE0 level result in a much larger zero point energy correction as discussed above, and causes worse agreement with the TS barrier measured experimentally, Table 4.4. In general, however, single point energy calculations obtained at the CCSD(T,full)/cc-pVXZ-DK3 level with X = T and Q using optimized geometries at the B3LYP/ANO level should closely reflect the energies of the true minima. This is also supported by the potential energy surfaces constructed from single point energies extrapolated to the complete basis set limit in Figure 4.9b.

Table 4.4. Comparison of optimized geometries, vibrational frequencies, and energies for GdO^+ ($^8\Sigma^-$), O-Gd-O^+ ($^8A_2$), Gd^+-O_2 ($^{10}B_2$), and TS ($^{10}B_2$) between various basis sets and levels of theory.

Level	Basis Set	∠O-Gd^+-O (°)	r(Gd^+-O) (Å)	r(O-O) (Å)	Frequencies (cm^{-1})[a]	E (E_h)	D_0 (eV)[b]
Expt. GdO^+							7.69 ± 0.10[c]
B3LYP	ANO		1.752		900	-840.714362	6.98
	cc-pVTZ-DK3		1.760		895	-11340.456395	7.19
	cc-pVQZ-DK3		1.759		895	-11340.469290	7.19
PBE0	ANO		1.737		929	-840.514921	7.01
	cc-pVTZ-DK3		1.744		925	-11339.894034	7.19
	cc-pVQZ-DK3		1.743		925	-11339.905902	7.19
CCSD(T,full)	ANO		1.755		893	-840.010139	7.04
	cc-pVTZ-DK3		1.760		892	-11337.575401	7.35
	cc-pVQZ-DK3		1.756		902	-11337.939909	7.65
Expt. OGd^+-O							2.86 ± 0.08
B3LYP	ANO	44.71	1.962	1.492	561, 592, 865	-915.898116	2.46
	cc-pVTZ-DK3	44.51	1.970	1.492	564, 596, 870	-11415.692236	2.47
	cc-pVQZ-DK3	44.47	1.969	1.490	563, 594, 867	-11415.715212	2.47

Table 4.4 continued

Level	Basis Set	∠O-Gd^+-O (°)	r(Gd^+-O) (Å)	r(O-O) (Å)	Frequencies (cm^{-1})[a]	E (E_h)	D_0 (eV)[b]
PBE0	ANO	44.16	1.945	1.462	581, 619, 919	-915.620902	2.72
	cc-pVTZ-DK3	44.07	1.952	1.464	586, 623, 922	-11415.052745	2.48
	cc-pVQZ-DK3	44.00	1.952	1.462	583, 621, 920	-11415.074528	2.49
CCSD(T,full)	ANO	45.20	1.961	1.507	577, 582, 820	-915.092768	2.34
Expt. Gd^+-O_2							0.75 ± 0.11
B3LYP	ANO	33.89	2.294	1.338	389, 901, 1151	-915.770816	0.67
PBE0	ANO	33.72	2.275	1.320	398, 1161, 1220	-915.494294	0.68
CCSD(T,full)	ANO	34.22	2.291	1.348	400, 1109, 1167	-914.961618	0.81
Expt. TS							0.31 ± 0.07
B3LYP	ANO	40.99	2.153	1.507	1713i, 570, 1170	-915.752554	0.45
PBE0	ANO	41.45	2.123	1.503	1962i, 590, 4521	-915.470871	0.78

[a] Calculated vibrational frequencies are scaled by 0.989. Imaginary frequencies indicated by i.
[b] Calculated BDEs have not been spin-orbit corrected. This correction is small and does not affect the values significantly.
[c] Reference 7.

4.8 Acknowledgements

This project is supported by the U.S. Air Force Office of Scientific Reasearch (FA9550-16-1-0095). The authors thank Professor Kirk A. Peterson for providing the all-electron basis sets for Gd and the Center for High Performance Computing at the University of Utah for generous allocation of computer time.

4.9 References

(1) Gong, Y.; Zhou, M.; Andrews, L. Spectroscopic and Theoretical Studies of Transition Metal Oxides and Dioxygen Complexes. *Chem. Rev.* **2009,** *109*, 6765-6808.

(2) Shuman, N. S.; Hunton, D. E.; Viggiano, A. A. Ambient and Modified Atmospheric Ion Chemistry: From Top to Bottom. *Chem. Rev.* **2015,** *115*, 4542-4570.

(3) Schofield, K. An Overlooked Series of Gas Phase Diatomic Metal Oxide Ions that Are Long-lived. *J. Phys. Chem. A* **2006,** *110*, 6938-6947.

(4) Ard, S. G.; Shuman, N. S.; Martinez, O.; Brumbach, M. T.; Viggiano, A. A. Kinetics of Chemi-Ionization Reactions of Lanthanide Metals (Nd, Sm) from 150 to 450 K. *J. Chem. Phys.* **2015,** *143*, 204303.

(5) Konings, R. J. M.; Beneš, O.; Kovács, A.; Manara, D.; Sedmidubský, D.; Gorokhov, L.; Iorish, V. S.; Yungman, V.; Shenyavskaya, E.; Osina, E. The Thermodynamic Properties of the f-Elements and their Compounds. Part 2. The Lanthanide and Actinide Oxides. *J. Phys. Chem. Ref. Data* **2014,** *43*, 013101.

(6) Cox, R. M.; Kim, J.; Armentrout, P. B.; Bartlett, J.; VanGundy, R. A.; Heaven, M. C.; Ard, S. G.; Melko, J. J.; Shuman, N. S.; Viggiano, A. A. Evaluation of the Exothermicity of the Chemi-Ionization Reaction $Sm + O \rightarrow SmO^+ + e^-$. *J. Chem. Phys.* **2015,** *142*, 134307.

(7) Demireva, M.; Kim, J.; Armentrout, P. B. Gadolinium (Gd) Oxide, Carbide, and Carbonyl Cation Bond Energies and Evaluation of the $Gd + O \rightarrow GdO^+ + e^-$ Chemi-Ionization Reaction Enthalpy. *J. Phys. Chem. A* **2016,** *120*, 8550-8563.

(8) Armentrout, P. B. Mass Spectrometry—Not Just a Structural Tool: The Use of Guided Ion Beam Tandem Mass Spectrometry to Determine Thermochemistry. *J. Am. Soc. Mass. Spectrom.* **2002,** *13*, 419-434.

(9) Armentrout, P. B. Kinetic Energy Dependence of Ion–Molecule Reactions: Guided Ion Beams and Threshold Measurements. *Int. J. Mass Spectrom.* **2000,** *200*, 219-241.

(10) Clemmer, D. E.; Weber, M. E.; Armentrout, P. B. Reactions of Al^+ (^1S) with NO_2, N_2O, and CO_2: Thermochemistry of AlO and AlO^+. *J. Phys. Chem.* **1992,** *96*, 10888-10893.

(11) Dalleska, N. F.; Armentrout, P. B. Guided Ion Beam Studies of Reactions of Alkaline Earth Ions with O_2. *Int. J. Mass Spectrom. Ion Processes* **1994,** *134*, 203-212.

(12) Aristov, N.; Armentrout, P. B. Collision-Induced Dissociation of Vanadium Monoxide Ion. *J. Phys. Chem.* **1986,** *90*, 5135-5140.

(13) Loh, S. K.; Fisher, E. R.; Lian, L.; Schultz, R. H.; Armentrout, P. B. State-Specific Reactions of Fe^+ (^6D, ^4F) with O_2 and cyclo-C_2H_4O: $D°_0(Fe^+\text{-}O)$ and Effects of Collisional Relaxation. *J. Phys. Chem.* **1989,** *93*, 3159-3167.

(14) Clemmer, D. E.; Elkind, J. L.; Aristov, N.; Armentrout, P. B. Reaction of Sc^+, Ti^+, and V^+ with CO. MC^+ and MO^+ Bond Energies. *J. Chem. Phys.* **1991,** *95*, 3387-3393.

(15) Rodgers, M. T.; Walker, B.; Armentrout, P. B. Reactions of Cu^+ (^1S and ^3D) with O_2, CO, CO_2, N_2, NO, N_2O, and NO_2 Studied by Guided Ion Beam Mass Spectrometry. *Int. J. Mass Spectrom.* **1999,** *182–183*, 99-120.

(16) Fisher, E. R.; Elkind, J. L.; Clemmer, D. E.; Georgiadis, R.; Loh, S. K.; Aristov, N.; Sunderlin, L. S.; Armentrout, P. B. Reactions of Fourth-Period Metal Ions (Ca^+−Zn^+) with O_2: Metal-Oxide Ion Bond Energies. *J. Chem. Phys.* **1990,** *93*, 2676-2691.

(17) Clemmer, D. E.; Dalleska, N. F.; Armentrout, P. B. Gas-Phase Thermochemistry of the Group 3 Dioxides: ScO_2, YO_2 and LaO_2. *Chem. Phys. Lett.* **1992,** *190*, 259-265.

(18) Sievers, M. R.; Armentrout, P. B. Potential Energy Surface for Carbon-Dioxide Activation by V^+: A Guided Ion Beam Study. *J. Chem. Phys.* **1995,** *102*, 754-762.

(19) Chen, Y.-M.; Armentrout, P. B. Kinetic Energy Dependence of the Reactions of Ru^+, Rh^+, Pd^+, and Ag^+ with O_2. *J. Chem. Phys.* **1995,** *103*, 618-625.

(20) Sievers, M. R.; Chen, Y.-M.; Armentrout, P. B. Metal Oxide and Carbide Thermochemistry of Y^+, Zr^+, Nb^+, and Mo^+. *J. Chem. Phys.* **1996,** *105*, 6322-6333.

(21) Sievers, M. R.; Armentrout, P. B. Gas Phase Activation of Carbon Dioxide by

Niobium and Niobium Monoxide Cations. *Int. J. Mass Spectrom.* **1998,** *179–180*, 103-115.

(22) Sievers, M. R.; Armentrout, P. B. Oxidation of CO and Reduction of CO_2 by Gas Phase Zr^+, ZrO^+, and ZrO_2^+. *Int. J. Mass Spectrom.* **1999,** *185–187*, 117-129.

(23) Sievers, M. R.; Armentrout, P. B. Activation of Carbon Dioxide: Gas-Phase Reactions of Y^+, YO^+, and YO_2^+ with CO and CO_2. *Inorg. Chem.* **1999,** *38*, 397-402.

(24) Sievers, M. R.; Armentrout, P. B. Reactions of CO and CO_2 with Gas-Phase Mo^+, MoO^+, and MoO_2^+. *J. Phys. Chem. A* **1998,** *102*, 10754-10762.

(25) Hinton, C. S.; Citir, M.; Manard, M.; Armentrout, P. B. Collision-Induced Dissociation of MO^+ and MO_2^+ (M = Ta and W): Metal Oxide and Dioxide Cation Bond Energies. *Int. J. Mass Spectrom.* **2011,** *308*, 265-274.

(26) Armentrout, P. B. The Bond Energy of ReO^+: Guided Ion-Beam and Theoretical Studies of the Reaction of Re^+ (^7S) with O_2. *J. Chem. Phys.* **2013,** *139*, 084305.

(27) Zhang, X.-G.; Armentrout, P. B. Activation of O_2, CO, and CO_2 by Pt^+: The Thermochemistry of PtO^+. *J. Phys. Chem. A* **2003,** *107*, 8904-8914.

(28) Hinton, C. S.; Li, F.; Armentrout, P. B. Reactions of Hf^+, Ta^+, and W^+ with O_2 and CO: Metal Carbide and Metal Oxide Cation Bond Energies. *Int. J. Mass Spectrom.* **2009,** *280*, 226-234.

(29) Hinton, C. S.; Citir, M.; Armentrout, P. B. Guided Ion-Beam and Theoretical Studies of the Reaction of Os^+ (^6D) with O_2: Adiabatic and Nonadiabatic Behavior. *Int. J. Mass Spectrom.* **2013,** *354–355*, 87-98.

(30) Zhang, X.-G.; Armentrout, P. B. Activation of O_2 and CO_2 by PtO^+: The Thermochemistry of PtO_2^+. *J. Phys. Chem. A* **2003,** *107*, 8915-8922.

(31) Cox, R. M.; Citir, M.; Armentrout, P. B.; Battey, S. R.; Peterson, K. A. Bond Energies of ThO^+ and ThC^+: A Guided Ion Beam and Quantum Chemical Investigation of the Reactions of Thorium Cation with O_2 and CO. *J. Chem. Phys.* **2016,** *144*, 184309.

(32) Ackermann, R. J.; Rauh, E. G.; Thorn, R. J. The Thermodynamics of Ionization of Gaseous Oxides; The First Ionization Potentials of the Lanthanide Metals and Monoxides. *J. Chem. Phys.* **1976,** *65*, 1027-1031.

(33) Kordis, J.; Gingerich, K. A. Mass Spectrometric Observations of Some Polyatomic Gaseous Rare Earth Oxides and Their Atomization Energies. *J. Chem. Phys.* **1977,** *66*, 483-491.

(34) Cockett, M. C. R.; Nyulászi, L.; Veszprémi, T.; Wright, T. G.; Dyke, J. M. A Study of Some Gas-Phase Lanthanide Plus Oxidant Chemiionization Reactions with Chemielectron Spectroscopy. *J. Electron. Spectrosc. Relat. Phenom.* **1991,** *57*, 373-397.

(35) Loh, S. K.; Hales, D. A.; Lian, L.; Armentrout, P. B. Collision-Induced Dissociation of Fe_n^+ (n=2–10) with Xe: Ionic and Neutral Iron Binding Energies. *J. Chem. Phys.* **1989,** *90*, 5466-5485.

(36) Daly, N. R. Scintillation Type Mass Spectrometer Ion Detector. *Rev. Sci. Instrum.* **1960,** *31*, 264-267.

(37) Ervin, K. M.; Armentrout, P. B. Translational Energy Dependence of $Ar^+ + XY \rightarrow ArX^+ + Y$ ($XY = H_2, D_2, HD$) from Thermal to 30 eV C.M. *J. Chem. Phys.* **1985,** *83*, 166-189.

(38) Muntean, F.; Armentrout, P. B. Guided Ion Beam Study of Collision-Induced Dissociation Dynamics: Integral and Differential Cross Sections. *J. Chem. Phys.* **2001,** *115*, 1213-1228.

(39) Johnson III, R. D. NIST Computational Chemistry Comparison and Benchmark Database, NIST Standard Reference Database Number 101 Release 18, NIST, 2016, available online: http://cccbdb.nist.gov/.

(40) Weber, M. E.; Elkind, J. L.; Armentrout, P. B. Kinetic Energy Dependence of $Al^+ + O_2 \rightarrow AlO^+ + O$. *J. Chem. Phys.* **1986,** *84*, 1521-1529.

(41) Frisch, M. J.; Trucks, G. W.; Schlegel, H. B.; Scuseria, G. E.; Robb, M. A.; Cheeseman, J. R.; Scalmani, G.; Barone, V.; Mennucci, B.; Petersson, G. A.et al.; Gaussian, Inc.: Wallingford, CT, USA, 2009.

(42) Becke, A. D. Density-Functional Thermochemistry. III. The Role of Exact Exchange. *J. Chem. Phys.* **1993,** *98*, 5648-5652.

(43) Lee, C.; Yang, W.; Parr, R. G. Development of the Colle-Salvetti Correlation-Energy Formula into a Functional of the Electron Density. *Phys. Rev. B* **1988,** *37*, 785-789.

(44) Dolg, M.; Stoll, H.; Preuss, H. Energy-Adjusted Ab Initio Pseudopotentials for the Rare Earth Elements. *J. Chem. Phys.* **1989,** *90*, 1730-1734.

(45) Cao, X.; Dolg, M. Valence Basis Sets for Relativistic Energy-Consistent Small-Core Lanthanide Pseudopotentials. *J. Chem. Phys.* **2001,** *115*, 7348-7355.

(46) Raghavachari, K.; Trucks, G. W.; Pople, J. A.; Head-Gordon, M. A Fifth-Order Perturbation Comparison of Electron Correlation Theories. *Chem. Phys. Lett.* **1989,**

157, 479-483.

(47) Bartlett, R. J.; Watts, J. D.; Kucharski, S. A.; Noga, J. Non-Iterative Fifth-Order Triple and Quadruple Excitation Energy Corrections in Correlated Methods. *Chem. Phys. Lett.* **1990,** *165*, 513-522.

(48) Scuseria, G. E.; Lee, T. J. Comparison of Coupled-Cluster Methods which Include the Effects of Connected Triple Excitations. *J. Chem. Phys.* **1990,** *93*, 5851-5855.

(49) Crawford, T. D.; Stanton, J. F. Investigation of an Asymmetric Triple-Excitation Correction for Coupled-Cluster Energies. *Int. J. Quantum Chem.* **1998,** *70*, 601-611.

(50) Cao, X.; Dolg, M. Segmented Contraction Scheme for Small-Core Lanthanide Pseudopotential Basis Sets. *J. Mol. Struct.: THEOCHEM* **2002,** *581*, 139-147.

(51) Douglas, M.; Kroll, N. M. Quantum Electrodynamical Corrections to the Fine Structure of Helium. *Ann. Phys.* **1974,** *82*, 89-155.

(52) Reiher, M.; Wolf, A. Exact Decoupling of the Dirac Hamiltonian. II. The Generalized Douglas–Kroll–Hess Transformation up to Arbitrary Order. *J. Chem. Phys.* **2004,** *121*, 10945-10956.

(53) Lu, Q.; Peterson, K. A. Correlation Consistent Basis Sets for Lanthanides: The Atoms La–Lu. *J. Chem. Phys.* **2016,** *145*, 054111.

(54) Perdew, J. P.; Ernzerhof, M.; Burke, K. Rationale for Mixing Exact Exchange with Density Functional Approximations. *J. Chem. Phys.* **1996,** *105*, 9982-9985.

(55) Adamo, C.; Barone, V. Toward Reliable Density Functional Methods without Adjustable Parameters: The PBE0 Model. *J. Chem. Phys.* **1999,** *110*, 6158-6170.

(56) Schuchardt, K. L.; Didier, B. T.; Elsethagen, T.; Sun, L.; Gurumoorthi, V.; Chase, J.; Li, J.; Windus, T. L. Basis Set Exchange: A Community Database for Computational Sciences. *J. Chem. Inf. Model.* **2007,** *47*, 1045-1052.

(57) Feller, D. The Role of Databases in Support of Computational Chemistry Calculations. *J. Comput. Chem.* **1996,** *17*, 1571-1586.

(58) Foresman, J. B.; Frisch, A. *Exploring Chemistry with Electronic Structure Methods*; Gaussian: Pittsburgh, Pa., 1996.

(59) Gioumousis, G.; Stevenson, D. P. Reactions of Gaseous Molecule Ions with Gaseous Molecules. V. Theory. *J. Chem. Phys.* **1958,** *29*, 294-299.

(60) Koyanagi, G. K.; Bohme, D. K. Oxidation Reactions of Lanthanide Cations with

N_2O and O_2: Periodicities in Reactivity. *J. Phys. Chem. A* **2001,** *105*, 8964-8968.

(61) Burley, J. D.; Ervin, K. M.; Armentrout, P. B. Translational Energy Dependence of $O^+(^4S) + H_2(D_2, HD) \rightarrow OH^+(OD^+) + H(D)$ from Thermal Energies to 30 eV C.M. *Int. J. Mass Spectrom. Ion Processes* **1987,** *80*, 153-175.

(62) Darwent, B. d. *Bond Dissociation Energies in Simple Molecules*; U.S. National Bureau of Standards; for sale by the Supt. of Docs., U.S. Govt. Print. Off.: Washington, 1970.

(63) Chesnavich, W. J.; Bowers, M. T. Theory of Translationally Driven Reactions. *J. Phys. Chem.* **1979,** *83*, 900-905.

(64) Waber, J. T.; Cromer, D. T. Orbital Radii of Atoms and Ions. *J. Chem. Phys.* **1965,** *42*, 4116-4123.

(65) Huber, K. P.; Herzberg, G. *Molecular Spectra and Molecular Structure: IV. Constants of Diatomic Molecules*; Van Nostrand Reinhold: New York, 1979.

(66) Rodgers, M. T.; Armentrout, P. B. A Critical Evaluation of the Experimental and Theoretical Determination of Lithium Cation Affinities. *Int. J. Mass Spectrom.* **2007,** *267*, 167-182.

(67) Maier, T. M.; Boese, A. D.; Sauer, J.; Wende, T.; Fagiani, M.; Asmis, K. R. The Vibrational Spectrum of FeO_2^+ Isomers—Theoretical Benchmark and Experiment. *J. Chem. Phys.* **2014,** *140*, 204315.

(68) Lee, T. J.; Taylor, P. R. A Diagnostic for Determining the Quality of Single-Reference Electron Correlation Methods. *Int. J. Quantum Chem.* **1989,** *36*, 199-207.

(69) Gibson, J. K. Role of Atomic Electronics in f-Element Bond Formation: Bond Energies of Lanthanide and Actinide Oxide Molecules. *J. Phys. Chem. A* **2003,** *107*, 7891-7899.

(70) Koyanagi, G. K.; Caraiman, D.; Blagojevic, V.; Bohme, D. K. Gas-Phase Reactions of Transition-Metal Ions with Molecular Oxygen: Room-Temperature Kinetics and Periodicities in Reactivity. *J. Phys. Chem. A* **2002,** *106*, 4581-4590.

(71) Andrews, L.; Zhou, M.; Chertihin, G. V.; Bauschlicher, C. W. Reactions of Laser-Ablated Y and La Atoms, Cations and Electrons with O_2. Infrared Spectra and Density Functional Calculations of the MO, MO^+, MO_2, MO_2^+, and MO_2^- Species in Solid Argon. *J. Phys. Chem. A* **1999,** *103*, 6525-6532.

(72) Bauschlicher, C. W.; Zhou, M.; Andrews, L.; Tobias Johnson, J. R.; Panas, I.; Snis, A.; Roos, B. O. A Further Study of the Products of Scandium and Dioxygen

Reactions. *J. Phys. Chem. A* **1999,** *103,* 5463-5467.

(73) Todorova, T. K.; Infante, I.; Gagliardi, L.; Dyke, J. M. Theoretical Study of the Gas-Phase Chemiionization Reactions La + O and La + O_2. *J. Phys. Chem. A* **2008,** *112,* 7825-7830.

CHAPTER 5

ACTIVATION OF CO_2 BY GADOLINIUM CATION (Gd^+): ENERGETICS AND MECHANISM FROM EXPERIMENT AND THEORY

This chapter is reprinted with permission from Demireva, M; Armentrout, P. B. Activation of CO_2 by Gadolinium Cation (Gd^+): Energetics and Mechanism from Experiment and Theory. *Top. Catal.* **2017**, https://doi.org/10.1007/s11244-017-0858-1. https://link.springer.com/article/10.1007/s11244-017-0858-1

5.1 Graphical Abstract

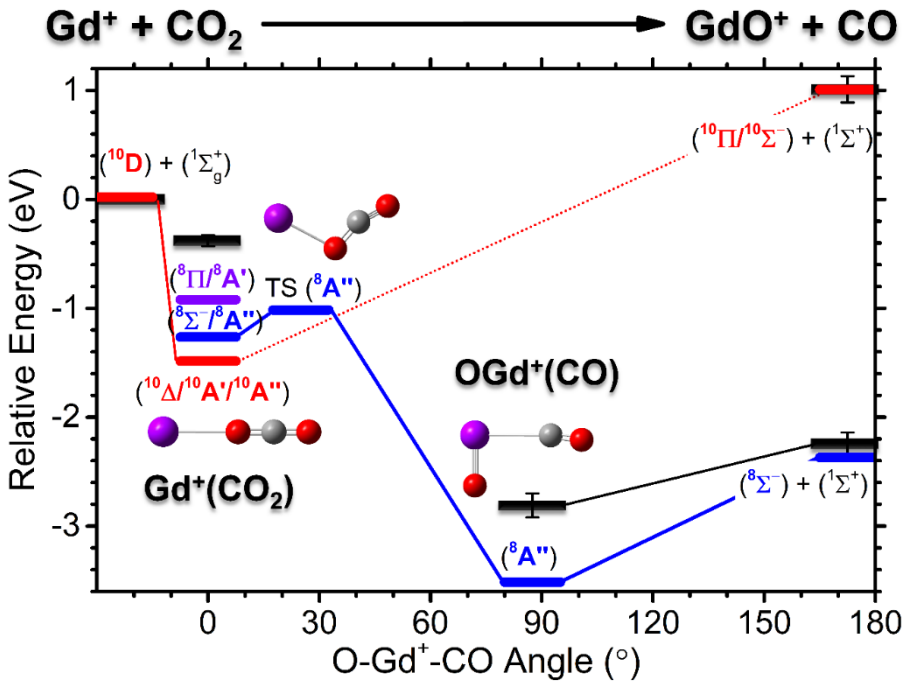

5.2 Abstract

The exothermic and barrierless activation of CO_2 by the lanthanide gadolinium cation (Gd^+) to form GdO^+ and CO is investigated in detail using guided ion beam tandem mass spectrometry (GIBMS) and theory. Kinetic energy dependent product ion cross sections from collision-induced dissociation (CID) experiments of $GdCO_2^+$ are measured to determine the energetics of $OGd^+(CO)$ and $Gd^+(OCO)$ intermediates. Modeling these cross sections yields bond dissociation energies (BDEs) for OGd^+-CO and Gd^+-OCO of 0.57 ± 0.05 and 0.38 ± 0.05 eV, respectively. The OGd^+-CO BDE is similar to that previously measured for Gd^+-CO, which can be attributed to the comparable electrostatic interaction with CO in both complexes. The $Gd^+(OCO)$ adduct is identified from calculations to correspond to an electronically excited state. The thermochemistry here and the recently measured GdO^+ BDE allows for the potential energy surface (PES) of the Gd^+ reaction with CO_2 to be deduced from experiment in some detail. Theoretical calculations are performed for comparison with the experimental thermochemistry and for insight into the electronic states of the $GdCO_2^+$ intermediates, transition states, and the reaction mechanism. Although the reaction between ground state Gd^+ (^{10}D) and CO_2 ($^1\Sigma_g^+$) reactants to form ground state GdO^+ ($^8\Sigma^-$) and CO ($^1\Sigma^+$) products is formally spin-forbidden, calculations indicate that there are octet and dectet surfaces having a small energy gap in the entrance channel, such that they can readily mix. Thereby, the reaction can efficiently proceed along the lowest energy octet surface to yield ground state products, consistent with the experimental observations of an efficient, barrierless process. At high collision energies, the measured GdO^+ cross section from the Gd^+ reaction with CO_2 exhibits a distinct feature, attributed to formation of electronically excited GdO^+ products along a

single dectet PES in a diabatic and spin-allowed process. Modeling this high-energy feature gives an excitation energy of 3.25 ± 0.16 eV relative to the GdO^+ ($^8\Sigma^-$) ground state, in good agreement with calculated excitation energies for GdO^+ ($^{10}\Pi$, $^{10}\Sigma^-$) electronic states. The reactivity of Gd^+ with CO_2 is compared with the group 3 transition metal cations and other lanthanide cations and periodic trends are discussed.

5.3 Introduction

The interest in carbon dioxide reactivity has increased in recent years, in part because of the role of CO_2 as a greenhouse gas and its potential use as a natural source of carbon in chemical synthesis.[1-4] Conversion of CO_2 to more useful forms requires activation by catalysts, where, for example, reduction of CO_2 to CO by O atom transfer can be induced by several metals and their complexes or clusters.[4] Understanding the reactivity and interactions of these metals and complexes with CO_2 can provide useful insight for the design of new and improved catalysts. In the gas phase, these interactions can be probed directly, without interference from solvent or substrate molecules, where such studies can offer important thermochemical information and help elucidate mechanistic details.

Gas-phase reactions of metal cations with CO_2 have previously been carried out at thermal energies using ion cyclotron resonance (ICR) and selected-ion drift or flow tube techniques.[5-11] From the ICR studies, thermochemical information has been reported from bracketing experiments that determine whether oxygen atom transfer occurs from an oxidant with a known oxygen affinity.[7,8] Kinetic information at thermal energies has also been obtained from measurements of the rate coefficients.[5-8] More recently, Bohme and coworkers have systematically investigated the reactivity of 46 main group and transition

metal cations[11] and in a separate study[9] the reactivity of lanthanide metal cations with CO_2 using an inductively-coupled plasma selected-ion flow tube (ICP/SIFT) instrument. In these experiments, the rate coefficients for reaction (5.1) have been measured for the metal cations that react under thermal conditions.

$$M^+ + CO_2 \rightarrow MO^+ + CO \qquad (5.1)$$

Reaction (5.1) is observed for the early transition metal cations and several of the lanthanide cations, where the kinetics appear to be influenced by both electronic spin conservation and the exothermicity of the reaction.[9,11]

More detailed kinetic and thermochemical information can be obtained from studying the energy dependence of these reactions, where endothermic processes or those exhibiting a barrier can also be investigated. For example, using guided ion beam tandem mass spectrometry (GIBMS),[12,13] reaction cross sections can be measured over a wide range of energies (thermal – 1000 eV, lab) and this technique has previously been used to investigate the gas-phase activation of CO_2 by first,[14-17] second,[18-21] and third[22] row transition metal cations, along with Al^+,[23] Sm^+,[24] and U^+.[25] These experiments have provided the energetics of the potential energy surfaces (PESs) and detailed mechanistic information, including the role of spin conservation and PES crossings, for many of these metal cations.

Few experimental gas-phase studies have focused on the reactivity of lanthanide metal atoms and ions with CO_2. These include the study noted above by Bohme and coworkers as well as a systematic study by Campbell,[26] who measured the temperature dependent rate coefficients for the lanthanide metal atoms. More recently, the reaction of Sm^+ with CO_2 has been investigated in great detail by GIBMS.[24] The lanthanide metals are

unusual in that many of them have larger metal oxide bond dissociation energies (BDEs) than ionization energies (IEs) and can combine exothermically with atomic oxygen to release an electron and form the metal oxide cation in a chemi-ionization reaction.[27-30] Thus, many of these lanthanides form stable oxide cations, where the BDEs of these oxides exceed that of OC-O such that reaction (5.1) is exothermic.[9,27,31] Of the lanthanide cations for which reaction (5.1) is expected to be exothermic, Bohme and coworkers have determined that La^+, Ce^+, Pr^+, Nd^+, Gd^+, Tb^+, and Lu^+ react with CO_2 at thermal energies, whereas Sm^+, Dy^+, Er^+, and Ho^+ do not.[9] These authors suggest that there is a kinetic energy barrier to the reaction of the latter species, where the barrier height correlates inversely with the exothermicity of reaction (5.1).[9] Because reaction (5.1) is not significantly exothermic for Sm^+, Dy^+, Er^+, and Ho^+, the barrier height exceeds the reactant asymptote and no reaction occurs at thermal energies.[9] The nature of this barrier for Sm^+ has recently been identified to arise from a crossing (which occurs above the reactant asymptote) between the diabatic surface of the $Sm^+(OCO)$ intermediate ($4f^6 6s^1$ configuration) in the entrance channel with the diabatic surface of the $OSm^+(CO)$ intermediate ($4f^5 5d^2$ configuration) that readily leads to ground state products in the exit channel.[24] Theoretical studies have investigated the activation of CO_2 by the early lanthanide metal cations, La^+,[32,33] Ce^+,[34] and Pr^+,[34] for which reaction (5.1) is significantly exothermic, and suggest that these lanthanide cations will react according to a two-state reactivity (TSR)[35] mechanism, involving a crossing of two PESs with different spin.[32-34] Although these theoretical studies provide some information about the PESs and reaction mechanism, the calculations[34] for Ce^+ suggest that no reaction will occur at thermal energies, which is at odds with the experiments of Bohme and coworkers,[9] where a relatively large rate

coefficient is measured for Ce^+. Spin-orbit and relativistic effects and the many electronic configurations that are possible from the 4f electrons make these heavy elements challenging to describe theoretically, illustrating the need for good experimental data that can be used as theoretical benchmarks.

In the present study, the gas-phase activation of CO_2 by the lanthanide gadolinium cation (Gd^+) is investigated in detail using GIBMS and theory. BDEs at 0 K are measured for $OGd^+(CO)$ and $Gd^+(OCO)$ from collision-induced dissociation (CID) experiments of $GdCO_2^+$ precursor ions. Using this thermochemistry and the recently[36] measured BDE for GdO^+, a PES for reaction (5.1) is constructed from experiment. Quantum chemical calculations are performed and tested against the experimental thermochemistry and provide insight into the electronic states of the intermediates and the reaction mechanism. The thermochemistry and reactivity of Gd^+ with CO_2 is compared with the group 3 metal cations and other lanthanide cations and periodic trends are discussed.

5.4 Experimental and Theoretical Methods

5.4.1 Experiments. The guided ion beam tandem mass spectrometer and the experimental procedure have been described in detail previously.[12,13,37,38] Briefly, singly charged Gd^+ ions were produced from Gd foil (Sigma-Aldrich, St. Louis, MO) using a direct current discharge flow tube (DC/FT) ion source.[39] A potential of -1000 to -1500 V was applied to a cathode consisting of the Gd foil attached to a tantalum holder. A gas mixture of 90% He and 10% Ar was continuously introduced into the source at a pressure of ~0.4 Torr. The DC discharge produced Ar^+ cations, which were accelerated toward and collided with the cathode, sputtering singly charged Gd^+ ions. To form $GdCO_2^+$ precursor

ions, CO_2 gas was leaked into the source about ~15 cm downstream from the cathode where Gd^+ ions were produced. This yielded the putative $Gd^+(OCO)$ adduct. The putative inserted $OGd^+(CO)$ precursor ion was formed by introducing O_2 and CO gases via separate inlets at ~15 and 30 cm downstream from the cathode, respectively. The precursor ions traveled through a meter-long flow tube, undergoing ~10^5 thermalizing collisions with the He/Ar gas mixture. Gd^+ precursor ions are assumed to have electronic energies of 0.04 ± 0.03 eV (temperature of 700 ± 400 K) as described elsewhere.[36] $GdCO_2^+$ precursor ions are assumed to be thermalized to the flow tube temperature at ~300 K. After ions were skimmed and focused, the precursor ion of interest was mass selected using a magnetic momentum analyzer. For sufficient mass separation, the ^{160}Gd isotope, being at least 2 Da heavier than all other naturally occurring isotopes, was used. Ions were decelerated to a specific kinetic energy prior to entering a radio frequency (rf) octopole ion beam guide, a section of which is surrounded by a reaction cell (effective length of ~8.26 cm). Xe and CO_2 gases were introduced into the cell at pressures of ~0.1 to ~0.4 mTorr for reaction with the precursor ions. In this pressure regime, single collisions dominate the reactions as was confirmed from cross section measurements at different neutral reactant pressures exhibiting no pressure dependence. Precursor and resulting product ions were extracted from the octopole and subsequently mass analyzed using a quadrupole mass filter and their intensities were measured as a function of precursor ion kinetic energy in the lab frame using a Daly detector.[40] Product ion intensities were corrected for any background reaction that does not occur in the cell and were converted to cross sections as a function of center-of-mass (CM) energy as detailed previously.[38] Precursor ion kinetic energy distributions measured from retarding experiments had a full-width at half maximum of ~0.5 eV, and

the uncertainty in the energy scale for this instrument was ± 0.1 eV (lab).

5.4.2 Data analysis. Threshold energies at 0 K, E_0, for the endothermic reactions studied here were obtained by modeling the product ion cross sections with the modified line-of-centers equation (5.2) using the data analysis program CRUNCH as described in detail elsewhere.[13,41]

$$\sigma(E) = \sigma_0 \sum_i g_i(E + E_i + E_{el} - E_0)^n/E \qquad (5.2)$$

In equation (5.2), E corresponds to the CM collision energy, σ_0 is an empirical scaling factor (which describes the efficiency of energy deposition for CID reactions),[41] *n* is an empirical fitting parameter that determines the shape of the cross section, and E_i is the rotational and vibrational energy of the reactants for state i, having a population degeneracy g_i ($\Sigma g_i = 1$). Calculation of E_i utilizes vibrational frequencies and rotational constants for the $GdCO_2^+$ reactants that were obtained from theoretical calculations described below. The reactant kinetic energy distributions were convolved with equation (5.2) before comparison with the experimental cross sections. E_0, σ_0, and *n* were determined from optimized fits to the experimental cross sections obtained by varying these parameters using a nonlinear least-squares procedure. The uncertainty in E_0 was determined from optimized fits to several independent data sets (4 to 18) and from the range of *n* parameters that can reproduce the experimental cross section. For exchange reactions between an ion and a neutral, there is a decrease in the product ion cross section at CM energies that exceed the BDE of the neutral because the product ion has sufficient energy to dissociate at these energies. A modified version of equation (5.2) that includes this dissociation probability as described in detail previously[42] was used to model this decrease. For CID experiments, BDEs correspond directly to the measured E_0 values, whereas for exchange reactions, M^+

+ AB → MA^+ + B, the BDE was obtained from expression (5.3), which assumes no barrier in excess of the reaction endothermicity.

$$D_0\left(M^+\text{-}A\right) = D_0(A\text{-}B) - E_0 \quad (5.3)$$

5.4.3 Theoretical calculations. To determine the ground and low-energy states for the $GdCO_2^+$ intermediates investigated experimentally, quantum chemical calculations were performed using the Gaussian09 package.[43] Most calculations, including relaxed potential energy scans where the O-Gd^+-CO angle is varied, were performed with density functional theory (DFT) at the B3LYP[44,45] level. These calculations use the relativistic Stuttgart Dresden[46] (SDD) effective small (28 electron) core potential (ECP) and the atomic natural orbital[47] (ANO) basis set for Gd and the Pople 6-311+G(3df) basis set for C and O. Theoretical BDEs were obtained from the difference in calculated energies between ground state intact and dissociated $GdCO_2^+$ species. BDEs for the $GdCO_2^+$ intermediates were additionally calculated at the PBE0[48,49] and CCSD(T,full)[50-53] levels of theory using the same ECP and basis sets. Calculations that utilize the 2nd-order Douglas-Kroll-Hess Hamiltonian (DKH2)[54,55] with the correlation consistent all-electron basis sets (cc-pVXZ-DK3 where X = T and Q)[56] for Gd developed by the Peterson group and corresponding aug-cc-pVXZ-DK basis sets for C and O were also carried out. Single point energies at the CCSD(T,full) level were computed using the optimized geometries and corresponding frequencies for the zero point energy correction obtained at the B3LYP/ANO level. Energies reported at all levels of theory include zero point energy corrections where vibrational frequencies were scaled by 0.989.[57] Rotational constants and vibrational frequencies for Gd^+(OCO) and OGd^+(CO) needed in the modeling of the experimental cross sections were obtained from calculations at the B3LYP/ANO level.

With the exception of the cc-pVXZ-DK3 basis sets for Gd, which were provided by Professor Peterson, the other basis sets (and SDD ECP) were obtained from the EMSL basis set exchange.[58,59]

5.5 Experimental and Theoretical Results

5.5.1 Gd^+ reaction with CO_2 to form GdO^+ and CO. In the energy dependent reaction between Gd^+ and CO_2, three product ions, GdO^+, $GdCO^+$, and GdO_2^+, are observed as shown recently.[36] The cross section for these product ions as a function of energy in the CM frame are shown here in Figure 5.1a. The GdO^+ product is formed via reaction (5.1). At the lowest collision energy (~0.02 eV), the cross section exceeds 100 $Å^2$, slightly below the theoretical collision limit according to the Langevin-Gioumousis-Stevenson (LGS)[60] model, which assumes an ion-induced dipole interaction potential, as shown by the black line in Figure 5.1a. The experimental cross section decreases with increasing collision energy, indicating that GdO^+ is formed in an exothermic and barrierless reaction, as discussed previously.[36] The rate coefficient, k, for reaction (5.1) can be computed from the cross section as described elsewhere.[38] At the two energies below 0.1 eV, the rate coefficients are 4.9 ± 1.0 and 4.0 ± 0.8 × 10^{-10} cm^3/s, respectively, compared with k_{LGS} = 6.3 × 10^{-10} cm^3/s, indicating that the reaction proceeds with 77 ± 15% and 64 ± 13% efficiency relative to the LGS collision limit at these two energies (corresponding to effective temperatures of 329 ± 167 and 724 ± 167 K, respectively). These coefficients compare fairly well with the rate coefficient of 3.4 ± 1.0 × 10^{-10} cm^3/s reported for this reaction at thermal (295 K) kinetic energies by Bohme and coworkers.[61]

A similar efficiency (64%) was also observed for the analogous reaction between

Figure 5.1. (a) Experimental product ion cross sections (symbols) as a function of center-of-mass (bottom *x*-axis) and laboratory (top *x*-axis) frame kinetic energy for the Gd^+ reaction with CO_2 at a pressure of ~0.31 mTorr. The black line corresponds to the theoretical collision limit given by the Langevin-Gioumousis-Stevenson (LGS) model, and the black arrows indicate D_0(OC-O) = 5.45 eV and the predicted decline in the cross section from the spectator stripping model (SSM) at 12.9 eV. For collision energies above 0.2 eV, an optimized composite fit for the ground and excited state GdO^+ products is indicated by the red solid line, see text, where the dashed line corresponds to the 0 K model (i.e., excluding convolution over reactant internal and kinetic energies) for the high-energy feature. An optimized fit for the $GdCO^+$ cross section is indicated by the solid green line, obtained by convolving the reactant kinetic energy distributions with equation (5.2). The dashed green line indicates the 0 K modeled $GdCO^+$ cross section, excluding convolution over the reactant kinetic and internal energy distributions. (b) Comparison between the experimental (open circles) and calculated GdO^+ cross sections from phase space theory using an exothermicity of 2.24 eV and scaling factor of 0.33 (red solid line) or an exothermicity of 0.19 eV and scaling factor of 0.38 (black solid line). The red and black dashed lines indicate the corresponding phase space theory cross sections for returning to reactants.

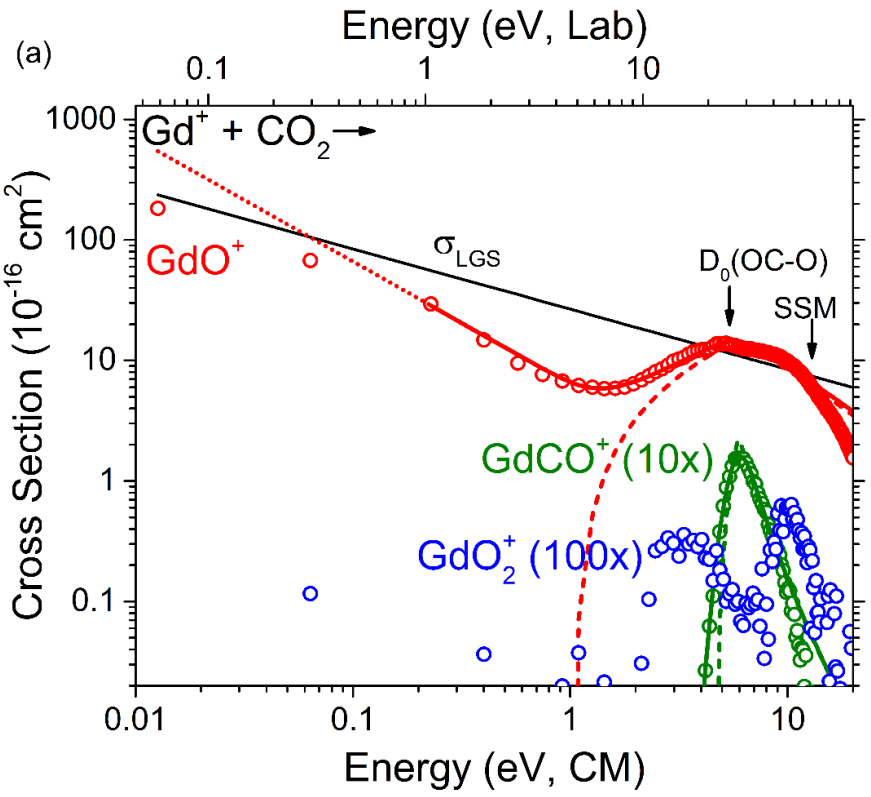
(a)
Energy (eV, Lab)
0.1
1
10
Gd+ + CO2
GdO+
σLGS
D0(OC-O)
SSM
GdCO+ (10x)
GdO2+ (100x)
Cross Section (10-16 cm2)
1000
100
10
1
0.1
0.01
0.1
1
10
Energy (eV, CM)

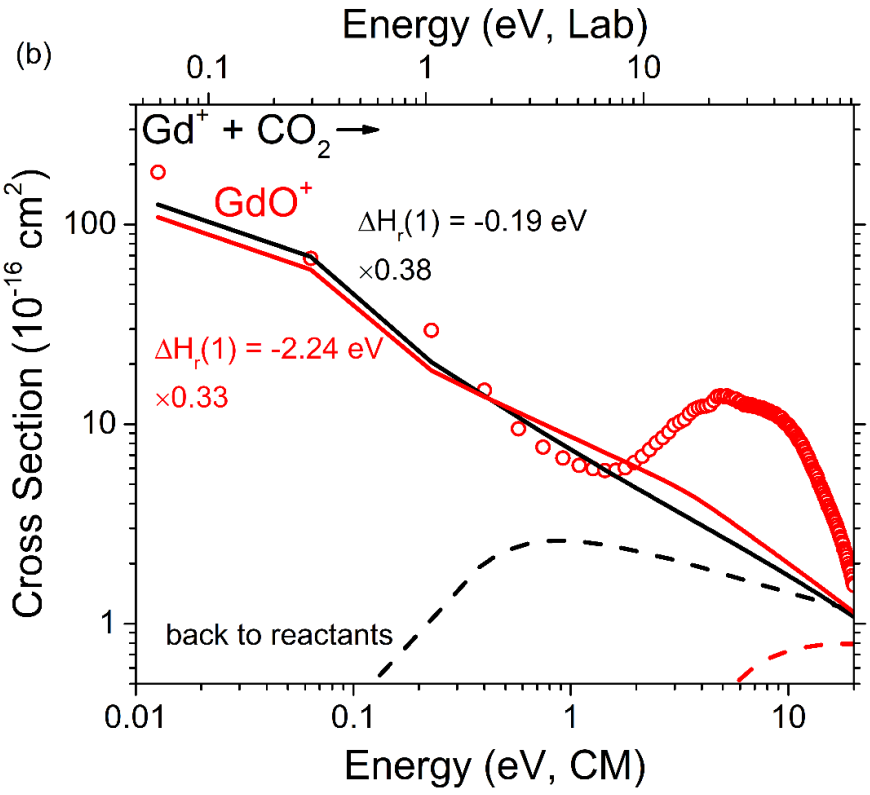
(b)
Energy (eV, Lab)
0.1
1
10
Gd+ + CO2
GdO+
ΔHr(1) = -0.19 eV
×0.38
ΔHr(1) = -2.24 eV
×0.33
back to reactants
Cross Section (10-16 cm2)
100
10
1
0.01
0.1
1
10
Energy (eV, CM)

CO_2 and the group 3 metal cation, Y^+, in GIBMS experiments.[19] Disregarding the half-filled 4f shell of Gd^+, Y^+ is isovalent with Gd^+ and has a reaction (5.1) exothermicity of 1.79 ± 0.18 eV,[19] which is slightly smaller but comparable with that for Gd^+, 2.24 ± 0.10 eV (determined from $D_0(Gd^+\text{-}O) = 7.69 \pm 0.10$ eV[36] and $D_0(OC\text{-}O) = 5.45$ eV[62]). The GdO^+ cross section has an energy dependence of $E^{-0.6\pm0.1}$ for energies below 0.2 eV and an energy dependence of $E^{-1.0\pm0.1}$ for energies in the range of 0.2 to 1.5 eV (red solid line, Figure 5.1a). This contrasts with the behavior of the YO^+ cross section, which follows the expected energy dependence of $E^{-0.5}$ from the LGS model up to 1 eV.[19] The possible origins for these differences in reactivity between Gd^+ and Y^+ are discussed further below.

To investigate the energy dependent GdO^+ cross section from reaction (5.1) in more detail, phase space theory (PST) calculations were carried out using modified programs based on those developed by Chesnavich and Bowers.[63,64] The PST cross section calculated using an exothermicity of 2.24 eV is shown by the red line in Figure 5.1b. Here, the PST cross section has been scaled by 0.33 to improve the agreement with the experimental data (Figure 5.1b). The reduced efficiency of the reaction is also evident from the smaller cross section compared with that predicted from the LGS model. Slightly better agreement can be obtained using an exothermicity of 0.19 eV and a scaling factor of 0.38 (black line, Figure 5.1b). These results contrast with PST calculations for the exothermic reaction of Gd^+ with O_2 to form GdO^+ and O, where relatively good agreement between the calculated and experimental GdO^+ cross sections was obtained without the need to scale the calculated cross section.[65] The lower exothermicity and scaling factor needed in the PST calculations to reproduce the experimental data suggest that the reaction proceeds less efficiently than what would be expected on the basis of the relatively large reaction (5.1) exothermicity for

Gd^+. This could presumably be a result of $Gd^+(OCO)$ adducts that do not yield GdO^+ and CO products, but preferentially dissociate back to Gd^+ and CO_2 reactants. As discussed in more detail below, this hypothesis agrees with our observation of an electronically excited $Gd^+(OCO)$ adduct for which loss of CO_2 is energetically favored over rearrangement to an inserted $OGd^+(CO)$ complex that forms GdO^+ and CO. Such unreactive adducts that compete and reduce the efficiency of reaction (5.1) are not explicitly accounted for in the PST calculations and could therefore contribute to the scaling factor needed to reproduce the experimental results in Figure 5.1b.

5.5.2 High-energy GdO^+ feature. At higher energies, the GdO^+ cross section from reaction (5.1) exhibits a distinct second feature with an apparent threshold near 1 eV and a cross section that exceeds the LGS limit by ~20% from ~4.5 – 10 eV (Figure 5.1). This feature peaks near $D_0(OC\text{-}O)$ = 5.45 eV as expected. At higher energies, the GdO^+ cross section remains relatively constant and only begins to decline sharply at around 10 eV, much greater than $D_0(OC\text{-}O)$. A similar delay was observed in the Gd^+ reaction with O_2,[65] and suggests that the GdO^+ product may be formed via an impulsive reaction mechanism at these higher energies. A simple model for an impulsive mechanism is the spectator stripping model (SSM), which assumes that reaction will occur from the interaction of Gd^+ with one of the oxygen atoms while the rest of the CO_2 molecule (i.e., CO) remains a "spectator."[66] This constrains the available energy for reaction such that GdO^+ will only have sufficient energy to dissociate at significantly higher energies than $D_0(OC\text{-}O)$. The SSM predicts that GdO^+ will have enough energy to dissociate at CM energies exceeding 12.9 eV (Figure 5.1a), which is slightly higher than the experimental onset.

The origins of this distinctive high-energy GdO^+ feature could be the formation of

electronically excited GdO^+ products, as also postulated in the reactions of V^+,[14] Zr^+,[20] and Nb^+[18] with CO_2. To estimate the threshold energy for the high-energy GdO^+ feature from the data in Figure 5.1a, the contribution from the ground state GdO^+ product can be subtracted from the data and the remaining cross section can be modeled with equation (5.2). Assuming the cross section for the ground state GdO^+ product follows an energy dependence of $E^{-1.0\pm0.1}$ above 0.2 eV, modeling the remaining high-energy feature yields an E_0 value of 1.01 ± 0.12 eV (dashed line, with the composite cross section shown by the solid line, Figure 5.1a). Combining this E_0 value with the reaction (5.1) exothermicity of 2.24 ± 0.10 eV gives an excitation energy of 3.25 ± 0.16 eV relative to the GdO^+ ground state. The optimized parameters used in the modeling of this reaction and in all other endothermic reactions here are summarized in Table 5.1.

Table 5.1. Optimized parameters of equation (5.2) obtained by modeling the experimental cross sections.[a]

Reaction	σ_0	*n*	E_0 (eV)	D_0 (eV)
$Gd^+ + CO_2 \rightarrow GdO^+ + CO$[b]	5.3 ± 1.4	1.7 ± 0.2	1.01 ± 0.12	3.25 ± 0.16
$Gd^+ + CO_2 \rightarrow GdCO^+ + O$[c]	0.8 ± 0.2	2.0 ± 0.2	4.80 ± 0.06	0.65 ± 0.06
$GdO^+ + CO \rightarrow Gd^+ + CO_2$[c, d]	0.003 ± 0.002	2.4 ± 0.2	2.16 ± 0.27	2.16 ± 0.27
$OGd^+(CO) + Xe \rightarrow GdO^+ + CO + Xe$	16.0 ± 0.5	1.3 ± 0.2	0.57 ± 0.05	0.57 ± 0.05
$Gd^+(OCO) + Xe \rightarrow Gd^+ + CO_2 + Xe$	71 ± 8	1.3 ± 0.2	0.38 ± 0.05	0.38 ± 0.05

[a] Uncertainties correspond to one standard deviation.
[b] High-energy feature. The excitation energy relative to the ground state of GdO^+ is provided instead of D_0, by adding E_0 to the exothermicity (2.24 ± 0.10 eV) of reaction (5.1).
[c] From reference 36.
[d] The endothermicity of the reaction, i.e., E_0, is provided instead of D_0.

5.5.3 Gd^+ reaction with CO_2 to form $GdCO^+$ and O. In the reaction between Gd^+ and CO_2, the $GdCO^+$ product ion is formed in an endothermic reaction, as shown in Figure 5.1a (scaled up by a factor of 10). The cross section has an apparent onset of ~4 eV and peaks around 5.5 eV, consistent with the OC-O BDE of 5.45 eV.[62] This cross section declines at higher energies because the $GdCO^+$ product ion has enough energy to dissociate to $Gd^+ + CO$. Modeling these data with equation (5.2) yields a 0 K threshold energy of 4.80 ± 0.06 eV, which gives a BDE for Gd^+-CO of 0.65 ± 0.06 using equation (5.3).[36]

5.5.4 Gd^+ reaction with CO_2 to form GdO_2^+. The energy dependent cross section (scaled by a factor of 100) for the GdO_2^+ product, also observed in the reaction between Gd^+ and CO_2, is shown in Figure 5.1a. This cross section exhibits two distinct features, which do not exceed 10^{-18} cm^2. Examination of the pressure dependence of this cross section demonstrates that the low-energy feature depends linearly on the pressure of CO_2, indicating it is formed in a sequential reaction, whereas the higher energy feature has no dependence on pressure. Thus, the low and high energy features can be attributed to reactions (5.4) and (5.5), respectively.

$$GdO^+ + CO_2 \rightarrow GdO_2^+ + CO \qquad (5.4)$$

$$Gd^+ + CO_2 \rightarrow GdO_2^+ + C \qquad (5.5)$$

Using $D_0(OGd^+\text{-}O) = 2.86 \pm 0.08$ eV[65] and $D_0(Gd^+\text{-}O) = 7.69 \pm 0.10$ eV,[36] reaction (5.5) is expected to have a threshold of 6.01 ± 0.13 eV with the GdO_2^+ product having sufficient energy to dissociate at energies exceeding 8.87 ± 0.10 eV. These values are in relatively good agreement with the apparent threshold and decline in the higher energy feature of the experimental data (Figure 5.1a).

When GdO_2^+ is formed sequentially in reaction (5.4), its cross section is more

appropriately envisioned by using the GdO^+ product as the precursor ion, as was performed for the dioxides in the Re^+, Os^+, and Gd^+ reactions with O_2.[65,67,68] Figure 5.2 shows the reanalyzed GdO_2^+ cross section as a function of CM energy, where the energy scale reflects that of the $GdO^+ + CO_2$ reactants and includes the 2.24 eV exothermicity for reaction (5.1). Figure 5.2 also shows a direct measurement of the cross section for reaction (5.4). The apparent thresholds of the sequential and direct cross sections are in the same general

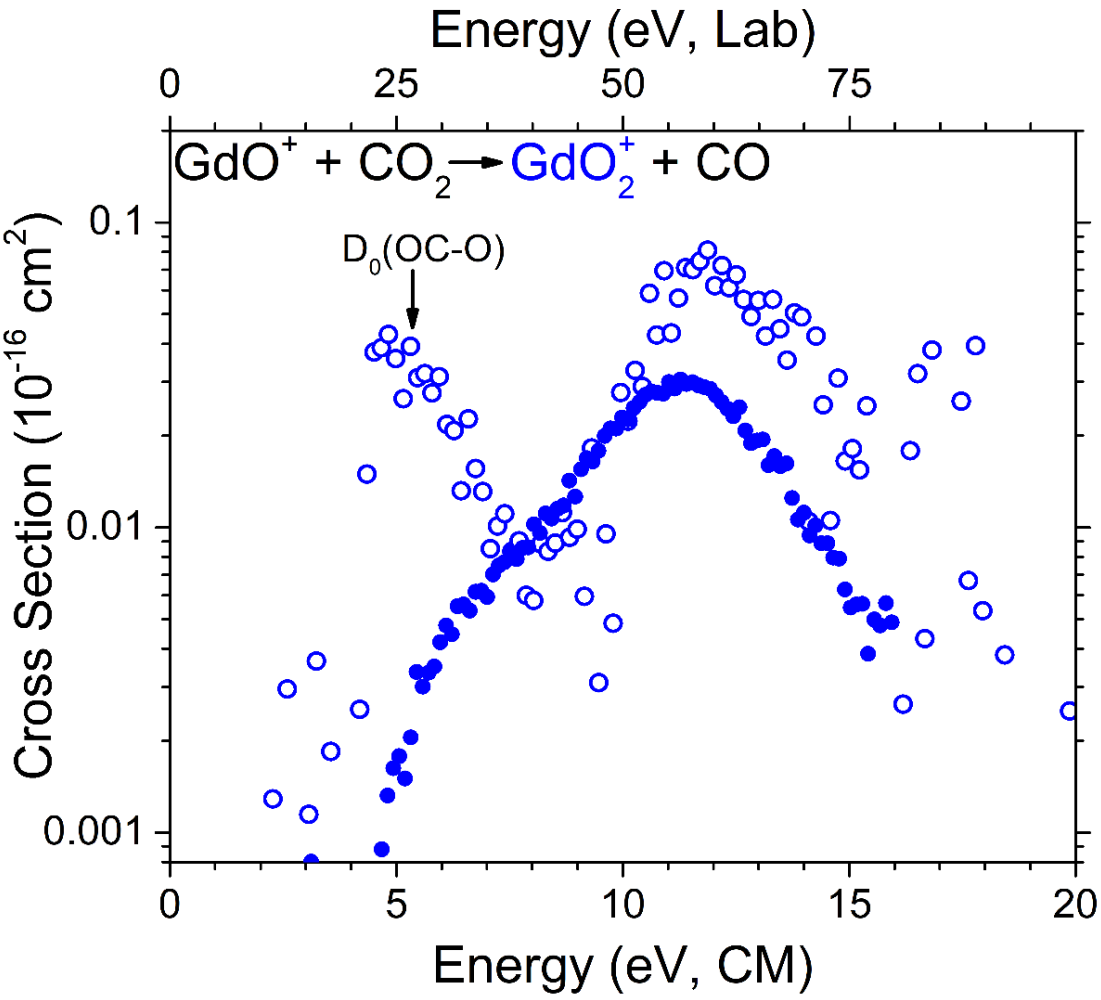

Figure 5.2. Reanalysis of the GdO_2^+ cross section (open blue circles) from Figure 5.1a assuming GdO^+ is the precursor ion reacting in a sequential reaction with CO_2. The 2.24 eV exothermicity of reaction (5.1) is included in the CM energy scale. The GdO_2^+ cross section from a direct reaction between GdO^+ and CO_2 is shown by the solid blue circles.

vicinity, but elevated compared with the thermodynamic threshold of 2.59 ± 0.08 eV = D_0(O-CO) – D_0(OGd^+-O). This indicates that reaction (5.4) has a substantial barrier, not unlike the recent examination of the $Sm^+ + CO_2$ system[24] and previous results for the reaction of YO^+ with CO_2 to form $YO_2^+ + CO$.[19] In both these cases, measurements of the reverse reactions demonstrated the presence of a barrier in excess of the reaction endothermicities. At higher energies, the shapes of the sequential and direct cross sections for GdO_2^+ differ appreciably (even considering that the higher energy feature is the result of reaction (5.5), which will not occur in the direct reaction). This result can be attributed to the fact that in the sequential reaction, the GdO^+ "reactant" has a very different distribution of internal and kinetic energies than in the better controlled direct reaction.

5.5.5 Reverse reaction, $GdO^+ + CO$ to form $Gd^+ + CO_2$. Additional insight into the Gd^+ reaction with CO_2 to form GdO^+ and CO can be obtained by investigating the reverse reaction (5.6), which should be endothermic by 2.24 ± 0.10 eV.

$$GdO^+ + CO \rightarrow Gd^+ + CO_2 \qquad (5.6)$$

GdO^+ reacts with CO in endothermic reactions to form Gd^+ and GdO_2^+ as shown recently.[36] The resulting energy dependent cross section for Gd^+ from this reaction is shown in Figure 5.3. The Gd^+ cross section exhibits two features: a low-energy feature arising from process (5.6) and a high-energy feature resulting from CID of GdO^+ with an onset consistent with D_0(Gd^+-O), as modeled and discussed elsewhere.[36] The magnitude of the Gd^+ cross section from process (5.6) does not exceed 2×10^{-18} cm^2, indicating that this reaction is relatively inefficient. As shown previously,[36] modeling this cross section with equation (5.2) yields a threshold energy of 2.16 ± 0.27 eV, which is consistent with the exothermicity determined for the forward reaction of 2.24 ± 0.10 eV obtained from measurements of $D_0(GdO^+)$ from

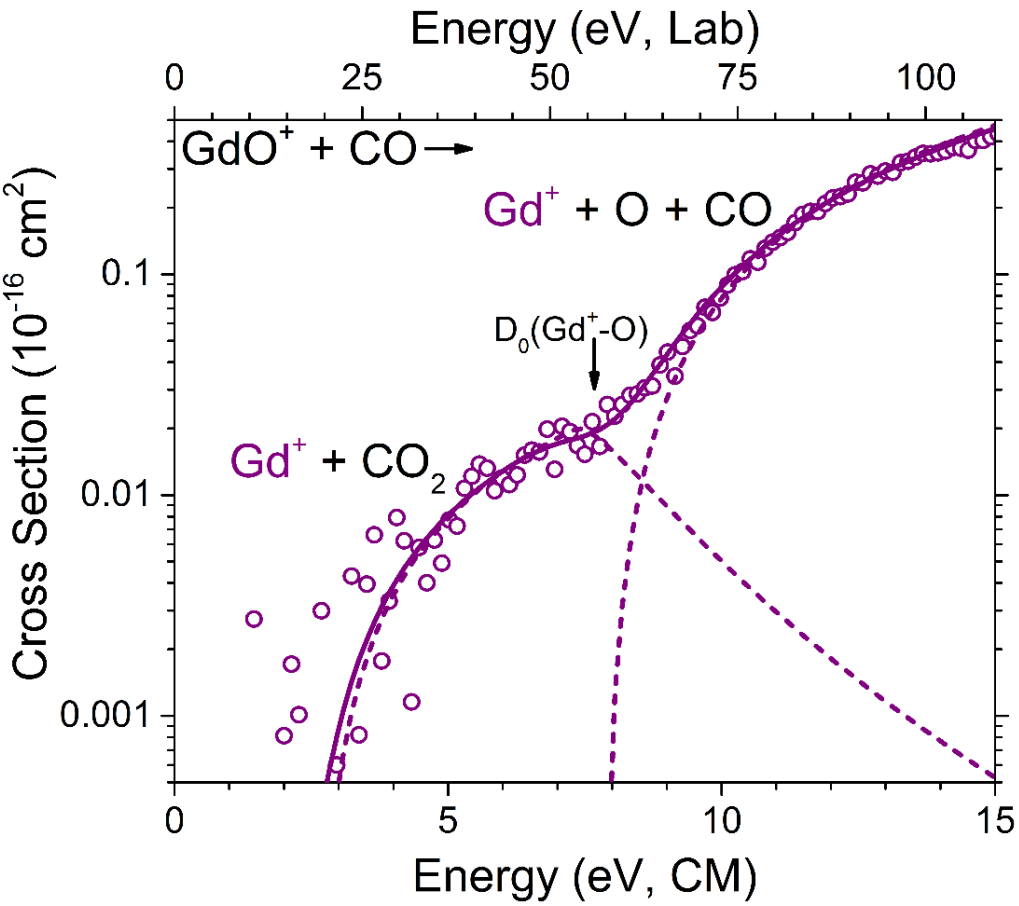

Figure 5.3. Gd^+ cross section as a function of center-of-mass (bottom *x*-axis) and laboratory (top *x*-axis) frame kinetic energy resulting from the reaction between GdO^+ and CO. The arrow indicates the GdO^+ BDE of 7.69 ± 0.10 eV.[36] A combined optimized fit for the two Gd^+ features, as described in reference 36, is indicated by the solid line and includes convolution of equation (5.2) over the reactant kinetic energies. The dashed lines correspond to the modeled cross sections at 0 K excluding convolution over the reactant kinetic and internal energies.

several different reactions.[36] The good agreement suggests that ground state Gd^+ and CO_2 products must be formed, and these results confirm that there is no barrier in excess of the endothermicity of reaction (5.6), consistent with the cross section for the forward reaction (5.1), Figure 5.1.

5.5.6 CID of $Gd^+(OCO)$. The energetics of the intermediates along the PES for the Gd^+ reaction with CO_2 can potentially be measured by forming these complexes in the

source and dissociating them using Xe as collision gas. CID of $GdCO_2^+$ precursor ions formed by introducing CO_2 gas into the source resulted in exclusive loss of CO_2 to form Gd^+ as the only product ion according to process (5.7).

$$Gd^+(OCO) + Xe \rightarrow Gd^+ + CO_2 + Xe \qquad (5.7)$$

This indicates that only a weakly bound $Gd^+(OCO)$ adduct is formed. The energy dependent cross section for Gd^+ is shown in Figure 5.4 and has an apparent threshold near

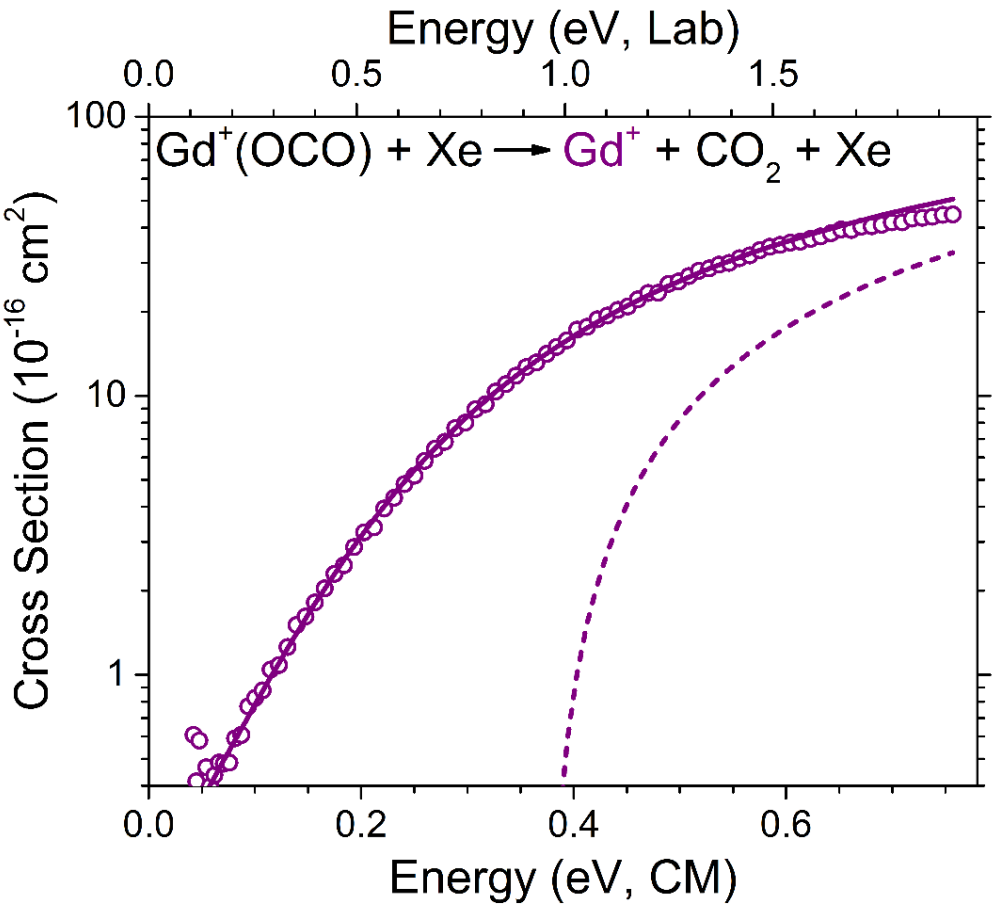

Figure 5.4. Product ion cross sections as a function of center-of-mass (bottom *x*-axis) and laboratory (top *x*-axis) frame kinetic energy for CID of $Gd^+(OCO)$ with Xe. This precursor ion is formed by introducing CO_2 into the source. An optimized fit for the Gd^+ cross section obtained by convolving equation (5.2) with the reactant kinetic energy distributions is indicated by the solid line. The dashed line corresponds to the modeled cross section at 0 K, which excludes convolution over the internal and kinetic energy distributions of the reactants.

0 eV. The cross section increases with increasing energy, exceeding 40 $Å^2$ at the highest energies measured, which indicates that process (5.7) is relatively efficient as a result of the weak interaction between Gd^+ and the CO_2 molecule. Modeling the cross section with equation (5.2) yields an E_0 value and corresponding $D_0(Gd^+\text{-}OCO)$ of 0.38 ± 0.05 eV (dashed line, Figure 5.4). Attempts were made to form an inserted $OGd^+(CO)$ precursor ion by altering the source conditions, including changing the CO_2 pressure and the DC discharge voltage used to generate Gd^+. However, the GdO^+ product ion corresponding to loss of CO could not be observed even at CM energies up to 8 eV (data not shown). If present, CID of $Gd^+(OCO)$ yields GdO^+ + CO with a cross section below ~0.5×10^{-18} $Å^2$.

5.5.7 CID of $OGd^+(CO)$. The inserted $OGd^+(CO)$ precursor ion could be formed by first introducing O_2 in the source to form GdO^+ and separately introducing CO farther downstream for reaction with GdO^+. CID of this $GdCO_2^+$ precursor ion resulted in exclusive loss of CO to produce GdO^+ according to reaction (5.8).

$$OGd^+(CO) + Xe \rightarrow GdO^+ + CO + Xe \qquad (5.8)$$

The cross section for the GdO^+ product is shown as a function of CM energy in Figure 5.5. The apparent threshold energy is near 0.1 eV. The GdO^+ cross section does not exceed 10 $Å^2$ at the highest energies measured, indicating that this process is less efficient than reaction (5.7), consistent with the slightly larger threshold for process (5.8). Modeling the cross section yields an E_0 and corresponding $D_0(OGd^+\text{-}CO)$ value of 0.57 ± 0.05 eV (Table 5.1), which is about a factor of two larger than the BDE of the CO_2 adduct.

5.5.8 Theoretical calculations for $GdCO_2^+$. Quantum chemical calculations were performed to determine the electronic states of stable $GdCO_2^+$ intermediates for comparison with those probed in the experiments, and to gain insight into the reaction

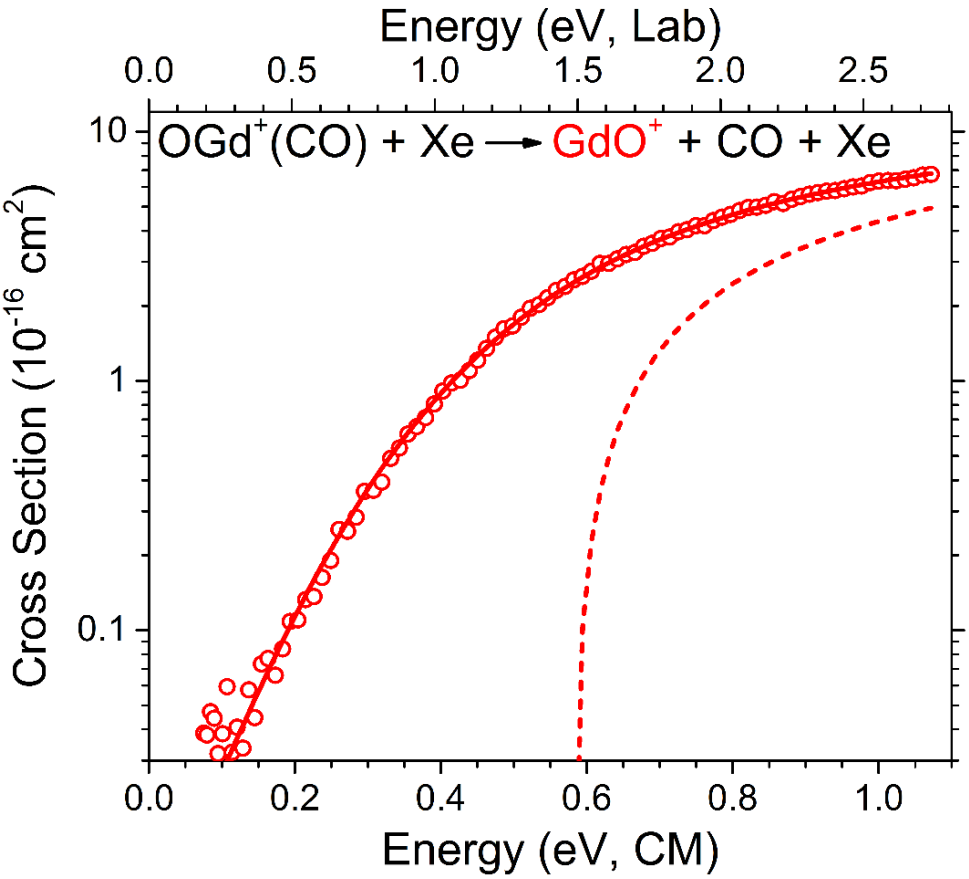

Figure 5.5. Product ion cross sections as a function of center-of-mass (bottom *x*-axis) and laboratory (top *x*-axis) frame kinetic energy for CID of $OGd^+(CO)$ with Xe. This precursor ion is formed by introducing O_2 and CO at ~15 and 30 cm, respectively, downstream from the cathode, where Gd^+ ions are produced. An optimized fit for the GdO^+ cross section obtained by convolving equation (5.2) with the reactant kinetic energy distributions is indicated by the solid line. The dashed line corresponds to the modeled cross section at 0 K, which excludes convolution over the internal and kinetic energy distributions of the reactants.

mechanism of process (5.1). Most of these calculations were carried out at the B3LYP level using the ANO basis set and the SDD ECP for Gd and the 6-311+G(3df) basis set for O and C. Various geometries and electronic states with multiplicities of 10 and 8 were explored. The energies, bond lengths, angles, and vibrational frequencies from these calculations for various optimized $GdCO_2^+$ complexes are summarized in the Supporting Information (Section 5.7). Molecular orbitals (mos) that result from the interactions of the

valence electrons of Gd^+ ($4f^75d^16s^1$), the two O atoms ($2p^4$), and C ($2p^2$) are shown in Figure 5.6 for different $GdCO_2^+$ geometries and electronic states. The mos resulting from the seven 4f valence electrons of Gd^+ are omitted for simplicity because these form mostly nonbonding orbitals similar to their atomic orbitals. Representative mos for the 4f electrons of different $GdCO_2^+$ geometries with $C_{\infty v}$ and C_s symmetry are shown in the Supporting Information (Section 5.7).

The interaction between Gd^+ and CO_2 in linear $Gd^+(OCO)$ adducts (having $C_{\infty v}$ symmetry) is primarily electrostatic in nature such that the valence electrons of the two O atoms and C combine to form mos like those in free CO_2. This is demonstrated in Figure 5.6a, where the $2p_z$ orbitals of O and C combine in-phase to form a 2σ bonding mo, the $2p_x$ and $2p_y$ orbitals combine in-phase to form 2π bonding mos, and the out-of-phase combination of the $2p_x$ and $2p_y$ orbitals of the O atoms form nonbonding 3π mos. In these linear $Gd^+(OCO)$ structures, the 5d and 6s valence electrons of Gd^+ form mainly nonbonding mos. The lowest energy linear $Gd^+(OCO)$ structure is found to have a $^8\Sigma^-$ electronic state, where both valence electrons of Gd^+ fill the nonbonding 3σ mo comprising primarily the 6s (with some $5d_z^2$ character) atomic orbital of Gd^+. A $Gd^+(OCO)$ adduct with a $^{10}\Delta$ electronic state is calculated to be only 0.03 eV higher in energy, where one of the 3σ electrons has moved to occupy a 5d orbital comprising a nonbonding 2δ mo, with both these electrons high-spin coupling with the 4f electrons (Supporting Information, Section 5.7). The electron in the 3σ mo can also be low-spin coupled resulting in a $^8\Delta$ electronic state, Figure 5.6a, which is 0.64 eV higher in energy than the $^8\Sigma^-$ state. Alternatively, the 5d electron of Gd^+ can be in a mostly nonbonding 4π orbital to give a Π electronic state. The resulting high-spin coupled $^{10}\Pi$ state is 0.16 eV higher in energy than

Figure 5.6. Electronic states and molecular orbitals resulting from the valence electrons of Gd^+, C, and O for various optimized $GdCO_2^+$ structures with (a) $C_{\infty v}$ and (b) C_s symmetry calculated at the B3LYP/ANO level of theory. The 4f electrons of Gd^+ form mainly nonbonding molecular orbitals similar to their atomic orbitals and are omitted (see Supporting Information, Section 5.7). Unless otherwise noted, the electronic configurations shown are those for a multiplicity of 8, with electrons indicated in red resulting in states with a multiplicity of 10 if both electrons are high-spin coupled with the seven 4f electrons.

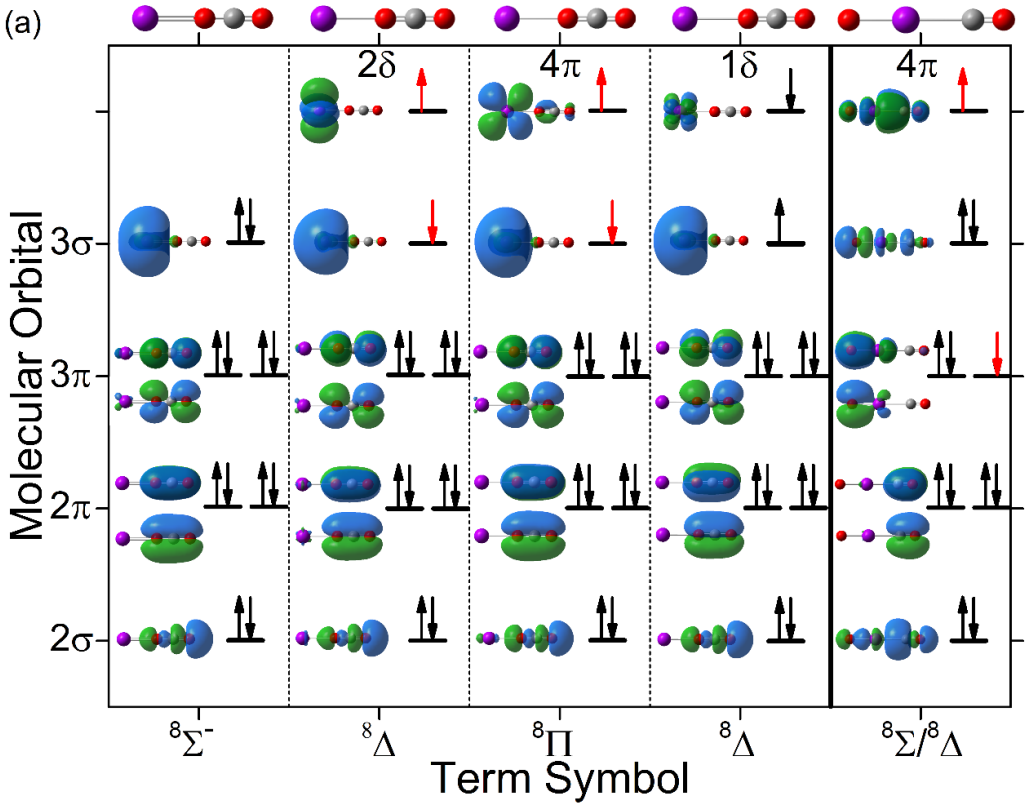
(a)
2δ
4π
1δ
4π
Molecular Orbital
3σ
3π
2π
2σ
$^8\Sigma^-$
$^8\Delta$
$^8\Pi$
$^8\Delta$
$^8\Sigma/^8\Delta$
Term Symbol

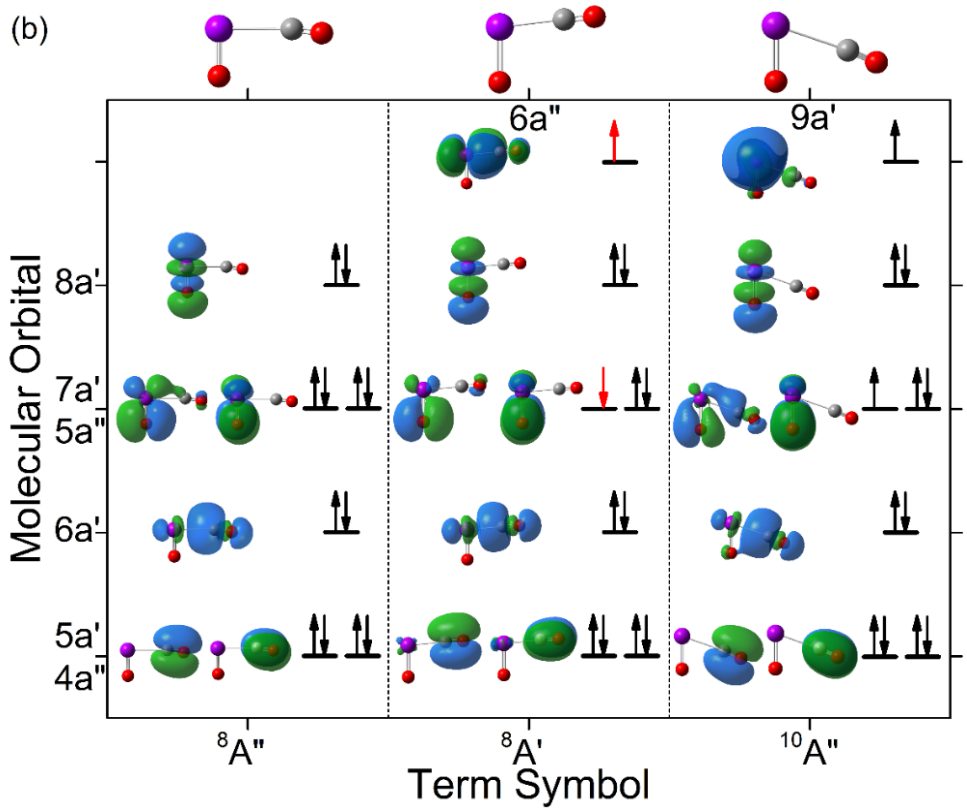
(b)
6a"
9a'
Molecular Orbital
8a'
7a'
5a"
6a'
5a'
4a"
^{8}A"
^{8}A'
^{10}A"
Term Symbol

the $^{8}\Sigma^{-}$ state, whereas the low-spin $^{8}\Pi$ state is significantly higher in energy at 0.58 eV above the $^{8}\Sigma^{-}$ state. Another $^{8}\Delta$ electronic state moves the 5d valence electron of Gd^{+} to occupy a $4f_{\delta}$ atomic orbital in a low-spin configuration. This $4f^{8}$ ($^{7}\Delta$) $6s^{1}$ configuration is predicted to be 0.12 and 0.18 eV lower in energy than the $^{8}\Delta$ and $^{8}\Pi$ states (with $4f^{7}5d^{1}6s^{1}$ configurations on Gd^{+}), respectively. The B3LYP/ANO calculations likely overestimate the stability of the $4f^{8}$ electronic configuration because calculations utilizing the same basis set and level of theory predict the ^{8}F ($4f^{8}6s^{1}$) electronically excited state of Gd^{+} to have an excitation energy relative to the ^{10}D ($4f^{7}5d^{1}6s^{1}$) ground state that is smaller by ~0.75 eV compared with experiment.[36]

For linear $OGd^{+}(CO)$ geometries ($C_{\infty v}$ symmetry), two stable local minima were identified having multiplicities of 8 and 10 and electronic states of Σ or Δ. In these linear structures, the valence electrons of C and O form 2σ and 2π bonding mos similar to those in free CO (experimental r = 1.128 Å) resulting in C-O bond lengths of 1.13 Å (Figure 5.6a, Supporting Information, Section 5.7). The 2σ mo has some bonding character from the $5d_{z}^{2}$ Gd^{+} atomic orbital. The mos formed between Gd^{+} and O are similar to those in GdO^{+},[36] where the 2p orbitals of O interact with three 5d orbitals of Gd^{+} to form 3π and 3σ bonding mos. Five of the six valence electrons occupy these mos with one electron remaining unpaired in the 3π mos, while a single unpaired electron occupies a 4π mo, resulting predominantly from an in-phase combination between a 5d Gd^{+} orbital and 2p O and C orbitals. Multiplicities of 10 and 8 are obtained by high or low-spin coupling the unpaired 3π electron with the 4f electrons (Figure 5.6a). We also located a $^{8}\Sigma^{-}$ electronic state in which the 3π mo is doubly occupied, but this optimized linear $OGd^{+}(CO)$ structure has two imaginary bending frequencies (Supporting Information, Section 5.7).

The search for stable inserted $OGd^+(CO)$ complexes with C_s symmetry yielded a global minimum $^8A''$ electronic state with an O-Gd^+-CO angle of 87° and Gd^+-O and Gd^+-CO bond lengths of 1.77 and 2.70 Å, respectively (Figure 5.6b). The C-O bond length of the adduct is calculated as 1.12 Å, consistent with the experimental (calculated) bond length of free CO of 1.128 Å (1.124 Å). In this $OGd^+(CO)$ complex, two of the 2p atomic orbitals of the CO adduct combine in-phase to form bonding 5a′ and 4a″ mos similar to the π bonding mos in free CO, as shown in Figure 5.6b. An in-phase combination of the remaining 2p C and O orbitals in the adduct with a 5d (having $5d_z^2$ character) atomic orbital of Gd^+ gives rise to a σ-type bonding 6a′ mo. Thus, the interaction between Gd^+ and CO in this inserted $OGd^+(CO)$ structure should be slightly stronger than just electrostatics. The bonding of the O atom in this inserted $OGd^+(CO)$ complex is similar to that of GdO^+, where effectively a triple bond is formed from the interaction of two 5d valence electrons of Gd^+ with the four 2p valence electrons of the O atom.[36] In this structure, two 5d orbitals of Gd^+ combine with 2p orbitals of O to form bonding 7a′ and 5a″ mos (like the π bonding mos in GdO^+), and the remaining 2p orbital of O combines with a 5d orbital of Gd^+ having $5d_z^2$ character to form a bonding 8a′ mo (like the σ bonding mo in GdO^+), Figure 5.6b.[36] Several other optimized $OGd^+(CO)$ structures resulting in local minima with $^{10}A'$, $^{10}A''$, and $^8A'$ electronic states were also found that were significantly higher in energy at ~1.5 to 3 eV above the global $^8A''$ minimum (Supporting Information, Section 5.7). The A′ electronic states have similar mos as those of the $^8A''$ ground state, except that one of the 7a′ electrons has moved to occupy a 6a″ mo comprising a slightly bonding 5d Gd^+ atomic orbital with the 2p C orbital (Figure 5.6b). A multiplicity of 10 or 8 results if the 7a′ electron high or low spin-couples with the 6a″ and 4f electrons. For the $^8A'$ state, two different geometries

yielded local minima, with O-Gd^+-CO bond angles of 31 and 96° (Figure 5.6b), respectively, where the former corresponds to a CO_2 adduct rather than an inserted $OGd^+(CO)$ complex (Supporting Information, Section 5.7). For the $^{10}A'$ state, a local minimum was located having a similar geometry (O-Gd^+-CO angle of 97°) as the inserted $OGd^+(CO)$ $^8A'$ state. The inserted $OGd^+(CO)$ complexes with A′ states are about 2.9 eV higher in energy than the $^8A''$ ground state, whereas the $Gd^+(OCO)$ $^8A'$ adduct is slightly lower in energy at 2.2 eV above the ground state (Supporting Information, Section 5.7). Three optimized structures with $^{10}A''$ electronic states were obtained where one of the 7a′ electrons has moved to occupy a 9a′ orbital that corresponds to a mostly nonbonding 6s atomic orbital of Gd^+ with some $5d_z^2$ character (Figure 5.6b). These structures include a nonlinear CO_2 adduct with O-Gd^+-CO angle of 29° and two inserted structures with angles of 71° (Figure 5.6b) and 129°, respectively. The $Gd^+(OCO)$ adduct is 1.6 eV higher in energy than the $^8A''$ ground state, whereas both inserted structures are 3.0 eV above the global minimum (Supporting Information, Section 5.7).

5.5.9 Theoretical potential energy surfaces (PESs). Reaction (5.1) between ground state Gd^+ (^{10}D) and CO_2 ($^1\Sigma_g^+$) reactants to form ground state GdO^+ ($^8\Sigma^-$) and CO ($^1\Sigma^+$) products is formally spin-forbidden. Thus, the reaction with CO_2 must proceed via a two-state reactivity (TSR)[35] mechanism involving a crossing of potential energy surfaces (PESs) with different spin. This is consistent with the exothermic reaction (5.1) exhibiting an energy dependence of E^{-1} (Figure 5.1) for ground state products,[69,70] where the deviation from the expected $E^{-0.5}$ energy dependence of the LGS model can possibly be attributed to the effect of the surface crossing.[35] Additionally, the high-energy GdO^+ feature that appears in Figure 5.1a can be explained by the formation of an electronically excited GdO^+ product

in a spin-allowed process, as has been observed for other metal systems.[14,18,20] To explore the reaction mechanism, relaxed PES scans were calculated at the B3LYP/ANO level as a function of O-Gd^+-CO angle for multiplicities of 10 (reactants) and 8 (products) having A′ and A″ symmetries. These surfaces are shown in Figure 5.7 and have minima that correspond to the optimized $GdCO_2^+$ structures already discussed. The geometries, energies, and vibrational frequencies for the stationary points along these surfaces, including the transition states (TS), are listed in the Supporting Information (Section 5.7).

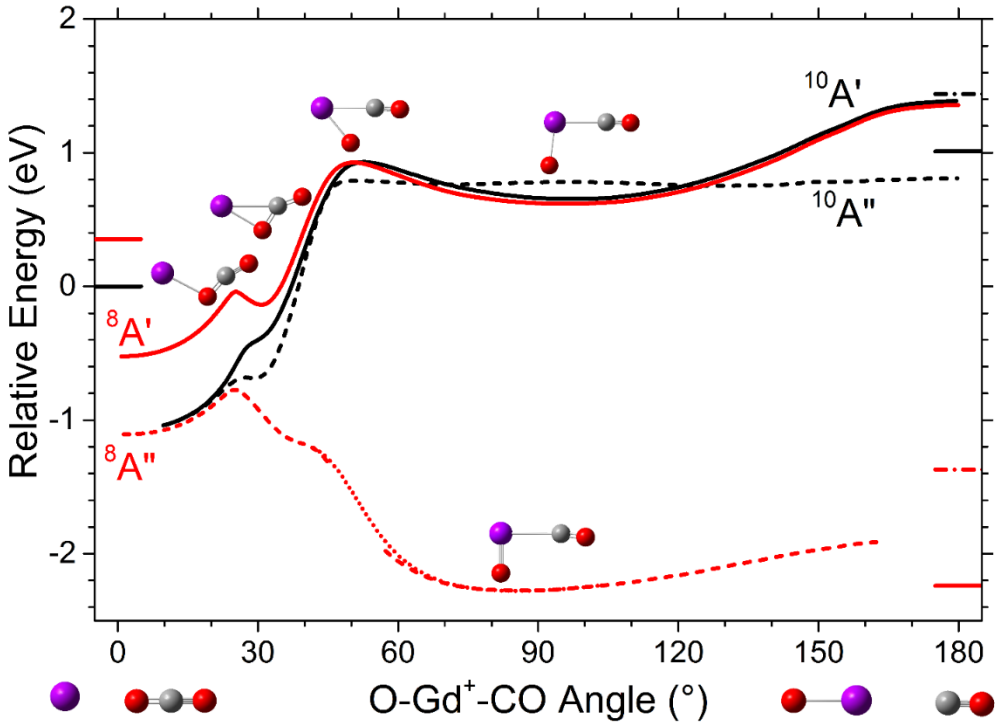

Figure 5.7. Relaxed potential energy surface scans as a function of $OGd^+(CO)$ angle calculated at the B3LYP/ANO level of theory. Surfaces are separated into A′ (solid) and A″ (dash) symmetry having dectet (black) and octet (red) multiplicities. Horizontal bars indicate the experimental (solid) and calculated (dash-dot) energies for the ground and electronically excited states of the reactants, Gd^+ (^{10}D and ^8D) + CO_2 ($^1\Sigma_g^+$), and products, GdO^+ ($^8\Sigma$, $^{10}\Pi$) + CO ($^1\Sigma^+$). The red dotted $^8A''$ surface was obtained from a relaxed potential energy surface scan that varied the O and CO distance (which essentially changes the O-Gd^+-CO angle in this range) because scans that explicitly varied the O-Gd^+-CO angle resulted in a break in the $^8A''$ surface such that the CO adduct was no longer as closely bound to GdO^+.

The results in Figure 5.7 indicate that the reaction between ground state Gd^+ (^{10}D) and CO_2 ($^1\Sigma_g^+$) reactants can be initiated on $^{10}A'$ and $^{10}A''$ surfaces by forming linear $Gd^+(OCO)$ adducts that are both about ~1.1 eV below the reactant asymptote. Interestingly, there is an $^8A''$ PES that is even slightly lower in energy than the $^{10}A'$ and $^{10}A''$ surfaces for adducts with O-Gd^+-CO angles less than ~25°. The small energy gap between these octet and dectet surfaces in the entrance channel of the reaction can lead to rapid spin pre-equilibrium,[71,72] such that reaction (5.1) can proceed efficiently along the $^8A''$ surface to form the ground state $^8A''$ $OGd^+(CO)$ intermediate, which can subsequently dissociate to ground state GdO^+ ($^8\Sigma^-$) and CO ($^1\Sigma^+$) products. This is consistent with the experimental observation of the relatively efficient exothermic reaction (Figure 5.1). The small energy gap between the octet and dectet surfaces is also demonstrated in the Supporting Information (Section 5.7), where calculated PES scans are shown for linear $Gd^+(OCO)$ adducts as a function of the Gd^+ and CO_2 separation distance. These PESs have minima corresponding to the stable linear $Gd^+(OCO)$ adducts already discussed and indicate that adducts with $^{10}\Delta$ and $^8\Sigma^-$ electronic states have wells that are very close in energy.

The origin for the shape exhibited by the calculated PESs in Figure 5.7 has recently been described for the Sm^+ reaction with CO_2,[24] where the early barrier at an O-Gd^+-CO angle of ~25° arises from the need to bend the CO_2 adduct such that the metal cation can insert into one of the CO bonds of CO_2 (Figure 5.7). The transition state (TS) found along this PES (Supporting Information, Section 5.7) can yield intermediates with O-Gd^+-CO angles of ~30° along the $^8A'$ and $^{10}A'$ surfaces that are stabilized by the additional interaction between Gd^+ and C (Figure 5.7). As the angle increases further, another TS results along the $^8A'$, $^{10}A'$, and $^{10}A''$ surfaces at ~50° corresponding to cleaving the C-O

bond, which then leads to the stable inserted $OGd^+(CO)$ complexes. The $^8A''$ surface begins to deviate from the rest of the PESs after the first TS barrier (Figure 5.7), where there is a significant energy drop with increasing angle. This is attributed to the ability of Gd^+ to more effectively bind (i.e., form a triple bond) with the O atom in the $^8A''$ electronic configuration, which eventually leads to the ground state inserted $OGd^+(CO)$ complex (Figure 5.6b).

The calculated PESs in Figure 5.7 also support the conclusion that the distinct high-energy feature observed for reaction (5.1) in Figure 5.1a results from electronically excited GdO^+ products. These can be formed by following either the $^{10}A'$ and $^{10}A''$ surfaces in diabatic and spin-allowed processes, and have calculated barriers of ~1 eV above the reactant asymptote, consistent with the measured threshold energy of 1.01 ± 0.12 eV for the high-energy GdO^+ feature (Table 5.1). It should also be noted that extraction of an O atom directly from the CO_2 molecule by Gd^+ to form GdO^+ and CO products can proceed along diabatic surfaces and has a calculated barrier of 1 to 2 eV in excess of the reactant asymptote (Supporting Information, Section 5.7). This process is consistent with an impulsive reaction mechanism, postulated to explain the delayed onset in the decline of the high-energy feature, and thus likely contributes to the high-energy feature (*vide supra*).

5.5.10 Comparison between experimental and theoretical thermochemistry. To determine the electronic states of the $GdCO_2^+$ intermediates probed in the CID experiments and the electronically excited GdO^+ product formed at higher collision energies in reaction (5.1), the experimental thermochemistry is compared with theory at the B3LYP, PBE0, and CCSD(T,full) levels of theory using the ANO and all-electron cc-pVXZ-DK3[56] (where X = T, Q) basis sets for Gd. Because the calculations using the all-

electron Gd basis sets are computationally expensive only single point energies were calculated for the $GdCO_2^+$ complexes. For the B3LYP and PBE0 calculations, single point energies were calculated from the optimized $GdCO_2^+$ geometries obtained with the ANO basis set and SDD ECP for Gd at the corresponding level of theory. At the CCSD(T,full) level, single point energies were calculated using B3LYP/ANO geometries.

The inserted $OGd^+(CO)$ species probed in the CID experiments is easily identified from the calculations as the $^8A''$ $OGd^+(CO)$ ground state. The measured BDE for CO of 0.57 ± 0.05 eV is in relatively good agreement with the theoretical values calculated at the DFT level ranging from 0.63 to 0.70 eV, summarized in Table 5.2. At the CCSD(T,full) level, the values obtained with the all-electron cc-pVXZ-DK3 basis sets for Gd are somewhat larger at 0.89 and 1.05 eV for X = T and Q, respectively, in slightly worse agreement with experiment.

The electronic state of the $Gd^+(OCO)$ adduct probed in the experiments is more difficult to determine, because the lowest energy adduct with $^8\Sigma^-$ electronic state has a calculated BDE of 0.77 eV at the B3LYP/ANO level, which is significantly larger than the experimental value of 0.38 ± 0.05 eV. The calculated BDEs at the B3LYP/ANO level for various linear $Gd^+(OCO)$ adducts (Supporting Information, Section 5.7) range from ~0.2 to 0.7 eV, suggesting that an electronically excited adduct might be probed in the experiments, as was observed for the Gd^+ reaction with O_2.[65] This adduct could correspond to that found along the $^8A'$ surface in Figure 5.7 (having a $^8\Pi$ state in $C_{\infty v}$ symmetry), which is about 0.6 eV higher in energy than those on the $^{10}A'$, $^{10}A''$, and $^8A''$ surfaces. The calculated BDE for this adduct is 0.20 eV at the B3LYP/ANO level, which is somewhat lower than the value measured experimentally. BDEs calculated at the DFT level for the

Table 5.2. Comparison between experimental and theoretical energies (in eV) for the Gd^+-CO ($^{10}\Pi$), Gd^+-OCO ($^{8}\Pi$), and OGd^+-CO ($^{8}A''$) BDEs, the exothermicity, $\Delta_rH(5.1)$, for reaction (5.1), and the excitation energies of the GdO^+ $^{10}\Pi$ and $^{10}\Sigma^-$ states relative to the $^{8}\Sigma^-$ ground state.[a]

Level	Basis Set	GdO^+ ($^{10}\Pi$ / $^{10}\Sigma^-$)	Gd^+-CO	OGd^+-CO	Gd^+-OCO	$\Delta_rH(5.1)$
Expt.		3.25 ± 0.16	0.65 ± 0.06[b]	0.57 ± 0.05	0.38 ± 0.05	-2.24 ± 0.10
B3LYP	ANO	2.81 (*2.75*) / 2.98	0.87 (*0.81*)	0.67	0.20 (*0.14*)	-1.37 (*-1.25*)
	cc-pVTZ-DK3	3.00 (*2.94*) / 3.16	0.90[c] (*0.84*)	0.63[c]	0.19[c] (*0.13*)	-1.65 (*-1.53*)
	cc-pVQZ-DK3	2.99 (*2.93*) / 3.15	0.89[c] (*0.83*)	0.63[c]	0.19[c] (*0.13*)	-1.63 (*-1.51*)
PBE0	ANO	2.98 (*2.92*) / 3.13	0.95 (*0.89*)	0.70	0.11 (*0.05*)	-1.24 (*-1.12*)
	cc-pVTZ-DK3	3.10 (*3.04*) / 3.27	1.04[c] (*0.98*)	0.66[c]	0.06[c] (*0.00*)	-1.49 (*-1.37*)
	cc-pVQZ-DK3	3.09 (*3.03*) / 3.26	1.03[c] (*0.97*)	0.66[c]	0.06[c] (*0.00*)	-1.48 (*-1.36*)
CCSD(T,full)	ANO	3.21 (*3.15*) / 3.28	0.71[d] (*0.65*)	0.72[d]	0.28[d] (*0.22*)	-1.62 (*-1.50*)
	cc-pVTZ-DK3	3.22 (*3.16*) / 3.28[d]	0.85[d] (*0.79*)	0.89[d]	0.47[d] (*0.41*)	-1.92 (*-1.80*)
	cc-pVQZ-DK3	3.32 (*3.26*) / 3.38[d]	1.12[d] (*1.06*)	1.05[d]	0.76[d] (*0.70*)	-2.20 (*-2.08*)
	CBS[e]	3.38 (*3.32*) / 3.44	1.28 (*1.22*)	1.15	0.92 (*0.86*)	-2.37 (*-2.25*)

[a] Spin-orbit corrected values are in parentheses and italics.
[b] From reference 36.
[c] Single point energy calculation using the geometry and corresponding frequency from the optimization calculation with the ANO basis set.
[d] Single point energy calculation using the geometry and corresponding frequency at the B3LYP/ANO level.
[e] Complete basis set limit.

$^{8}\Pi$ electronically excited $Gd^{+}(OCO)$ adduct are generally smaller than experiment (Table 5.2). Better agreement is obtained at the CCSD(T,full) level of theory with BDEs of 0.28 eV and 0.47 eV calculated using the ANO and cc-pVTZ-DK3 basis sets, respectively (Table 5.2). In contrast, the larger all-electron cc-pVQZ-DK3 basis set yields a significantly higher BDE of 0.76 eV. Assignment of the $Gd^{+}(OCO)$ adduct probed in the experiments as the $^{8}\Pi$ state is also consistent with the corresponding calculated $^{8}A'$ surface (Figure 5.7), which is isolated from the $^{10}A'$, $^{10}A''$, and $^{8}A''$ surfaces, such that this adduct cannot easily couple with these surfaces to yield the inserted $^{8}A''$ $OGd^{+}(CO)$ ground state. Thus, the $Gd^{+}(OCO)$ adduct on the $^{8}A'$ surface will dissociate preferentially by CO_2 rather than CO loss upon activation. This is supported by RRKM calculations, which indicate that the rate constant for CO_2 loss is at least about two orders of magnitude larger than that to form the inserted $OGd^{+}(CO)$ complex for collision energies up to ~2 eV. At higher energies, the barrier for rearrangement can be surmounted, such that an inserted complex might be formed that dissociates via CO loss. This product channel, however, was not observed in the experiments at collision energies of up to 8 eV. In contrast, the $^{8}A''$, $^{10}A'$, $^{10}A''$ adducts can readily dissociate to GdO^{+} and CO because of the relatively shallow well of the $OGd^{+}(CO)$ intermediate (Figure 5.7) and high exothermicity of reaction (5.1). Indeed, RRKM calculations indicate that the ground state $Gd^{+}(OCO)$ adduct can rearrange to $OGd^{+}(CO)$ and dissociate to GdO^{+} and CO on a time scale that is about ~10^{5} faster than the collision frequency in the source, thereby explaining the unsuccessful attempts to form the $^{8}A''$ $OGd^{+}(CO)$ intermediate from reaction with CO_2 in the source.

Modeling the high-energy feature in reaction (5.1) results in an excitation energy of 3.25 ± 0.16 eV for the electronically excited GdO^{+} product relative to the ground state.

Calculations indicate that this high-energy state could correspond to a $^{10}\Pi$ or $^{10}\Sigma^-$ state. At the DFT level, slightly lower excitation energies are obtained for the $^{10}\Pi$ state compared with experiment, ranging from 2.81 to 3.10 eV (Table 5.2), while slightly better agreement with experiment is obtained for the $^{10}\Sigma^-$ state, where excitation energies range from 2.98 to 3.27 eV. At the CCSD(T,full) level, the difference in excitation energies between the $^{10}\Pi$ and $^{10}\Sigma^-$ states is smaller, with energies for the $^{10}\Pi$ state ranging from 3.21 to 3.32 eV and those for the $^{10}\Sigma^-$ state ranging from 3.28 to 3.38 eV for the different basis sets. These results suggest that both the $^{10}\Pi$ and $^{10}\Sigma^-$ states likely contribute to the high-energy feature in Figure 5.1.

Using the BDEs for the $Gd^+(OCO)$ and $OGd^+(CO)$ intermediates and the exothermicity for reaction (5.1) determined from our recent GdO^+ BDE measurement,[36] an experimental PES can be constructed for Gd^+ reacting with CO_2 to yield GdO^+ and CO. This PES is shown in Figure 5.8 and is compared with theoretical values obtained by extrapolating those from the all-electron cc-pVXZ-DK3 basis sets where X = T and Q to the complete basis set (CBS) limit at the CCSD(T,full) level of theory using the formula E[CBS] = 1.577163 E[Q] - 0.577163 E[T].[73,74] Figure 5.8 includes theoretical CBS energies for the ground and low-energy octet and dectet $Gd^+(OCO)$ adducts and the $^8A''$ TS, which could not be probed experimentally, but should be found along the lowest energy pathway to yield ground state GdO^+ and CO products. The CBS calculations predict that the linear $Gd^+(OCO)$ adduct with a $^{10}\Delta$ electronic state is lower in energy than the $^8\Sigma^-$ state by 0.22 eV, which contrasts with the B3LYP/ANO calculations that found the $^8\Sigma^-$ state to be lower in energy by 0.03 eV. Thus, the reaction to form ground state products may be limited by a surface crossing from the dectet to the octet surface, which occurs early in the

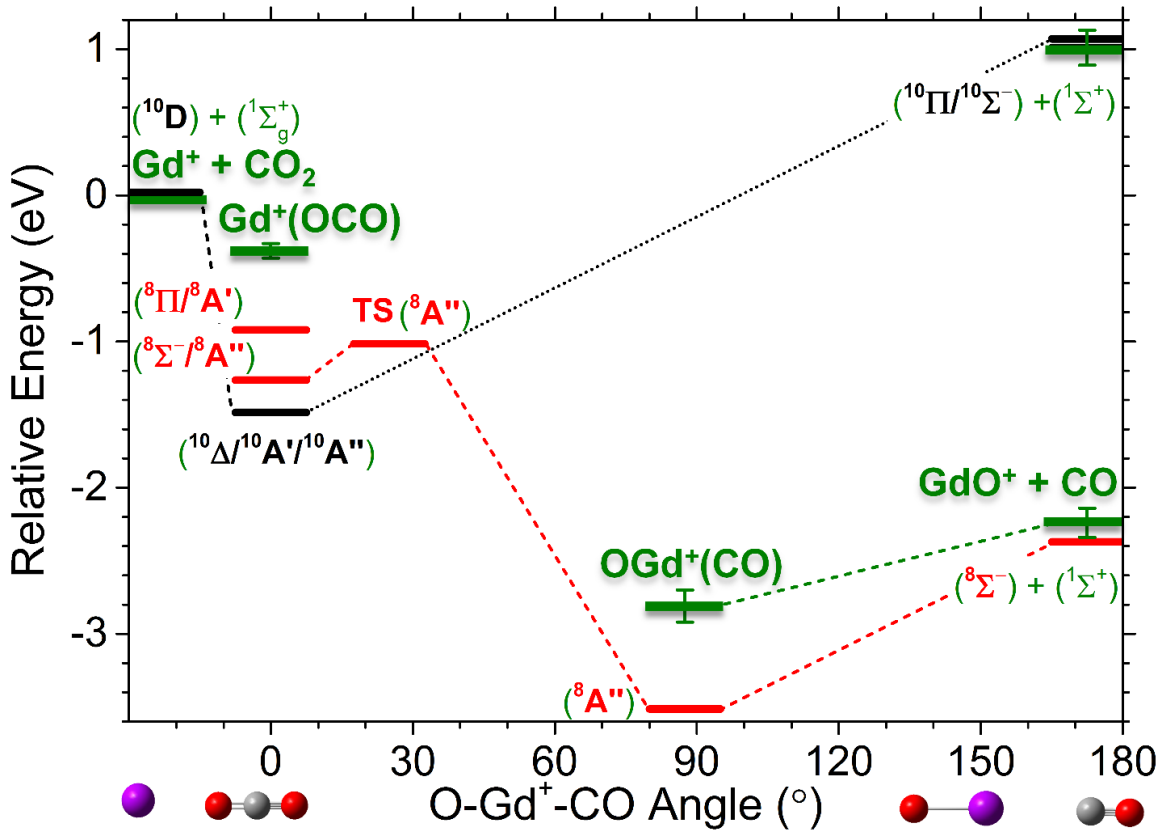

Figure 5.8. Potential energy surface for the Gd^+ reaction with CO_2 to form GdO^+ and CO mapped from guided ion beam tandem mass spectrometry measurements (green horizontal lines with error bars). This thermochemistry is compared with theoretical calculations at the CCSD(T,full)/CBS//B3LYP/ANO level of theory, where dectet and octet states are shown by black and red bars, respectively, with the term symbols given in the figure. Included are also the calculated values for the low-energy and ground state octet and dectet $Gd^+(OCO)$ adducts and the transition state along the $^8A''$ potential energy surface, which are the intermediates along the lowest energy pathway to form ground state GdO^+ ($^8\Sigma^-$) + CO ($^1\Sigma^+$) products from ground state Gd^+ (^{10}D) + CO_2 ($^1\Sigma_g^+$) reactants.

entrance channel and well below the reactant asymptote. A summary of the pathways and thermochemistry for reaction (5.1) along the octet and dectet surfaces in spin-allowed processes is shown in Scheme 5.1. The comparison of the CBS values with experiment indicates that the calculations reproduce the experimental exothermicity (which depends on the GdO^+ BDE) and the threshold of the electronically excited GdO^+ product (Figure 5.8). However, the CBS extrapolated calculations perform poorly in reproducing the BDEs

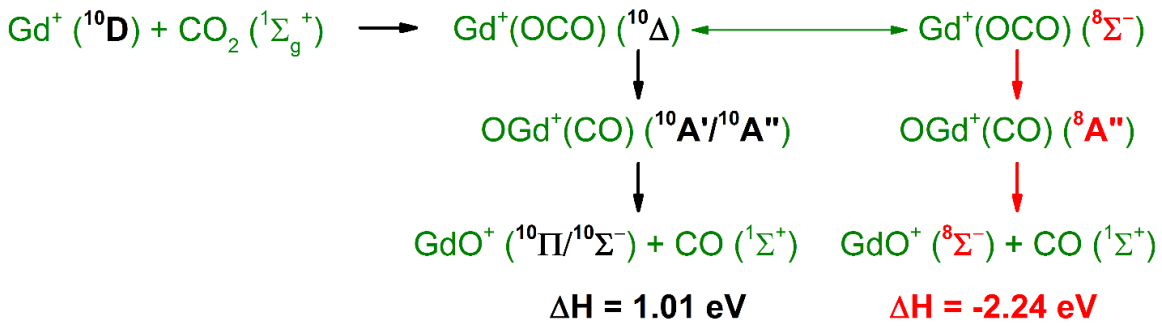

Scheme 5.1. Schematic of the reaction proceeding along the octet and dectet surfaces to form ground state and electronically excited GdO^+ product ions, respectively. Black and red arrows indicate spin-allowed processes along dectet and octet surfaces, respectively.

of OGd^+-CO and Gd^+-OCO, predicting larger values of 1.15 and 0.92 eV, compared with experiment of 0.57 ± 0.05 and 0.38 ± 0.05 eV, respectively (Table 5.2, Figure 5.8).

Part of the deviation in the calculated BDEs could potentially arise from spin-orbit effects. The calculated energies for a given state do not reflect the lowest spin-orbit (SO) level, but instead give the energy averaged over all SO levels for that state. The experimental threshold should correspond to the energy difference between the lowest energy SO levels of reactants and products. Thus, for a more accurate comparison between experiment and theory, a first-order semiempirical SO correction can be applied to the calculated energies to reflect the lowest energy SO levels as described in detail elsewhere.[36] For the Gd^+(OCO) adduct, assuming a $^8\Pi$ excited electronic state, the calculated BDE needs to be corrected by the SO averaged energy of the Gd^+ (^{10}D) ground state (0.12 eV) and the $^8\Pi$ state of the Gd^+(OCO) adduct (0.06 eV), resulting in an overall correction which lowers the theoretical BDE by 0.06 eV. This yields a CBS value of 0.86 eV, in better agreement with experiment. For the inserted OGd^+(CO) intermediate, the calculated BDE requires no SO correction because OGd^+(CO) (^{8}A″), GdO^+ ($^8\Sigma^-$), and CO ($^1\Sigma^+$) have zero

orbital angular momentum and thus have no first-order SO splittings. The calculated exothermicity for reaction (5.1) needs to be reduced by only the SO averaged energy for the ^{10}D ground state of Gd^+ (0.12 eV), giving an exothermicity of -2.25 eV at the CCSD(T,full)/CBS level in excellent agreement with experiment (-2.24 ± 0.10 eV). For the electronically excited GdO^+ product, only the calculated energy for the $^{10}\Pi$ state needs to be SO corrected, which lowers this state by 0.06 eV, increasing the difference with the $^{10}\Sigma^-$ state slightly. The SO corrected energies are included in Table 5.2. Generally, these results demonstrate that the SO corrections are not significant and cannot explain the larger deviations observed between experiment and theory at the CCSD(T,full)/CBS// B3LYP/ANO level for the $OGd^+(CO)$ and $Gd^+(OCO)$ BDEs.

5.5.11 CO binding to Gd^+ and GdO^+. As reported recently,[36] the BDE for $Gd^+(CO)$ measured from the exchange reaction between Gd^+ and CO_2 to form $GdCO^+$ and O is 0.65 ± 0.06 eV (Table 5.2). A $^{10}\Pi$ ground state was generally predicted from the calculations for $Gd^+(CO)$ where the 6s and 5d valence electrons of Gd^+ remain in their respective atomic orbitals to form mostly nonbonding mos, such that the CO adduct interacts with Gd^+ primarily through electrostatics.[36] For the previously reported theoretical BDEs at the B3LYP level, the zero point energy of CO (0.14 eV) was accidentally omitted. Applying this correction gives slightly larger BDEs of 0.81 and 0.63 eV (including the empirical SO correction) for the ANO and Seg. SDD basis sets, respectively. In the present work, additional BDEs for $Gd^+(CO)$ were calculated from single point energies using the all-electron cc-pVXZ-DK3 (with X = T and Q) basis sets for Gd and are summarized in Table 5.2. Similar trends in the calculated BDEs are seen for Gd^+-CO to those for OGd^+-CO (Table 5.2), where generally larger theoretical BDEs compared with experiment are

predicted.

The BDE measured for OGd^+-CO (0.57 ± 0.05 eV) is similar but slightly lower than that for Gd^+-CO (0.65 ± 0.06 eV). These binding interactions can be envisioned as combinations of electrostatics, σ donation (ligand to metal), and π backbonding (metal to ligand). Qualitatively, the similar bond energies suggest that the interaction is mainly electrostatic for both complexes, which is consistent with the calculated mos for the ground state $OGd^+(CO)$ (Figure 5.6b) and $Gd^+(CO)$[36] complexes (although $O^{2-}Gd^{3+}$ character would enhance the OGd^+-CO interaction). The slightly larger BDE for $Gd^+(CO)$ can potentially be explained by an additional π bonding interaction between Gd^+ and CO that is possible from the available 5d valence electron of Gd^+.[36] This backbonding interaction is absent for $OGd^+(CO)$ because the valence electrons of Gd^+ are involved in binding to the additional O atom. The calculations at the B3LYP and PBE0 levels reproduce qualitatively this trend, predicting larger BDEs by 0.14 - 0.32 eV for Gd^+-CO compared with those for OGd^+-CO (Table 5.2), whereas practically the same BDEs for both complexes are obtained at the CCSD(T,full) level (Table 5.2). Note that the differences calculated at this level using the cc-pVQZ-DK3 and CBS basis sets of 0.01 and 0.07 eV reproduce the experimental difference of 0.08 ± 0.08 eV the best.

5.5.12 Periodic trends. Gd^+ with its half-filled 4f shell and $5d^16s^1$ ground state valence electron configuration is unusual compared with most lanthanide metal cations, which generally have $4f^n6s^1$ ground state configurations (where n corresponds to the remaining valence electrons). In this regard, Gd^+ is similar to the lanthanides La^+ ($5d^2$), Ce^+ ($4f^15d^2$), and Lu^+ ($4f^{14}6s^2$). Ignoring the 4f electrons, these lanthanides have similar electronic configurations to the group 3 metal cations Sc^+ ($3d^14s^1$) and Y^+ ($5s^2$ with the

$4d^15s^1$ state only 0.15 eV higher in energy) with two valence electrons in d or s orbitals. Indeed, all these metal cations react in exothermic, and relatively efficient reactions with CO_2 to form MO^+ and CO as has been shown from ICP/SIFT experiments.[9,11] Of these metal cations, the reaction of Y^+ with CO_2 has previously been investigated in detail with GIBMS, and BDEs for Y^+-CO and OY^+-CO of 0.31 ± 0.11 and 0.71 ± 0.04 eV, respectively, have been determined.[19] Unlike the GdO^+ cross section, the corresponding YO^+ cross section does not exhibit a distinct high-energy feature. This difference is likely due to Y^+ having a $5s^2$ ground state, such that the reaction to form ground state products, YO^+ ($^1\Sigma^+$) + CO ($^1\Sigma^+$), is spin-allowed and still efficient at high energies, consistent with the YO^+ cross section exhibiting the expected LGS $E^{-0.5}$ energy dependence at collision energies below ~1 eV.[19] The weaker bond for Y^+-CO (0.31 ± 0.11 eV) compared with Gd^+-CO (0.65 ± 0.06 eV) can also be explained by the differences in the ground state electronic configurations of these two metal cations where the 5d valence electron of Gd^+ ($5d^16s^1$) can form an additional π interaction with the CO adduct, not possible for ground state Y^+ ($5s^2$). However, for the OM^+(CO) complexes, the available valence electrons for both Gd^+ and Y^+ are promoted to d orbitals to more effectively bind with the additional O atom, forming essentially a triple bond.[36] Thus, the CO adduct must interact primarily through electrostatics in both complexes, as also evident by the similar BDEs of 0.71 ± 0.04 eV and 0.57 ± 0.05 eV for OY^+-CO and OGd^+-CO, respectively. An interesting difference between Gd^+ and Y^+ is that the Gd^+(OCO) adduct could be stabilized in reactions with CO_2 in the source, but attempts to produce a Y^+(OCO) adduct failed and instead yielded only the inserted OY^+(CO) complex.[19] This suggests that the Y^+(OCO) adduct can readily rearrange to the inserted complex. Thus, the PESs for the Y^+ reaction with CO_2

must differ somewhat in the entrance channel from those obtained for Gd^+ in Figure 5.7, presumably a result of the differences in ground state electronic configurations of Gd^+ and Y^+. The ability to form the inserted $OY^+(CO)$ complex from the reaction with CO_2 in the source, which was not possible for Gd^+, might be aided by the slightly deeper well and lower reaction exothermicity (-1.79 ± 0.18 eV) for Y^+. To the best of our knowledge, the energy dependent product ion cross sections for the reactions of Sc^+, La^+, Ce^+, and Lu^+ with CO_2 have not been measured. However, on the basis of the ground state valence electron configuration of the metal cation and spin-conservation, it seems likely that Sc^+ will behave similarly to Gd^+, and likewise Lu^+ will exhibit comparable behavior to Y^+. Because both La^+ and Ce^+ have a high-spin $5d^2$ configuration, these metal cations should exhibit similar reactivity with CO_2, which should be more similar to that of Sc^+ and Gd^+ than that of Y^+ and Lu^+.

The results for Gd^+ here can also be compared with recent GIBMS results for Sm^+ ($4f^6 6s^1$), which has a ground state electronic configuration typical of most lanthanide cations. The reaction between Sm^+ and CO_2 to form SmO^+ + CO is exothermic, but the GIBMS results[24] indicate that this reaction clearly exhibits a barrier, which is consistent with the failure to observe this reaction in ICP/SIFT experiments.[9] From calculations and comparison with the GIBMS results, this barrier is identified to correspond to the crossings between $^8A''$ and $^6A''$ surfaces in the entrance channel with the $^6A'$ surface of the ground state inserted $OSm^+(CO)$ complex in the exit channel, which can readily dissociate into ground state products.[24] For Sm^+ to achieve effective binding with the O atom in the inserted $OSm^+(CO)$ intermediate, promotion of both a 4f electron and the 6s electron to 5d orbitals is required, corresponding to an atomic Sm^+ excitation of 2.35 eV.[24] However, for

Gd^+ only the 6s electron needs to be promoted. Because this promotion energy cost for Gd^+ is not too large (~0.55 eV, from the energy difference between the ^{10}D ($4f^75d^16s^1$) and ^{10}F ($4f^75d^2$) states averaged over the spin-orbit levels), a low-energy $Gd^+(OCO)$ adduct can be formed along the $^8A''$ surface (Figure 5.7). This allows the Gd^+ reaction with CO_2 to proceed entirely along the $^8A''$ surface, where the only barrier is well below the reactant asymptote. In contrast, because the promotion energy for Sm^+ is significant, the $Sm^+(OCO)$ adduct along the $^6A'$ surface is much higher in energy than the reactant asymptote.[24] Thus, to access the $^6A'$ surface requires a crossing from the lower energy $^8A''$ and $^6A''$ surfaces, which occurs above the reactant asymptote and gives rise to the 1.77 ± 0.11 eV barrier observed experimentally.[24] Similar behavior is likely to be exhibited by the other lanthanide cations with $4f^n6s^1$ ground states, for which process (5.1) is exothermic but no reaction was observed at thermal energies by Bohme and coworkers.[9] Because the $^8A''$ and $^6A''$ surfaces in the Sm^+ reaction are close in energy, they should readily mix, which means that the reaction is probably not limited by spin-conservation.[24] This also appears to be the case for Gd^+, as evidenced by the efficient exothermic reaction to ground state products on the octet surface. The pronounced high-energy feature in the Gd^+ reaction with CO_2 is therefore likely the result of the reaction proceeding along dectet surfaces in diabatic processes that maintain the electronic configurations of the reactants rather than due to spin-conservation. Additionally, direct cleavage of the C-O bond in the CO_2 molecule by Gd^+ becomes energetically possible at about the same threshold (Supporting Information, Section 5.7), which can also proceed along a single diabatic surface.

The BDEs for M^+-OCO and OM^+-CO should not differ significantly between Gd^+ and Sm^+ because the interactions of the OCO and CO adducts are primarily electrostatic in

these complexes. This is consistent with the measured BDE for ground state $Sm^+(OCO)$ of 0.42 ± 0.03 eV,[24] which is comparable with that for the electronically excited $Gd^+(OCO)$ adduct probed in the CID experiments of 0.38 ± 0.05 eV, where the BDE for the ground state $Gd^+(OCO)$ adduct will be somewhat higher. For the inserted $OSm^+(CO)$ complex,[24] a somewhat larger BDE of 0.97 ± 0.07 eV is measured compared with that for $OGd^+(CO)$ of 0.57 ± 0.05 eV. The weaker interaction between CO and GdO^+ might result from the much stronger bond that can be formed between the additional O atom and Gd^+ than Sm^+, where the BDEs for isolated M^+-O complexes are 7.69 ± 0.10 eV[36] and 5.72_5 ± 0.07 eV[75] for Gd^+ and Sm^+, respectively.

5.6 Conclusions

The BDEs for OGd^+-CO and Gd^+-OCO are measured using GIBMS to be 0.57 ± 0.05 and 0.38 ± 0.05 eV, respectively. This thermochemistry is used together with the recently measured BDE of GdO^+ to construct an experimental PES for the exothermic reaction between Gd^+ (^{10}D) and CO_2 ($^1\Sigma_g^+$). Although the reaction to form ground state GdO^+ ($^8\Sigma^-$) and CO ($^1\Sigma^+$) products is formally spin-forbidden, the experimental results indicate that this process occurs efficiently without any barriers, as also evident from the measured thermochemistry for the reverse reaction. A more complete picture of the PES is obtained from theory, which also helps elucidate the reaction mechanism in detail. The calculations indicate that low-energy $Gd^+(OCO)$ adducts can be formed on $^{10}A'$, $^{10}A''$, and $^8A''$ surfaces with similar energies such that these states can readily mix. An inserted ground state $OGd^+(CO)$ complex that can readily dissociate to ground state GdO^+ and CO products is found along the $^8A''$ surface. The $^8A''$ surface has no barriers exceeding the

reactant asymptote and thus the entire reaction from ground state reactants to products can efficiently occur along this surface. A distinct second feature in the measured GdO^+ cross section is observed at higher energies and is explained by the formation of electronically excited GdO^+ products along single PESs in diabatic processes that maintain the electronic configuration of the reactants. This is further confirmed by the good agreement between the experimentally determined excitation energy of 3.25 ± 0.16 eV from this feature and the values calculated for the $^{10}\Pi$ and $^{10}\Sigma^-$ states of GdO^+ relative to the $^8\Sigma^-$ground state.

From theory, the inserted $OGd^+(CO)$ complex probed in the CID experiments is identified as the $^8A''$ ground state with a calculated O-Gd^+-CO angle of ~87° and Gd^+-O and Gd^+-CO bond lengths of 1.8 and 2.7 Å, respectively. Here, the CO adduct primarily binds via electrostatics to GdO^+, which forms a triple bond like that in free GdO^+. Quantum chemical calculations at the DFT level using various basis sets perform reasonably well in reproducing the experimental BDE for OGd^+-CO. In contrast, the electrostatic interaction between GdO^+ and CO is significantly overestimated in CCSD(T,full) calculations that use the triple- and quadruple-ζ all-electron basis sets for Gd^+. The BDE for OGd^+-CO is found to be similar to that previously measured for Gd^+-CO of 0.65 ± 0.06 eV,[36] where the slightly larger value for the latter complex can potentially be attributed to an additional π interaction between Gd^+ and CO that is possible from the available 5d valence electron on Gd^+. The $Gd^+(OCO)$ adduct probed in the CID experiments is identified from theory to be an electronically excited adduct likely in a $^8\Pi$ state. This adduct is found along an isolated higher energy $^8A'$ PES, where formation of an inserted $OGd^+(CO)$ complex is not energetically favored over CO_2 loss. In contrast, the ground state and other low-energy $Gd^+(OCO)$ adducts can readily access the $^8A''$ surface to form the ground state inserted

$OGd^+(CO)$ complex, where CO loss is favored over CO_2 loss.

Gd^+ with its half-filled 4f shell and $5d^16s^1$ ground state valence electron configuration is different compared with most of the lanthanide cations, which have one 6s valence electron with the rest occupying 4f orbitals. This makes Gd^+ more similar to the group 3 metal cations, Sc^+ and Y^+, and the lanthanides La^+, Ce^+, and Lu^+, which have two valence electrons in d or s orbitals. Comparisons with previous GIBMS results for Y^+ and Sm^+ reacting with CO_2 indicate that Gd^+ reacts more similarly to Y^+, although there are still some interesting differences that can be attributed to spin-conservation and the different ground state electronic configurations of Gd^+ and Y^+. The difference with the Sm^+ reaction arises primarily as a result of the significant promotion energy cost of the 4f electron to a 5d orbital for Sm^+, such that there is a barrier resulting from a crossing between the ground state surface of the $Sm^+(OCO)$ adduct in the entrance channel with that of the inserted $OSm^+(CO)$ complex in the exit channel. This barrier is not present in the Gd^+ reaction because the promotion energy cost from the 6s to 5d orbital is small and both a low-energy $Gd^+(OCO)$ adduct and inserted $OGd^+(CO)$ complex can be formed along the same PES. Thus, on the basis of this promotion energy argument, similar reactivity is expected for the group 3 metal cations and the lanthanide cations with two s or d electrons as that of Gd^+, whereas most other lanthanide cations should exhibit similar behavior to Sm^+ and require a crossing between the ground state PESs of the CO_2 adduct and inserted complex.

5.7 Supporting Information

5.7.1 Quantum chemical calculations for $GdCO_2^+$. Extensive theoretical calculations were performed for different $GdCO_2^+$ complexes using the atomic natural orbital[47] (ANO) basis set and relativistic Stuttgart Dresden[46] (SDD) effective small (28 electron) core potential (ECP) for Gd and the 6-311+G(3df) basis set for O and C at the B3LYP level of theory. The energies, bond lengths, angles, and vibrational frequencies from these calculations are summarized in Table 5.3 and discussed in detail above. The molecular orbitals (mos) that form from the interactions of the valence electrons of Gd^+, the two O atoms, and C for different $GdCO_2^+$ structures are shown in Figure 5.6 and described above. For simplicity, the seven 4f valence electrons of Gd^+ were omitted from Figure 5.6 because these electrons form mainly nonbonding mos similar to their atomic orbitals. Representative mos for the seven 4f electrons in different geometries of $GdCO_2^+$ with $C_{\infty v}$ and C_s symmetry are shown in Figure 5.9.

Relaxed potential energy surfaces (PESs) where the O-Gd^+-CO angle is varied were calculated to obtain information about the reaction mechanism of the formally spin-forbidden process between ground state Gd^+ (^{10}D) + CO_2 ($^1\Sigma_g^+$) reactants and ground state GdO^+ ($^8\Sigma^-$) + CO ($^1\Sigma^+$) products. These surfaces are shown in Figure 5.7. At small O-Gd^+-CO angles, the energy gap between the $^{10}A'/^{10}A''$ and $^8A''$ surfaces is small (Figure 5.7), suggesting that efficient spin pre-equilibrium[71,72] can occur via spin-orbit coupling in the entrance channel as discussed above, such that the entire reaction from ground state reactants to products can practically occur on the $^8A''$ surface. The small energy gap between the $^{10}A'/^{10}A''$ and $^8A''$ adducts is also evident in PES scans where the Gd^+ and OCO separation distance is varied in linear Gd^+(OCO) adducts. These PESs are shown in

Table 5.3. Summary of bond lengths, angles, vibrational frequencies, and energies for various electronic states of $GdCO_2^+$ calculated at the B3LYP level of theory using the ANO basis set and SDD ECP for Gd and the 6-311+(3df) basis set for C and O.

State	s(s+1)[a]	∠O-Gd^+-CO (°)	r(Gd^+-CO) (Å)	r(Gd^+-O) (Å)	r(C-O) (Å)	Vibrational Frequencies (cm^{-1})[b]	E (E_h)	E_{rel} (eV)
O-Gd^+-CO								
$^8A''$	15.77	87.48	2.695	1.767	1.115	55, 182, 198, 252, 870, 2280	-954.097402	0.00
$^8A'$	16.72*	30.74	2.511	2.130	1.169, 1.284	169, 326, 355, 671, 1049, 1926	-954.018835	2.18
$^8A'$	16.76*	95.61	2.399	2.038	1.130	58, 252, 269, 324, 587, 2107	-953.991064	2.88
$^{10}A'$	24.76	97.47	2.399	2.043	1.130	61, 255, 269, 360, 596, 2107	-953.989756	2.92
$^{10}A''$	24.76	129.24	2.783	2.031	1.116	49, 136, 179, 192, 601, 2250	-953.986143	3.00
$^{10}A''$	24.76	70.64	2.733	2.036	1.114	65, 134, 154, 210, 601, 2282	-953.985795	3.01
$^{10}A''$	24.76	29.19	2.545	2.222	1.162, 1.241	142, 225, 438, 596, 1119, 2075,	-954.038992	1.64
$^{10}\Sigma/^{10}\Delta$	24.76	180.00	2.501	2.114	1.132	143, 170, 223, 249, 415, 546, 2092	-953.956401	3.84
$^8\Sigma/^8\Delta$	16.75*	180.00	2.491	2.111	1.134	112, 121, 258, 344, 527, 536, 2076	-953.949788	4.03
$^8\Sigma^-$ TS	15.77	180.00	3.206	1.761	1.117	65i, 65i, 99, 119, 119, 884, 2258	-954.083038	0.37
$^8A''$ TS	15.85	25.11	2.776	2.174	1.147, 1.226	299i, 183, 449, 519, 1131, 2210	-954.042234	1.54
$^8A'$ TS	16.71*	25.33	2.787	2.229	1.152, 1.227	363i, 153, 389, 466, 1112, 2174	-954.015255	2.26

Table 5.3 continued

State	s(s+1)[a]	∠O-Gd^+-CO (°)	r(Gd^+-CO) (Å)	r(Gd^+-O) (Å)	r(C-O) (Å)	Vibrational Frequencies (cm^{-1})[b]	E (E_h)	E_{rel} (eV)
$^{10}A''$ TS	24.75	27.33	2.657	2.265	1.155, 1.224	151i, 195, 473, 527, 1150, 2166	-954.038868	1.63
$^{8}A'$ TS	16.75*	50.52	2.417	2.015	1.132	333i, 217, 276, 303, 571, 2059	-953.979730	3.18
$^{10}A'$ TS	24.77	52.72	2.387	2.020	1.132	299i, 228, 290, 393, 560, 2049	-953.979614	3.19
$^{10}A''$ TS	24.76	51.51	2.758	2.021	1.117	108i, 112, 153, 246, 592, 2243	-953.984751	3.03
$^{10}A''$ TS	24.76	96.63	2.777	2.033	1.114	53i, 105, 150, 163, 606, 2288	-953.985098	3.02
Gd^+-OCO								
$^{10}\Delta$	24.75	0.000	3.594	2.416	1.178, 1.139	45, 45, 171, 641, 641, 1366, 2422	-954.053254	1.29
$^{10}\Pi$	24.75	0.000	3.641	2.465	1.175, 1.143	53, 61, 148, 618, 649, 1353, 2413	-954.048427	1.42
$^{8}\Sigma^-$	15.77	0.000	3.564	2.384	1.180, 1.138	22, 22, 165, 634, 634, 1362, 2417	-954.054238	1.26
$^{8}\Pi$	16.75*	0.000	3.628	2.452	1.175, 1.143	39, 49, 153, 613, 646, 1353, 2414	-954.033057	1.84
$^{8}\Delta$[c]	15.76	0.000	3.752	2.577	1.175, 1.142	79, 79, 127, 651, 1359, 2409	-954.037765	1.72
$^{8}\Delta$	16.73*	0.000	3.626	2.447	1.179, 1.139	37, 37, 152, 638, 1359, 2415	-954.030864	1.90

[a] * = spin-contaminated state.

[b] Calculated vibrational frequencies are scaled by 0.989 and imaginary frequencies are indicated by i.

[c] Gd^+ has a $4f^8$ electronic configuration.

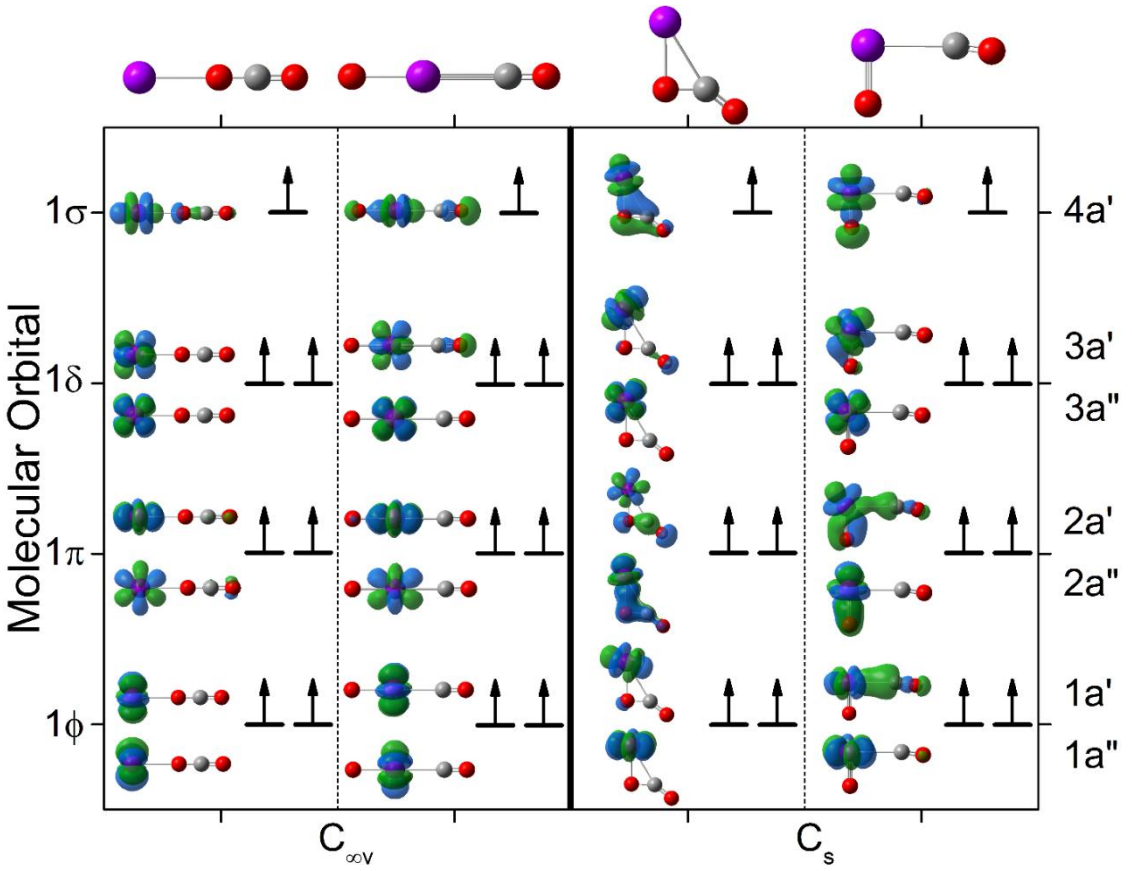

Figure 5.9. Representative molecular orbitals for the 4f electrons in different $GdCO_2^+$ geometries with $C_{\infty v}$ and C_s symmetry calculated at the B3LYP level using the ANO basis set and SDD ECP for Gd and the 6-311+G(3df) basis set for O and C.

Figure 5.10a and yield local minima corresponding to the linear $Gd^+(OCO)$ structures discussed above and summarized in Table 5.3. The $^{10}\Delta$ and $^{8}\Sigma^-$ surfaces, which in C_s symmetry transform into $^{10}A'/^{10}A''$ and $^{8}A''$ surfaces, respectively, also exhibit a small energy gap near the wells consistent with that observed for the $^{10}A'/^{10}A''$ and $^{8}A''$ surfaces in Figure 5.7. The energetics of forming ground state GdO^+ and CO products from O atom extraction by Gd^+ in the linear $Gd^+(OCO)$ adducts were also investigated by calculating PESs as a function of the GdO^+ and CO separation distance. However, as shown in Figure 5.10b, there is a significant barrier to breaking the O-CO bond for this process that is well

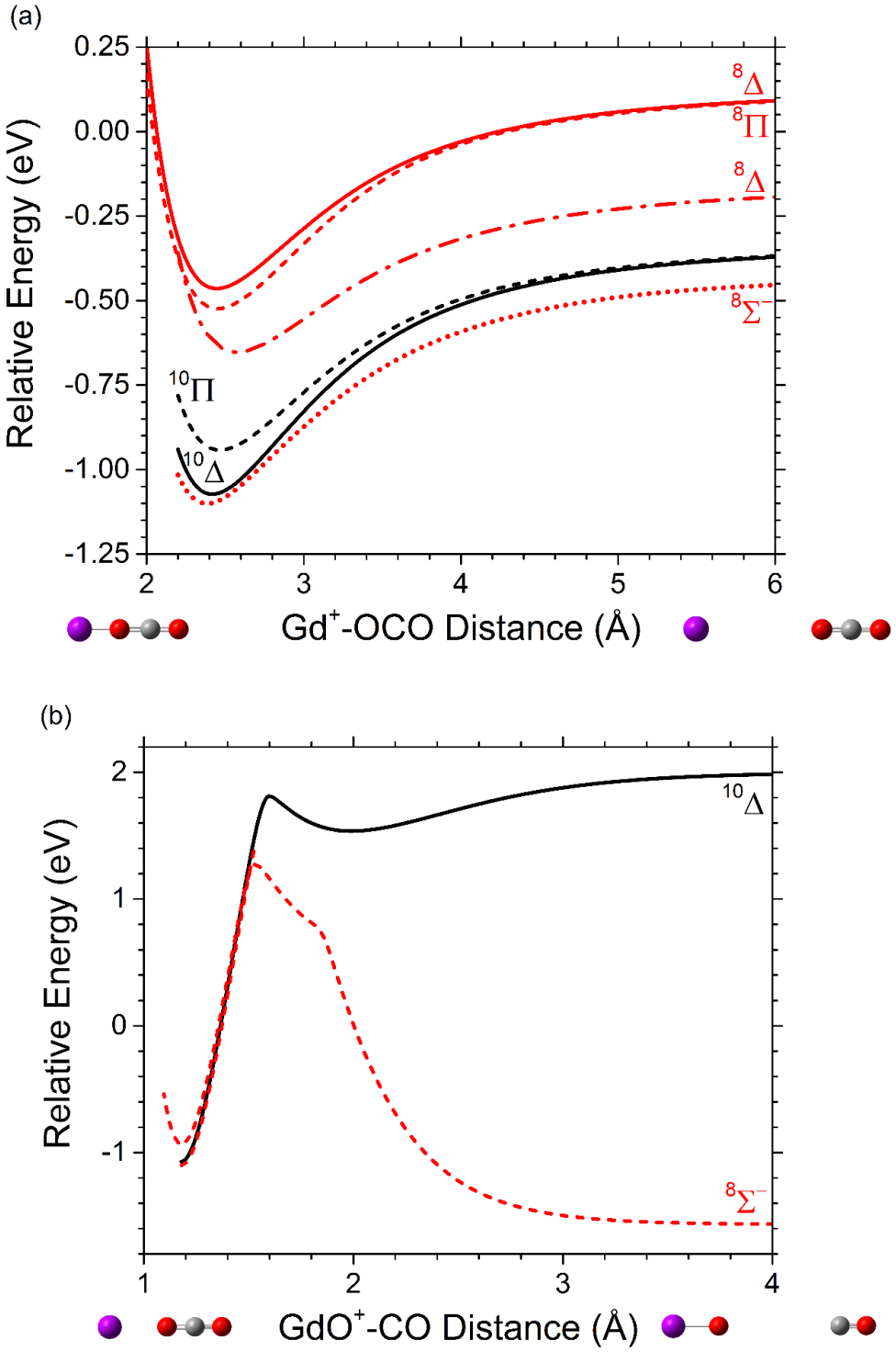

Figure 5.10. Relaxed potential energy surface scans as a function of the distance between (a) Gd^+ and OCO and (b) GdO^+ and CO obtained at the B3LYP level of theory using the ANO basis set for Gd and the 6-311+G(3df) basis set for C and O. Black and red curves correspond to $GdCO_2^+$ species with multiplicities of 10 and 8, respectively, with the corresponding term symbols given in the figures.

above the reactant asymptote and will thus not occur at thermal energies. This process may contribute to the high energy feature in the $GdO^+ + CO$ cross section, as discussed above.

5.8 Acknowledgements

The authors thank the U.S. Air Force Office of Scientific Research (FA9550-16-1-0095) for financial support, Professor Kirk A. Peterson for providing the all-electron basis sets, and the Center for High Performance Computing at the University of Utah for generous allocation of computer time. Additionally, some of the more computationally demanding calculations were performed on the large shared-memory cluster at the Pittsburgh Supercomputing Center at Carnegie Mellon University via the Extreme Science and Engineering Discovery Environment (XSEDE), under grant number TG-CHE170012. Christopher McNary is thanked for help with using these resources.

5.9 References

(1) Sakakura, T.; Choi, J.-C.; Yasuda, H. Transformation of Carbon Dioxide. *Chem. Rev.* **2007,** *107*, 2365-2387.

(2) Cokoja, M.; Bruckmeier, C.; Rieger, B.; Herrmann, W. A.; Kühn, F. E. Transformation of Carbon Dioxide with Homogeneous Transition-Metal Catalysts: A Molecular Solution to a Global Challenge? *Angew. Chem. Int. Ed.* **2011,** *50*, 8510-8537.

(3) Appel, A. M.; Bercaw, J. E.; Bocarsly, A. B.; Dobbek, H.; DuBois, D. L.; Dupuis, M.; Ferry, J. G.; Fujita, E.; Hille, R.; Kenis, P. J. A.et al. Frontiers, Opportunities, and Challenges in Biochemical and Chemical Catalysis of CO_2 Fixation. *Chem. Rev.* **2013,** *113*, 6621-6658.

(4) Schwarz, H. Metal-Mediated Activation of Carbon Dioxide in the Gas Phase: Mechanistic Insight Derived from a Combined Experimental/Computational Approach. *Coord. Chem. Rev.* **2017,** *334*, 112-123.

(5) Irikura, K. K.; Beauchamp, J. L. Electronic Structure Considerations for Methane Activation by Third-Row Transition-Metal Ions. *J. Phys. Chem.* **1991,** *95*, 8344-8351.

(6) Wesendrup, R.; Schwarz, H. Tantalum-Mediated Coupling of Methane and Carbon Dioxide in the Gas Phase. *Angew. Chem. Int. Ed. Engl.* **1995,** *34*, 2033-2035.

(7) Kappes, M. M.; Staley, R. H. Oxidation of Transition-Metal Cations in the Gas Phase. Oxygen Bond Dissociation Energies and Formation of an Excited-State Product. *J. Phys. Chem.* **1981,** *85*, 942-944.

(8) Kappes, M. M.; Staley, R. H. Gas-Phase Oxidation Catalysis by Transition-Metal Cations. *J. Am. Chem. Soc.* **1981,** *103*, 1286-1287.

(9) Cheng, P.; Koyanagi, G. K.; Bohme, D. K. Gas-Phase Reactions of Atomic Lanthanide Cations with CO_2 and CS_2: Room-Temperature Kinetics and Periodicities in Reactivity. *J. Phys. Chem. A* **2006,** *110*, 12832-12838.

(10) Dheandhanoo, S.; Chatterjee, B. K.; Johnsen, R. Rate Coefficients for the Oxidation Reactions of Zirconium Ions with Oxygen, Nitric Oxide, and Carbon Dioxide. *J. Chem. Phys.* **1985,** *83*, 3327-3329.

(11) Koyanagi, G. K.; Bohme, D. K. Gas-Phase Reactions of Carbon Dioxide with Atomic Transition-Metal and Main-Group Cations: Room-Temperature Kinetics and Periodicities in Reactivity. *J. Phys. Chem. A* **2006,** *110*, 1232-1241.

(12) Armentrout, P. B. Mass Spectrometry—Not Just a Structural Tool: The Use of Guided Ion Beam Tandem Mass Spectrometry to Determine Thermochemistry. *J. Am. Soc. Mass. Spectrom.* **2002,** *13*, 419-434.

(13) Armentrout, P. B. Kinetic Energy Dependence of Ion–Molecule Reactions: Guided Ion Beams and Threshold Measurements. *Int. J. Mass Spectrom.* **2000,** *200*, 219-241.

(14) Sievers, M. R.; Armentrout, P. B. Potential Energy Surface for Carbon-Dioxide Activation by V^+: A Guided Ion Beam Study. *J. Chem. Phys.* **1995,** *102*, 754-762.

(15) Griffin, J. B.; Armentrout, P. B. Guided Ion-Beam Studies of the Reactions of Fe_n^+(n=1–18) with CO_2: Iron Cluster Oxide Bond Energies. *J. Chem. Phys.* **1997,** *107*, 5345-5355.

(16) Griffin, J. B.; Armentrout, P. B. Guided Ion Beam Studies of the Reactions of Cr_n^+ (n=2–18) with O_2: Chromium Cluster Oxide and Dioxide Bond Energies. *J. Chem. Phys.* **1998,** *108*, 8062-8074.

(17) Rodgers, M. T.; Walker, B.; Armentrout, P. B. Reactions of Cu^+ (^{1}S and ^{3}D) with

O_2, CO, CO_2, N_2, NO, N_2O, and NO_2 Studied by Guided Ion Beam Mass Spectrometry. *Int. J. Mass Spectrom.* **1999,** *182–183*, 99-120.

(18) Sievers, M. R.; Armentrout, P. B. Gas Phase Activation of Carbon Dioxide by Niobium and Niobium Monoxide Cations. *Int. J. Mass Spectrom.* **1998,** *179–180*, 103-115.

(19) Sievers, M. R.; Armentrout, P. B. Activation of Carbon Dioxide: Gas-Phase Reactions of Y^+, YO^+, and YO_2^+ with CO and CO_2. *Inorg. Chem.* **1999,** *38*, 397-402.

(20) Sievers, M. R.; Armentrout, P. B. Oxidation of CO and Reduction of CO_2 by Gas Phase Zr^+, ZrO^+, and ZrO_2^+. *Int. J. Mass Spectrom.* **1999,** *185–187*, 117-129.

(21) Sievers, M. R.; Armentrout, P. B. Reactions of CO and CO_2 with Gas-Phase Mo^+, MoO^+, and MoO_2^+. *J. Phys. Chem. A* **1998,** *102*, 10754-10762.

(22) Zhang, X.-G.; Armentrout, P. B. Activation of O_2, CO, and CO_2 by Pt^+: The Thermochemistry of PtO^+. *J. Phys. Chem. A* **2003,** *107*, 8904-8914.

(23) Clemmer, D. E.; Weber, M. E.; Armentrout, P. B. Reactions of Al^+ (^1S) with NO_2, N_2O, and CO_2: Thermochemistry of AlO and AlO^+. *J. Phys. Chem.* **1992,** *96*, 10888-10893.

(24) Armentrout, P. B.; Cox, R. M. Potential Energy Surface for the Reaction $Sm^+ + CO_2 \rightarrow SmO^+ + CO$: Guided Ion Beam and Theoretical Studies. *Phys. Chem. Chem. Phys.* **2017,** *19*, 11075-11088.

(25) Armentrout, P. B.; Beauchamp, J. L. Reactions of U^+ and UO^+ with O_2, CO, CO_2, COS, CS_2 and D_2O. *Chem. Phys.* **1980,** *50*, 27-36.

(26) Campbell, M. L. Temperature Dependent Rate Constants for the Reactions of Gas Phase Lanthanides with CO_2. *Phys. Chem. Chem. Phys.* **1999,** *1*, 3731-3735.

(27) Schofield, K. An Overlooked Series of Gas Phase Diatomic Metal Oxide Ions that Are Long-lived. *J. Phys. Chem. A* **2006,** *110*, 6938-6947.

(28) Ard, S. G.; Shuman, N. S.; Martinez, O.; Brumbach, M. T.; Viggiano, A. A. Kinetics of Chemi-Ionization Reactions of Lanthanide Metals (Nd, Sm) from 150 to 450 K. *J. Chem. Phys.* **2015,** *143*, 204303.

(29) Konings, R. J. M.; Beneš, O.; Kovács, A.; Manara, D.; Sedmidubský, D.; Gorokhov, L.; Iorish, V. S.; Yungman, V.; Shenyavskaya, E.; Osina, E. The Thermodynamic Properties of the f-Elements and their Compounds. Part 2. The Lanthanide and Actinide Oxides. *J. Phys. Chem. Ref. Data* **2014,** *43*, 013101.

(30) Ard, S. G.; Shuman, N. S.; Martinez, O.; Armentrout, P. B.; Viggiano, A. A. Chemi-Ionization Reactions of La, Pr, Tb, and Ho with Atomic O and La with N_2O from 200 to 450 K. *J. Chem. Phys.* **2016,** *145*, 084302.

(31) Gibson, J. K. Role of Atomic Electronics in f-Element Bond Formation: Bond Energies of Lanthanide and Actinide Oxide Molecules. *J. Phys. Chem. A* **2003,** *107*, 7891-7899.

(32) Dai, G.-L.; Wang, C.-F. Carbon Dioxide Activation by La Atom and La^+ Cation in the Gas Phase: A Density Functional Theoretical Study. *J. Mol. Struct.: THEOCHEM* **2009,** *909*, 122-128.

(33) Wang, Y.-C.; Yang, X.-y.; Geng, Z.-Y.; Liu, Z.-Y. Theoretical Study of Carbon Dioxide-Carbon Monoxide Conversion by La^+, Hf^+ and Ta^+. *Chem. Phys. Lett.* **2006,** *431*, 39-44.

(34) Wang, Y.-C.; Liu, H.-W.; Geng, Z.-Y.; Lv, L.-L.; Si, Y.-B.; Wang, Q.-Y.; Wang, Q.; Cui, D.-D. Theoretical Study of the Reactions of Lanthanide Ions (Ce^+, Pr^+) with CO_2 in the Gas Phase. *Int. J. Quantum Chem.* **2011,** *111*, 2021-2030.

(35) Schröder, D.; Shaik, S.; Schwarz, H. Two-State Reactivity as a New Concept in Organometallic Chemistry. *Acc. Chem. Res.* **2000,** *33*, 139-145.

(36) Demireva, M.; Kim, J.; Armentrout, P. B. Gadolinium (Gd) Oxide, Carbide, and Carbonyl Cation Bond Energies and Evaluation of the $Gd + O \rightarrow GdO^+ + e^-$ Chemi-Ionization Reaction Enthalpy. *J. Phys. Chem. A* **2016,** *120*, 8550-8563.

(37) Loh, S. K.; Hales, D. A.; Lian, L.; Armentrout, P. B. Collision-Induced Dissociation of Fe_n^+ (n=2–10) with Xe: Ionic and Neutral Iron Binding Energies. *J. Chem. Phys.* **1989,** *90*, 5466-5485.

(38) Ervin, K. M.; Armentrout, P. B. Translational Energy Dependence of $Ar^+ + XY \rightarrow ArX^+ + Y$ ($XY = H_2, D_2, HD$) from Thermal to 30 eV C.M. *J. Chem. Phys.* **1985,** *83*, 166-189.

(39) Schultz, R. H.; Crellin, K. C.; Armentrout, P. B. Sequential Bond Energies of Iron Carbonyl $Fe(CO)_x^+$ (x = 1-5): Systematic Effects on Collision-Induced Dissociation Measurements. *J. Am. Chem. Soc.* **1991,** *113*, 8590-8601.

(40) Daly, N. R. Scintillation Type Mass Spectrometer Ion Detector. *Rev. Sci. Instrum.* **1960,** *31*, 264-267.

(41) Muntean, F.; Armentrout, P. B. Guided Ion Beam Study of Collision-Induced Dissociation Dynamics: Integral and Differential Cross Sections. *J. Chem. Phys.* **2001,** *115*, 1213-1228.

(42) Weber, M. E.; Elkind, J. L.; Armentrout, P. B. Kinetic Energy Dependence of $Al^+ + O_2 \rightarrow AlO^+ + O$. *J. Chem. Phys.* **1986,** *84*, 1521-1529.

(43) Frisch, M. J.; Trucks, G. W.; Schlegel, H. B.; Scuseria, G. E.; Robb, M. A.; Cheeseman, J. R.; Scalmani, G.; Barone, V.; Mennucci, B.; Petersson, G. A.et al.; Gaussian, Inc.: Wallingford, CT, USA, 2009.

(44) Becke, A. D. Density-Functional Thermochemistry. III. The Role of Exact Exchange. *J. Chem. Phys.* **1993,** *98*, 5648-5652.

(45) Lee, C.; Yang, W.; Parr, R. G. Development of the Colle-Salvetti Correlation-Energy Formula into a Functional of the Electron Density. *Phys. Rev. B* **1988,** *37*, 785-789.

(46) Dolg, M.; Stoll, H.; Preuss, H. Energy-Adjusted Ab Initio Pseudopotentials for the Rare Earth Elements. *J. Chem. Phys.* **1989,** *90*, 1730-1734.

(47) Cao, X.; Dolg, M. Valence Basis Sets for Relativistic Energy-Consistent Small-Core Lanthanide Pseudopotentials. *J. Chem. Phys.* **2001,** *115*, 7348-7355.

(48) Perdew, J. P.; Ernzerhof, M.; Burke, K. Rationale for Mixing Exact Exchange with Density Functional Approximations. *J. Chem. Phys.* **1996,** *105*, 9982-9985.

(49) Adamo, C.; Barone, V. Toward Reliable Density Functional Methods without Adjustable Parameters: The PBE0 Model. *J. Chem. Phys.* **1999,** *110*, 6158-6170.

(50) Raghavachari, K.; Trucks, G. W.; Pople, J. A.; Head-Gordon, M. A Fifth-Order Perturbation Comparison of Electron Correlation Theories. *Chem. Phys. Lett.* **1989,** *157*, 479-483.

(51) Bartlett, R. J.; Watts, J. D.; Kucharski, S. A.; Noga, J. Non-Iterative Fifth-Order Triple and Quadruple Excitation Energy Corrections in Correlated Methods. *Chem. Phys. Lett.* **1990,** *165*, 513-522.

(52) Scuseria, G. E.; Lee, T. J. Comparison of Coupled-Cluster Methods which Include the Effects of Connected Triple Excitations. *J. Chem. Phys.* **1990,** *93*, 5851-5855.

(53) Crawford, T. D.; Stanton, J. F. Investigation of an Asymmetric Triple-Excitation Correction for Coupled-Cluster Energies. *Int. J. Quantum Chem.* **1998,** *70*, 601-611.

(54) Douglas, M.; Kroll, N. M. Quantum Electrodynamical Corrections to the Fine Structure of Helium. *Ann. Phys.* **1974,** *82*, 89-155.

(55) Reiher, M.; Wolf, A. Exact Decoupling of the Dirac Hamiltonian. II. The Generalized Douglas–Kroll–Hess Transformation up to Arbitrary Order. *J. Chem.*

Phys. **2004,** *121*, 10945-10956.

(56) Lu, Q.; Peterson, K. A. Correlation Consistent Basis Sets for Lanthanides: The Atoms La–Lu. *J. Chem. Phys.* **2016,** *145*, 054111.

(57) Foresman, J. B.; Frisch, A. *Exploring Chemistry with Electronic Structure Methods*; Gaussian: Pittsburgh, Pa., 1996.

(58) Schuchardt, K. L.; Didier, B. T.; Elsethagen, T.; Sun, L.; Gurumoorthi, V.; Chase, J.; Li, J.; Windus, T. L. Basis Set Exchange: A Community Database for Computational Sciences. *J. Chem. Inf. Model.* **2007,** *47*, 1045-1052.

(59) Feller, D. The Role of Databases in Support of Computational Chemistry Calculations. *J. Comput. Chem.* **1996,** *17*, 1571-1586.

(60) Gioumousis, G.; Stevenson, D. P. Reactions of Gaseous Molecule Ions with Gaseous Molecules. V. Theory. *J. Chem. Phys.* **1958,** *29*, 294-299.

(61) Koyanagi, G. K.; Bohme, D. K. Oxidation Reactions of Lanthanide Cations with N_2O and O_2: Periodicities in Reactivity. *J. Phys. Chem. A* **2001,** *105*, 8964-8968.

(62) Darwent, B. d. *Bond Dissociation Energies in Simple Molecules*; U.S. National Bureau of Standards; for sale by the Supt. of Docs., U.S. Govt. Print. Off.: Washington, 1970.

(63) Chesnavich, W. J.; Bowers, M. T. Theory of Translationally Driven Reactions. *J. Phys. Chem.* **1979,** *83*, 900-905.

(64) Hinton, C. S.; Citir, M.; Manard, M.; Armentrout, P. B. Collision-Induced Dissociation of MO^+ and MO_2^+ (M = Ta and W): Metal Oxide and Dioxide Cation Bond Energies. *Int. J. Mass Spectrom.* **2011,** *308*, 265-274.

(65) Demireva, M.; Armentrout, P. B. Gadolinium Cation (Gd^+) Reaction with O_2: Potential Energy Surface Mapped Experimentally and with Theory. *J. Chem. Phys.* **2017,** *146*, 174302.

(66) Burley, J. D.; Ervin, K. M.; Armentrout, P. B. Translational Energy Dependence of $O^+(^4S) + H_2(D_2, HD) \rightarrow OH^+(OD^+) + H(D)$ from Thermal Energies to 30 eV C.M. *Int. J. Mass Spectrom. Ion Processes* **1987,** *80*, 153-175.

(67) Armentrout, P. B. The Bond Energy of ReO^+: Guided Ion-Beam and Theoretical Studies of the Reaction of Re^+ (^7S) with O_2. *J. Chem. Phys.* **2013,** *139*, 084305.

(68) Hinton, C. S.; Citir, M.; Armentrout, P. B. Guided Ion-Beam and Theoretical Studies of the Reaction of Os^+ (^6D) with O_2: Adiabatic and Nonadiabatic Behavior. *Int. J. Mass Spectrom.* **2013,** *354–355*, 87-98.

(69) Kretzschmar, I.; Schröder, D.; Schwarz, H.; Rue, C.; Armentrout, P. B. Experimental and Theoretical Studies of Vanadium Sulfide Cation. *J. Phys. Chem. A* **1998,** *102*, 10060-10073.

(70) Rue, C.; Armentrout, P. B.; Kretzschmar, I.; Schröder, D.; Harvey, J. N.; Schwarz, H. Kinetic-Energy Dependence of Competitive Spin-Allowed and Spin-Forbidden Reactions: $V^+ + CS_2$. *J. Chem. Phys.* **1999,** *110*, 7858-7870.

(71) Shaik, S. An Anatomy of the Two-State Reactivity Concept: Personal Reminiscences in Memoriam of Detlef Schröder. *Int. J. Mass Spectrom.* **2013,** *354–355*, 5-14.

(72) Harris, N.; Shaik, S.; Schröder, D.; Schwarz, H. Single- and Two-State Reactivity in the Gas-Phase C−H Bond Activation of Norbornane by `Bare' FeO^+. *Helv. Chim. Acta* **1999,** *82*, 1784-1797.

(73) Rodgers, M. T.; Armentrout, P. B. A Critical Evaluation of the Experimental and Theoretical Determination of Lithium Cation Affinities. *Int. J. Mass Spectrom.* **2007,** *267*, 167-182.

(74) Martin, J. M. L. Ab Initio Total Atomization Energies of Small Molecules — Towards the Basis Set Limit. *Chem. Phys. Lett.* **1996,** *259*, 669-678.

(75) Cox, R. M.; Kim, J.; Armentrout, P. B.; Bartlett, J.; VanGundy, R. A.; Heaven, M. C.; Ard, S. G.; Melko, J. J.; Shuman, N. S.; Viggiano, A. A. Evaluation of the Exothermicity of the Chemi-Ionization Reaction $Sm + O \rightarrow SmO^+ + e^-$. *J. Chem. Phys.* **2015,** *142*, 134307.

CHAPTER 6

ACTIVATION OF H_2 BY GADOLINIUM CATION (Gd^+): BOND ENERGY OF GdH^+ AND MECHANISTIC INSIGHTS FROM GUIDED ION BEAM AND THEORETICAL STUDIES

This chapter is reprinted with permission from Demireva, M; Armentrout, P. B. Activation of H_2 by Gadolinium Cation (Gd^+): Bond Energy of GdH^+ and Mechanistic Insights from Guided Ion Beam and Theoretical Studies. *J. Phys. Chem. A* **2018**, *122*, 750-761. © 2018 American Chemical Society. http://pubs.acs.org/doi/full/10.1021/acs.jpca.7b11471

6.1 Graphical Abstract

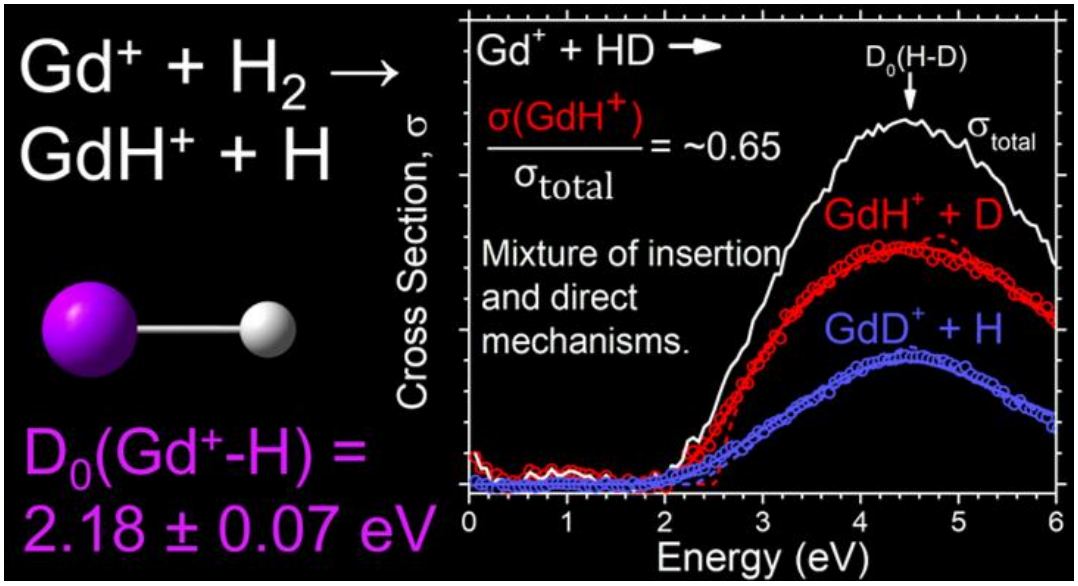

6.2 Abstract

The energy dependent reactions of the lanthanide gadolinium cation (Gd^+) with H_2, D_2, and HD are investigated using guided ion beam tandem mass spectrometry. From analysis of the resulting endothermic product ion cross sections, the 0 K bond dissociation energy for GdH^+ is measured to be 2.18 ± 0.07 eV. Theoretical calculations on GdH^+ are performed for comparison with the experimental thermochemistry and generally appear to overestimate the experimental GdH^+ bond dissociation energy. The branching ratio of the products in the HD reaction suggests that Gd^+ reacts primarily via a statistical insertion mechanism to form the hydride product ion with contributions from direct mechanisms. Relaxed potential energy surfaces for GdH_2^+ are computed and are consistent with the availability of both statistical and direct reaction pathways. The reactivity and hydride bond energy for Gd^+ is compared with previous results for the group 3 metal cations, Sc^+ and Y^+, and the lanthanides, La^+ and Lu^+, and periodic trends are discussed.

6.3 Introduction

Dihydrogen plays an important role in many chemical and industrial processes, including hydrogenation of organic molecules. As the most abundant molecule in the universe and as a clean fuel, the hydrogen molecule has also potential to be an important energy source in the future, if appropriate storage materials can be developed. Activation of the relatively strong H-H bond (4.5 eV) requires the use of catalysts such as metals and their complexes. Understanding the activation of this strong bond was aided by the discovery a little over 30 years ago that H_2 could bind to a metal center as an intact molecule to form a stable three-center "sigma complex."[1-3] This research helped establish the initial

step in the activation mechanism of H_2. An active field of research has been to understand the interactions and reactivity of the hydrogen molecule with various transition metals and their complexes. Not only can this knowledge lead to insight into creating new catalysts and suitable storage materials, but it can also be extended to other types of systems because the bond cleavage of H_2 can more generally serve as a simple model for the activation of single covalent bonds.

One means to probe the reactivity and interactions of H_2 with a metal center directly, without complicating effects from solvent or substrate molecules, is via gas-phase experiments. The interactions of H_2 with metal cations have been studied in the gas phase using temperature-dependent cluster equilibria methods, from which the binding energies and entropies of successively bound H_2 molecules to different metal cations have been measured.[4-8] These experiments offer insight into the effects of the metal cation electronic configuration on the H_2 bond strength, on the structure of these complexes as a function of the number of H_2 molecules attached, and mechanistic details for metal ion insertion into H_2. More recently, gas-phase infrared photodissociation spectroscopy has been used to determine the structures of several metal cation dihydrogen complexes.[9-14] Because changes in the H_2 bond in the complexes will register as frequency shifts, this method can provide detailed information about the binding and extent of activation of H_2 on the metal cation center.

The energy dependent activation of H_2 by metal cations via reaction (6.1) can be investigated directly using guided ion beam tandem mass spectrometry (GIBMS), which allows for accurate thermochemistry to be measured.[15,16]

$$M^+ + H_2 \rightarrow MH^+ + H \qquad (6.1)$$

GIBMS experiments of reaction (6.1) have been performed extensively for transition metal cations, where metal hydride cation bond dissociation energies (BDEs) have been determined for most first,[17-24] second,[23-26] and third[27-33] row transition metal cations and the actinide thorium.[34] Investigations of the analogous reactions with HD have allowed for characterization of the reaction mechanisms for these metal cations. The wealth of results from these studies have helped elucidate periodic trends, providing insight into the role of the metal ion electronic configurations on reactivity, activation mechanism, and hydride bond strength.[23,24,35]

In contrast to the many studies for the transition metal cations, the activation and binding of H_2 by lanthanide cations remains largely unexplored both experimentally and theoretically. The heavy lanthanides are relatively challenging to describe theoretically, due to complicating spin-orbit and relativistic effects and the many possible electronic configurations arising from the 4f valence electrons. Thus, another advantage of gas-phase studies is that they can provide thermochemical information for small systems that can more easily be modeled by theoretical calculations. Because reaction (6.1) is relatively simple and can more generally represent bond cleavage of single bonds, the experimental thermochemistry obtained for this reaction can serve as a useful benchmark for theory.[34] Reaction (6.1) has been studied for the lanthanides, La^+ and Lu^+ with two non-4f valence electrons and empty and completely filled 4f orbitals, respectively, using GIBMS.[23] In this study, the reactivity of La^+ and Lu^+ with H_2 was compared with that of Sc^+ and Y^+ to determine trends moving down the periodic table along group 3. Theoretical calculations for LaH^+ and LaH_2^+ have also been performed and were able to reproduce the experimental thermochemistry and help elucidate the reactivity observed in the GIBMS experiment.[36]

The present study extends the GIBMS research of reaction (6.1) to the lanthanide gadolinium cation (Gd^+), which has a half-filled 4f shell and two non-4f valence electrons. Comparisons with La^+ and Lu^+ allow for insight into the effects of systematically increasing the number of 4f electrons. The energy dependent product ion cross sections for the Gd^+ reactions with H_2, HD, and D_2 are measured and analyzed to obtain the 0 K BDE for GdH^+. The product ion branching ratio in the HD reaction is used to infer information about the mechanism for H_2 activation. Theoretical calculations are performed for comparison with the experimental thermochemistry and to obtain potential energy surfaces for GdH_2^+, which provide additional insight into the reaction mechanism. The Gd^+ hydride BDE and reactivity with H_2 are compared with previous results for Sc^+, Y^+, La^+, and Lu^+ for insight into periodic trends.

6.4 Methods

6.4.1 Experimental methods. The guided ion beam tandem mass spectrometer and experimental procedure used for this work have been described in detail elsewhere.[15,16,37,38] Briefly, a direct current discharge flow tube (DC/FT) ion source was used to generate singly charged Gd cations from Gd foil (Sigma-Aldrich, St. Louis, MO). A potential of approximately -1200 to -1500 V was applied to a cathode consisting of the Gd foil mounted on a tantalum holder, while a gas mixture consisting of about 10% argon and 90% helium was continuously introduced into the source at ~0.4 Torr. Ar cations produced in the DC discharge were accelerated toward the cathode containing the Gd foil, where collisions with the foil resulted in sputtering of Gd^+. Gd ions were swept into a 1 m long flow tube, where they underwent approximately 10^5 thermalizing collisions with the He and Ar gas

mixture. On the basis of previous characterizations of the electronic temperature of metal ions formed from this same ion source,[26,39] the Gd precursor ions here are assumed to have an electronic temperature of 700 ± 400 K. As detailed previously,[40] this corresponds to an average electronic energy (E_{el}) for Gd^+ of 0.04 ± 0.03 eV, which is taken into account in the modeling described below to obtain the 0 K threshold energies. Precursor ions were skimmed, focused, and subsequently mass selected using a momentum analyzer, where the heaviest ^{160}Gd isotope (21.86% natural abundance, at least 2 Da heavier than the other naturally abundant Gd isotopes) was used to ensure adequate mass separation. Precursor ions were decelerated to well-defined kinetic energies prior to entering a radio frequency octopole.[41] Part of the octopole is surrounded by a reaction cell in which H_2, D_2, or HD gases at pressures ranging from ~0.15 to 0.4 mTorr were introduced for reaction with Gd^+. This range of pressures is sufficiently low to ensure that single collisions dominate, which was confirmed by measurements indicating that cross sections had no pressure dependence. The precursor and product ions were mass analyzed with a quadrupole mass filter and counted using a Daly detector.[42] Precursor and product ion intensities were measured as a function of collision energy in the lab frame, corrected for background reaction not occurring in the cell, and converted to cross sections as a function of energy in the center-of-mass (CM) frame as outlined previously.[38] Retarding experiments were performed to measure the full width at half maximum of the precursor ion kinetic energy distributions, which was approximately 0.5 eV in the lab frame with an uncertainty in the energy scale of ± 0.1 eV.

6.4.2 Data analysis. Threshold energies at 0 K, E_0, for the endothermic exchange reactions studied here were obtained, as described in detail previously,[16,43] by fitting the

product ion cross sections using a modified line-of-centers model given in equation (6.2).

$$\sigma(E) = \sigma_0 \sum_i g_i (E + E_i + E_{el} - E_0)^n / E \quad (6.2)$$

In equation (6.2), E corresponds to the CM collision energy, σ_0 is an empirical scaling factor, *n* corresponds to an empirical fitting parameter that determines the shape of the cross section, E_i gives the vibrational and rotational energy of the reactants in state i with the corresponding population degeneracy given by g_i ($\Sigma g_i = 1$), and E_{el} is the average electronic energy of Gd^+ (0.04 ± 0.03 eV). Vibrational frequencies and rotational constants for H_2, D_2, and HD needed to calculate E_i were obtained from the NIST WebBook.[44] Prior to comparison with the experimental cross sections, equation (6.2) was convolved with the reactant kinetic energy distributions, and optimized fits were subsequently obtained by varying σ_0, *n*, and E_0 using a nonlinear least-squares method.[15,16,38,45] The reported uncertainty (one standard deviation) in E_0 was determined from optimal fits to at least four independent data sets and includes the uncertainty in the range of *n* values that can reasonably reproduce the data, as well as the uncertainties associated with E_{el} and the absolute energy scale.

In the exchange reactions investigated here, the product ion formed can have sufficient energy to dissociate at energies exceeding the bond dissociation energy (BDE) of the corresponding neutral (H_2, D_2, or HD), which results in a decrease in the product ion cross section. This decline is modeled using a modified version of equation (6.2), which includes a dissociation probability as outlined in detail previously.[46] The measured E_0 values are used to determine 0 K BDEs (D_0) via expression (6.3), where A-B refers to the reactant neutral.

$$D_0\left(Gd^+\text{-}A\right) = D_0(A\text{-}B) - E_0 \quad (6.3)$$

6.4.3 Theoretical methods. Theoretical calculations were carried out using the Gaussian09 suite of programs[47] to determine the ground and low-energy states for GdH^+ and GdH_2^+ and the BDE of GdH^+. The latter value was determined from the energy difference between ground state intact and dissociated GdH^+. Geometry optimization and vibrational frequency calculations for GdH^+ were performed at the B3LYP,[48,49] BHandHLYP (BHLYP),[50] PBE0,[51,52] and CCSD(T)[53-56] levels of theory. These calculations utilized the atomic natural orbital[57] (ANO) basis set together with the relativistic Stuttgart Dresden[58] (SDD) effective small (28 electron) core potential (ECP) for Gd and the Pople 6-311++G(3df,3p) basis set for H, or the correlation consistent all-electron basis sets cc-pVXZ-DK3[59] (where X = T, Q) for Gd developed by the Peterson group with the corresponding aug-cc-pVXZ-DK (where X = T, Q) basis sets for H performed using the 2nd-order Douglas-Kroll-Hess Hamiltonian (DKH2).[60,61] With the exception of the all-electron basis sets for Gd provided by Professor Peterson, the other basis sets were obtained from the EMSL basis set exchange.[62,63] CCSD(T) calculations using the ANO basis set for Gd included all electrons in the correlation calculation (with the "full" keyword), whereas those using the all-electron basis sets included only the outer electrons of Gd in 4f, 5s, 5p, 5d, and 6s orbitals (with the "window=24" keyword). To determine the bond length and frequency of GdH^+ for calculations utilizing the large cc-pVQZ-DK3 Gd basis set at the CCSD(T) level, potential energy surfaces were mapped from seven single point energies by varying the bond length of Gd^+-H around the equilibrium bond distance determined from the calculations using the smaller cc-pVTZ-DK3 basis set at the same level of theory. These potential energy curves were fitted with fifth-order polynomials to determine the equilibrium bond lengths, and energies and

vibrational frequencies were subsequently obtained from frequency calculations using the determined equilibrium bond lengths.[64] Extensive calculations for GdH_2^+, including potential energy surface scans and optimizations of local minima and transition states, were performed at the BHLYP/ANO level. All computed energies of optimized structures were zero point energy corrected using frequencies scaled by 0.989.[65]

6.5 Results and Discussion

6.5.1 Gd^+ reactions with H_2 and D_2. In reactions of Gd^+ with H_2 and D_2, GdH^+ and GdD^+ products are formed according to reactions (6.1) and (6.4), respectively.

$$Gd^+ + D_2 \rightarrow GdD^+ + D \qquad (6.4)$$

The energy dependent cross sections resulting from these respective processes are shown in Figures 6.1a and b. The apparent thresholds for formation of the products are near 1.5 eV with the product ion cross sections peaking near the neutral BDEs (i.e., 4.478 eV and 4.556 eV for H_2 and D_2,[66] respectively). At energies exceeding the neutral BDEs, the product cross sections decline because the GdH^+ and GdD^+ products have sufficient energy to dissociate. The cross section for GdH^+ reaches a maximum of approximately 1.05 $Å^2$. This cross section is slightly smaller than the maximum of the GdD^+ cross section at approximately 1.33 $Å^2$, where the two cross sections are nearly equal within the estimated 20% absolute uncertainty in the measurement. In guided ion beam experiments, the resolution of the quadrupole mass filter is kept relatively low to ensure high collection efficiency of products.[15] This makes separation of the low-abundant GdH^+ product peak difficult from the much more intense Gd^+ precursor, which is only 1 Da lower in mass. Thus, there is a significant overlap between the precursor and product peaks, which leads

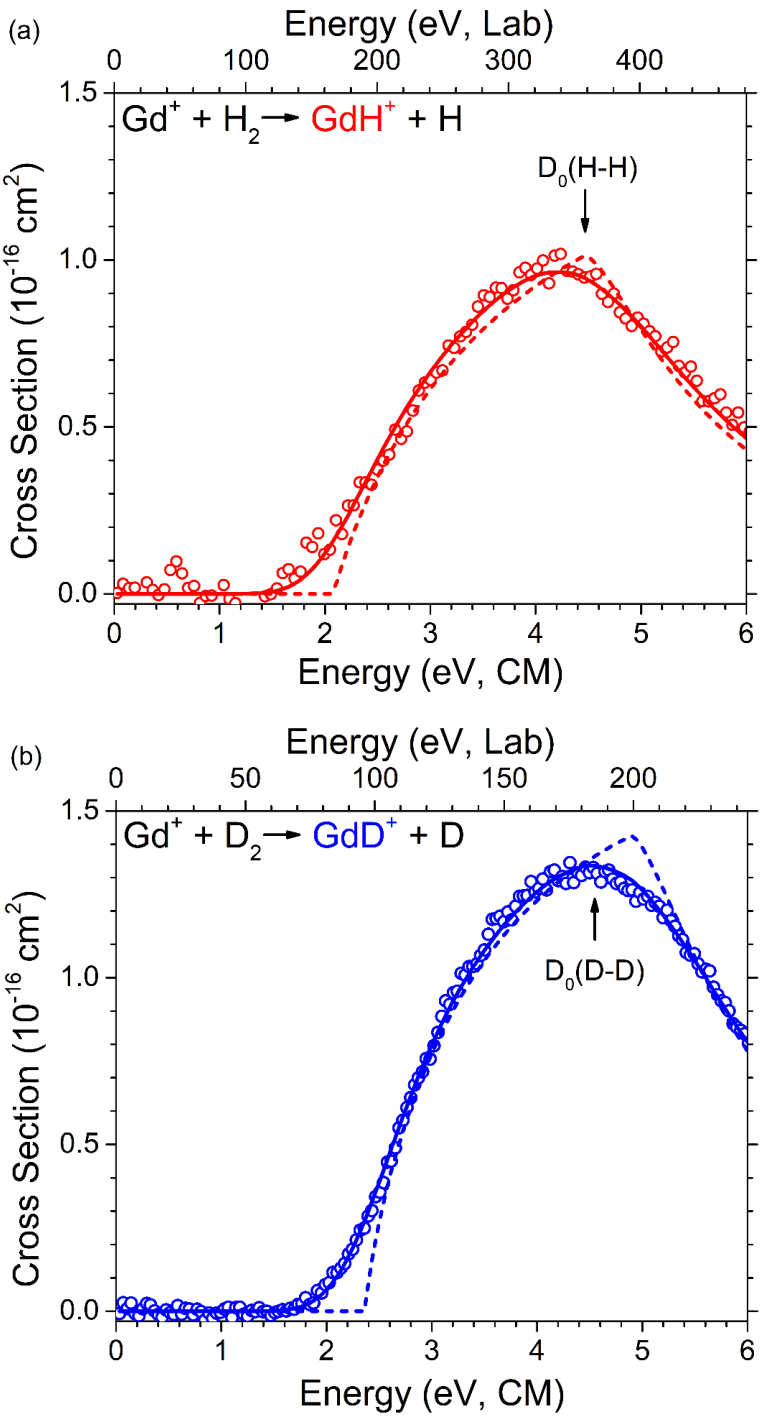

Figure 6.1. The product cross sections resulting from the reaction between Gd^+ and H_2 (part a) and D_2 (part b) as function of kinetic energy in the center-of-mass (bottom x-axis) and lab (top x-axis) frames. The arrows indicate the BDEs of H_2 at 4.478 eV and D_2 at 4.556 eV. Optimized fits using equation (6.2) are given by the solid lines, which include convolution over the reactant internal and kinetic energies. The dashed lines indicate the modeled cross sections excluding convolution over the reactant internal and kinetic energy distributions.

to the noisier data for GdH^+ compared with those for GdD^+ where, at a 2 Da separation, the overlap with the precursor peak is substantially smaller. The slightly lower cross section for reaction (6.1) could potentially be attributed to artifacts from the correction of the significant overlap. Additionally, the GdH^+ data in Figure 6.1a needed to be corrected for a negative baseline such that a constant value (the average of the baseline) was added to the cross section to center the baseline around zero. The uncertainty in the constant was taken as the standard deviation in this baseline and was accounted for in the uncertainty of the E_0 value reported from the modeling.

The GdH^+ and GdD^+ cross sections can be modeled using equation (6.2) to determine the BDE of GdH^+. Modeling the less noisy GdD^+ cross section should potentially yield more reliable results. The fitting parameters used in the modeling and the thermochemistry obtained from these data are summarized in Table 6.1. Optimized fits are shown by the solid lines in Figure 6.1 and yield 0 K threshold energies here of 2.22 ± 0.29 eV and 2.39 ± 0.11 eV for forming GdH^+ and GdD^+, respectively. Using equation (6.3), these E_0 values can be converted to yield 0 K BDEs for GdH^+ of 2.26 ± 0.29 eV and 2.14

Table 6.1. Summary of optimized modeling parameters used in equation (6.2) to reproduce the experimental cross sections.

Reaction	σ_0	*n*	E_0 (eV)	$D_0(Gd^+\text{-}H)$ (eV)
$Gd^+ + H_2 \rightarrow GdH^+ + H$	2.2 ± 0.3	0.9 ± 0.2	2.22 ± 0.29	2.26 ± 0.29
$Gd^+ + D_2 \rightarrow GdD^+ + D$	4.3 ± 0.6	1.0 ± 0.2	2.39 ± 0.11	2.14 ± 0.11[a]
$Gd^+ + HD \rightarrow GdH^+ + D$	1.6 ± 0.2	0.9 ± 0.2	2.43 ± 0.17	2.08 ± 0.17
$Gd^+ + HD \rightarrow GdD^+ + H$	0.6 ± 0.1	1.4 ± 0.2	2.24 ± 0.11	2.24 ± 0.11[a]

[a] The 0 K BDE for Gd^+-H obtained from Gd^+-D includes a -0.03 eV correction because of zero point energy differences.[23]

± 0.11 eV, respectively, where the BDE obtained from the GdD^+ measurement has been corrected for the zero point energy difference (i.e., 0.03 eV as determined from the calculated frequency for GdH^+ of 1685 cm^{-1} at the B3LYP/ANO level) of the heavier D isotope. The two GdH^+ BDE values agree with each other within the experimental uncertainties.

6.5.2 Gd^+ reaction with HD. In the reaction between Gd^+ and HD, both GdH^+ and GdD^+ products are observed and formed according to processes (6.5) and (6.6), respectively.

$$Gd^+ + HD \rightarrow GdH^+ + D \quad (6.5)$$

$$\rightarrow GdD^+ + H \quad (6.6)$$

The resulting product ion cross sections as a function of energy are shown in Figure 6.2, where the GdH^+ cross section has been corrected for a negative baseline similar to the GdH^+ cross section in reaction (6.1) discussed above. Processes (6.5) and (6.6) both have apparent threshold energies near 2 eV, consistent with those observed for reactions (6.1) and (6.4). As expected, the total cross section peaks near the BDE of HD at 4.514 eV and its maximum reaches about 1.18 $Å^2$, consistent within the 20% uncertainty with the cross sections resulting from reactions (6.1) and (6.4). The GdH^+ cross section in the HD reaction is approximately a factor of two larger than that of GdD^+ where the origins for this behavior are discussed in more detail below. Additional 0 K BDEs for GdH^+ can be obtained by separately modeling the GdH^+ and GdD^+ cross sections using equation (6.2) as shown in Figure 6.2 with parameters in Table 6.1. Modeling these data yields $D_0(Gd^+\text{-}H)$ of 2.08 ± 0.17 eV and 2.24 ± 0.11 eV (Table 6.1) from reactions (6.5) and (6.6), respectively, where these values are in generally good agreement with those obtained from reactions (6.1) and

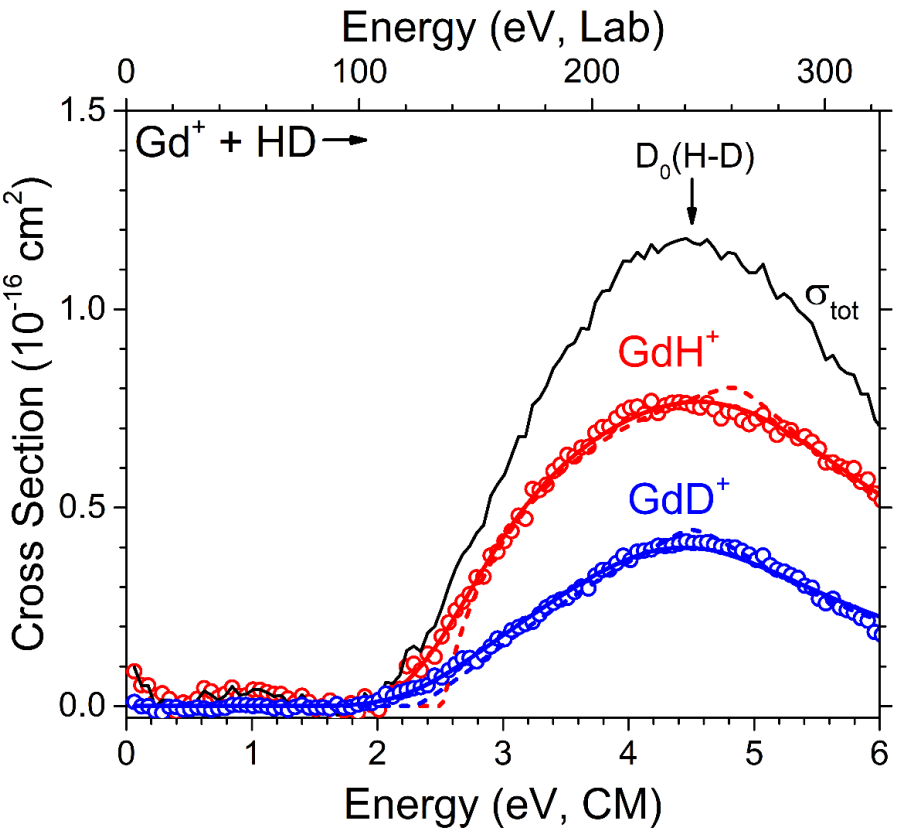

Figure 6.2. GdH^+ and GdD^+ cross sections resulting from the reaction between Gd^+ and HD as a function of kinetic energy in the center-of-mass (bottom x-axis) and lab (top x-axis) frames. The total cross section is given by the black line. The arrow indicates the BDE of H-D at 4.514 eV. Optimized fits for GdH^+ and GdD^+ using equation (6.2) are given by the solid lines, which include convolution over the reactant internal and kinetic energies. The dashed lines indicate the modeled cross sections excluding convolution over the reactant internal and kinetic energy distributions.

(6.4). Combining all four GdH^+ BDE measurements yields a weighted average of $D_0(Gd^+\text{-}H) = 2.18 \pm 0.07$ eV.

6.5.3 Theoretical results for GdH^+. Quantum chemical calculations using various basis sets and levels of theory were carried out to determine the ground and low-energy states of GdH^+ and to calculate theoretical BDEs for GdH^+ for comparison with the experimental thermochemistry. Several electronic states and multiplicities of 7 and 9 for GdH^+ were considered. The bond lengths, energies, and vibrational frequencies from these

calculations are summarized in the Supporting Information (Section 6.7). Representative molecular orbitals (mos), calculated at the B3LYP/ANO level, that result from the interactions of the valence electrons of Gd^+ (^{10}D, $4f^7\ 5d^1\ 6s^1$) and H (^2S, $1s^1$) for different GdH^+ electronic states are shown in Figure 6.3a. All theoretical results indicate that GdH^+ has a $^9\Sigma^-$ ($[\varphi^2\delta^2\pi^2\sigma^1]\ \sigma^2\sigma^1$) ground state, where the mos resulting from the half-filled 4f electron shell are given in square brackets and form mostly nonbonding mos similar in character to the atomic orbitals (Figure 6.3a). In this $^9\Sigma^-$ state, a predominantly $5d_{z^2}$ orbital on Gd^+ interacts with the 1s orbital of H to form a σ bonding mo, such that the bond strength in GdH^+ should primarily reflect that of a 5dσ-H(1s) interaction. Additionally, an unpaired electron occupies a mostly nonbonding mo comprised of the 6s (with some $5d_{z^2}$ character) orbital of Gd^+. Thus, Gd^+ practically retains its ground state valence electron configuration ($4f^75d^16s^1$) in the GdH^+ $^9\Sigma^-$ ground state. $^9\Delta$ and $^9\Pi$ electronic states result if the 6s valence electron of Gd^+ is moved to occupy mostly nonbonding 5dδ and 5dπ mos, respectively. Depending on the basis set and level of theory used, the lowest spin-orbit (SO) levels for the $^9\Delta$ and $^9\Pi$ states are 0.07 - 0.33 eV and 0.38 - 0.66 eV, respectively, higher in energy than the $^9\Sigma^-$ ground state, as seen in Figure 6.3b. To obtain the energy for the lowest SO levels, the calculated energies for the $^9\Delta$ and $^9\Pi$ states were corrected by a semiempirical SO energy correction. Details about how this SO energy correction was calculated can be found in the Supporting Information (Section 6.7) and this correction has been applied previously[67-69] for other heavy metal cations. The energy difference between the $^9\Sigma^-$ ground state and the $^9\Delta$ and $^9\Pi$ states is similar to the energy required to promote the 6s electron of Gd^+ to a 5d orbital (i.e., the energy difference between the $^{10}D_{5/2}$ and $^{10}F_{3/2}$ states of Gd^+, ~0.50 eV).[70]

Figure 6.3. (a) Molecular orbitals resulting from the valence electrons of Gd^+ and H for different electronic states of GdH^+ as optimized at the B3LYP/ANO level of theory. Unless otherwise noted, the electronic configuration shown is that for a multiplicity of 9, where states with multiplicities of 7 result if the electron indicated in red is low-spin coupled with the 4f electrons. (b) Theoretical energies of the lowest spin-orbit level for different GdH^+ electronic states relative to the $^9\Sigma^-$ ground state using the ANO, cc-pVTZ-DK3, and cc-pVQZ-DK3 basis sets for Gd at the B3LYP, BHLYP, PBE0, and CCSD(T) levels of theory. (c) Comparison between the experimentally measured GdH^+ BDE (solid line with the uncertainty indicated by the dashed lines) and theoretical values (which include an empirical spin-orbit correction) calculated at the B3LYP, BHLYP, PBE0, and CCSD(T) levels of theory using the ANO (black squares), cc-pVTZ-DK3 (red circles), and cc-pVQZ-DK3 (blue triangles) basis sets for Gd. Complete basis set (CBS) extrapolated BDE using the cc-pVXZ-DK3 (where X = T, Q) basis sets at the CCSD(T) level is shown by the purple diamond.

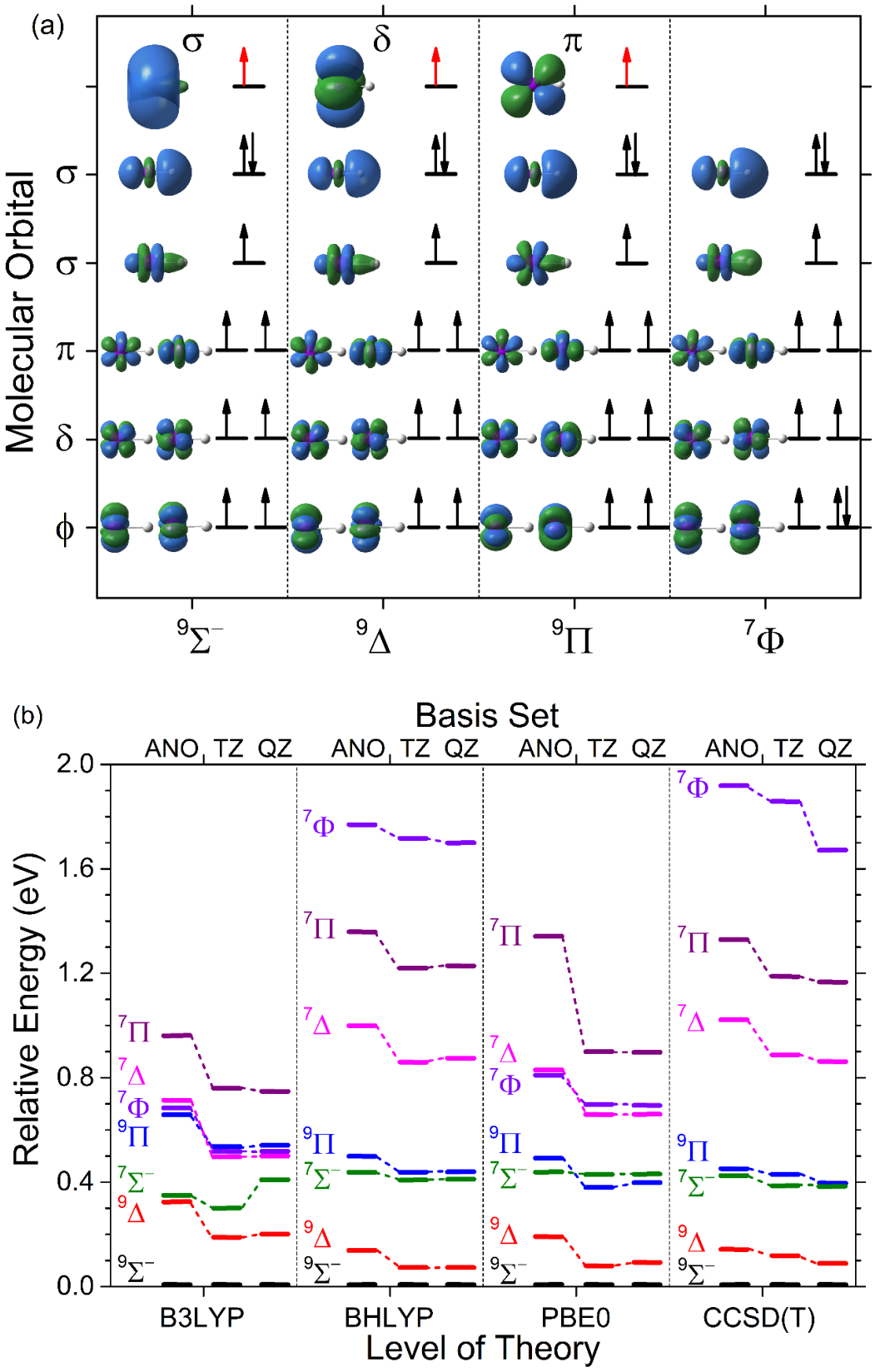
(a)
σ
δ
π
Molecular Orbital
σ
σ
π
δ
ϕ
$^9\Sigma^-$
$^9\Delta$
$^9\Pi$
$^7\Phi$
(b)
Basis Set
ANO TZ QZ
Relative Energy (eV)
2.0
1.6
1.2
0.8
0.4
0.0
$^7\Phi$
$^7\Pi$
$^7\Delta$
$^9\Pi$
$^7\Sigma^-$
$^9\Delta$
$^9\Sigma^-$
B3LYP
BHLYP
PBE0
CCSD(T)
Level of Theory

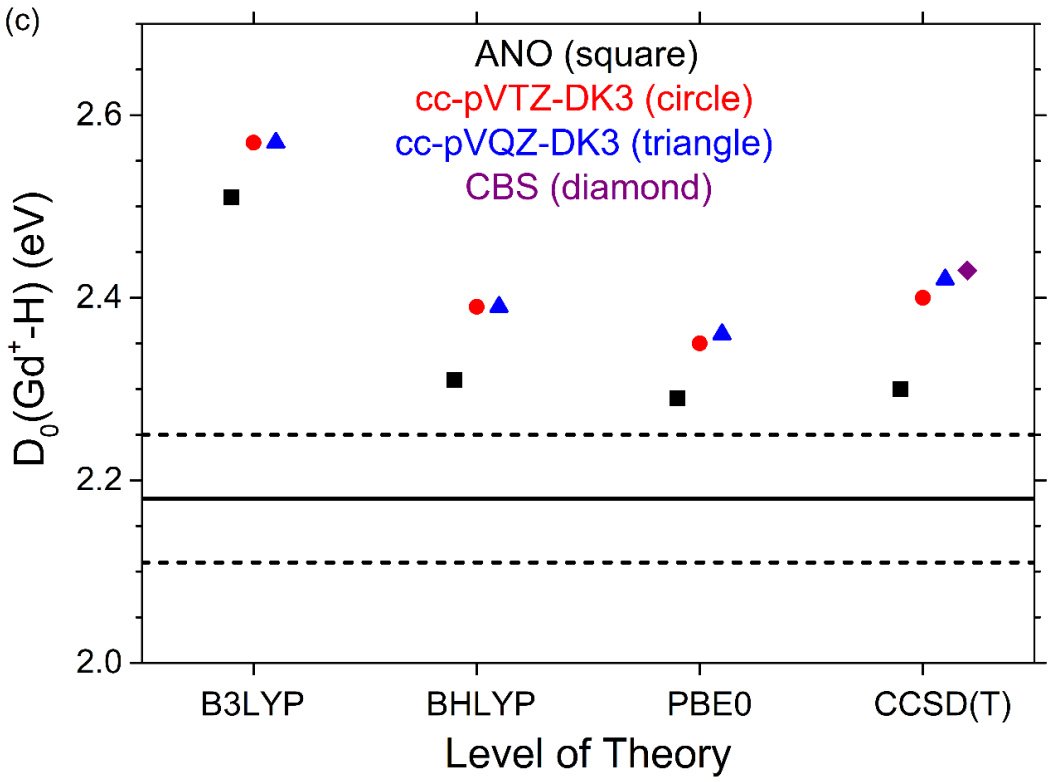

Figure 6.3 continued

In the GdH^+ nonet states, the unpaired electron is high-spin coupled with the 4f electrons (Figure 6.3a). Corresponding $^7\Sigma^-$, $^7\Delta$, and $^7\Pi$ electronic states are obtained if the unpaired electron in the σ, δ, and π valence mos, respectively, is low spin-coupled with the 4f electrons of Gd^+. The relative energies for these septet states depend on the basis sets and level of theory, where generally the $^7\Sigma^-$ state is found to have an energy similar to the $^9\Pi$ state, whereas both the $^7\Delta$ and $^7\Pi$ states lie higher in energy. For the septet states, the unpaired electron can also occupy a 4f orbital in a low-spin $4f^8$ configuration. The lowest such state results from occupying a φ mo to yield a $^7\Phi$ electronic state (Figure 6.3a). At the BHLYP and CCSD(T) levels, the $^7\Phi$ electronic state is predicted to be more than 1.5 eV higher in energy than the $^9\Sigma^-$ ground state, whereas at the B3LYP and PBE0 levels, this state is predicted to have an energy similar to the $^7\Delta$ state, at 0.51 – 0.69 eV and 0.69 – 0.81 eV, respectively, above the ground state (Figure 6.3b). The B3LYP and PBE0 calculations appear to overestimate the stability of the Gd^+ $4f^8$ configuration as also concluded from previous calculations.[40] Figure 6.3b indicates that fairly similar ordering and relative energies are predicted for the various GdH^+ electronic states using BHLYP and CCSD(T) approaches for the different basis sets. Because the calculations using CCSD(T) should potentially be the most accurate, the results in Figure 6.3b suggest that nearly equivalent results can be achieved using the much cheaper computational BHLYP method. The BHLYP method has also proven to provide reasonable results for other metal cation hydrides and methyl complexes.[27,29,34,71] This level of theory was therefore used for the extensive GdH_2^+ calculations discussed below.

6.5.4. Theoretical GdH^+ BDE. Theoretical BDEs are calculated from the difference in energy between intact GdH^+ ($^9\Sigma^-$) and dissociated Gd^+ (^{10}D) and H (^2S). The

theoretical energy obtained for each species corresponds to an average energy over all SO levels of the corresponding electronic state. However, because the experiments here generally measure the energy difference between ground state SO levels of reactants and products, the theoretical BDEs need to be adjusted by an empirical SO energy correction for a potentially more accurate comparison with experiment (see Supporting Information, Section 6.7, for details on calculating the SO correction). Both the $^{9}\Sigma^{-}$ ground state for GdH^{+} and the ^{2}S state for H have no first-order SO corrections. In contrast, Gd^{+}, which has a ^{10}D ground state requires an SO correction, where the lowest energy $^{10}D_{5/2}$ SO level is 0.123 eV lower in energy than the average energy for the ^{10}D state. Thus, the theoretical BDEs obtained from the calculations need to be lowered by 0.123 eV. Both SO corrected and uncorrected BDEs calculated at different levels of theory and basis sets are listed in the Supporting Information (Section 6.7). Figure 6.3c shows a comparison between the experimental $D_0(Gd^{+}\text{-}H)$ of 2.18 ± 0.07 and the SO corrected BDEs calculated at the B3LYP, BHLYP, PBE0, and CCSD(T) levels of theory using the ANO, cc-pVTZ-DK3, and cc-pVQZ-DK3 basis sets for Gd. Generally, the BDEs for all basis sets at the B3LYP level are predicted to be larger than the experimental value by ~0.35 eV, whereas those at the BHLYP and PBE0 levels are only about 0.15 eV larger, in better agreement with experiment. At the CCSD(T) level, the GdH^{+} BDE calculated using the ANO basis set for Gd is in relatively good agreement with experiment, whereas the calculations utilizing the all-electron cc-pVTZ-DK3 and cc-pVQZ-DK3 basis sets result in BDEs for GdH^{+} that are larger than experiment by about 0.2 eV (Figure 6.3c). Extrapolation to the complete basis set (CBS) limit at the CCSD(T) level using the BDEs calculated with cc-pVXZ-DK3 (with X = T and Q) and the formula $E[CBS] = 1.577163\ E[Q] - 0.577163\ E[T]$[72,73] yields a BDE

for GdH^+ of 2.43 eV, Supporting Information, Section 6.7. Similar theoretical methods have previously been shown to also overestimate (by ~0.1 to 0.4 eV) the hydride BDEs of the actinide cation Th^+,[34] and the third-row transition metal cations Hf^+ and Os^+.[27,29] It is possible that the slight deviation between experiment and theory arises from the $^9\Sigma^-$ GdH^+ ground state having multireference character, which is not accounted for in the present calculations. However, DFT calculations indicate that there is no significant spin-contamination for this state (Supporting Information, Section 6.7). Moreover, the T1 diagnostics obtained at the CCSD(T) level are 0.013, 0.016, and 0.018 for the ANO, cc-pVTZ-DK3, and cc-pVQZ-DK3 basis sets for Gd, suggesting that the GdH^+ $^9\Sigma^-$ ground state does not have significant multiconfigurational character.

6.5.5 Theoretical results for GdH_2^+. To obtain information about the mechanism of reaction (6.1), theoretical calculations on various GdH_2^+ species were performed. Extensive calculations were carried out at the BHLYP/ANO level of theory as this method is relatively inexpensive and provided similar results for the GdH^+ BDE and for the various electronic states of GdH^+ to the results obtained at the CCSD(T)/ANO level (Figures 6.3b and 6.3c). Various geometries, including linear and cyclic (side-on) Gd^+-H_2 adducts and inserted cyclic and linear H-Gd^+-H structures with multiplicities of 8 and 10 were considered. The electronic configurations, bond angles, bond lengths, energies, and vibrational frequencies for these structures are summarized in the Supporting Information (Section 6.7). Representative mos that consider only the valence electrons of Gd^+ and the two H atoms for stable cyclic GdH_2^+ structures having C_{2v} symmetry are shown in Figures 6.4a and b. For cyclic GdH_2^+ adducts shown in Figure 6.4a, Gd^+ essentially has a $5d^16s^1$ configuration, whereas for the cyclic adducts and inserted structures shown in Figure 6.4b,

Figure 6.4. Molecular orbitals resulting from the valence electrons of Gd^+ and H_2 calculated at the BHLYP/ANO level of theory for (a) cyclic GdH_2^+ structures that result from $5d^16s^1$ Gd^+ configurations (b) cyclic GdH_2^+ structures that result from $5d^2$ or $6s^2$ Gd^+ configurations and (c) linear inserted H-Gd^+-H structures. The electronic configurations shown are those for a multiplicity of 8, where states with a multiplicity of 10 result if both electrons indicated in red are high-spin coupled with the 4f electrons. The electron shown by the solid blue arrow for $^8A_2$ can be moved into an a_1 orbital and high-spin coupled with the 4f electrons as shown by the dotted blue arrow to give a dectet state.

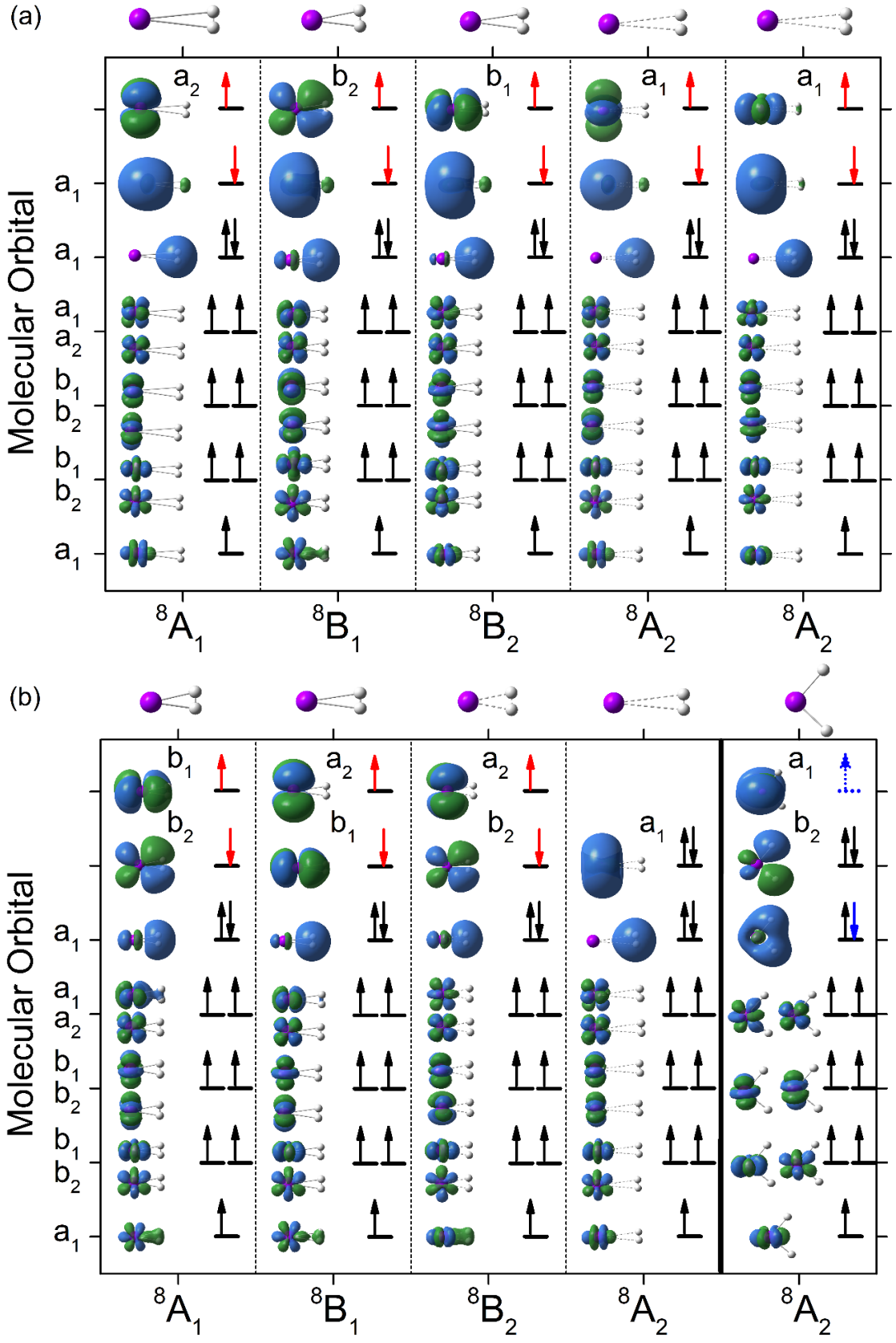
(a)
Molecular Orbital
a2
b2
b1
a1
a1
a1
a1
a2
b1
b2
b1
b2
a1
8A1
8B1
8B2
8A2
8A2
(b)
Molecular Orbital
b1
b2
a2
b1
a2
b2
a1
a1
b2
a1
a2
b1
b2
b1
b2
a1
8A1
8B1
8B2
8A2
8A2

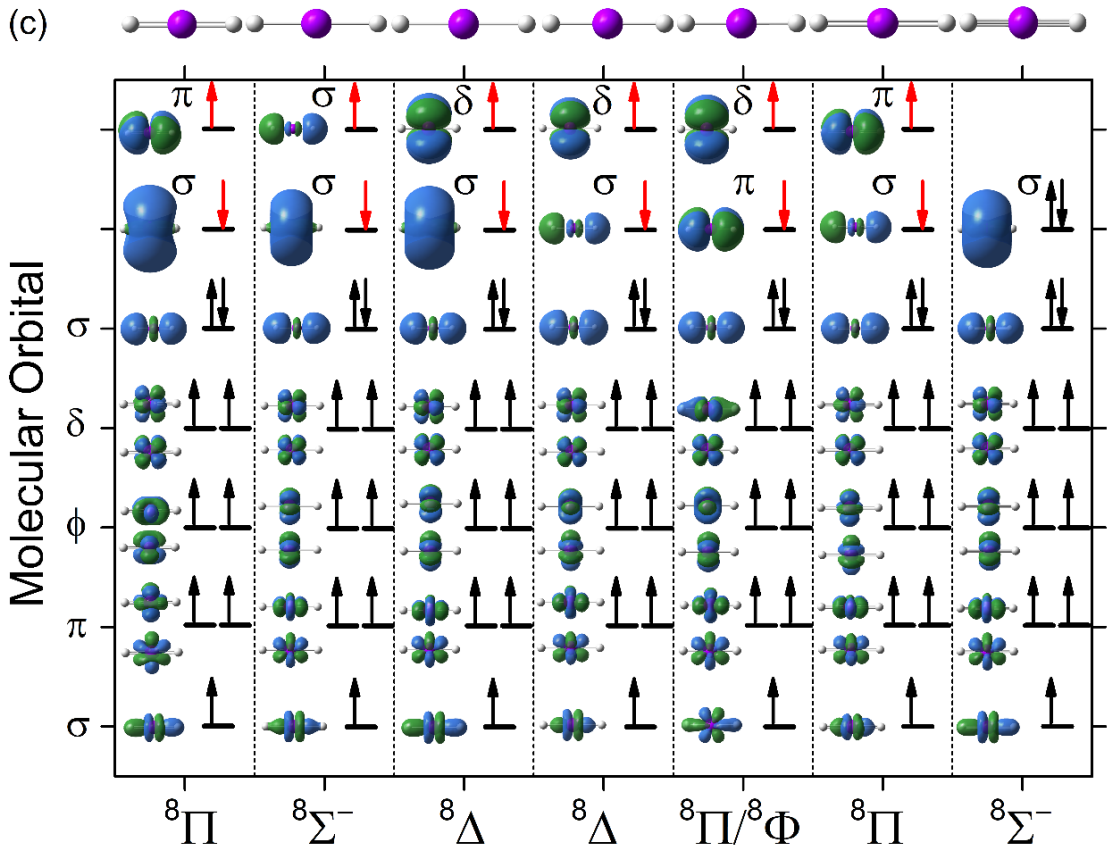

Figure 6.4 continued

Gd^+ has a $5d^2$ or $6s^2$ configuration. In these structures, the seven 4f electrons of Gd^+ occupy largely nonbonding ($[a_1^1\ b_1^1\ b_2^1\ b_1^1\ b_2^1\ a_1^1\ a_2^1]$) mos similar in character to their atomic orbitals. In most of the cyclic H_2 adducts, a slightly bonding a_1 mo arises from the interaction of the two electrons in the H_2 σ bonding orbital with the Gd^+ $5d_{z^2}$ orbital (Figures 6.4a and b). Various electronic states for the cyclic Gd^+-H_2 adducts are obtained from variations in the occupied mos of the two valence electrons of Gd^+ (i.e., $5d^16s^1$) as shown in Figures 6.4a and b. For example, these electrons can occupy a 6s/5d hybrid a_1 mo and a mo with mostly 5d character (of a_2, b_2, b_1, a_1, or a_1 symmetry), such that Gd^+ essentially retains the $5d^16s^1$ ground state configuration (Figure 6.4a), or both electrons can occupy two mos composed of predominantly 5d atomic orbitals, such that the 6s valence electron of Gd^+ has been promoted to a 5d orbital (Figure 6.4b). Alternatively, the 5d valence electron of Gd^+ can be promoted to a mo composed of mostly the 6s atomic orbital such that Gd^+ has a $6s^2$ configuration, yielding an adduct with an $^8A_2$ electronic state (Figure 6.4b). These different mos can lead to additional σ or π-type interactions (e.g., dπ (b_2) → H_2(σ*) donation) between Gd^+ and the H_2 adduct (Figures 6.4a and b). Because of the energy cost associated with promoting the 6s electron to a 5d orbital or the 5d electron to a 6s orbital, Gd^+-H_2 adducts with a $5d^2$ or $6s^2$ configuration are generally found to be higher in energy (Supporting Information, Section 6.7) than those for which Gd^+ retains its $5d^16s^1$ ground state configuration. Dectet states for these cyclic Gd^+-H_2 adducts result if unpaired electrons associated with the two valence electrons of Gd^+ are high spin-coupled with the 4f electrons, whereas octet states result if one of these electrons is low-spin coupled (Figures 6.4a and b). Generally, the calculations find that a lower energy octet state is obtained if the unpaired electrons in the 6s and 5d type mos are low and high-spin

coupled with the 4f electrons, respectively, rather than if the opposite spin-coupling is true (Figure 6.4a). For simplicity, only the former octet state is considered here as the two states should generally exhibit similar behavior.

The global minimum for GdH_2^+ is found to be an inserted H-Gd^+-H structure with a bond angle of 102°, Gd^+-H bond lengths of 1.903 Å, and an $^8A_2$ electronic state (Figure 6.4b). In this geometry, the two H(1s) orbitals can interact in-phase with the 6s orbital of Gd^+ to form a bonding a_1 mo. Furthermore, the bond angle in this structure allows for an additional bonding mo (b_2) to be formed from the out-of-phase combination of the two H(1s) orbitals with the Gd^+ $5d_{yz}$ orbital (Figure 6.4b). Inserted stable structures with $^{10}A_2$ and $^{10}B_2$ electronic states having bond angles of 94° and 157°, respectively, were also found. The $^{10}A_2$ state is obtained by moving the low-spin coupled electron from the a_1 orbital in the $^8A_2$ state (shown by the solid blue arrow in Figure 6.4b) into a new a_1 orbital in a high-spin configuration (shown by the dotted blue arrow). For the $^{10}B_2$ inserted structure, the mos are not shown but are similar in character to those of the corresponding Gd^+-H_2 adduct with a $5d^2$ electronic configuration, where the electrons occupy b_2 and a_2 mos (Figure 6.4b).

A search for stable linear Gd^+-H-H adducts yielded only structures with imaginary frequencies. This can be explained by the more favorable electrostatic and covalent interactions that can be achieved in cyclic (side-on) rather than linear M^+-H_2 adducts.[9] In contrast, several linear inserted H-Gd^+-H structures with multiplicities of 8 and 10 could be optimized to yield local minima. Representative mos for these structures are shown in Figure 6.4c. In all these linear inserted structures, a bonding σ mo results from an in-phase combination of the H(1s) orbitals with the Gd^+ $5d_{z^2}$ orbital (Figure 6.4c). A slightly

bonding σ mo also arises in some of the structures from an out-of-phase combination of the H(1s) orbitals with the Gd^+ $4f_z^3$ atomic orbital. However, this interaction is relatively weak such that, for the $^{10}\Pi$ state, the linear structure has an imaginary frequency and collapses to the stable inserted structure with a $^{10}B_2$ electronic state discussed above.

Most of the linear inserted H-Gd^+-H structures have electronic configurations that correlate with those of the adducts and are connected by the potential energy surfaces (PESs) shown in Figures 6.5a and b as a function of the H-Gd^+-H bond angle. In the experiments, reactive collisions between Gd^+ and H_2 have C_s rather than C_{2v} symmetry and thus the surfaces are separated into A′ (A_1, B_2) and A″ (A_2, B_1) surfaces (Figures 6.5a and b, respectively) to more clearly show the approximate avoided crossings. The minima of the PESs in Figures 6.5a and b correspond to the optimized GdH_2^+ structures already discussed. In total, 19 surfaces are shown. Ten surfaces (A_1, B_1, B_2, A_2, and A_2 with multiplicities of 8 and 10) evolve from the cyclic Gd^+-H_2 adducts in Figure 6.4a that retain of 8 and 10) arise from the adducts with a Gd^+ $5d^2$ electronic configuration. An $^8A_2$ surface that correlates with the $6s^2$ electronic configuration of Gd^+ is also shown as well as two other surfaces with A_2 symmetry (having multiplicities of 8 and 10) that have minima corresponding to the inserted cyclic H-Gd^+-H structures already discussed with bond angles of about 100°, where that along the octet surface corresponds to the global minimum. The results in Figure 6.5b indicate that the reaction cannot be initiated along the $^8A_2$ surface of the global GdH_2^+ ground state (located ~0.5 eV below the reactant asymptote), because this surface is very high in energy in the entrance channel, exceeding even the reaction endothermicity. However, the reaction can be initiated on $^{10}A_1$ and $^{10}B_2$ a Gd^+ $5d^16s^1$ electronic configuration. Six other surfaces (A_1, B_1, and B_2 with multiplicities

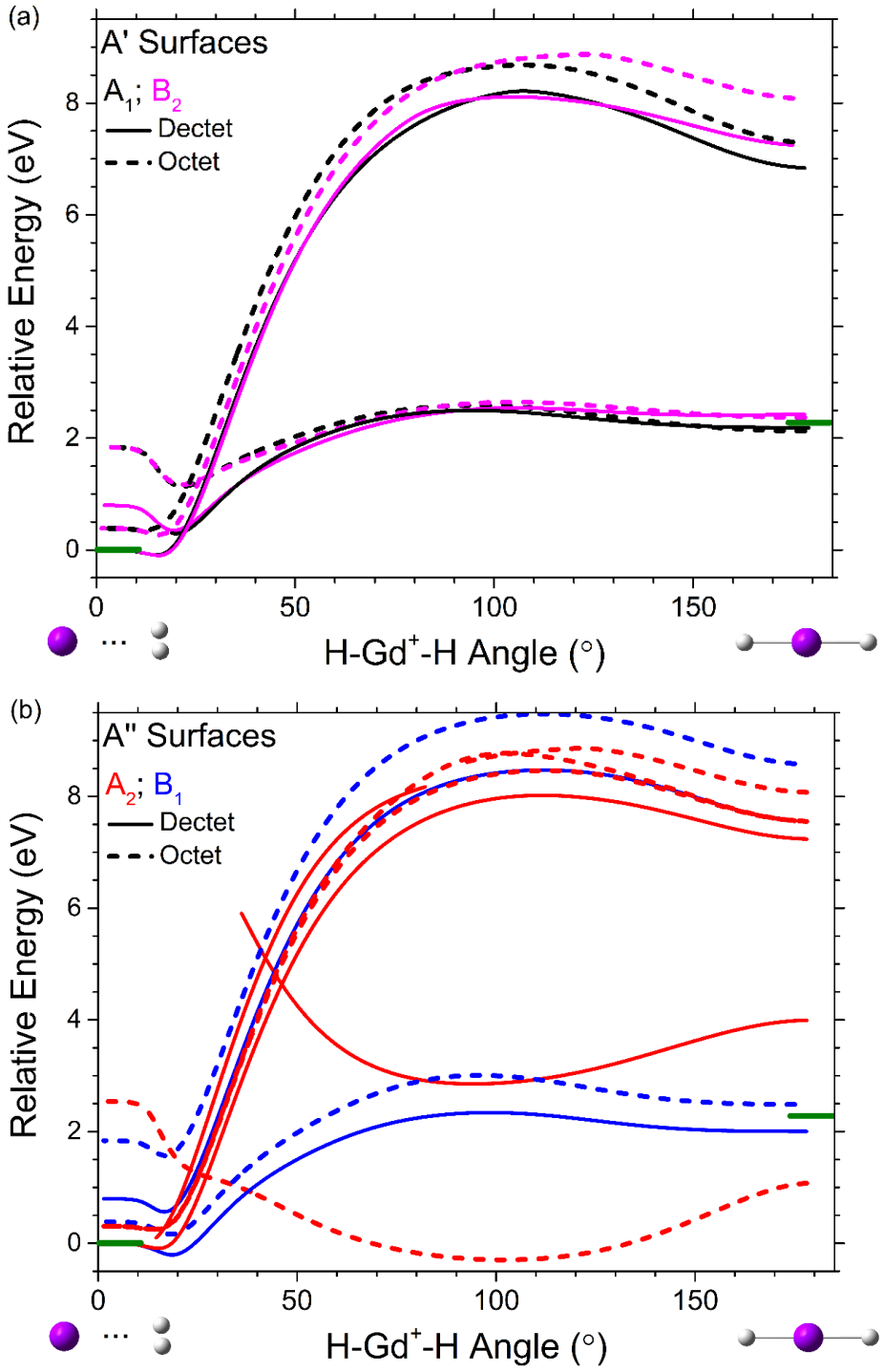

Figure 6.5. Relaxed potential energy surface scans, separated into (a) A′ and (b) A″ surfaces in C_s symmetry, as a function of H-Gd^+-H angle obtained at the BHLYP/ANO level of theory. Dectet and octet surfaces are given by solid and dashed lines, respectively, with A_1, A_2, B_1, and B_2 symmetries indicated by black, red, blue, and magenta, respectively. Green horizontal bars (at 0° and 180°) indicate the relative experimental energies of ground state reactants, Gd^+ (^{10}D) + H_2 ($^1\Sigma_g$), and products, GdH^+ ($^9\Sigma^-$) + H (^2S).

(A′), and $^{10}A_2$, $^{10}A_2$, and $^{10}B_1$ (A″) surfaces forming cyclic Gd^+-H_2 adducts (with $5d^16s^1$ configurations) that are below the reactant asymptote. The $^{10}A_1$, $^{10}B_2$, and the two $^{10}A_2$ surfaces have significant barriers (> 7 eV) for insertion of Gd^+ into H_2 (Figures 6.5a and b). However, for the A′ surfaces, the $^{10}A_1$ and $^{10}B_2$ surfaces can couple with $^{10}A_1$ and $^{10}B_2$ surfaces resulting from $5d^2$ Gd^+ configurations, which exhibit only small barriers above the reaction endothermicity (Figure 6.5a). These surfaces intersect at an approximate H-Gd^+-H angle of 20° and at energies well below the reaction endothermicity. Reactions along these surfaces could potentially contribute to the experimental results. For the A″ surfaces, the entire reaction could essentially proceed diabatically along the $^{10}B_1$ surface because the barrier along this surface does not exceed the reaction endothermicity (Figure 6.5b). Alternatively, the two $^{10}A_2$ surfaces and the $^{10}B_1$ surface could couple with the $^8A_2$ surface to yield ground state products via the inserted GdH_2^+ intermediate in adiabatic processes. These crossings occur at approximate H-Gd^+-H angles of 20, 25°, and 40°, respectively, at energies below the reaction endothermicity. Thus, the surfaces in Figure 6.5 demonstrate that reaction (6.1) can proceed via several pathways that do not exceed the reaction endothermicity. This is consistent with the measured thermochemistry from the experiments reflecting the true BDE of GdH^+ rather than a barrier along the reaction pathway.

6.5.6 Experimental reaction mechanism. The product ion branching ratio in the reaction with HD can provide information about the mechanism of reaction (6.1). From previous work on metal cation reactions with H_2,[23,25,26,35] three possible mechanisms have been established that result in different MH^+/MD^+ branching ratios in reactions with HD. The three types of mechanisms are (1) insertion, (2) direct, and (3) impulsive as

characterized by [$\sigma(MH^+)/\sigma_{total}$] ratios of ~0.5, ~0.7 – 0.80, and << 0.5, respectively. The type of mechanism involved generally depends on the electronic configuration of the metal cation and the "rules" described next are valid for reactions that occur along diabatic surfaces that maintain the metal cation electronic configuration. For example, an empty s or dσ orbital and filled dπ orbitals on the metal cation can lead to forming the bonding a_1 and b_2 mos (Figures 6.4a and b) from interaction with the occupied σ and empty σ* H_2 orbitals. Thus, metal cations with empty s and dσ orbitals, i.e., with d^n configurations where $n < 5$, are predicted to react efficiently via an insertion mechanism, which leads to a long-lived intermediate and produces a statistical distribution of MH^+ and MD^+ products, i.e., [$\sigma(MH^+)/\sigma_{total}$] = ~0.5. In contrast, if the s or dσ orbital on the metal cation is occupied, there is a repulsive interaction with H_2 leading to short-lived interactions and a direct reaction mechanism where MH^+ is favored over MD^+ by a factor of 2 to 4 resulting from angular momentum conservation, i.e., [$\sigma(MH^+)/\sigma_{total}$] = ~0.7 – 0.8. The latter ratio is exemplified by late transition metal cations,[26] which are taken as most characteristic of the direct process. An impulsive reaction mechanism is expected for high-spin metal cations with occupied s or dσ orbitals for which reactivity with H_2 is inefficient. The impulsive character shifts the thresholds up in energy compared with the thermodynamic thresholds in a mass dependent factor that leads to the MD^+ product being favored over MH^+ by a large factor such that the [$\sigma(MH^+)/\sigma_{total}$] ratio should be significantly smaller than 0.5.

In the reaction between Gd^+ and HD, the GdH^+ product is formed with a maximum cross section that is about a factor of two larger than that of GdD^+ (Figure 6.2) indicating a [$\sigma(GdH^+)/\sigma_{total}$] ratio of roughly 0.7. The energy dependence of the [$\sigma(GdH^+)/\sigma_{total}$] ratio is shown in Figure 6.6, where this ratio is ~0.7 at threshold and decreases slightly to 0.65 with

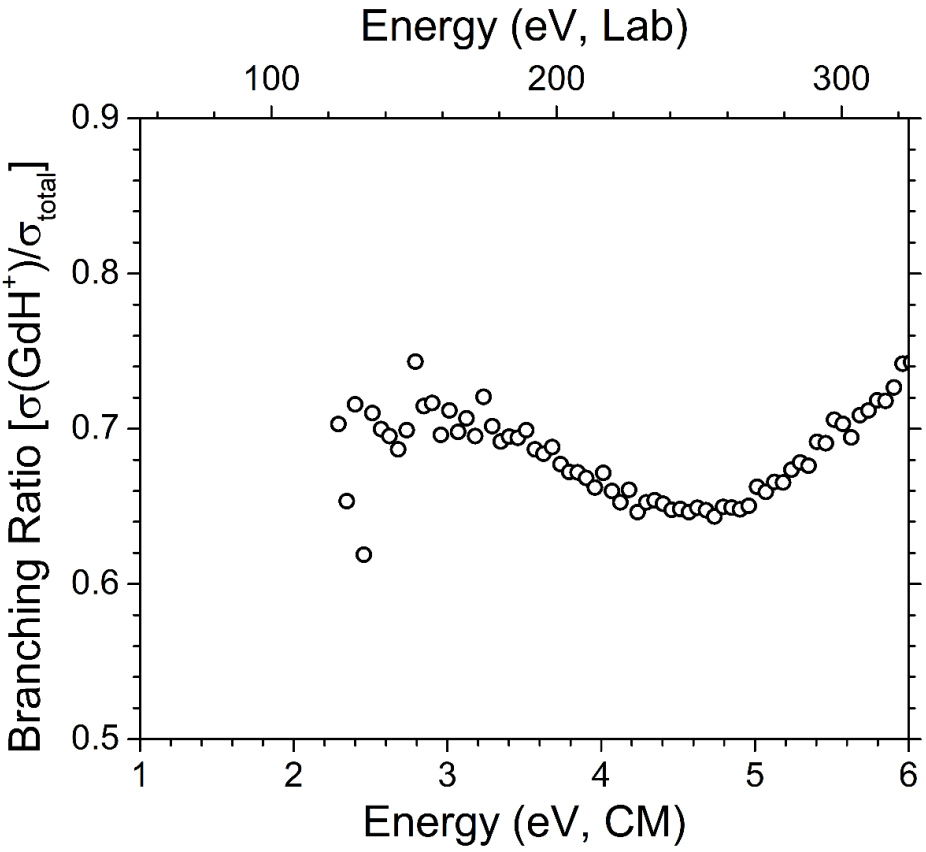

Figure 6.6. The product branching ratio plotted as $[\sigma(MH^+)/\sigma_{total}]$ for the Gd^+ reaction with HD as a function of kinetic energy in the center-of-mass (bottom x-axis) and lab (top x-axis) frames.

increasing energy, and then remains constant for CM energies between 4 and 5 eV. At energies larger than ~5 eV, the ratio increases, where this effect has been explained previously[17] and results from the fact that the heavier D atom can take away a larger amount of translational energy than the lighter H atom. The MD^+ product will therefore contain a larger amount of excess internal energy than MH^+ and will thus dissociate more readily at energies exceeding D_0(H-D) = 4.514 eV, leading to a steeper decline in the MD^+ cross section relative to that of MH^+ and a larger ratio.

On the basis of the reactivity rules outlined above, a ratio of ~0.7 suggests that Gd^+

reacts via a direct mechanism, which is consistent with the Gd^+ reaction proceeding diabatically along the $^{10}B_1$ PES (Figure 6.5b). Moreover, coupling between $^{10}A_1$ and $^{10}B_2$ surfaces in the entrance channel could also yield ground state products via direct mechanisms, albeit with slight barriers that exceed the reaction endothermicity (Figure 6.5b). Although the ratio of ~0.7 suggests a direct mechanism, the behavior and magnitude of the HD branching ratio for Gd^+ differs from that of the late transition metal ions,[26] which exhibited the clearest evidence of direct reaction behavior (with formation of the MH^+ product favored over the MD^+ product by factors closer to 4). Rather, Gd^+ behaves more similarly to Sc^+, Y^+,[23] Zr^+, Nb^+, and Mo^+,[25] attributed to exhibit predominantly statistical mechanisms, as explained by coupling between high-spin reactant surfaces with low-spin surfaces of the MH_2^+ intermediates to yield the $MH^+ + H$ products in adiabatic processes.[25] For these cations, the slightly favored production of MH^+ over MD^+ was attributed to constraints in the reactions arising from the coupling of the different surfaces and in some cases also contributions from a direct mechanism. The results in Figure 6.5 indicate that Gd^+ and H_2 can indeed react by coupling with the $^8A_2$ surface via the two $^{10}A_2$ surfaces and the $^{10}B_1$ surface in adiabatic processes that do not exceed the reaction endothermicity. Because the $^8A_2$ surface forms the GdH_2^+ inserted intermediate, this pathway should lead to statistical behavior. Thus, because there are both direct and statistical pathways that can lead to products from ground state reactants (without exceeding the reaction endothermicity), the reaction mechanism for Gd^+ is expected to be a mixture, consistent with the branching ratio in Figure 6.6 and its similar behavior to Sc^+, Y^+,[23] Zr^+, Nb^+, and Mo^+.[25]

6.5.7 Periodic trends in BDEs. In contrast to the $4f^n6s^1$ configurations (where n

indicates the remaining valence electrons) of most lanthanide cations, the ground state configuration of Gd^+ is unusual stemming from its half-filled 4f shell resulting in two valence electrons occupying non-4f orbitals, i.e., a 5d and 6s orbital. In this regard, Gd^+ resembles the group 3 metal cations Sc^+ ($3d^14s^1$) and Y^+ ($5s^2$ with the $4d^15s^1$ state only 0.15 eV higher in energy) rather than most lanthanide cations. Indeed, we have previously shown that Gd^+ has a similar oxide bond energy to Sc^+ and Y^+ and generally exhibits similar reactivity with O_2 and CO_2.[40,74,75] This can be attributed to the similar ground states, such that these metal cations require similar promotion energies of the two valence electrons to achieve the reactive d^2 configuration needed for effective binding with O.[40]

In the metal hydride cation bond, only one valence electron on the metal cation is needed in either a dσ or s orbital to achieve the reactive configuration. Which of the metal orbitals (s or d) interacts more favorably with H(1s) to form a σ bonding mo depends on several factors, including the relative energy and ordering of the s and d orbitals in the metal cation ground state configuration and the size of these atomic orbitals.[76] Additionally, extensive hybridization between s and d orbitals can occur that affects the BDE strength as the individual intrinsic interaction strengths of H(1s) with s and dσ orbitals are different.[76] Thus, it would be useful to investigate the periodic trends in the hydride BDEs for Gd^+, Sc^+, and Y^+, as well as for La^+ ($5d^2$) and Lu^+ ($4f^{14}6s^2$), which can also provide insight into the effects of systematically increasing the number of 4f electrons, from an empty (La^+) to half-filled (Gd^+) to completely filled (Lu^+) 4f shell. Figure 6.7 shows the GdH^+ BDE measured here with previous literature values of $D_0(M^+\text{-}H)$ for M = Sc^+, Y^+, La^+, and Lu^+.[23] The trend in hydride BDEs follows $D_0(Y^+\text{-}H) > D_0(Sc^+\text{-}H) \approx D_0(La^+\text{-}H) > D_0(Gd^+\text{-}H) \geq D_0(Lu^+\text{-}H)$, where the predicted ground states for these metal

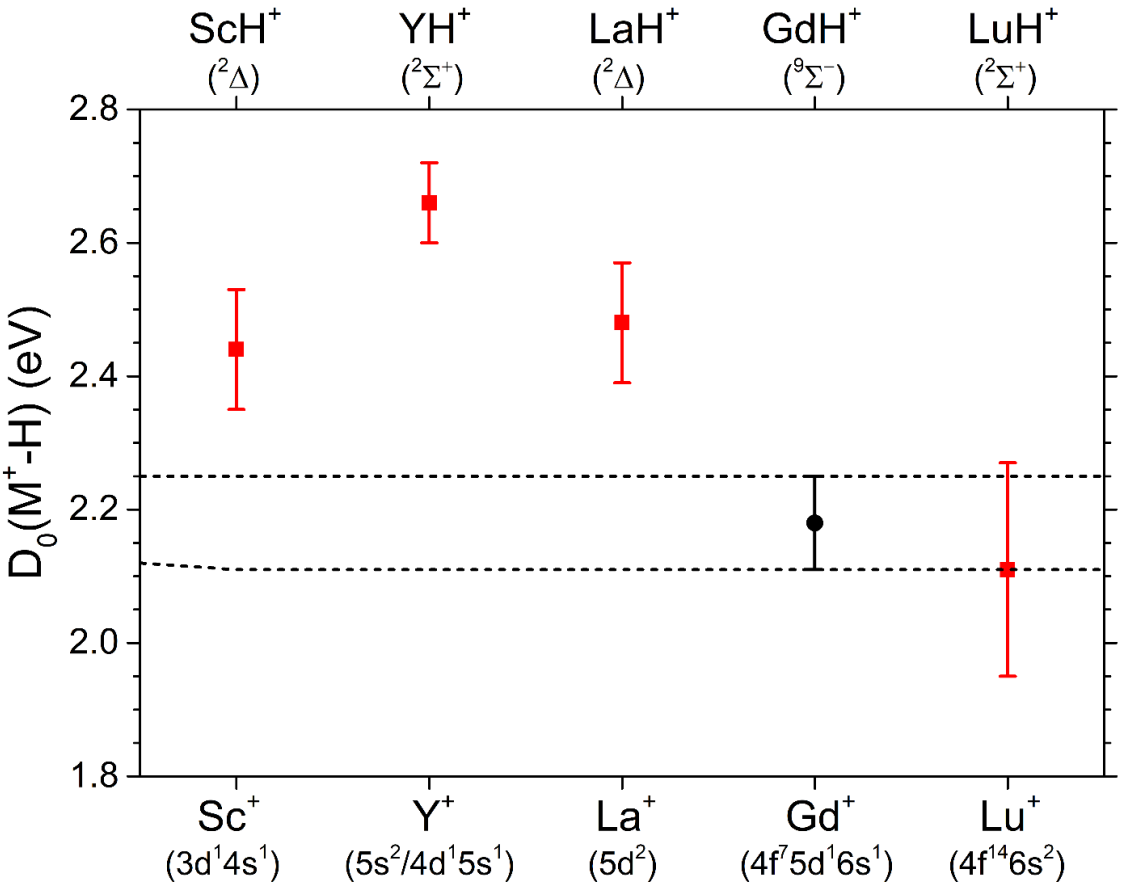

Figure 6.7. Comparison of experimental hydride bond dissociation energies for the group 3 metal cations Sc^+ and Y^+, and the lanthanides La^+ and Lu^+ (red squares)[23] with that measured here for Gd^+ (black circle). Dashed lines indicate the uncertainty in the measured $D_0(Gd^+\text{-}H)$ and are used as guides to the eye.

hydride cations are ScH^+ ($^2\Delta$, $\sigma^2\delta^1$),[77] YH^+ ($^2\Sigma^+$, $\sigma^2\sigma^1$),[78,79] LaH^+ ($^2\Delta$, $\sigma^2\delta^1$),[36] and GdH^+ ($^9\Sigma^-$, $\sigma^2\sigma^1$). Theoretical calculations have not been performed for LuH^+, but as discussed previously,[23] this species likely has a $^2\Sigma^+$ ($^2\Sigma^+$, $\sigma^2\sigma^1$) ground state as a result of the Lu^+ $6s^2$ ground state. The MH^+ ground states depend on both the metal cation ground state configuration and the type of metal cation orbital (s or d) that primarily interacts with H(1s). For Sc^+ ($3d^14s^1$) and Y^+ ($5s^2$), the σ bond in the hydrides arises predominantly from a 4s-H(1s) and 5s-H(1s) interaction, respectively, where the remaining valence electron of the metal cation occupies a largely nonbonding 3dδ and 4dσ mo to give the $^2\Delta$ and $^2\Sigma^+$ ground

states, respectively. For La^+ and Gd^+, the σ bond appears to arise primarily from a 5d-H(1s) interaction, and the unpaired electrons occupy mos such that the metal cations retain their ground state configurations, i.e., a 5dδ mo for La^+ ($5d^2$) and a 6sσ mo for Gd^+ ($4f^75d^16s^1$), giving $^2\Delta$ and $^9\Sigma^-$ ground states, respectively.

The large hydride BDE measured for Y^+ has been explained[25] as arising from this metal cation needing only a small promotion energy to achieve the reactive configuration for binding, such that the measured BDE of 2.65 ± 0.08 eV could nearly correspond to the intrinsic bond energy for a (5s)-H(1s) interaction.[25] Likewise, the measured hydride BDE for Sc^+ of 2.44 ± 0.09 eV might reflect the intrinsic bond energy for a predominantly (4s)-H(1s) interaction,[24] where the loss of exchange energy in Sc^+ upon spin-pairing with H potentially weakens this bond slightly. The BDE for LaH^+ (2.48 ± 0.09 eV) is comparable to that for ScH^+ but slightly lower than that for YH^+ and could potentially correspond to the intrinsic bond energy for a 5dσ-H(1s) interaction because there is no promotion energy cost to form LaH^+ ($^2\Delta$) (only a small loss in exchange energy). The intrinsic bond energy for a 4dσ-H(1s) interaction has been suggested as 2.11 ± 0.12 eV[24,26] (determined from measured hydride thermochemistry of late second-row transition metal cations). This 4dσ-H(1s) bond energy is smaller than that for LaH^+ (i.e., a 5dσ-H(1s) bond) consistent with the expected increase in the intrinsic d bond strength going down the periodic table.[76] The somewhat lower BDE for GdH^+ (2.18 ± 0.07 eV) compared to that of LaH^+ is likely a result of the unpaired electron in GdH^+ occupying a mo composed of mainly the 6s orbital, resulting in a slightly repulsive interaction with the 5dσ-H(1s) bonding mo. This interaction is not present for LaH^+ because the unpaired electron resides in a nonbonding 5dδ orbtial. The BDE for LuH^+ (2.11 ± 0.16 eV) is comparable to the GdH^+ BDE. On the basis of

promotion energy cost, the BDE for LuH^+ should be significantly smaller than that for GdH^+ because to achieve the reactive $5d^16s^1$ configuration from the $6s^2$ ground state in Lu^+ requires a promotion energy of about 1.6 eV. Some of this energy cost could be offset by the exchange energy, where no loss occurs in the formation of the hydride bond for Lu^+ unlike for Gd^+. Furthermore, the nature of the bond in LuH^+ might be different from that of GdH^+, with different extent of sd-hybridization such that the σ bonding orbital in LuH^+ contains significantly more 6s character.[76] This would be consistent with the effect of the lanthanide contraction and the relative ordering in energy of the 5d and 6s orbitals across the lanthanide series, where the stability of the 6s orbital increases with the increasing number of 4f electrons as evident from the ground state of Lu^+.

Because only one valence electron on the metal cation is required for hydride bonding, most lanthanide cations with $4f^n6s^1$ configurations will likely have BDEs in the vicinity of those for Gd^+ and Lu^+. These BDEs will depend on the extent of sd-hybridization involved in the bonding σ mo. Hydride BDEs arising from the interaction of predominantly the 6s orbital with H(1s) should be relatively large because no promotion energy cost is required, whereas those with primarily a 5d interaction will be weakened by the corresponding promotion energy needed to move a 4f or the 6s electron to a 5d orbital. Because the amount of 6s character in the interaction with H(1s) is expected to increase for the late lanthanide cations these should potentially exhibit stronger hydride bonds compared with their early counterparts.

6.5.8 Periodic trends in reactivity and mechanism. Previous guided ion beam results[23] have compared the reactivity of Sc^+, Y^+, La^+, and Lu^+ with HD and concluded that most of these cations, except Lu^+, react predominantly via an insertion (statistical)

mechanism. Here, the HD branching ratios ([$\sigma(MH^+)/\sigma_{total}$]) are ~0.67 for Sc^+, 0.58 for the ^3D excited state (~0.7 for the ^1S ground state[25]) of Y^+, and 0.55 for La^+. In contrast, Lu^+ reacts impulsively at threshold (MD^+ favored over MH^+ by a large factor) and via a direct mechanism at larger energies (as indicated by a branching ratio of ~0.85).[23] Thus, Gd^+ with a [$\sigma(GdH^+)/\sigma_{total}$] branching ratio of ~0.65 (Figure 6.6) exhibits behavior consistent with Sc^+, Y^+, and La^+, and as discussed above likely reacts with H_2 via a statistical mechanism with contributions from a direct mechanism. It should be noted that Sc^+, Y^+, and La^+ were formed using a hotter ionization source (i.e., via surface ionization[23]) than that used for Gd^+, such that electronically excited states contributed to the reactivity observed, where, for example, 80% of the Y^+ precursor ions were predicted to populate the ^3D ($4d^15s^1$) electronically excited state. Different states can exhibit different reactivity as demonstrated by previous results[25] for Y^+, where the ^1S ($5s^2$) ground and ^3D ($4d^15s^1$) electronically excited states yield different HD branching ratios with different energy behaviors. For Gd^+, the reactivity with H_2 should result from exclusively the Gd^+ ^{10}D ground state because only this state should be significantly populated at the estimated average electronic temperature of 700 ± 400 K for metal ions produced with the DC/FT ion source.[26,39,40] Nonetheless, the similarities in reactivity between Gd^+, Sc^+, Y^+, and La^+ can generally be attributed to the similar ground and low-energy states of these metal cations, giving rise to similar PESs as seen from comparison of previous theoretical calculations for ScH_2^+,[80] YH_2^+,[78] and LaH_2^+[36] with the calculated PESs for GdH_2^+ shown in Figure 6.5. The results generally indicate that many of the pathways for reaction require coupling from high-spin surfaces of reactants to the low-spin surfaces of the ground state MH_2^+ intermediate to yield ground state MH^+ + H products in adiabatic and statistical processes. The significantly different reactivity for

Lu^+ indicates different PESs in the entrance channel, consistent with Lu^+ having no low-lying electronically excited states, where the first (^3D, $5d^16s^1$) and second (^1D, $5d^16s^1$) excited states are 1.6 eV and 2.15 eV above the ^1S ($6s^2$) ground state. Thus, to form the inserted MH_2^+ intermediate requires a substantial promotion energy (i.e., to form the a_1 and b_2 bonding mos, Figure 6.4a). PESs arising from the Lu^+ ground state will lead to large barriers because of a repulsive interaction with the electrons of H_2. As discussed before,[23] this can explain the impulsive reactivity observed at threshold, while at higher energies coupling with surfaces originating from the excited states of Lu^+ can potentially occur to yield products according to a direct mechanism.

For the rest of the lanthanide cations with $4f^n6s^1$ configurations, promotion of valence electrons would also be necessary to form a stable inserted MH_2^+ intermediate. Because this promotion energy cost can be substantial for many of these lanthanide cations, such an intermediate would be unstable and thus the activation of H_2 for these cations will likely proceed via a direct (or impulsive) rather than statistical mechanism. The results and conclusions here are generally consistent with results from an early ion beam study on the activation of small alkanes and alkenes,[81] demonstrating that Gd^+ activates C-H and C-C bonds similarly to Sc^+, Y^+, and La^+, while differing from the lanthanide cations Pr^+ ($4f^36s^1$) and Eu^+ ($4f^76s^1$). These latter lanthanide cations exhibited for the most part unreactive behavior that was explained by the lack of an additional valence electron outside the 4f shell, necessary for forming two σ bonds in the activation process.[81]

6.6 Conclusions

The energy dependent Gd^+ reactions with H_2 and its isotopologues, HD and D_2, were studied with guided ion beam tandem mass spectrometry. All processes are endothermic and analysis of the corresponding product ion cross sections yields a value of 2.18 ± 0.07 eV for the hydride BDE of Gd^+. Theoretical calculations indicate that the ground state of GdH^+ is $^9\Sigma^-$, where the bond arises primarily from a 5dσ-H(1s) interaction. Generally, theory predicts larger BDEs compared with experiment, with calculations at the PBE0, BHLYP, and CCSD(T) levels providing reasonable agreement. The semiempirical SO correction applied to the theoretical values does improve the agreement with experiment.

The results indicate that the Gd^+ hydride BDE is similar to that for Lu^+, whereas the BDEs for Sc^+, Y^+, and La^+ are somewhat larger. These differences are attributed to differences in the type of orbital on the metal (s or d) favored to interact with the H(1s) orbital, the ground state electronic configuration of the metal, and differences in exchange energy loss upon forming the hydride bond. For the first- and second-row group 3 metal cations (Sc^+ and Y^+), previous results indicate that the s orbital primarily interacts with the H(1s) orbital, whereas for La^+, Gd^+, and Lu^+ the dσ orbital appears to be the favored bonding orbital (although the amount of s character possibly increases across the lanthanide series as the number of 4f electrons increases). A repulsive interaction arising from the unpaired 6s electron in GdH^+ likely leads to the weaker hydride bond compared with LaH^+. This interaction is not present for LaH^+ because the unpaired electron occupies a 5dδ mo as a result of the different ground states between La^+ ($5d^2$) and Gd^+ ($4f^75d^16s^1$).

The energy dependent product ion branching ratio in the Gd^+ reaction with HD is

generally similar to that observed for Sc^+, Y^+, and La^+, and indicates that Gd^+ reacts similarly to these ions, via a largely statistical insertion mechanism. There is some contribution of direct mechanisms, which can be explained by theoretical calculations of the PESs for GdH_2^+. The similar reaction mechanism for Sc^+, Y^+, La^+, and Gd^+ arises from the similar PESs for these ions, where ground state MH^+ + H products can generally be formed in adiabatic processes via coupling of reactant high-spin surfaces with the low-spin surface of the stable ground state MH_2^+ intermediate (for Gd^+, along A″ surfaces). A′ surfaces lead to reactivity that should be more direct. In contrast, Lu^+ has a closed-shell $6s^2$ ground state configuration with no low-lying excited states, such that a stable low-energy MH_2^+ intermediate cannot likely be formed. Thus, the reaction cannot proceed statistically via an insertion intermediate, and instead exhibits impulsive behavior at low energies and a direct mechanism at high energies. Because most lanthanide cations have $4f^n6s^1$ configurations, forming the MH_2^+ intermediate will require promotion of valence electrons and might thus also be energetically costly. Therefore, activation of H_2 by these cations will likely follow a direct and/or impulsive mechanism rather than an insertion mechanism via a MH_2^+ intermediate. The hydride BDEs of these lanthanide cations are expected to be comparable to those for Gd^+ and Lu^+, where effects of promotion energy could play some role depending on whether the bonding interaction arises primarily from the 6s or 5dσ orbital.

6.7 Supporting Information

6.7.1 Spin-orbit (SO) energy correction. Theoretical calculations were performed to determine the electronic ground states for GdH^+ and GdH_2^+ and for insight into the

reaction mechanism of Gd^+ inserting into H_2 to form GdH^+ and H. The energies, bond lengths, and vibrational frequencies for various electronic states of GdH^+ calculated at different levels of theory and basis sets are summarized in Table 6.2. The results of these calculations are discussed in detail above. The energy obtained from the calculations for a given GdH^+ electronic state corresponds to the average energy over all spin-orbit (SO) levels of that state. In contrast, the guided ion beam experiments typically measure the energy difference of the lowest SO energy level between reactants and products. Therefore, for a potentially more accurate comparison between theory and experiment, the calculated energies are corrected to reflect the lowest SO energy levels as previously[40,67-69] performed for other heavy metal cations (including Gd^+). When possible, this SO energy correction can be determined from a weighted (by the 2J + 1 degeneracy) average over the experimental SO energy levels. This is for example the case for Gd^+, where the ^{10}D electronic ground state is 0.123 eV higher in energy than the $^{10}D_{5/2}$ ground state SO level.[70] Thus, the theoretical energy for Gd^+ needs to be lowered by 0.123 eV to reflect the energy of the ground $^{10}D_{5/2}$ SO level. For GdH^+, the SO levels of different electronic states have not been determined experimentally. Therefore, a semiempirical SO energy (E^{SO}) correction is applied, with the first-order correction given by $E^{SO} = A\ \Lambda\ M_S$, where A corresponds to the SO splitting constant, Λ to the orbital angular momentum quantum number, and M_S to the spin quantum number for a specific SO level ($\Omega = \Lambda + M_S$). The first-order SO energy correction, E^{SO}, is thus zero for states with zero angular momentum ($\Lambda = 0$) and for singlet states with zero spin quantum number ($M_S = 0$). E^{SO} can also be determined by summing the individual SO energy contributions of each unpaired electron using the expression $E^{SO} = \Sigma\ a_i \bullet l_i \bullet s_i$, with a_i corresponding to the splitting constant, l_i to the

Table 6.2. Summary of bond lengths, energies, and vibrational frequencies (cm^{-1}) for different electronic states of GdH^+ calculated at various levels of theory and basis sets.

State	Config.[a]	Level	Basis Set	s(s+1)[b]	r(Gd^+-H), r(H-H) (Å)	Vibrational Frequency[c]	E (E_h)	E_{rel} (eV)
GdH^+								
$^9\Sigma^-$	$\sigma^2\,\sigma^1$	B3LYP	ANO	20.01	1.880	1685	-765.967701	0.00 (*0.00*)
			cc-pVTZ-DK3	20.01	1.892	1694	-11265.652406	0.00 (*0.00*)
			cc-pVQZ-DK3	20.01	1.892	1695	-11265.655728	0.00 (*0.00*)
		BHLYP	ANO	20.01	1.886	1693	-765.585020	0.00 (*0.00*)
			cc-pVTZ-DK3	20.01	1.897	1695	-11265.358643	0.00 (*0.00*)
			cc-pVQZ-DK3	20.01	1.896	1698	-11265.360215	0.00 (*0.00*)
		PBE0	ANO	20.01	1.875	1686	-765.835822	0.00 (*0.00*)
			cc-pVTZ-DK3	20.01	1.887	1698	-11265.158891	0.00 (*0.00*)
			cc-pVQZ-DK3	20.01	1.888	1695	-11265.161379	0.00 (*0.00*)
		CCSD(T)	ANO	20.03	1.882	1638	-765.347497	0.00 (*0.00*)
			cc-pVTZ-DK3	20.02	1.898	1616	-11261.985047	0.00 (*0.00*)

Table 6.2 continued

State	Config.[a]	Level	Basis Set	s(s+1)[b]	r(Gd^+-H), r(H-H) (Å)	Vibrational Frequency[c]	E (E_h)	E_{rel} (eV)
			cc-pVQZ-DK3	20.02	1.893	1625	-11262.032415	0.00 (*0.00*)
$^9\Delta$	$\sigma^2\,\delta^1$	B3LYP	ANO	20.01	1.929	1581	-765.951110	0.45 (*0.33*)
			cc-pVTZ-DK3	20.01	1.934	1583	-11265.640781	0.31 (*0.19*)
			cc-pVQZ-DK3	20.01	1.935	1585	-11265.643851	0.32 *(0.20*)
		BHLYP	ANO	20.01	1.933	1593	-765.575374	0.26 (*0.14*)
			cc-pVTZ-DK3	20.01	1.940	1596	-11265.351443	0.19 (*0.07*)
			cc-pVQZ-DK3	20.01	1.940	1595	-11265.352826	0.19 (*0.07*)
		PBE0	ANO	20.01	1.921	1604	-765.824213	0.31 (*0.19*)
			cc-pVTZ-DK3	20.01	1.928	1604	-11265.151354	0.20 (*0.08*)
			cc-pVQZ-DK3	20.01	1.928	1609	-11265.153579	0.21 (*0.09*)
		CCSD(T)	ANO	20.02	1.932	1554	-765.337701	0.26 (*0.14*)
			cc-pVTZ-DK3	20.02	1.946	1544	-11261.976091	0.24 (*0.12*)
			cc-pVQZ-DK3	20.02	1.940	1557	-11262.024792	0.20 (*0.08*)

Table 6.2 continued

State	Config.[a]	Level	Basis Set	s(s+1)[b]	r(Gd^+-H), r(H-H) (Å)	Vibrational Frequency[c]	E (E_h)	E_{rel} (eV)
$^9\Pi$	$\sigma^2\pi^1$	B3LYP	ANO	20.02	1.919	1563	-765.940837	0.72 (*0.66*)
			cc-pVTZ-DK3	20.01	1.923	1580	-11265.630301	0.59 (*0.53*)
			cc-pVQZ-DK3	20.01	1.923	1576	-11265.633373	0.60 (*0.54*)
		BHLYP	ANO	20.02	1.926	1568	-765.564246	0.56 (*0.50*)
			cc-pVTZ-DK3	20.02	1.932	1578	-11265.340126	0.50 (*0.44*)
			cc-pVQZ-DK3	20.02	1.931	1581	-11265.341500	0.50 (*0.44*)
		PBE0	ANO	20.02	1.909	1589	-765.815483	0.55 (*0.49*)
			cc-pVTZ-DK3	20.02	1.914	1604	-11265.142534	0.44 (*0.38*)
			cc-pVQZ-DK3	20.02	1.913	1607	-11265.144768	0.45 (*0.39*)
		CCSD(T)	ANO	20.03	1.921	1526	-765.328484	0.51 (*0.45*)
			cc-pVTZ-DK3	20.03	1.933	1518	-11261.966944	0.49 (*0.43*)
			cc-pVQZ-DK3	20.03	1.926	1532	-11262.015664	0.45 (*0.39*)
$^7\Sigma^-$	$\sigma^2\sigma^1$	B3LYP	ANO	12.83*	1.878	1638	-765.954853	0.35 (*0.35*)

Table 6.2 continued

State	Config.[a]	Level	Basis Set	s(s+1)[b]	r(Gd^+-H), r(H-H) (Å)	Vibrational Frequency[c]	E (E_h)	E_{rel} (eV)
			cc-pVTZ-DK3	12.77*	1.895	1631	-11265.641090	0.30 (*0.30*)
			cc-pVQZ-DK3	13.00*	1.892	1784	-11265.640821	0.41 (*0.41*)
		BHLYP	ANO	13.01*	1.875	1704	-765.569017	0.44 (*0.44*)
			cc-pVTZ-DK3	13.01*	1.886	1714	-11265.343681	0.41 (*0.41*)
			cc-pVQZ-DK3	13.01*	1.887	1713	-11265.345237	0.41 (*0.41*)
		PBE0	ANO	12.97*	1.862	1686	-765.819592	0.44 (*0.44*)
			cc-pVTZ-DK3	12.96*	1.874	1702	-11265.143029	0.43 (*0.43*)
			cc-pVQZ-DK3	12.96*	1.874	1705	-11265.145465	0.43 (*0.43*)
		CCSD(T)	ANO	13.02*	1.870	1658	-765.331574	0.43 (*0.43*)
			cc-pVTZ-DK3	13.02*	1.888	1633	-11261.970728	0.39 (*0.39*)
			cc-pVQZ-DK3	13.02*	1.882	1646	-11262.017997	0.39 (*0.39*)
$^7\Delta$	$\sigma^2\,\delta^1$	B3LYP	ANO	12.32*	1.989	1372	-765.936203	0.84 (*0.72*)
			cc-pVTZ-DK3	12.39*	1.987	1404	-11265.628800	0.62 (*0.50*)
			cc-pVQZ-DK3	12.38*	1.987	1404	-11265.632221	0.62 (*0.50*)

Table 6.2 continued

State	Config.[a]	Level	Basis Set	s(s+1)[b]	r(Gd^+-H), r(H-H) (Å)	Vibrational Frequency[c]	E (E_h)	E_{rel} (eV)
		BHLYP	ANO	13.00*	1.929	1608	-765.543685	1.12 (*1.00*)
			cc-pVTZ-DK3	13.01*	1.935	1610	-11265.322291	0.98 (*0.86*)
			cc-pVQZ-DK3	13.01*	1.936	1615	-11265.323735	0.99 (*0.87*)
		PBE0	ANO	12.49*	1.967	1410	-765.800248	0.95 (*0.83*)
			cc-pVTZ-DK3	12.57*	1.965	1456	-11265.129814	0.78 (*0.66*)
			cc-pVQZ-DK3	12.56*	1.965	1458	-11265.132227	078 (*0.66*)
		CCSD(T)	ANO	13.02*	1.928	1560	-765.305492	1.14 (*1.02*)
			cc-pVTZ-DK3	13.02*	1.943	1548	-11261.947826	1.01 (*0.89*)
			cc-pVQZ-DK3	13.02*	1.937	1565	-11261.996350	0.98 (*0.86*)
$^7\Pi$	$\sigma^2\pi^1$	B3LYP	ANO	12.31*	1.995	1360	-765.929294	1.02 (*0.96*)
			cc-pVTZ-DK3	12.37*	1.993	1388	-11265.621553	0.82 (*0.76*)
			cc-pVQZ-DK3	12.36*	1.994	1386	-11265.625148	0.81 (*0.75*)
		BHLYP	ANO	13.00*	1.921	1592	-765.532610	1.42 (*1.36*)

Table 6.2 continued

State	Config.[a]	Level	Basis Set	s(s+1)[b]	r(Gd^+-H), r(H-H) (Å)	Vibrational Frequency[c]	E (E_h)	E_{rel} (eV)
			cc-pVTZ-DK3	13.00*	1.929	1594	-11265.311258	1.28 (*1.22*)
			cc-pVQZ-DK3	13.00*	1.929	1600	-11265.312738	1.29 (*1.23*)
		PBE0	ANO	12.95*	1.897	1616	-765.784252	1.40 (*1.34*)
			cc-pVTZ-DK3	12.51*	1.974	1429	-11265.123050	0.96 (*0.90*)
			cc-pVQZ-DK3	12.50*	1.974	1426	-11265.125594	0.96 (*0.90*)
		CCSD(T)	ANO	13.02*	1.917	1550	-765.296339	1.39 (*1.33*)
			cc-pVTZ-DK3	13.02*	1.931	1536	-11261.938837	1.25 (*1.19*)
			cc-pVQZ-DK3	13.02*	1.924	1542	-11261.987433	1.22 (*1.16*)
$^7\Phi$	$[\varphi^3 \delta^2 \pi^2 \sigma^1] \sigma^2$	B3LYP	ANO	12.00	2.004	1365	-765.929871	1.01 (*0.69*)
			cc-pVTZ-DK3	12.01	2.009	1381	-11265.620669	0.84 (*0.52*)
			cc-pVQZ-DK3	12.01	2.007	1382	-11265.624602	0.83 (*0.51*)
		BHLYP	ANO	12.01	2.010	1412	-765.507451	2.09 (*1.77*)
			cc-pVTZ-DK3	12.01	2.013	1431	-11265.283230	2.04 (*1.72*)

Table 6.2 continued

State	Config.[a]	Level	Basis Set	s(s+1)[b]	r(Gd^+-H), r(H-H) (Å)	Vibrational Frequency[c]	E (E_h)	E_{rel} (eV)
			cc-pVQZ-DK3	12.01	2.013	1429	-11265.285312	2.02 (*1.70*)
		PBE0	ANO	12.01	1.995	1386	-765.793743	1.13 (*0.81*)
			cc-pVTZ-DK3	12.01	1.998	1403	-11265.120877	1.02 (0.*70*)
			cc-pVQZ-DK3	12.01	1.998	1405	-11265.123750	1.01 (*0.69*)
		CCSD(T)	ANO	12.02	2.004	1429	-765.264608	2.24 (*1.92*)
			cc-pVTZ-DK3	12.02	2.014	1436	-11261.904657	2.18 (*1.86*)
			cc-pVQZ-DK3	12.02	2.007	1447	-11261.958995	1.99 (*1.55*)

[a] Unless noted by square brackets, the 4f electrons are omitted and occupy $\varphi^2\ \delta^2\ \pi^2\ \sigma^1$ molecular orbitals yielding overall Σ^- symmetry.
[b] Spin-contaminated state is indicated by *.
[c] Vibrational frequencies are scaled by 0.989.

orbital angular momentum, and s_i to the spin of electron i. The atomic SO splitting constants for a 5d ($\zeta_{5d}(Gd^+)$) or 4f ($\zeta_{4f}(Gd^+)$) electron of Gd^+ are used to approximate a_i. $\zeta 5d(Gd^+)$ and $\zeta 4f(Gd^+)$ are estimated as 957.7 cm^{-1} and 1712.7 cm^{-1} as described previously,[40] The theoretical calculations predict that the electronic ground state of GdH^+ is $^9\Sigma^-$ and thus has no E^{SO} correction because $\Lambda = 0$. This is also the case for $^7\Sigma^-$. In contrast, the Π, Δ, and Φ GdH^+ electronic states found in the calculations require nonzero E^{SO} corrections. For Π electronic states where the unpaired electron occupies a π molecular orbital comprised of a 5d Gd^+ orbital, E^{SO} can be determined from $\Sigma\, a_i \bullet l_i \bullet s_i = 0.5\, \zeta_{5d}(Gd^+)$ = 478.4 cm^{-1} (0.059 eV). For Δ electronic states where the unpaired electron resides in a δ molecular orbital comprised of a 5d Gd^+ orbital, $E^{SO} = \zeta_{5d}(Gd^+)$ = 957.7 cm^{-1} (0.118 eV). A $^7\Phi$ electronic state was also found where the unpaired valence electron occupies a φ molecular orbital comprised of a 4f Gd^+ atomic orbital such that the configuration of Gd^+ is $4f^8$. To obtain the energy for the lowest SO level of this electronic state, the calculated energy needs to be lowered by $E^{SO} = \Sigma\, a_i \bullet l_i \bullet s_i = 1.5\, \zeta_{4f}(Gd^+)$ = 2569.1 cm^{-1} (0.319 eV). The SO corrected and uncorrected energies for the various GdH^+ electronic states relative to the $^9\Sigma^-$ground state are listed in Table 6.2. Theoretical BDEs for GdH^+ are obtained from the difference in calculated energies between ground state GdH^+ and Gd^+ + H. Only Gd^+ with its ^{10}D electronic ground state needs to be SO corrected because GdH^+ ($^9\Sigma^-$) and H (^2S) have zero angular momentum and therefore have no first-order SO splittings as discussed above. Therefore, the theoretical Gd^+-H BDEs need to be lowered by 0.123 eV, i.e., the SO correction for Gd^+. SO corrected and uncorrected theoretical BDEs calculated using various basis sets and levels of theory are listed in Table 6.3. Generally, the theoretical results appear to overestimate the Gd^+-H BDE such that the small SO correction

Table 6.3. Comparison between the measured Gd^+-H BDE and values calculated at different basis sets and levels of theory.

Level	Basis Set	$D_0(Gd^+-H)$ (eV)[a]
Experiment		2.18 ± 0.07
B3LYP	ANO	2.63 (*2.51*)
	cc-pVTZ-DK3	2.69 (*2.57*)
	cc-pVQZ-DK3	2.69 (*2.57*)
BHLYP	ANO	2.43 (*2.31*)
	cc-pVTZ-DK3	2.51 (*2.39*)
	cc-pVQZ-DK3	2.51 (*2.39*)
PBE0	ANO	2.41 (*2.29*)
	cc-pVTZ-DK3	2.47 (*2.35*)
	cc-pVQZ-DK3	2.48 (*2.36*)
CCSD(T)	ANO	2.42 (*2.30*)
	cc-pVTZ-DK3	2.52 (*2.40*)
	cc-pVQZ-DK3	2.54 (*2.42*)
	CBS	2.55 (*2.43*)

[a] Values in parentheses include a spin-orbit correction for Gd^+ such that D_0 values are calculated relative to the lowest spin-orbit energy level of Gd^+.

helps to improve the agreement between experiment and theory slightly. Table 6.4 summarizes the results from the theoretical calculations for different structures and electronic states of GdH_2^+ performed at the BHLYP/ANO level.

6.8 Acknowledgements

This work is supported by the U.S. Air Force Office of Scientific Research (FA9550-16-1-0095). The authors thank Professor Kirk A. Peterson for providing the all-electron basis sets for Gd and the Center for High Performance Computing at the University of Utah and the Pittsburgh Supercomputing Center at Carnegie Mellon University via the Extreme Science and Engineering Discovery Environment (XSEDE) under grant TG-CHE170012 for generous allocations of computer time.

Table 6.4. Summary of bond angles, bond lengths, energies, and vibrational frequencies (cm^{-1}) for optimized structures of GdH_2^+ calculated at the BHLYP level of theory with the ANO basis set and SDD ECP for Gd and the 6-311++G(3df,3p) basis set for H.

State	Configuration [a]	s(s+1)[b]	∠H-Gd^+-H (°)	r(Gd^+-H), r(H-H) (Å)	Vibrational Frequencies[c]	E (E_h)	E_{rel} (eV)
Gd^+-H_2							
$^{10}A_1$	$a_1^2\ a_1^1\ a_2^1$	24.76	15.27	2.801, 0.744	222, 333, 4356	-766.166726	0.27
$^{8}A_1$	$a_1^2\ a_1^1\ a_2^1$	16.76*	11.97	3.547, 0.740	107, 266, 4421	-766.150404	0.71
$^{10}A_1$	$a_1^2\ b_2^1\ b_1^1$	24.76	19.98	2.229,0.773	652, 1032, 3789	-766.152736	0.69
$^{8}A_1$	$a_1^2\ b_2^1\ b_1^1$	16.75*	21.65	2.148, 0.807	824, 1241, 3199	-766.121629	1.52
$^{10}B_1$	$a_1^2\ a_1^1\ b_2^1$	24.76	18.55	2.359, 0.761	486, 897, 4031	-766.171096	0.19
$^{8}B_1$	$a_1^2\ a_1^1\ b_2^1$	16.76*	18.46	2.371, 0.761	488, 894, 4035	-766.157543	0.56
$^{10}B_1$	$a_1^2\ b_1^1\ a_2^1$	24.76	16.59	2.577, 0.744	430, 618, 4369	-766.142728	0.96
$^{8}B_1$	$a_1^2\ b_1^1\ a_2^1$	16.76*	16.89	2.534, 0.744	451, 639, 4362	-766.105843	1.96
$^{10}B_2$	$a_1^2\ a_1^1\ b_1^1$	24.75	15.72	2.718, 0.743	263, 458, 4375	-766.167058	0.28
$^{8}B_2$	$a_1^2\ a_1^1\ b_1^1$	16.76*	15.85	2.696, 0.743	304, 489, 4373	-766.153510	0.65
$^{10}B_2$	$a_1^2\ b_2^1\ a_2^1$	24.76	19.45	2.290, 0.774	613, 1023, 3778	-766.150557	0.74
$^{8}B_2$	$a_1^2\ b_2^1\ a_2^1$	16.75*	21.62	2.177, 0.816	772, 1232, 3057	-766.120493	1.54

Table 6.4 continued

State	Configuration [a]	s(s+1)[b]	∠H-Gd^+-H (°)	r(Gd^+-H), r(H-H) (Å)	Vibrational Frequencies[c]	E (E_h)	E_{rel} (eV)
$^8A_2$	$a_1^2\ a_1^2$	16.26*	12.42	3.421, 0.740	108, 309, 4408	-766.152245	0.66
$^{10}A_2$	$a_1^2\ a_1^1\ a_1^1$	24.76	15.28	2.798, 0.744	225, 504, 4360	-766.166734	0.28
$^8A_2$	$a_1^2\ a_1^1\ a_1^1$	16.76*	12.06	3.520, 0740	116, 252, 4417	-766.150353	0.71
$^{10}A_2$	$a_1^2\ a_1^1\ a_1^1$	24.75	10.72	3.953, 0.738	97, 108, 4442	-766.163879	0.33
$^8A_2$	$a_1^2\ a_1^1\ a_1^1$	16.75*	11.26	3.766, 0.739	116, 201, 4436	-766.150228	0.71
H-Gd^+-H							
$^8A_2$	$a_1^2\ b_2^2$	15.77	101.91	1.903, 2.956	494, 1642, 1695	-766.174329	0.00
$^{10}A_2$	$a_1^2\ b_2^1\ a_1^1$	24.77	94.29	2.067, 3.030	535, 1217, 2638	-766.058602	3.18
$^{10}B_2$	$a_1^2\ b_2^1\ a_2^1$	24.80	156.67	2.057, 4.029	219, 716, 1169	-766.074772	2.60
TS $^{10}A_1$	$a_1^2\ a_1^1\ a_2^1$	24.76	107.40	2.362, 3.807	835i, 679, 695	-765.861586	8.36
$^8A_1$[d]	$a_1^2\ a_1^1\ a_2^1$	16.76*	107.50	2.781, 4.486	415i, 404i, 347	-765.844381	8.76
TS $^{10}A_1$	$a_1^2\ b_2^1\ b_1^1$	24.80	94.33	2.121, 3.110	428i, 1071, 1189	-766.071730	2.69
TS $^8A_1$	$a_1^2\ b_2^1\ b_1^1$	16.83*	94.84	2.162, 3.184	425i, 1107, 1334	-766.068389	2.80

Table 6.4 continued

State	Configuration [a]	s(s+1)[b]	∠H-Gd^+-H (°)	r(Gd^+-H), r(H-H) (Å)	Vibrational Frequencies[c]	E (E_h)	E_{rel} (eV)
TS $^{10}B_1$	$a_1^2\ b_1^1\ a_2^1$	24.76	111.78	2.409, 3.988	448i, 639, 675	-765.852102	8.61
TS $^{8}B_1$	$a_1^2\ b_1^1\ a_2^1$	16.76*	111.98	2.405, 3.987	451i, 641, 687	-765.815210	9.62
TS $^{10}B_2$	$a_1^2\ a_1^1\ b_1^1$	24.76	104.71	2.451, 3.882	452i, 505, 567	-765.865374	8.24
$^{8}B_2$[d]	$a_1^2\ a_1^1\ b_1^1$	16.76*	123.72	2.913, 5.138	426i, 307i, 254	-765.837403	8.95
TS $^{10}B_2$	$a_1^2\ b_2^1\ a_2^1$	24.80	105.92	2.108, 3.365	384i, 745, 1177	-766.070104	2.72
TS $^{8}B_2$	$a_1^2\ b_2^1\ a_2^1$	16.85*	104.96	2.157, 3.422	390i, 531, 1115	-766.066183	2.81
TS $^{8}A_2$	$a_1^2\ a_1^2$	16.69*	102.51	2.456, 3.831	664i, 427, 547	-765.841143	8.89
TS $^{10}A_2$	$a_1^2\ a_1^1\ a_1^1$	24.76	111.60	2.415, 3.996	467i, 561, 632	-765.868786	8.15
TS $^{8}A_2$	$a_1^2\ a_1^1\ a_1^1$	16.70*	112.23	2.493, 4.140	462i, 289, 473	-765.852365	8.57
$^{8}\Sigma^-$	$\sigma^2\ \sigma^2$	15.76	180.00	1.863, 3.725	788, 788, 978, 1482	-765.883507	7.93
$^{10}\Sigma^-$	$\sigma^2\ \sigma^1\ \sigma^1$	24.77	180.00	2.067, 4.134	90, 90, 542, 1241	-766.089802	2.18
$^{8}\Sigma^-$	$\sigma^2\ \sigma^1\ \sigma^1$	16.78*	180.00	2.056, 4.111	164, 164, 705, 1261	-766.072134	2.69
$^{10}\Pi$	$\sigma^2\ \sigma^1\ \pi^1$	24.76	180.00	1.792, 3.584	887, 1064, 1304, 1610	-765.912210	7.20

Table 6.4 continued

State	Configuration [a]	s(s+1)[b]	∠H-Gd^+-H (°)	r(Gd^+-H), r(H-H) (Å)	Vibrational Frequencies[c]	E (E_h)	E_{rel} (eV)
$^8\Pi$	$\sigma^2\ \sigma^1\ \pi^1$	16.76*	180.00	1.789, 3.578	907, 1063, 1323, 1605	-765.895732	7.65
$^{10}\Delta$	$\sigma^2\ \sigma^1\ \delta^1$	24.76	180.00	1.898, 3.796	694, 694, 938, 1456	-765.897535	7.53
$^8\Delta$	$\sigma^2\ \sigma^1\ \delta^1$	16.76*	180.00	1.883, 3.777	731, 731, 926, 1448	-765.866766	8.37
$^{10}\Pi$[e]	$\sigma^2\ \sigma^1\ \pi^1$	24.78	180.00	2.069, 4.137	168i, 593, 744, 1211	-766.074419	2.64
$^8\Pi$	$\sigma^2\ \sigma^1\ \pi^1$	16.80*	180.00	2.087, 4.173	244, 760, 949, 1155	-766.076272	2.62
$^{10}\Delta$	$\sigma^2\ \sigma^1\ \delta^1$	24.79	180.00	2.104, 4.208	119, 119, 666, 1211	-766.083067	2.38
$^8\Delta$	$\sigma^2\ \sigma^1\ \delta^1$	16.79*	180.00	2.108, 4.127	290. 290, 714, 1175	-766.085187	2.34
$^{10}\Pi/^{10}\Phi$	$\sigma^2\ \pi^1\ \delta^1$	24.76	180.00	1.825, 3.651	809, 980, 1141, 1551	-765.883988	7.94
$^8\Pi/^8\Phi$	$\sigma^2\ \pi^1\ \delta^1$	16.76*	180.00	1.847, 3.694	791, 991, 1025, 1533	-765.850552	8.84

[a] The 4f electrons are omitted and occupy $a_1^1\ b_1^1\ b_2^1\ b_1^1\ b_2^1\ a_1^1\ a_2^1$ molecular orbitals in C_{2v} symmetry with overall A_2 symmetry or $\varphi^2\ \delta^2\ \pi^2\ \sigma^1$ molecular orbitals in $D_{\infty h}$ symmetry yielding overall Σ^- symmetry.
[b] Spin-contaminated state is indicated by *.
[c] Vibrational frequencies are scaled by 0.989. For transition states (TS), the imaginary frequency is indicated by i.
[d] Second-order saddle point.
[e] Has one imaginary frequency and by following this reaction coordinate yields the stable inserted $^{10}B_2$ structure.

6.9 References

(1) Kubas, G. J.; Ryan, R. R.; Swanson, B. I.; Vergamini, P. J.; Wasserman, H. J. Characterization of the First Examples of Isolable Molecular Hydrogen Complexes, $M(CO)_3(PR_3)_2(H_2)$ (M = Mo, W; R = Cy, *i*-Pr). Evidence for a Side-On Bonded Dihydrogen Ligand. *J. Am. Chem. Soc.* **1984,** *106*, 451-452.

(2) Kubas, G. J. Fundamentals of H_2 Binding and Reactivity on Transition Metals Underlying Hydrogenase Function and H_2 Production and Storage. *Chem. Rev.* **2007,** *107*, 4152-4205.

(3) Kubas, G. J. Activation of Dihydrogen and Coordination of Molecular H_2 on Transition Metals. *J. Organomet. Chem.* **2014,** *751*, 33-49.

(4) Bushnell, J. E.; Kemper, P. R.; Maitre, P.; Bowers, M. T. Insertion of Sc^+ into H_2: The First Example of Cluster-Mediated σ-Bond Activation by a Transition Metal Center. *J. Am. Chem. Soc.* **1994,** *116*, 9710-9718.

(5) Bushnell, J. E.; Kemper, P. R.; van Koppen, P.; Bowers, M. T. Mechanistic and Energetic Details of Adduct Formation and σ-Bond Activation in $Zr^+(H_2)_n$ Clusters. *J. Phys. Chem. A* **2001,** *105*, 2216-2224.

(6) Weis, P.; Kemper, P. R.; Bowers, M. T. $Mn^+(H_2)_n$ and $Zn^+(H_2)_n$ Clusters: Influence of 3d and 4s Orbitals on Metal−Ligand Bonding. *J. Phys. Chem. A* **1997,** *101*, 2809-2816.

(7) Kemper, P. R.; Bushnell, J.; Von Helden, G.; Bowers, M. T. $Co^+(H_2)_n$ Clusters: Binding Energies and Molecular Parameters. *J. Phys. Chem.* **1993,** *97*, 52-58.

(8) Kemper, P. R.; Weis, P.; Bowers, M. T.; Maître, P. Origin of Bonding Interactions in $Cu^+(H_2)_n$ Clusters: An Experimental and Theoretical Investigation. *J. Am. Chem. Soc.* **1998,** *120*, 13494-13502.

(9) Dryza, V.; Poad, B. L. J.; Bieske, E. J. Attaching Molecular Hydrogen to Metal Cations: Perspectives from Gas-Phase Infrared Spectroscopy. *Phys. Chem. Chem. Phys.* **2012,** *14*, 14954-14965.

(10) Dryza, V.; Poad, B. L. J.; Bieske, E. J. Spectroscopic Study of the Benchmark Mn^+−H_2 Complex. *J. Phys. Chem. A* **2009,** *113*, 6044-6048.

(11) Dryza, V.; Bieske, E. J. Structure and Properties of the Zn^+–D_2 Complex. *J. Chem. Phys.* **2009,** *131*, 224304.

(12) Dryza, V.; Bieske, E. J. Non-Covalent Interactions Between Metal Cations and Molecular Hydrogen: Spectroscopic Studies of M^+–H_2 Complexes. *Int. Rev. Phys. Chem.* **2013,** *32*, 559-587.

(13) Dryza, V.; Bieske, E. J. Infrared Spectroscopy of the Ag^+-H_2 Complex: Exploring the Connection Between Vibrational Band-Shifts and Binding Energies. *J. Phys. Chem. Lett.* **2011,** *2*, 719-724.

(14) Dryza, V.; Bieske, E. J. The $Cr^+–D_2$ Cation Complex: Accurate Experimental Dissociation Energy, Intermolecular Bond Length, and Vibrational Parameters. *J. Chem. Phys.* **2009,** *131*, 164303.

(15) Armentrout, P. B. Mass Spectrometry—Not Just a Structural Tool: The Use of Guided Ion Beam Tandem Mass Spectrometry to Determine Thermochemistry. *J. Am. Soc. Mass. Spectrom.* **2002,** *13*, 419-434.

(16) Armentrout, P. B. Kinetic Energy Dependence of Ion–Molecule Reactions: Guided Ion Beams and Threshold Measurements. *Int. J. Mass Spectrom.* **2000,** *200*, 219-241.

(17) Elkind, J. L.; Armentrout, P. B. Effect of Kinetic and Electronic Energy on the Reaction of V^+ with H_2, HD, and D_2. *J. Phys. Chem.* **1985,** *89*, 5626-5636.

(18) Elkind, J. L.; Armentrout, P. B. Effect of Kinetic and Electronic Energy on the Reactions of Ti^+ with H_2, HD, and D_2. *Int. J. Mass Spectrom. Ion Processes* **1988,** *83*, 259-284.

(19) Elkind, J. L.; Armentrout, P. B. Effect of Kinetic and Electronic Energy on the Reactions of Cr^+ with H_2, HD, and D_2. *J. Chem. Phys.* **1987,** *86*, 1868-1877.

(20) Elkind, J. L.; Armentrout, P. B. Effect of Kinetic and Electronic Energy on the Reactions of Mn^+ with H_2, HD, and D_2. *J. Chem. Phys.* **1986,** *84*, 4862-4871.

(21) Elkind, J. L.; Armentrout, P. B. Effect of Kinetic and Electronic Energy on the Reactions of Fe^+ with H_2, HD, and D_2: State-Specific Cross Sections for Fe^+ (^{6}D) and Fe^+ (^{4}F). *J. Phys. Chem.* **1986,** *90*, 5736-5745.

(22) Elkind, J. L.; Armentrout, P. B. Effect of Kinetic and Electronic Energy on the Reactions of Co^+, Ni^+, and Cu^+ with H_2, HD, and D_2. *J. Phys. Chem.* **1986,** *90*, 6576-6586.

(23) Elkind, J. L.; Sunderlin, L. S.; Armentrout, P. B. Periodic Trends in Chemical Reactivity: Reactions of Sc^+, Y^+, La^+, and Lu^+ with H_2, D_2 and HD. *J. Phys. Chem.* **1989,** *93*, 3151-3158.

(24) Elkind, J. L.; Armentrout, P. B. Transition-Metal Hydride Bond Energies: First and Second Row. *Inorg. Chem.* **1986,** *25*, 1078-1080.

(25) Sievers, M. R.; Chen, Y.-M.; Elkind, J. L.; Armentrout, P. B. Reactions of Y^+, Zr^+, Nb^+, and Mo^+ with H_2, HD, and D_2. *J. Phys. Chem.* **1996,** *100*, 54-62.

(26) Chen, Y.-M.; Elkind, J. L.; Armentrout, P. B. Reactions of Ru^+, Rh^+, Pd^+, and Ag^+ with H_2, HD, and D_2. *J. Phys. Chem.* **1995,** *99*, 10438-10445.

(27) Hinton, C. S.; Armentrout, P. B. Guided Ion Beam and Theoretical Study of the Reactions of Hf^+ with H_2, D_2, and HD. *J. Chem. Phys.* **2010,** *133*, 124307.

(28) Zhang, X.-G.; Rue, C.; Shin, S.-Y.; Armentrout, P. B. Reactions of Ta^+ and W^+ with H_2, D_2, and HD: Effect of Lanthanide Contraction and Spin–Orbit Interactions on Reactivity and Thermochemistry. *J. Chem. Phys.* **2002,** *116*, 5574-5583.

(29) Hinton, C. S.; Citir, M.; Armentrout, P. B. Guided Ion Beam and Theoretical Study of the Reactions of Os^+ with H_2, D_2, and HD. *J. Chem. Phys.* **2011,** *135*, 234302.

(30) Li, F.-X.; Zhang, X.-G.; Armentrout, P. B. Guided Ion Beam and Theoretical Study of the Reactions of Ir^+ with H_2, D_2, and HD. *J. Phys. Chem. B* **2005,** *109*, 8350-8357.

(31) Zhang, X.-G.; Armentrout, P. B. Reactions of Pt^+ with H_2, D_2, and HD: Effect of Lanthanide Contraction on Reactivity and Thermochemistry. *J. Chem. Phys.* **2002,** *116*, 5565-5573.

(32) Li, F.; Hinton, C. S.; Citir, M.; Liu, F.; Armentrout, P. B. Guided Ion Beam and Theoretical Study of the Reactions of Au^+ with H_2, D_2, and HD. *J. Chem. Phys.* **2011,** *134*, 024310.

(33) Armentrout, P. B.; Li, F.-X. Probes of Spin Conservation in Heavy Metal Reactions: Experimental and Theoretical Studies of the Reactions of Re^+ with H_2, D_2, and HD. *J. Chem. Phys.* **2004,** *121*, 248-256.

(34) Cox, R. M.; Armentrout, P. B.; de Jong, W. A. Reactions of $Th^+ + H_2$, D_2, and HD Studied by Guided Ion Beam Tandem Mass Spectrometry and Quantum Chemical Calculations. *J. Phys. Chem. B* **2016,** *120*, 1601-1614.

(35) Elkind, J. L.; Armentrout, P. B. State-Specific Reactions of Atomic Transition-Metal Ions with Molecular Hydrogen, Hydrogen Deuteride, and Molecular Deuterium: Effects of d Orbitals on Chemistry. *J. Phys. Chem.* **1987,** *91*, 2037-2045.

(36) Das, K. K.; Balasubramanian, K. Potential Energy Surfaces of LaH^+ and LaH_2^+. *J. Chem. Phys.* **1991,** *94*, 3722-3729.

(37) Loh, S. K.; Hales, D. A.; Lian, L.; Armentrout, P. B. Collision-Induced Dissociation of Fe_n^+ (n=2–10) with Xe: Ionic and Neutral Iron Binding Energies. *J. Chem. Phys.* **1989,** *90*, 5466-5485.

(38) Ervin, K. M.; Armentrout, P. B. Translational Energy Dependence of

$Ar^+ + XY \rightarrow ArX^+ + Y$ (XY=H_2,D_2,HD) from Thermal to 30 eV C.M. *J. Chem. Phys.* **1985,** *83*, 166-189.

(39) Kickel, B. L.; Armentrout, P. B. Guided Ion Beam Studies of the Reactions of Group 3 Metal Ions (Sc^+, Y^+, La^+, and Lu^+) with Silane. Electronic State Effects, Comparison to Reactions with Methane, and M^+-SiH_x (x = 0-3) Bond Energies. *J. Am. Chem. Soc.* **1995,** *117*, 4057-4070.

(40) Demireva, M.; Kim, J.; Armentrout, P. B. Gadolinium (Gd) Oxide, Carbide, and Carbonyl Cation Bond Energies and Evaluation of the $Gd + O \rightarrow GdO^+ + e^-$ Chemi-Ionization Reaction Enthalpy. *J. Phys. Chem. A* **2016,** *120*, 8550-8563.

(41) Gerlich, D. Inhomogeneous RF Fields: A Versatile Tool for the Study of Processes with Slow Ions. *Adv. Chem. Phys.* **1992,** *82*, 1-176.

(42) Daly, N. R. Scintillation Type Mass Spectrometer Ion Detector. *Rev. Sci. Instrum.* **1960,** *31*, 264-267.

(43) Muntean, F.; Armentrout, P. B. Guided Ion Beam Study of Collision-Induced Dissociation Dynamics: Integral and Differential Cross Sections. *J. Chem. Phys.* **2001,** *115*, 1213-1228.

(44) Johnson III, R. D. NIST Computational Chemistry Comparison and Benchmark Database, NIST Standard Reference Database Number 101 Release 18, NIST, 2016, available online: http://cccbdb.nist.gov/.

(45) Lifshitz, C.; Wu, R. L. C.; Tiernan, T. O.; Terwilliger, D. T. Negative Ion–Molecule Reactions of Ozone and Their Implications on the Thermochemistry of O_3^-. *J. Chem. Phys.* **1978,** *68*, 247-260.

(46) Weber, M. E.; Elkind, J. L.; Armentrout, P. B. Kinetic Energy Dependence of $Al^+ + O_2 \rightarrow AlO^+ + O$. *J. Chem. Phys.* **1986,** *84*, 1521-1529.

(47) Frisch, M. J.; Trucks, G. W.; Schlegel, H. B.; Scuseria, G. E.; Robb, M. A.; Cheeseman, J. R.; Scalmani, G.; Barone, V.; Mennucci, B.; Petersson, G. A.et al.; Gaussian, Inc.: Wallingford, CT, USA, 2009.

(48) Becke, A. D. Density-Functional Thermochemistry. III. The Role of Exact Exchange. *J. Chem. Phys.* **1993,** *98*, 5648-5652.

(49) Lee, C.; Yang, W.; Parr, R. G. Development of the Colle-Salvetti Correlation-Energy Formula into a Functional of the Electron Density. *Phys. Rev. B* **1988,** *37*, 785-789.

(50) Becke, A. D. A New Mixing of Hartree–Fock and Local Density-Functional Theories. *J. Chem. Phys.* **1993,** *98*, 1372-1377.

(51) Perdew, J. P.; Ernzerhof, M.; Burke, K. Rationale for Mixing Exact Exchange with Density Functional Approximations. *J. Chem. Phys.* **1996,** *105*, 9982-9985.

(52) Adamo, C.; Barone, V. Toward Reliable Density Functional Methods without Adjustable Parameters: The PBE0 Model. *J. Chem. Phys.* **1999,** *110*, 6158-6170.

(53) Raghavachari, K.; Trucks, G. W.; Pople, J. A.; Head-Gordon, M. A Fifth-Order Perturbation Comparison of Electron Correlation Theories. *Chem. Phys. Lett.* **1989,** *157*, 479-483.

(54) Bartlett, R. J.; Watts, J. D.; Kucharski, S. A.; Noga, J. Non-Iterative Fifth-Order Triple and Quadruple Excitation Energy Corrections in Correlated Methods. *Chem. Phys. Lett.* **1990,** *165*, 513-522.

(55) Scuseria, G. E.; Lee, T. J. Comparison of Coupled-Cluster Methods which Include the Effects of Connected Triple Excitations. *J. Chem. Phys.* **1990,** *93*, 5851-5855.

(56) Crawford, T. D.; Stanton, J. F. Investigation of an Asymmetric Triple-Excitation Correction for Coupled-Cluster Energies. *Int. J. Quantum Chem.* **1998,** *70*, 601-611.

(57) Cao, X.; Dolg, M. Valence Basis Sets for Relativistic Energy-Consistent Small-Core Lanthanide Pseudopotentials. *J. Chem. Phys.* **2001,** *115*, 7348-7355.

(58) Dolg, M.; Stoll, H.; Preuss, H. Energy-Adjusted Ab Initio Pseudopotentials for the Rare Earth Elements. *J. Chem. Phys.* **1989,** *90*, 1730-1734.

(59) Lu, Q.; Peterson, K. A. Correlation Consistent Basis Sets for Lanthanides: The Atoms La–Lu. *J. Chem. Phys.* **2016,** *145*, 054111.

(60) Douglas, M.; Kroll, N. M. Quantum Electrodynamical Corrections to the Fine Structure of Helium. *Ann. Phys.* **1974,** *82*, 89-155.

(61) Reiher, M.; Wolf, A. Exact Decoupling of the Dirac Hamiltonian. II. The Generalized Douglas–Kroll–Hess Transformation up to Arbitrary Order. *J. Chem. Phys.* **2004,** *121*, 10945-10956.

(62) Schuchardt, K. L.; Didier, B. T.; Elsethagen, T.; Sun, L.; Gurumoorthi, V.; Chase, J.; Li, J.; Windus, T. L. Basis Set Exchange: A Community Database for Computational Sciences. *J. Chem. Inf. Model.* **2007,** *47*, 1045-1052.

(63) Feller, D. The Role of Databases in Support of Computational Chemistry Calculations. *J. Comput. Chem.* **1996,** *17*, 1571-1586.

(64) Dunham, J. L. The Energy Levels of a Rotating Vibrator. *Phys. Rev.* **1932,** *41*, 721-731.

(65) Foresman, J. B.; Frisch, A. *Exploring Chemistry with Electronic Structure Methods*; Gaussian: Pittsburgh, Pa., 1996.

(66) Huber, K. P.; Herzberg, G. *Molecular Spectra and Molecular Structure: IV. Constants of Diatomic Molecules*; Van Nostrand Reinhold: New York, 1979.

(67) Armentrout, P. B. The Bond Energy of ReO^+: Guided Ion-Beam and Theoretical Studies of the Reaction of Re^+ (^7S) with O_2. *J. Chem. Phys.* **2013,** *139*, 084305.

(68) Armentrout, P. B.; Li, F.-X. Bond Energy of IrO^+: Guided Ion-Beam and Theoretical Studies of the Reaction of Ir^+ (^5F) with O_2. *J. Phys. Chem. A* **2013,** *117*, 7754-7766.

(69) Hinton, C. S.; Citir, M.; Armentrout, P. B. Guided Ion-Beam and Theoretical Studies of the Reaction of Os^+ (^6D) with O_2: Adiabatic and Nonadiabatic Behavior. *Int. J. Mass Spectrom.* **2013,** *354–355*, 87-98.

(70) Sansonetti, J. E.; Martin, W. C. Handbook of Basic Atomic Spectroscopic Data. *J. Phys. Chem. Ref. Data* **2005,** *34*, 1559-2259.

(71) Holthausen, M. C.; Heinemann, C.; Cornehl, H. H.; Koch, W.; Schwarz, H. The Performance of Density-Functional/Hartree–Fock Hybrid Methods: Cationic Transition-Metal Methyl Complexes MCH_3^+ (M=Sc–Cu,La,Hf–Au). *J. Chem. Phys.* **1995,** *102*, 4931-4941.

(72) Rodgers, M. T.; Armentrout, P. B. A Critical Evaluation of the Experimental and Theoretical Determination of Lithium Cation Affinities. *Int. J. Mass Spectrom.* **2007,** *267*, 167-182.

(73) Martin, J. M. L. Ab Initio Total Atomization Energies of Small Molecules — Towards the Basis Set Limit. *Chem. Phys. Lett.* **1996,** *259*, 669-678.

(74) Demireva, M.; Armentrout, P. B. Gadolinium Cation (Gd^+) Reaction with O_2: Potential Energy Surface Mapped Experimentally and with Theory. *J. Chem. Phys.* **2017,** *146*, 174302.

(75) Demireva, M.; Armentrout, P. B. Activation of CO_2 by Gadolinium Cation (Gd^+): Energetics and Mechanism from Experiment and Theory. *Top. Catal.* **2017,** in press, DOI: 10.1007/s11244-017-0858-1.

(76) Ohanessian, G.; Brusich, M. J.; Goddard, W. A. Theoretical Study of Transition-Metal Hydrides. 5. HfH^+ through HgH^+, BaH^+ and LaH^+. *J. Am. Chem. Soc.* **1990,** *112*, 7179-7189.

(77) Alvarado-Swaisgood, A. E.; Harrison, J. F. Electronic and Geometric Structures of Scandium Hydride Cations (ScH^+ and ScH_2^+). *J. Phys. Chem.* **1985,** *89*, 5198-5202.

(78) Das, K. K.; Balasubramanian, K. Potential Energy Surfaces for YH_2^+ and ZrH_2^+. *J. Chem. Phys.* **1989,** *91*, 2433-2442.

(79) Pettersson, L. G. M.; Bauschlicher, C. W. Jr.; Langhoff, S. R.; Partridge, H. Positive Ions of the First- and Second-Row Transition Metal Hydrides. *J. Chem. Phys.* **1987,** *87*, 481-492.

(80) Rappé, A. K.; Upton, T. H. Activation of Dihydrogen by Scandium Ions. *J. Chem. Phys.* **1986,** *85*, 4400-4410.

(81) Schilling, J. B.; Beauchamp, J. L. Hydrocarbon Activation by Gas-Phase Lanthanide Cations: Interaction of Pr^+, Eu^+, and Gd^+ with Small Alkanes, Cycloalkanes, and Alkenes. *J. Am. Chem. Soc.* **1988,** *110*, 15-24.

CHAPTER 7

CONCLUSIONS AND OUTLOOK

In this dissertation, the reactivity and properties of gadolinium cation (Gd^+) have been investigated via gas-phase reactions with H_2, O_2, and CO_2 using guided ion beam tandem mass spectrometry (GIBMS) and quantum chemical calculations. These studies have demonstrated that Gd^+ behaves more similarly to the early transition metal cations scandium (Sc^+) and yttrium (Y^+) than most of the lanthanide cations, both in the activation of single covalent (H_2) and multiple covalent bonds (O_2 and CO_2). This has been attributed to the unusual ground state valence electron configuration of Gd^+ (^{10}D, $4f^7 5d^1 6s^1$), having two non-4f electrons, which is similar to the configurations of Sc^+ and Y^+ (which also have two valence electrons in d and/or s orbitals) compared with most lanthanide cations with $4f^n 6s^1$ configurations, where n refers to the remaining valence electrons.

GIBMS experiments have shown that Gd^+ reacts with O_2 and CO_2 to yield GdO^+ in exothermic and barrierless processes. These reactions are exothermic as a result of the strong bond that can be formed in GdO^+. As demonstrated in this dissertation, strong bonds between Gd^+ and O and Gd^+ and C are achieved from promotion of the 6s valence electron of Gd^+ to a 5d orbital. This essentially leads to formation of triple and double bonds in the oxide and carbide complexes, respectively, from interaction of two Gd^+ 5d electrons with the 2p electrons of O and C, as illustrated in Figure 7.1. Similar types of interactions,

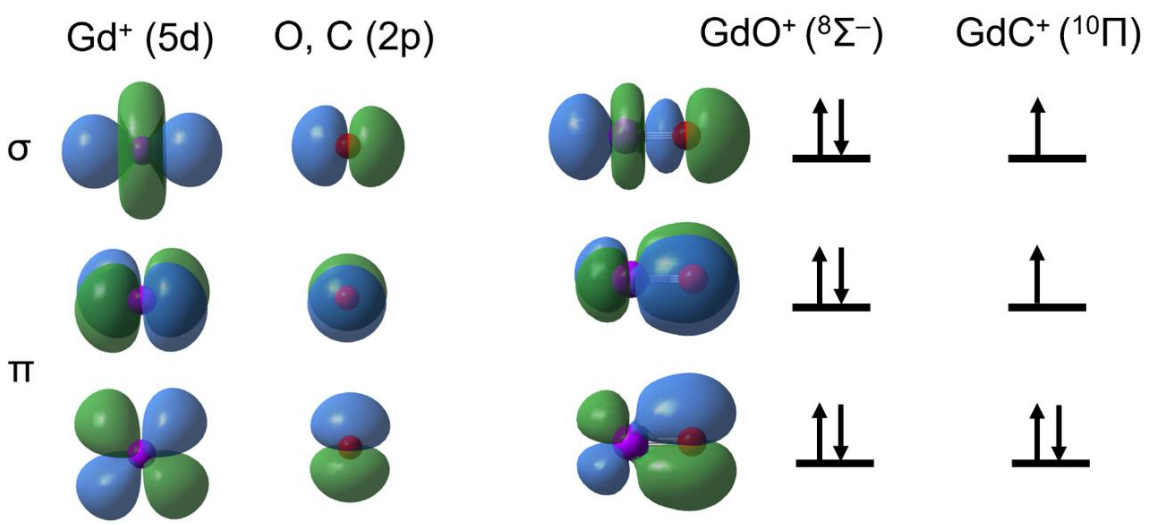

Figure 7.1. Bonding molecular orbitals resulting from the interaction between the 5d orbitals of Gd^+ and the 2p orbitals of O and C. Promotion of the 6s valence electron of Gd^+ to a 5d orbital to give a $5d^2$ configuration allows for triple and double bonds to be formed in GdO^+ and GdC^+, respectively, from interactions with the four and two 2p electrons of O and C, respectively.

requiring similar promotion energy costs, lead to strong oxide bonds for Sc^+ and Y^+ and result in similar reactivity with O_2 and CO_2. By probing the energetics of the intermediates in the Gd^+ reactions with O_2 and CO_2, nearly complete potential energy surfaces have been mapped from experiment for these processes. With the aid of theoretical calculations, interesting mechanistic differences between the activation of O_2 and CO_2 can be understood to arise predominantly from the required change of spin between ground state reactants and products. The CO_2 reaction is more constrained than the O_2 reaction, requiring a surface crossing in the entrance channel between ground state reactant and product surfaces. However, the CO_2 reaction can still essentially take place along a single surface below the reactant asymptote because of the unusual ground state valence electron configuration of Gd^+. In contrast, for many lanthanide cations the activation of CO_2 will exhibit a barrier because this crossing will occur above the reactant asymptote as a result

of the large promotion energy needed to access the potential energy surface correlated with the products, as has been observed in the activation of CO_2 by Sm^+.

Contrary to the results for the oxide and carbide bonds, the results for the hydrides have shown that Gd^+ differs in its interaction with H from Sc^+ and Y^+, which have somewhat larger hydride bond strengths than Gd^+. For Sc^+ and Y^+, the 4s and 5s orbitals primarily interact with the H(1s) orbital to form the hydride bond. In contrast, a 5dσ orbital (rather than the 6s orbital) of Gd^+ interacts with the 1s orbital of H to form the hydride bond, as illustrated in Figure 7.2. Moreover, because the 6s valence electron of Gd^+ remains in this atomic orbital in the ground state configuration of GdH^+ (Figure 7.2), it contributes a slightly repulsive interaction that weakens the GdH^+ 5dσ-H(1s) bond. Effects of promotion energy in the lanthanide cations will play a smaller role in the hydride bond strengths, which will depend on whether the bonding arises primarily from a 6s or 5dσ

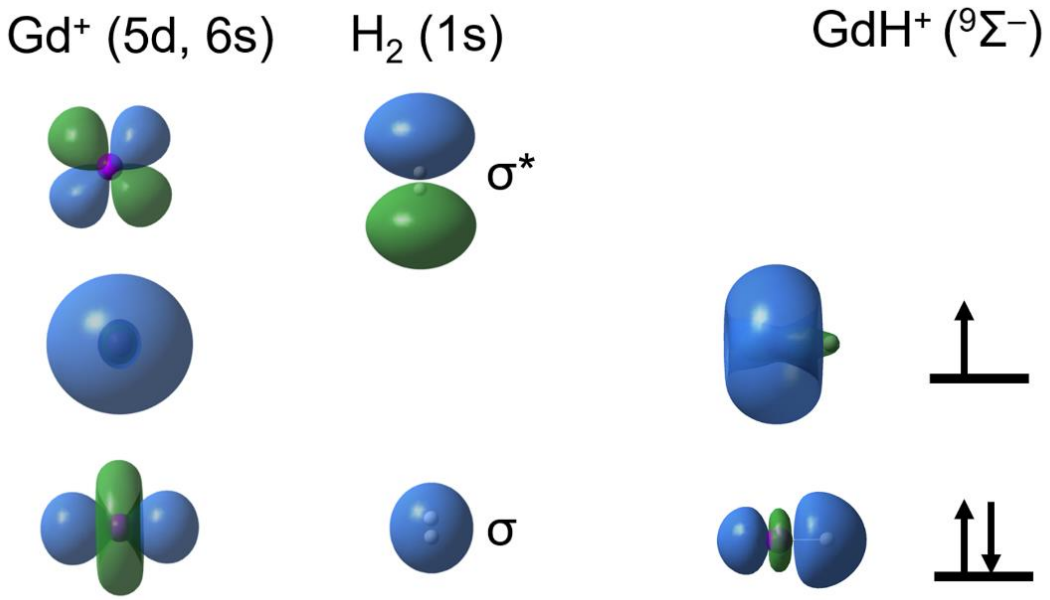

Figure 7.2. Illustration of the interactions arising from the Gd^+ 5d and H_2 σ bonding and σ* antibonding orbitals, that favor side-on reactions between Gd^+ and H_2. The ground state electronic configuration for GdH^+ indicates that the hydride bond is primarily formed from a Gd^+ 5dσ and H(1s) interaction.

interaction. This means that the hydride bond energies for many of these lanthanide cations will likely be comparable to that of Gd^+. In the endothermic activation of H_2 by Gd^+, theoretical calculations have demonstrated that the reaction can proceed via an inserted GdH_2^+ intermediate stabilized by interactions between two 5d orbitals of Gd^+ and the σ bonding and σ* antibonding molecular orbitals of H_2 (Figure 7.2). Reactions via this long-lived intermediate yield products through an insertion (statistical) mechanism. Direct pathways have also been shown to contribute to the reaction. Although the bonding interaction in GdH^+ has been shown to differ from that of Sc^+ and Y^+, the reactivity and mechanism with H_2 are nonetheless similar because of similar potential energy surfaces and promotion energies needed to form the MH_2^+ intermediate. In contrast, the activation mechanism of H_2 will likely differ for most lanthanide cations because forming an inserted MH_2^+ intermediate requires promotion of two valence electrons to 5d orbitals, such that this intermediate should be unstable (Figure 7.2). Therefore, reaction with H_2 for most lanthanide cations should follow a direct and/or impulsive mechanism rather than an insertion mechanism via a long-lived MH_2^+ intermediate. Similarly, the reactivities of these lanthanide cations with O_2 and CO_2 should generally differ from Gd^+. These reactions will be less exothermic (if exothermic at all) because both a 4f and 6s electron will need to be promoted to 5d orbitals resulting in a significant energy cost to form the triple bond in the corresponding oxide cations (Figure 7.1), and could also lead to barriers from required surface crossings to form ground state products.

The results presented in this dissertation have demonstrated that Gd^+ will generally exhibit similar properties and reactivities to Sc^+ and Y^+ compared with most lanthanide cations and can thus be considered for similar applications (e.g., in oxidation and

organometallic catalysis) as these metals. The high spin-quantum number for Gd^+ as a result of its seven unpaired electrons and its paramagnetism might provide additional properties that can be tailored for more specific purposes, for example in applications that utilize applied magnetic fields. Moreover, because Gd^+ forms a strong oxide bond as a result of the two available non-4f valence electrons (requiring only a small promotion energy cost), the chemi-ionization reaction for Gd is significantly exothermic. Therefore, Gd, which has a reasonably low boiling temperature, should be a promising candidate for atmospheric chemical release experiments that aim to create artificial electron dense plasmas in the ionosphere to prevent disruptions in satellite communications.